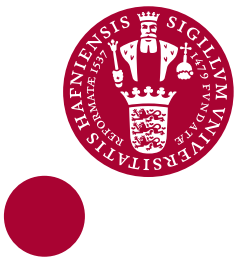

A Waveguide Platform for Collective Light-Atom Interaction

Sørensen, Heidi Lundgaard

Publication date:
2015

Document version
Publisher's PDF, also known as Version of record

Niels Bohr Institute, Faculty of Science
University of Copenhagen

PHD THESIS

HEIDI LUNDGAARD SØRENSEN

A waveguide platform for collective light-atom interaction

Danish Center for Quantum Optics (QUANTOP)
Niels Bohr Institute (NBI)
Graduate School of Science
Faculty of Science
University of Copenhagen (KU), Denmark

Academic supervisors:
Prof. Eugene S. Polzik
Assoc. Prof. Jürgen Appel
Assoc. Prof. Jörg H. Müller

A WAVEGUIDE PLATFORM FOR COLLECTIVE LIGHT-ATOM INTERACTION

HEIDI LUNDGAARD SØRENSEN

Principal supervisor:	Prof. Eugene S. Polzik
Additional supervisors:	Assoc. Prof. Jürgen Appel
	Assoc. Prof. Jörg H. Müller
PhD committee:	
External experts:	Prof. Luis A. Orozco (University of Maryland)
	Assoc. Prof. Jan Arlt (Aarhus University)
Local head:	Assoc. Prof. Namiko Mitarai (NBI)
Submission date:	December 21, 2015
Defense date:	January 22, 2016

This thesis has been submitted to the PhD School of The Faculty of Science, KU, and concludes Part B of the 4+4 PhD program.

ABSTRACT

In this work a tapered optical fiber is studied as a waveguide platform for efficient collective light-atom interaction. We present an all-computer controlled heat-and-pull setup with which a standard optical fiber can reproducible be tapered down to sub-micron waist size. The resulting fiber shape is compared against a prediction derived from a numerical model build upon an easy experimental calibration of the viscosity profile within the heater. Very good agreement between the modeled and measured fiber shape is found.

We next study the coherent back-scattering off atoms confined as two one-dimensional strings in the evanescent field of a tapered optical fiber. By applying a near-resonant standing wave field, the atoms are arranged into a periodic Bragg structure in close analogy to a photo-refractive medium with a refractive index grating. We observe more than 10 % power reflection off about 1000 structured atoms, corresponding to an enhancement of two orders of magnitude when compared to reflections off an unstructured atomic ensemble.

RESUME

Denne afhandling præsenterer et studie af en indsnævret optisk fiber, der virker som en lysleder platform for øget kollektiv vekselvirkning mellem lys og atomer. Heri præsenteres en computerstyret opstilling med hvilken almindelige optiske fibre på kontrolleret vis kan varmes og trækkes, indtil en diameter på kun 500 nm opnås. Formen af den resulterende overgang, der forbinder den oprindelige fiber med den tynde sektion, er blevet sammenholdt med en numerisk model. Denne bygger på en nem eksperimentel kalibrering af viskositetsprofilen i fiberen som følger af varmeelementet i opstillingen. Der er fundet god overensstemmelse mellem den målte form af den indsnævrede fiber og modellens forudsigelser.

Dernæst er den kohærente lysrefleksion fra to rækker af atomer, fastholdt i lysfeltet langs den indsnævrede fiber, undersøgt. Ved at påtrykke et stående bølgefelt med optisk frekvens nær den atomare resonans, drives atomerne ind i en periodisk struktur der giver anledning til Bragg spredning. Mere end 10 % lysrefleksion er målt for omkring 1000 strukturerede atomer, som til sammenligning er to størrelsesordener højere end den målte refleksion for ustrukturerede atomer.

PUBLICATIONS AND PRESENTATIONS

PEER-REVIEWED

[Béguin *et al.*, 2014] J.-B. Béguin, E. M. Bookjans, S. L. Christensen, H. L. Sørensen, J. H. Müller, E. S. Polzik, and J. Appel (2014). "Generation and Detection of a Sub-Poissonian Atom Number Distribution in a One-Dimensional Optical Lattice." *Physical Review Letters* **113.26**, p. 263603. DOI: 10.1103/PhysRevLett.113.263603.

[Christensen *et al.*, 2014] S. L. Christensen, J. B. Béguin, E. Bookjans, H. L. Sørensen, J. H. Müller, J. Appel, and E. S. Polzik (2014). "Quantum interference of a single spin excitation with a macroscopic atomic ensemble." *Physical Review A* **89.3**, p. 033801. DOI: 10.1103/PhysRevA.89.033801.

[Christensen *et al.*, 2013] S. L. Christensen, J. B. Béguin, H. L. Sørensen, E. Bookjans, D. Oblak, J. H. Müller, J. Appel, and E. S. Polzik (2013). "Toward quantum state tomography of a single polariton state of an atomic ensemble." *New Journal of Physics* **15.1**, p. 015002. DOI: 10.1088/1367-2630/15/1/015002.

[Sørensen *et al.*, 2014] H. L. Sørensen, E. S. Polzik, and J. Appel (2014). "Heater Self-Calibration Technique for Shape Prediction of Fiber Tapers." *Journal of Lightwave Technology* **32.10**, pp. 1886–1891. DOI: 10.1109/JLT.2014.2314319.

SUBMITTED

[Sørensen *et al.*, n.d.] H. L. Sørensen, J.-B. Béguin, K. W. Kluge, I. Iakoupov, A. S. Sørensen, J. H. Müller, E. S. Polzik, and J. Appel. "Coherent back-scattering of light off one-dimensional atomic strings." Submitted to Nature Physics.

PRESENTATIONS

[Sørensen, 2012] H. L. Sørensen (2012). *Nanofiber light-atom quantum interface*. Poster presentation at the Predoctorial School on Atom-Based Quantum Interfaces, Les Houches - France.

[Sørensen, 2013] H. L. Sørensen (2013). *Controlling the shape of tapered nanofibers*. Contributed talk at the ONNA 2013 workshop on Optical Nanofiber Applications: From Quantum to Bio Technologies, Okinawa - Japan.

[Sørensen, 2014] – (2014). *Heater self-calibration technique for shape prediction of fiber tapers*. Talk at a group seminar in Prof. Jakob Reichel's group, Laboratoire Kastler Brossel, Paris - France.

[Sørensen, 2015] – (2015). *One-dimensional atomic crystal mirror*. Poster presentation at the QUTE-EUROPE Summer School on Quantum Simulation and Computation: From fundamentals to applications and implementations, Gothenburg - Sweden.

ACKNOWLEDGMENTS

First, I would like to thank all my colleagues at QUANTOP. In particular, my teammates in the lab Stefan Lund Christensen, Jean-Baptiste Béguin, Eva Bookjans, and Kilian Kluge, and my theoretical colleague Ivan Iakoupov. I am aware, that I can have quite a temper at times (especially when there are things that I do not understand), but you have, nevertheless, always been calm and helpful when I needed it. For this I am grateful, and it has been a pleasure working with you.

Without good guidance I surely would not have made it far. I therefore want to especially thank my two co-supervisors Jürgen Appel and Jörg Helge Müller for all their help and patience, and for always keeping their doors open. And finally, a special thanks to Eugene Polzik, for giving me the opportunity of being part of this extraordinary research group and to dig deep into the quantum world.

Next, I would like to give a warm thanks to my family. Especially my parents and my sister for all their encouragement, extreme patience, and understanding of all the time I had to spend in a Copenhagen basement.

What is a person without good friends? I sincerely want to thank my closest friends, Sofie, Kenneth, and Stalden (aka Rebekka, Ane, and Hanne), for taking me out for a walk or run in the park, a cup of coffee, a good dinner and a beer, and for always being there when I need you.

Finally, above them all, thank you Helga. Thank you for making me laugh so much, and for always believing in me and supporting me. I simply couldn't have made it without you.

CONTENTS

1

INTRODUCTION

ENHANCING LIGHT-ATOM COUPLING

Nowadays, optical fibers are well-known objects to most people, as these low-loss waveguides, pioneered by Nobel laureate Charles K. Kao, offer fast internet connection via fiber cable networks utilizing light as a fast information carrier. For the realization of a quantum information network, guided light is likewise the obvious choice for the implementation of fast quantum communication channels between distant nodes [Cirac *et al.*, 1997; Duan *et al.*, 2001]. However, a challenge remains in reaching efficient coupling between the information carrying photons and stationary physical systems that serve as quantum memory stations or as units in which quantum gate operations can be performed for the implementation of quantum computational tasks [Nielsen *et al.*, 2000]. Here, optical waveguides are found to be promising platforms for efficient light-matter interactions [Bajcsy *et al.*, 2009; Goban *et al.*, 2015; Lodahl *et al.*, 2015]. Furthermore, such waveguides offer a natural extension to the already existing fiber network and thus provides an all-integrated and scalable "fiber-coupled quantum system".

Traditionally, enhanced coupling between light and atoms is realized in cavity QED experiments where a single or few atoms are trapped inside a high finesse optical resonator allowing for many interactions with the same photons [Miller *et al.*, 2005; Haroche *et al.*, 2006]. Another approach is to utilize collective effects where many atoms interact with the light field simultaneously [Hammerer *et al.*, 2010].

In 2003 Tong *et al.* demonstrated that low-loss optical waveguiding can be obtained from optical fibers tapered down to sub-micron diameters. This revived interest [Balykin *et al.*, 2004; Le Kien, Balykin, *et al.*, 2004] in the original proposal by Ovchinnikov *et al.* [1991] to trap cold atoms in the evanescent field near the dielectric-vacuum interface, in which strong coupling between atoms and a single guided mode in the tapered optical fiber can be achieved. After tackling numerous "trivial practical problems", this scheme has been realized experimentally and found to yield efficient collective light-atom coupling with optical depths of order 10 achieved with only about 10^3 atoms [Vetsch *et al.*, 2010; Goban *et al.*, 2012; Béguin *et al.*, 2014]. This constitutes a significant improvement compared to atoms trapped in

typical free-space optical dipole traps, where about 10^5 atoms are required to obtain similar values of the optical depth [Appel, Windpassinger, *et al.*, 2009].

This experimental progress, in turn, motivates now theorists to explore further the potential of the new platform. The strong coupling of photons with atoms placed in the proximity of a tapered optical fiber has been predicted recently to lead to long range interactions [Chang *et al.*, 2012; Chang *et al.*, 2013] with prospects to simulate quantum many-body models [Douglas *et al.*, 2015] in the spirit of the original proposal by Feynman [1982].

In this work we have taken the first steps towards such schemes and utilized the tight confinement of a guided mode in a tapered optical fiber to make about 10^3 atoms comprise an efficient one-dimensional mirror when the atoms are arranged in linear strings fulfilling the Bragg condition. As we shall see, an, in principle, simple experiment turned out to open Pandoras box revealing a rich system full of dynamics.

THESIS STRUCTURE

It has by now become a tradition in our group to write theses that are meant to be useful for the next generation of students. In this perspective, I have focused on writing in a pedagogical and enlightening style. As a result, there might appear paragraphs that are quite exhaustive and repeatable in style, especially for the reader that is already familiar with the subject. I can only hope, that I have managed to pass on the knowledge that I have accumulated over the last four years as a PhD student in Eugene Polzik's group.

PART I This thesis is centered around tapered optical fibers and we therefore start out by covering the important features of light propagating in such a waveguide. This includes a discussion of adiabatic tapers to ensure high light transmission through the tapered optical fiber, and a description of the field distribution of a quasi-linear polarization mode in the tapered optical fiber when configured as either a running wave or a standing wave. Control over the field polarization in the tapered optical fiber plays an important role in all our experiments and we therefore provide a description of how we experimentally configure it as a quasi-linear polarization mode. The part is concluded by first a description of our fiber pulling rig followed by a presentation on how the resulting shape of a tapered fiber can be numerically modeled by performing an initial calibration of the viscosity profile in the fiber provided by heater.

PART II Here a foundation to understand later parts involving light-atom interactions is provided. As such, it will be a rather theoretical section of the thesis where important concepts, such as the optical depth and the light dipole force, are introduced. Intended as an introduction of concepts and definitions, especially aimed towards the less experienced reader, an expert in the field might find most of the content trivial leisure reading. He or she should feel free to jump right ahead to PART III and use this part mainly as a reference guide for notation when necessary.

PART III In this part we present our experimental setup in which a tapered optical fiber is used as a quantum interface for light-atom interaction. We start out by showing how atoms are confined as two one-dimensional crystals in the evanescent field of a tapered optical fiber. This is followed by a description of the optical detection schemes that are implemented to probe the atoms. Finally, the part is concluded by a demonstration on how the number of trapped atoms is counted by a simple absorption measurement.

PART IV With all the basics ingredients now established, we here enter the main part of this thesis, in which we demonstrate how the atomic crystal can be made into a Bragg mirror. Starting with a general description of Bragg scattering we present two experimental schemes that have been utilized to create the atomic Bragg mirror, followed by a chapter in which the experimental details are further discussed. The remainder of the part is devoted to the presentation of a large fraction of the acquired experimental results.

PART V In this last part of the thesis, the experimental findings that have been obtained during this work are summarized and concluded, followed by an overview of future perspectives for collective light-atom interaction mediated by the platform provided by a tapered optical fiber.

Part I

AN INTRIGUING WAVEGUIDE

2

TAPERED OPTICAL FIBERS

This chapter serves to give an introduction to the concept of tapered optical fibers (TOFs). Starting with a brief introduction of step-index fibers (SIFs) in general, we move on to describe the spatial geometry of TOFs. This is followed by a brief discussion on how to solve Maxwell's equations for the guided mode propagation with the boundary conditions provided by the cylindrical fiber symmetry. The solutions form a discrete set of bounded modes of which a qualitative description is given. Before concluding the chapter with a graphical presentation of the field mode in the TOF waist, the field mode in the tapered part of the TOF is discussed and the adiabatic criterion is given.

Some parts of this chapter follow closely what has been reported previously in [Sørensen, 2013] concluding Part A of the 4+4 PhD program.

2.1 BRIEF INTRODUCTION TO STEP-INDEX FIBERS

A TOF is essentially the same as a regular SIF, *i.e.*, a long two-layered cylinder (Fig. 2.1) where the contrast in index of refraction between the two layers effectively creates an interface by which light can be guiding due to total internal reflection. From Snell's law it can be derived that this requires the inner layer, denoted the core, to have an index of refraction n_{co} greater than that of the surrounding cladding layer n_{cl}, see for example Hecht [2002]. For SIFs, made of high-purity fused silica, this is typically obtained by doping the core with germanium (Ge) which slightly in-

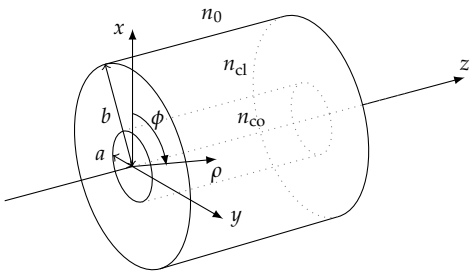

Figure 2.1.: *Step-index fiber.*

creases n_{co}. In the frame of cylindrical coordinates, with basis vectors[1] $\{\mathbf{u}_\rho, \mathbf{u}_\phi, \mathbf{u}_z\}$, we therefore have (*cf.* Fig. 2.1):

$$n(\rho) = \begin{cases} n_{co} & \text{if } \rho < a, \\ n_{cl} & \text{if } a < \rho < b, \\ n_0 & \text{if } b < \rho, \end{cases} \tag{2.1}$$

with $n_{cl} < n_{co}$, and with the index of refraction of the medium embedding the fiber often taken to be that of vacuum; $n_0 = 1$. For the single-mode fibers used in this work, typical values for the core (cladding) diameter and index of refraction are $2a = 5.5\,\mu m$ ($2b = 125\,\mu m$) and $n_{co} = 1.4650$ ($n_{cl} = 1.4573$).

2.2 TOF GEOMETRY

The geometry of a TOF can be described much like that of a SIF. Again, light is guided by a core-cladding interface due to the contrast in index of refraction between the two layers. The thickness of the fiber is, however, now comparable to the wavelength of the propagating light field, and the cladding is therefore taken to be that of the surrounding vacuum, such that:

$$n(\rho) = \begin{cases} n_{co} & \text{if } \rho < a, \\ n_{cl} & \text{if } \rho > a, \end{cases} \tag{2.2}$$

where a is now the radius of (the waist section of) the fiber and $n_{cl} = n_0$. As we shall see later, in Chapter 4, a TOF can be made by heating a small section of a SIF while pulling the two fiber ends apart. This results in the TOF geometry illustrated in Fig. 2.2. The thinnest section

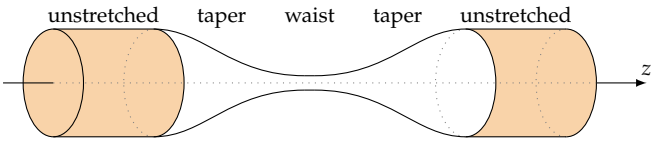

Figure 2.2.: *General geometry of a TOF together with the nomenclature used to label the different sections of the fiber.*

of the TOF, denoted the waist, is connected to the unstretched parts of the SIF, by two tapered sections. The waist, loosely referred to as the TOF or fiber throughout the thesis, is thus an integrated part of an ordinary SIF. This is an important detail, as light can then easily be coupled into the TOF by standard fiber coupling techniques into the SIF.

1 All vector quantities will be denoted by bold letters throughout the thesis and unit vectors will in addition be indicated by the letter u.

As the tapers form the spatial transitions between the three straight sections, they constitute the most critical part of the TOF. Preferably, they should be formed such that a guided field mode in the SIF adiabatically transforms into a guided mode in the TOF. This imposes a set of constraints to the spatial shape and challenges the fiber pulling. In Chapter 4 the fiber pulling is presented in greater details, together with a continued discussion on the taper shapes and the adiabatic criterion provided below in Section 2.4.1.

2.3 LIGHT PROPAGATION

To be able to use a TOF as an interface for light-atom interactions, it is of crucial importance that the field distribution of guided modes is known in detail. This can be calculated by solving Maxwell's famous equations[2]:

$$\boldsymbol{\nabla} \cdot \mathbf{D} = 0\,, \tag{2.3a}$$
$$\boldsymbol{\nabla} \cdot \mathbf{H} = 0\,, \tag{2.3b}$$
$$\boldsymbol{\nabla} \times \mathbf{E} = -\mu_0 \frac{\partial \mathbf{H}}{\partial t}\,, \tag{2.3c}$$
$$\boldsymbol{\nabla} \times \mathbf{H} = \frac{\partial \mathbf{D}}{\partial t}\,, \tag{2.3d}$$

with

$$\mathbf{D}(\mathbf{r},t) = \epsilon_0 \mathbf{E}(\mathbf{r},t) + \mathbf{P}(\mathbf{r},t) = \epsilon_0 n^2(\rho)\mathbf{E}(\mathbf{r},t) \tag{2.4}$$

being the electric field displacement, $\mathbf{E}$ the electric field, and

$$\mathbf{P}(\mathbf{r},t) = \epsilon_0 \chi(\omega)\mathbf{E}(\mathbf{r},t) \tag{2.5}$$

the polarization response of the medium to the electric field characterized by the (complex linear) dielectric susceptibility χ. $\mathbf{B} = \mu_0 \mathbf{H}$ is the magnetic field, and ϵ_0, μ_0 are the vacuum permittivity and vacuum permeability respectively.

Maxwell's equations, bounded by the two-layer geometry valid for the unstretched parts and the waist (*cf.* Eq. (2.2) and Fig. 2.2), have been solved in several textbooks, *e.g.*, [Boyd, 2008; Snyder *et al.*, 1983; Ghatak *et al.*, 1998] (with $n_{\mathrm{cl}} = n_{\mathrm{glass}}$) and theses oriented specifically towards TOFs (*i.e.*, with $n_{\mathrm{cl}} = n_0$) [Cassany, 2009; Béguin, 2015], which we encourage the reader to consult. In the following, we therefore restrict ourselves to a somewhat superficial treatment of the light propagation in fibers, highlighting only the main steps and results in the derivation of the guided field modes as obtained in the above mentioned references.

2 Written here for a non-conductive, non-magnetic, isotropic, and homogeneous dielectric medium such as glass.

2.3.1 *Main steps in solving Maxwell's equations*

From Maxwell's equations (2.3) the wave equation for an electric field propagating in a dielectric medium can be deduced:

$$\left(\nabla^2 - \mu_0\epsilon_0 n(\rho)^2 \frac{\partial^2}{\partial t^2}\right)\mathbf{E} = -\boldsymbol{\nabla}\left(\frac{\mathbf{E}\cdot\boldsymbol{\nabla}n^2(\rho)}{n^2(\rho)}\right). \tag{2.6}$$

Inserting the fiber boundary conditions (2.2) the gradient $\boldsymbol{\nabla}n^2(\rho)$ is found to be zero when $\rho \neq a$. The right-hand side (RHS) in Eq. (2.6) hence also equates to zero and the wave equation reduces to the simpler Helmholtz equation. Because of the cylindrical fiber geometry, the solutions should be translational invariant along the fiber axis. This makes it possible to separate them into a transverse and longitudinal part and leads to the following ansatz for the electric field at a given position $\mathbf{r}$ and time t:

$$\mathbf{E}(\mathbf{r}, t) = \boldsymbol{\mathcal{E}}(\rho, \phi)\mathrm{e}^{i(\omega t - \beta z)}. \tag{2.7}$$

Here $\boldsymbol{\mathcal{E}}$ is the electric field amplitude, ω is the angular frequency of the oscillating field, and β is the propagation constant. Inserting Eq. (2.7) into Eq. (2.6) we find for the z-component of the electric field

$$\left(\frac{\partial^2}{\partial\rho^2} + \frac{1}{\rho}\frac{\partial}{\partial\rho} + \frac{1}{\rho^2}\frac{\partial^2}{\partial\phi^2} + \left(k^2 - \beta^2\right)\right)\mathcal{E}_z(\rho, \phi) = 0, \tag{2.8}$$

where $k = \omega n(\rho)/c$ is the wavenumber of the electric field propagating inside the dielectric, and $c = (\mu_0\epsilon_0)^{-1/2}$ is the speed of light in vacuum. The transverse electric field in the Helmholtz equation (2.8) can be further separated in the remaining two variables, $\mathcal{E}(\rho, \phi) = R(\rho)\Phi(\phi)$, where the angular part can readily be obtained by introducing the separation constant [Riley *et al.*, 2006]:

$$l^2 = -\frac{1}{\Phi}\frac{\partial^2\Phi}{\partial\phi^2}, \tag{2.9}$$

with solution

$$\Phi(\phi) = \mathrm{e}^{\pm il\phi}. \tag{2.10}$$

Since the azimuthal solution has to be single-valued, *i.e.*, $\Phi(\phi + 2\pi) = \Phi(\phi)$, l is restricted to take on an integer value.

What remains is then to obtain the solution for the radial part $R(\rho)$. Inserting $\mathcal{E}(\rho, \phi) = R(\rho)\mathrm{e}^{\pm il\phi}$ into Eq. (2.8), multiplying through with ρ^2, and introducing a new variable $r^2 = \rho^2\left(k^2 - \beta^2\right)$ leads to:

$$\left(r^2\frac{\partial^2}{\partial r^2} + r\frac{\partial}{\partial r} + \left(r^2 - l^2\right)\right)R(r) = 0, \tag{2.11}$$

which can be recognized as Bessel's equation with general solutions given by the Bessel functions of order l. The exact form of the solutions depend on whether $k^2 < \beta^2$ or $k^2 > \beta^2$. Importantly, and

also rather intuitively, it is found from the solutions that guided fiber modes only exist if the inequality

$$n_{\mathrm{cl}} < \frac{\beta}{k_0} = n_{\mathrm{eff}} \leq n_{\mathrm{co}} \tag{2.12}$$

is fulfilled, where $k_0 = \omega/c$ is the free-space wavenumber, and the effective index of refraction n_{eff} has been introduced as the normalized propagation constant.

So far, we have only considered the electric field part of the propagating electro-magnetic wave. Conveniently, from the symmetry of Maxwell's equations (2.3), the magnetic field can be treated similarly. On top of that, it is sufficient to only solve for the z-component of the electric field. Here two things are worth noting: (i) From the solutions of $\mathcal{E}_z(\rho, \phi)$, and the equivalent for the magnetic field $\mathcal{H}_z(\rho, \phi)$, it is possible to obtain all the remaining components of the electric and magnetic fields from the cylindrical symmetry of the fiber. (ii) Contrary to an electro-magnetic wave propagating in free-space, the two longitudinal components along the propagation direction are not necessarily zero. In fact, as we shall see later in Section 2.5, the longitudinal field strength can be quite significant in the fiber waist and should therefore not be neglected.

In the following we give a more qualitative description of the solutions and present graphs for the electric field distribution of the fundamental mode. Especially these graphs contain crucial information that are necessary in order to understand any light-atom interactions that are mediated by the use of a TOF as a quantum interface.

2.3.2 *Exact solutions*

The solutions for the bounded field modes are usually divided into two subgroups: hybrid modes and transverse modes. The hybrid modes contain both electric and magnetic field components along the fiber axis and are denoted HE (EH) when $\mathcal{E}_z$ is smaller (larger) than $\mathcal{H}_z$. Each mode is characterized by a pair of indices: an azimuthal index $l = 1, 2, 3, \ldots$ (*cf.* Eq. (2.9)) for each of which there exists a range of radial solutions $m = 1, 2, 3, \ldots$, corresponding to a discrete set of guided modes in the fiber.

The transverse modes are nothing but a special case of the hybrid modes with $l = 0$. For the HE modes this means that the electric field component in the propagation direction vanish, and they are thus said to be TE. Similarly, the longitudinal magnetic field component vanish for the EH modes, when $l = 0$, and they are then called TM.

To get a feeling for the nature of the guided field modes, it is helpful to consider Fig. 2.3 depicting the guided light rays and accompanying

electric field lines for the transverse and hybrid modes. The light rays

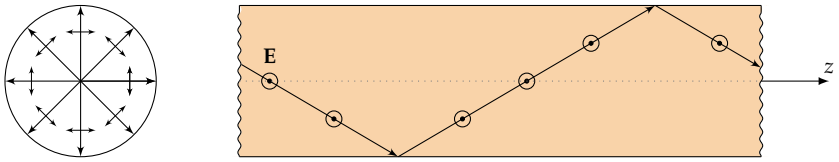

(a) TE_{01} mode. $\mathcal{E}_\phi, \mathcal{H}_\rho, \mathcal{H}_z \neq 0$, $\mathcal{E}_\rho = \mathcal{E}_z = \mathcal{H}_\phi = 0$.

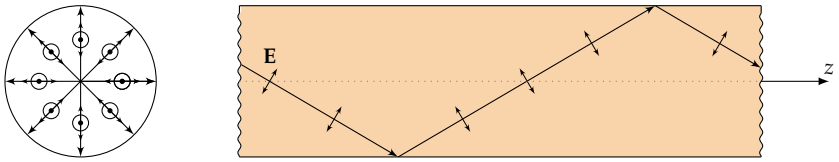

(b) TM_{01} mode. $\mathcal{E}_\rho, \mathcal{E}_z, \mathcal{H}_\phi \neq 0$, $\mathcal{E}_\phi = \mathcal{H}_\rho = \mathcal{H}_z = 0$.

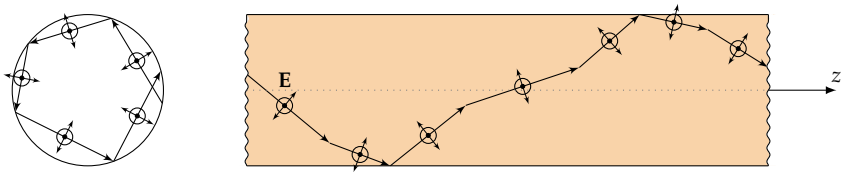

(c) Hybrid mode. $\mathcal{E}_\rho, \mathcal{E}_\phi, \mathcal{E}_z, \mathcal{H}_\rho, \mathcal{H}_\phi, \mathcal{H}_z \neq 0$.

Figure 2.3.: *Propagating light rays in the fiber, depicted together with the electric field lines. A transverse cross-section of the fiber is shown to the left, while a longitudinal cross-section is shown to the right (having a yellowish background). Note that only vertical light rays are shown in the longitudinal cross-section in (a) and (b), while both horizontal and vertical components are contained in the transverse cross-section. Inspired by [Cassany, 2009, Fig. 1.3 and 1.4], and [Snyder* et al., *1983, Fig. 11-2].*

of the transverse modes always intersect the fiber axis as necessary for the electric (Fig. 2.3(a)) or magnetic (Fig. 2.3(b)) field to be purely transverse. For the TE_{01} mode only circular field lines are present for the electric field, while the electric field lines for the TM_{01} mode can be decomposed into perpendicular and parallel components to the fiber axis. In contrary to the transverse modes, the hybrid modes have non-zero components of both the electric and magnetic field in all directions and hence circulate around the fiber axis without ever passing through it.

2.3.3 *Approximative solutions*

Most people familiar with SIFs often work with a set of approximate solutions to Maxwell's equations (2.3), known as the linearly polarized (LP) modes, instead of the exact solutions presented in Section 2.3.2. It can therefore be instructive to also consider these modes and their connection to the exacts solutions. From Snell's law, light

will be guided by the cladding-core interface of the fiber only if the angle of incidence θ_i, formed by the incoming wavevector and the fiber axis, fulfills the inequality:

$$\sin\theta_i \leq (n_{co}^2 - n_{cl}^2)^{1/2}, \quad \text{for } n_0 = 1. \tag{2.13}$$

For a typical SIF the core index of refraction is only slightly higher than the cladding: $n_{co} \approx n_{cl}$. For this reason, only incident light rays near parallel to the fiber axis are sustained, and the fiber is said to be weakly guiding[3]. In this limit, the field can therefore be assumed transverse to the fiber axis and its longitudinal components along the propagation direction can hence be neglected. The solutions to Maxwell's equations, within this approximation, are the LP modes. These are actually linear combinations of the exact modes and can be grouped according to:

$$\mathrm{LP}_{0m} : \mathrm{HE}_{1m} \tag{2.14a}$$

$$\mathrm{LP}_{1m} : \mathrm{HE}_{2m}, \mathrm{TE}_{0m}, \mathrm{TM}_{0m} \tag{2.14b}$$

$$\mathrm{LP}_{lm} : \mathrm{HE}_{l+1,m}, \mathrm{EH}_{l-1,m}, \quad \text{for } l \geq 2. \tag{2.14c}$$

As an example of this we consider Fig. 2.4. Here the TE_{01} and HE_{21} modes are combined to constitute the $\mathrm{LP}_{11} = \mathrm{TE}_{01} \pm \mathrm{HE}_{21}$ mode for two different spatial and polarization configurations. The shaded

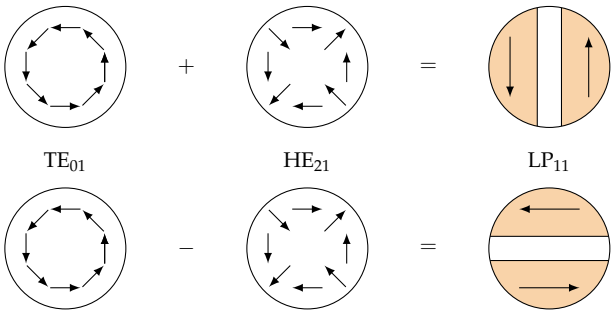

Figure 2.4.: *Combining the TE_{01} and HE_{21} modes forms the LP_{11} mode for two different polarization and spatial configurations. Only the transverse polarization in the fiber cross-section is shown thereby neglecting the z-component of the hybrid mode. Inspired by [Snyder* et al.*, 1983, Fig. 14-5(d)].*

regions indicate the intensity distribution similar to that shown in Fig. 2.5, which displays the intensity distribution for the four lowest order LP modes. Two more polarization configurations exist for the LP_{11} mode[4], and are obtained by combining the TM_{01} and HE_{21}

3 If the reader is familiar with optical fibers, he or she can most likely recall the frustrating experience of trying the first time to couple light into a single-mode fiber!

4 For all $lgeq1$ modes there exist four independent combinations of the polarization and intensity distribution. For the $l = 0$ modes only two independent combinations exist because of their circular symmetry.

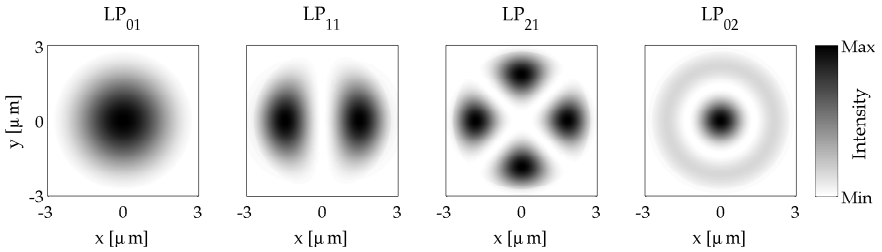

Figure 2.5.: *Intensity distribution for the four lowest order LP_{lm} modes in a SIF calculated for the parameters $2a = 5.5\,\mu m$, $\lambda = 852\,nm$, $n_{co} = 1.4650$, and $n_{co} = 1.4573$. The plot was generated using open-source MATLAB code provided by Bojor [2005].*

modes. This yields similar intensity distributions to the ones shown in Fig. 2.4 but with the polarization rotated by 90°.

When light is guided by the core-air interface, at the TOF waist, the approximation $n_{co} \approx n_{cl}$ breaks down. In this regime, the modes can no longer be regarded as mainly transversal and the LP modes are no longer an adequate description of the guided modes. They, nevertheless, provides a more convenient platform for the understanding on how different modes couple in the tapers via the arrangement in Eq. (2.14) (this will become more clear in Section 4.1.3).

2.3.4 *Propagation constant*

Since the field distribution of each bounded mode in the fiber is uniquely described by a set of azimuthal and radial indices, each mode is also characterized by a correspondingly unique propagation constant β_{lm}, *cf.* Eq. (2.12). This is actually not surprising, as each of the different spatial modes necessarily must be influenced differently by the spatial boundaries set by the two indices of refraction that characterizes the fiber, n_{co} and n_{cl}.

As an illustration of this we consider Fig. 2.5, showing the intensity distribution of the first four LP modes. The lowest order mode LP_{01} is seen to resemble much that of a Gaussian distributed mode with a high intensity along the fiber axis z that decays radially from the fiber axis[5]. A main part of this mode is hence contained inside the core, and its effective index of refraction is therefore expected to resemble the core index of refraction, *i.e.*, $n_{eff} = \beta/k_0 \lesssim n_{co}$. For the higher order modes, it is evident that their spatial distributions extend more and more into the surrounding cladding and n_{eff} for these modes should therefore be correspondingly lower and move closer to n_{cl}. The argumentation presented here for the LP modes also holds for

5 Mainly this mode is exited for an incident Gaussian beam to the fiber.

the exact solutions, and it should hopefully be clear now, why the inequality in Eq. (2.12) necessarily must be true.

The propagation constant is in the end nothing but the effective wavenumber k in the fiber. In Table 2.1 the free-space wavelengths of the three colors used in this work is listed together with their corresponding wavelengths in the TOF.

WAVELENGTH	
FREE-SPACE (λ)	TOF WAIST (λ^{TOF})
780 nm	661 nm
852 nm	743 nm
1057 nm	985 nm

Table 2.1.: *Effective wavelengths in the TOF $\lambda^{TOF} = 2\pi/\beta$ for the three colors used in this work listed together with their free-space wavelength. Calculated for the parameters $n_{co} = 1.45732$, $n_{cl} = 1$, $a = 250\,\mathrm{nm}$*

2.3.5 *V-number and cutoff*

When continuing the derivation of the electric field to Maxwell's equations, as started in Section 2.3.1, two quantities naturally emerge from the calculations, namely the core and cladding parameters, defined as [Snyder *et al.*, 1983]

$$U = a(k_0^2 n_{\mathrm{co}}^2 - \beta^2)^{1/2} = ak_0(n_{\mathrm{co}}^2 - n_{\mathrm{eff}}^2)^{1/2}\,, \tag{2.15a}$$

$$W = a(\beta^2 - k_0^2 n_{\mathrm{cl}}^2)^{1/2} = ak_0(n_{\mathrm{eff}}^2 - n_{\mathrm{cl}}^2)^{1/2}\,, \tag{2.15b}$$

respectively (also see Appendix A where the solution for the electric field of the HE_{11} mode with quasi-linear polarization is given together with relevant quantities). From Eq. (2.15) the waveguide parameter is defined as

$$V = (U^2 + W^2)^{1/2} = \frac{2\pi a}{\lambda}(n_{\mathrm{co}}^2 - n_{\mathrm{cl}}^2)^{1/2}\,, \tag{2.16}$$

also simply known as the V-number. Here $\lambda = 2\pi/k_0$ is the free-space wavelength of the input field to the fiber. The V-number is related to the number of bound modes that can propagate in the fiber[6]. As we already argued, the more a given mode extend into the cladding the closer its effective index of refraction n_{eff} gets to n_{cl}. Ultimately, if the core diameter keeps decreasing or yet higher order

6 For $V \gg 1$ the number of bound modes scales with V^2.

modes are considered, $n_{\text{eff}} \to n_{\text{cl}}$ and hence $W \to 0$ for a given mode. When this happens, the inequality $n_{\text{eff}} > n_{\text{cl}}$ is no longer satisfied and the (core) mode is no longer guided by the core-cladding interface. Depending on whether the fiber geometry is described by that of SIFs, Eq. (2.1), or TOFs, Eq. (2.2), *i.e.*, by three or two layers, the mode either becomes a cladding mode, guided by the cladding-vacuum interface, or a radiative mode completely lost from the waveguide. Using $W = 0$ in Eq. (2.16) the cutoff condition, that is, when a mode is no longer guided, is defined as

$$V_{\text{cut}} = U = \frac{2\pi a}{\lambda}(n_{\text{co}}^2 - n_{\text{cl}}^2)^{1/2}\,. \tag{2.17}$$

The particular cutoff values for each mode can be obtained by careful evaluation of the transcendental equation for the propagation constant given in Appendix A. Here, we will suffice to give the simple example for the TE_{0m} modes, for which the expression

$$\frac{J_1(U)}{UJ_0(U)} = -\frac{K_1(W)}{WK_0(W)} \tag{2.18}$$

has be to be fulfilled [Snyder *et al.*, 1983]. Here, J_l is the Bessel function of the first kind of order l, and K_l is the modified Bessel function of the second kind of order l. At cutoff, the RHS in Eq. (2.18) is seen to diverge as $W \to 0$. For the expression to be true, the left-hand side (LHS) then also has to diverge which can only be obtained by having $J_0(U) = 0$. Most known is perhaps the first zero for $J_0(U)$ occurring at $U = 2.405$. The cutoff value for the TE_{01} mode is thus given by $V_{\text{cut}} = 2.405$, for the TE_{02} mode it is $V_{\text{cut}} = 5.520$, the TE_{03} mode has $V_{\text{cut}} = 8.654$, *etc*.

As it turns out, all modes, but the HE_{11} mode, have a finite cutoff value associated with it for a given wavelength. The HE_{11} mode is thus a bound fiber mode for all values of the V-number and, for this reason, referred to as the fundamental mode in the fiber.

In Fig. 2.6 the effective index of refraction is shown, plotted against the V-number, Eq. (2.16), for a selection of lowest order modes bounded by the TOF geometry in Eq. (2.2).

As discussed above, it is evident from the blue dashed line that the TE_{01} mode is cutoff at $V = 2.405$. On top of that, we now also see, that this mode, together with the TM_{01} mode, are the most persistent modes in the fiber, which thus becomes single-mode when $V \leq 2.405$. As expected, n_{eff} for each modes is comparable to n_{co} for high V-numbers and then observed to decrease towards n_{cl} as the V-number decreases making each mode extend further into the cladding. The cutoff diameter for the different modes in Fig. 2.6 can be found in Table 2.2

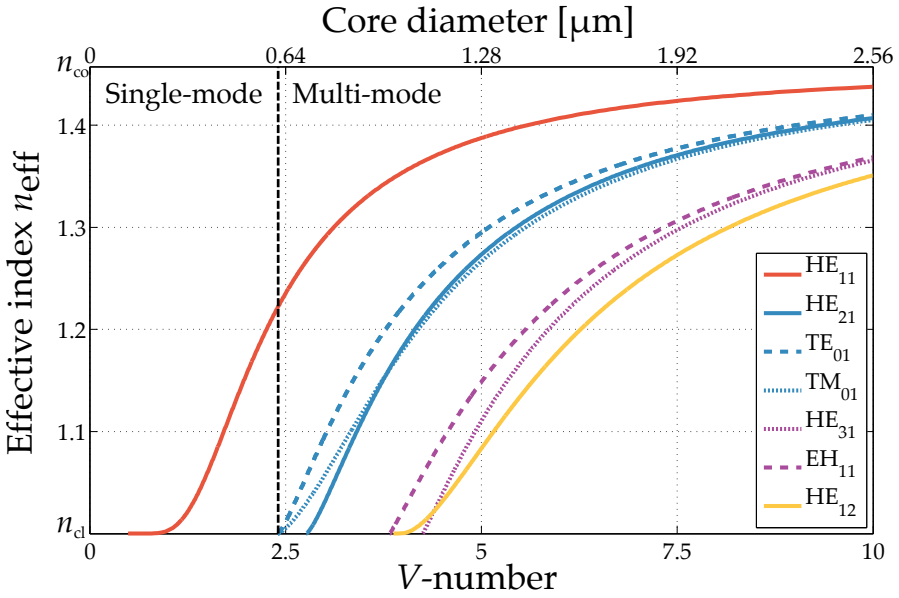

Figure 2.6.: *Effective index of refraction for a small collection of bounded modes as a function of the V-number (bottom) core diameter (top) for* $\lambda = 852\,\text{nm}$. *The plot is made using* $n_{cl} = n_0 = 1$, *and* $n_{co} = 1.45732$. *The modes are color grouped according to the approximative* LP_{lm} *modes: red,* LP_{01}; *blue,* LP_{11}; *purple,* LP_{21}; *and yellow,* LP_{02}. *The vertical black dashed line at* $V = 2.405$, $d = 0.615\,\mu\text{m}$ *indicates the boundary between single- and multi-mode guidance.*

2.4 SLOWLY-VARYING TAPERS

Until now, we have only discussed the solutions to Maxwell's equations for the cylindrical two-layer fiber geometry, whereas we have completely neglected the two spatial transitions connecting the TOF waist with the unstretched SIF, *cf.* Fig. 2.2. In the following we therefore turn our attention toward this part of the TOF. This is necessary in order to understand how the modes are transformed from the unstretched fiber to the waist and back again without experiencing severe loss in optical power.

As apparent from Fig. 2.2 the boundary conditions, Eq. (2.2), at the fiber tapers are non-static. At these sections the fiber can therefore not be regarded as translational invariant and no exact solutions exists for Maxwell's equations. It is, nonetheless, reasonable to assume that the modes of the uniform fiber can be used as approximative solutions if the tapers are slowly-varying [Snyder *et al.*, 1983, Chap. 19]. Within

APPROXIMATIVE	EXACT	CUTOFF DIAMETER [µm]
LP_{01}	HE_{11}	N/A
LP_{11}	HE_{21} , TE_{01} , TM_{01}	0.71, 0.62, 0.62
LP_{21}	HE_{31} , EH_{11}	1.09, 0.98
LP_{02}	HE_{12}	0.99

Table 2.2.: *Cutoff diameter for the first seven modes, grouped according to the LP modes, for the same parameters as in Fig. 2.6.*

this assumption an electric field mode in the taper can be described as[7]

$$\mathbf{E}(\mathbf{r}) = \boldsymbol{\mathcal{E}}(\rho, \phi, \beta(z))\mathrm{e}^{-i\int_0^z \beta(\zeta)\,\mathrm{d}\zeta}\,. \tag{2.19}$$

If the initial SIF, constituting the unstretched part of the fiber, is single-mode the taper necessarily also support only the fundamental mode in the core since the V-number, Eq. (2.16), exclusively decrease for decreasing core radius. But as the fiber becomes thinner, the guided core mode starts to leak out of the core into the cladding and is eventually guided by the glass-vacuum interface. When this happens, the TOF becomes (locally) highly multi-mode, as evident from Fig. 2.6 (where the new core is now the old cladding), and not until the fiber diameter reaches 0.62 µm does the fiber again become single-mode, *cf.* Table 2.2.

The transition of the fundamental mode from a core-guided mode to a cladding-guided mode is a critical step in the taper. If the transition happens too abrupt, higher order cladding-modes might get excited, which leads to losses in optical power when these modes are no longer supported by the thin fiber and hence lost as radiative modes. To ensure a high optical coupling from the unstretched part into the waist, an adiabatic transfer of the, initially core-guided, fundamental mode, into local cladding-guided fundamental modes along the taper only, is sought. In [Love *et al.*, 1986; Love *et al.*, 1991] this is accomplished by imposing the same criterion as that necessary for the validity of Eq. (2.19), namely slowly-varying tapers.

7 Basically, if we if zoom in sufficiently close to a point on the taper, the vicinity of it will appear as a flat cylindrical section (and not as a cone), at which we can apply the framework used in Section 2.3.1 to solve Maxwell's equations. We thus end up having a set of local solutions along the taper. This method is of course only valid as long as the boundaries only change gradually.

2.4.1 *Adiabatic criterion*

In [Snyder *et al.*, 1983], the slowly-varying criterion, also known as the adiabatic criterion, is quantified by introducing a local coupling length z_{beat}. This is defined as the wavelength of the beat note arising from the interference between the local fundamental mode, having propagation constant β_1, and the local higher order mode with propagation constant β_2 nearest to β_1:

$$z_{\text{beat}} = \frac{2\pi}{\beta_1(z) - \beta_2(z)}\,. \tag{2.20}$$

This is then to be compared with a relevant length scale of the taper, taken as the local taper length z_{taper} defined through the local taper angle:

$$\Omega(z) = \arctan\left(\frac{\rho(z)}{z_{\text{taper}}}\right) \approx \frac{\rho(z)}{z_{\text{taper}}}\,, \tag{2.21}$$

where $\rho(z)$ is the local core radius as illustrated in Fig. 2.7. When

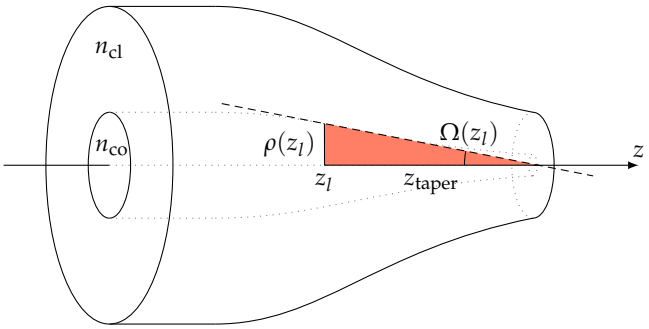

Figure 2.7.: *Fiber taper. The dashed line is tangent to the core slope at point z_l where the local core radius is $\rho(z_l)$. The local taper angle $\Omega(z_l)$ is the angle spanned by the tangent and the fiber axis. The local taper length z_{taper} is the cathetus adjacent to $\Omega(z_l)$.*

the local taper length is long compared to the local coupling length, $z_{\text{taper}} \gg z_{\text{beat}}$, the fundamental mode can follow the surrounding variations in the boundary conditions and only negligible coupling to other modes takes place. If instead $z_{\text{taper}} \ll z_{\text{beat}}$, the fiber boundaries change within a single beat wavelength and hence distort the propagating mode causing significant coupling to other local modes. This is quite analogous to the single-slit diffraction experiment. Here, light propagates unhindered along a single straight line as long as $\lambda \ll a$, where a is the characteristic length scale of the slit. If $\lambda \gtrsim a$, the light instead gets diffracted and thus couple into other propagation channels.

By equating the local taper length with the local coupling length, $z_{\text{taper}} = z_{\text{beat}}$, an upper bound can be placed on $\Omega(z)$. From Eq. (2.21)

and Eq. (2.20) the adiabatic criterion is thus established as the inequality

$$\Omega(z) \leq \frac{\rho(z)}{2\pi}\left(\beta_1(z) - \beta_i(z)\right), \tag{2.22}$$

that should be satisfied to minimize power loss from the fundamental mode.

In Fig. 2.8(a) the limiting upper bound on $\Omega(z)$ as a function of the normalized core radius $\rho(z)/a$ is shown, calculated[8] by the method described in [Love *et al.*, 1991]. Rather surprisingly at first, it is not a monotonically decreasing function for decreasing radius, as one would perhaps expect from the notion that when the fiber becomes thinner the mode also becomes more sensitive to its surroundings. This is true to some extend, for large core radii, where the upper

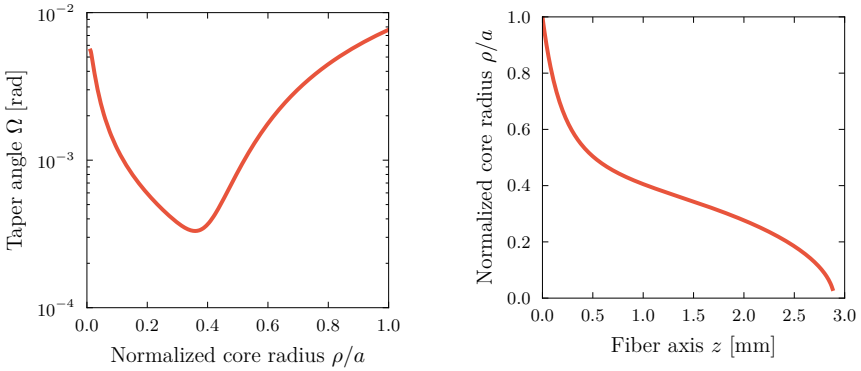

(a) (b)

Figure 2.8.: *Limiting taper angle (a) and resulting taper shape (b) calculated for the parameters* NA $= 0.115$, $n_{cl} = 1.45247$, $\rho_0 = 62.5\,\mu\text{m}$, $a = 2.75\,\mu\text{m}$, $\lambda = 852\,\text{nm}$ *corresponding to the fiber parameters used for the fiber pulling described in Chapter 4.*

bound of the taper angle indeed is found to reflect a stronger requirement of a gradual taper the thinner the core becomes. But then, suddenly, near $\rho = 0.4a$ a turning point is reached and the slowly-varying condition is loosened allowing for steeper taper angles as the core radius is further increased. Keeping in mind, that the fundamental mode undergoes a critical transition from a core-mode to a cladding-mode in the taper, the location of the minimum can be interpreted to correspond to the core radius at which this takes place, as was confirmed in [Love *et al.*, 1991] by thorough analytical investigation.

From the limiting taper angle in Fig. 2.8(a) the corresponding taper shape can be extracted as shown in Fig. 2.8(b). The limiting taper

8 For internal use: The script can be found in the `Mathematica` folder on `kahuna` saved as `lovefibermodes.nb`.

length turns out to be rather short, less than 3 mm, making it feasible[9] to actually produce adiabatic TOFs. To ensure that the adiabatic criteria is satisfied in practice, the taper can be made longer and more shallow, in fact, it might not even be possible with the available pulling equipment to actually make as short and steep tapers as that shown in Fig. 2.8(b). In Chapter 4 a more elaborate discussion on the pulling procedure and reported results for the optical power transmissions through TOFs are given.

2.5 QUASI-LINEAR FIELD MODE DISTRIBUTION AT THE TOF WAIST

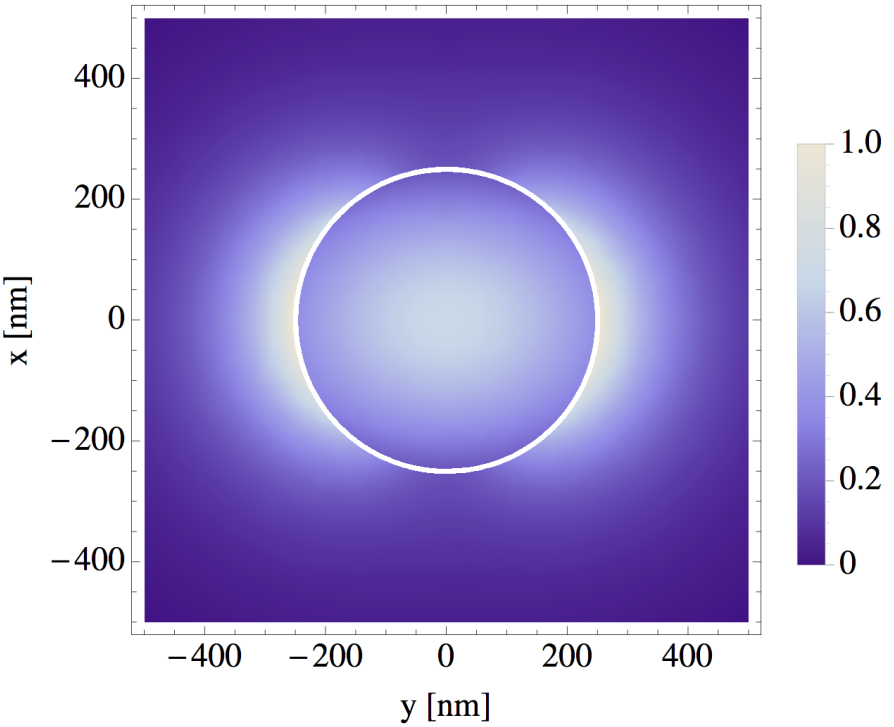

Figure 2.9.: *Transverse intensity distribution at $z = 0$ for the HE_{11} mode with quasi-linear y polarization. Calculated for the parameters $n_{co} = 1.4469$, $n_{cl} = 1$, $a = 250\,\text{nm}$, $\lambda = 1057\,\text{nm}$. The colorbar is normalized to the maximum intensity. The contribution from each of the three Cartesian components of the field to the total intensity is shown in Fig. A.3 in Appendix A.*

We conclude this chapter by presenting the graphical solution for the electric field mode to Maxwell's equations (2.3) at the TOF waist (the analytical expressions are given in Appendix A). To ensure that the guided field is single-mode at the TOF waist (*cf.* Fig. 2.6) and has a

9 The nightmare scenario would be TOFs with meter length tapers. Not only would this be rather impractical, it would also enhance the exposure of the un-coated fiber to environmental damages, such as scratching and dust particles.

significant portion of its field externally distributed, such that a sufficient evanescent field is present for atom trapping and probing, the waist diameter should be on the sub-wavelength scale and is typically given by $d_{\text{waist}} = 2a = 500\,\text{nm}$. In the following, it therefore suffices to consider the fundamental HE_{11} mode only. In addition, all measurements described in this thesis have been obtained with quasi-linearly polarized light fields only[10], and we therefore further restrict ourselves to the description of such modes. For the interested reader, the solutions for a field mode with rotating polarization can be found in [Le Kien, Liang, *et al.*, 2004; Cassany, 2009; Béguin, 2015]. Furthermore, the solutions for the higher order modes HE_{21}, TE_{01}, and TM_{01} are described in [Baade, 2009].

In Fig. 2.9 the transverse intensity distribution is shown for the fundamental HE_{11} mode with quasi-linear y-polarization[11]. A substan-

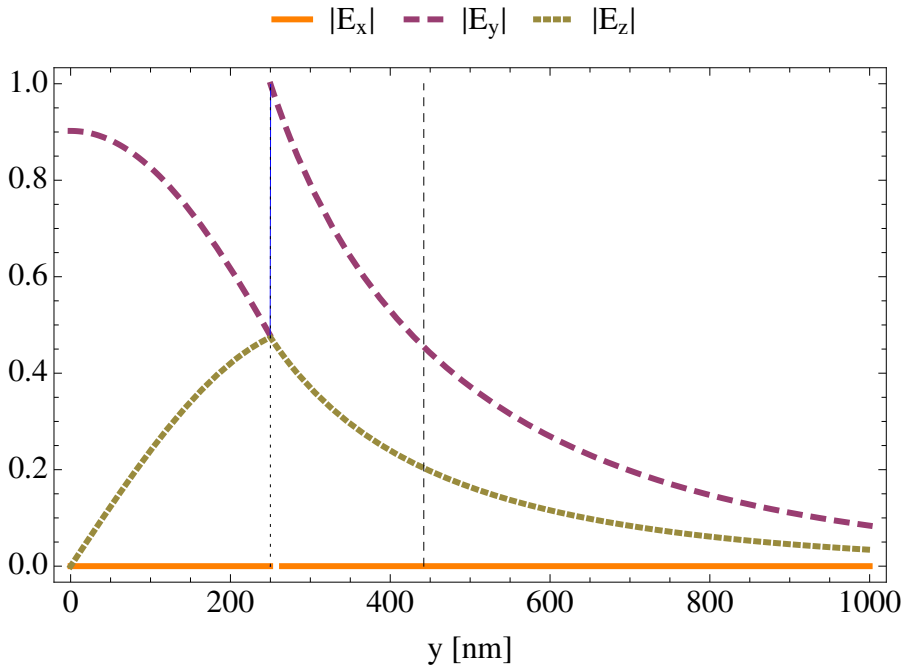

Figure 2.10.: *Electric field components as a function of the radial distance to the fiber axis along y, for a quasi-linearly y-polarized HE_{11} mode. All three components are normalized to the value of $\left|\mathcal{E}_y(\rho = a, \phi = \pi/2)\right|$. The vertical dotted line indicates the fiber edge. The vertical dashed line indicates the radial distance of the atomic trap sites to the* TOF, cf. *Section 9.4. Calculated for the parameters $n_{co} = 1.4469$, $n_{cl} = 1$, $a = 250\,\text{nm}$, and $\lambda = 1057\,\text{nm}$ at $x = 0$, $z = 0$, and $\phi = \pi/2$.*

10 This is only partially true. What is definitely true, is that only modes with quasi-linear polarization in the TOF were intended to be present. But, as will become apparent in Chapter 3, it is not a trivial task to control the polarization in the TOF.

11 Throughout the thesis the x-axis will be taken to be vertical, and the y-axis will be taken to be horizontal and perpendicular to the fiber axis oriented along the likewise horizontal z-axis, *cf.* Fig. 2.1.

tial fraction of the field is clearly seen to be distributed outside the TOF (marked by the white ring). It is brightest at the rim of the TOF when $x = 0$, and decays rapidly with the distance to the fiber. As expected for a y-polarized light field, the intensity is stronger along the y-direction for $x = 0$ than along the x-direction for $y = 0$. This

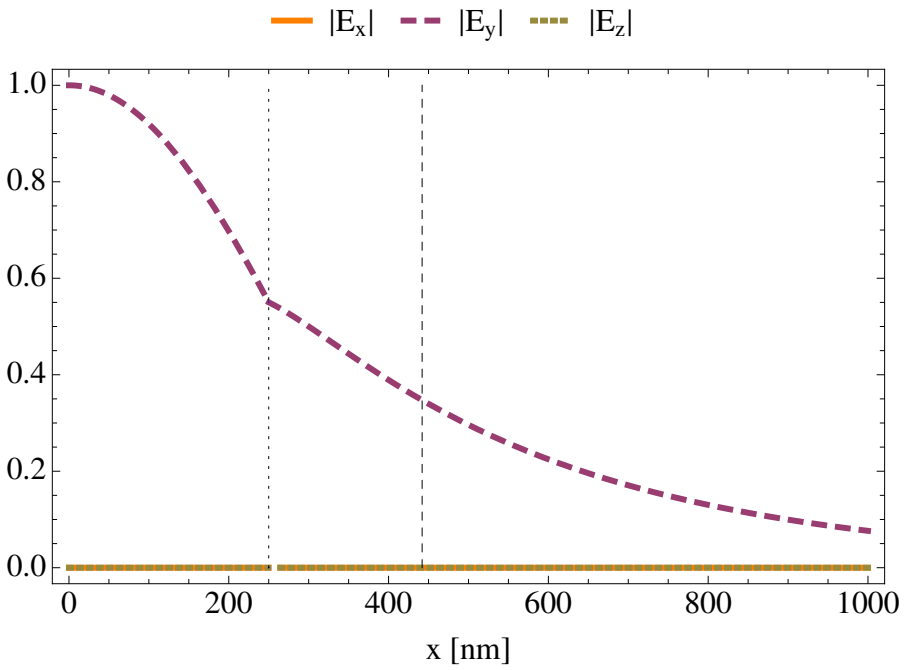

Figure 2.11.: *Electric field components as a function of the radial distance to the fiber axis along x, for a quasi-linearly y-polarized HE_{11} mode. All three components are normalized to the value of $|\mathcal{E}_y(\rho = a, \phi = \pi/2)|$. The vertical dotted line indicates the fiber edge. The vertical dashed line indicates the radial distance of the atomic trap sites to the TOF,* cf. *Section 9.4. Calculated for the parameters $n_{co} = 1.4469$, $n_{cl} = 1$, $a = 250\,\mathrm{nm}$, and $\lambda = 1057\,\mathrm{nm}$ at $y = 0$, $z = 0$, and $\phi = 0$.*

is even more clear in the two figures Fig. 2.10 and Fig. 2.11, where the magnitude of the three Cartesian components of the electric field is plotted as a function of the radial distance to the TOF axis, parallel and perpendicular to the orientation of the polarization respectively. The decay of the evanescent wave is nearly exponential, and can be quantified by introducing the evanescent wave penetration length defined from the cladding parameter W in Eq. (2.15b) [Le Kien, Liang, *et al.*, 2004]:

$$\Lambda(\lambda) \equiv \frac{a}{W} = (\beta^2 - k_0^2 n_{\mathrm{cl}}^2)^{-1/2}\,. \tag{2.23}$$

The penetration length for the three different colors used in this work is given in Table 2.3. From this table, it immediately becomes apparent that the decay length of the field is extremely short – on the sub-wavelength scale. This diffraction limited mode volume of the confined field is really what makes the TOF such an interesting in-

WAVELENGTH (λ)	PENETRATION LENGTH (Λ)
780 nm	198 nm
852 nm	241 nm
1057 nm	431 nm

Table 2.3.: *Evanescent wave penetration length for the three colors used in this work. Calculated for the parameters* $n_{co} = 1.45732$, $n_{cl} = 1$, *and* $a = 250\,\text{nm}$.

terface for light-atom interaction. Not only does the TOF efficiently guide the light fields, making a it a very practical instrument in the lab, it also provides a high local intensity in the vicinity of the fiber, which is essential for the strong interaction with only a few atoms.

From Fig. 2.10 it is evident that the polarization is not purely y-polarized in the yz-plane[12], *i.e.*, the plane parallel to the polarization, as a significant longitudinal component is present. For this reason, it is common practice to refer to the mode as *quasi*-linearly polarized rather than simply linearly polarized. The z-component of the electric field is $\pi/2$ phase shifted with respect to the other two components[13], and the resulting field in the yz-plane is therefore nearly circular.

In contrast to the yz-plane, the ellipticity of the electric field is absent in the xz-plane, since here both the transverse x and longitudinal z electric field components are zero as evident from Fig. 2.11. In this plane, perpendicular to the orientation of the polarization, it is thus possible to have purely y-polarized light. From the azimuthal dependence of the electric field component, shown in Fig. 2.12, it becomes clear that the xz-plane is particularly unique, as this is in fact the only plane, parallel to the fiber axis, where the field is fully linearly polarized.

From Fig. 2.12 the ellipticity of the polarization at the atomic trap minima can be extracted (details on the atomic confinement are given in Section 9.4). The degree of ellipticity depends on the wavelength of the field and the following numbers are found for $\lambda = 852\,\text{nm}$, which is the relevant wavelength for the D2 line in Cs used in this work (the corresponding field components are plotted in Fig. A.1 in Appendix A). At $\rho, \phi, z = 442\,\text{nm}, \pi/2, 0$ the electric field vector is

12 It is perhaps a bit abstract to talk about a plane when analysing a 1D figure. But since we are considering a running wave, and the fiber is translational invariant along the fiber axis, there is no z-dependence involved when considering the magnitudes of the electric field components. Of course, the z-dependence is present in the phase as apparent from Eq. (2.7).

13 This is not obvious from the figures shown here, where we plot the magnitude of the electric field components, but it can be seen in the expressions given in Appendix A.

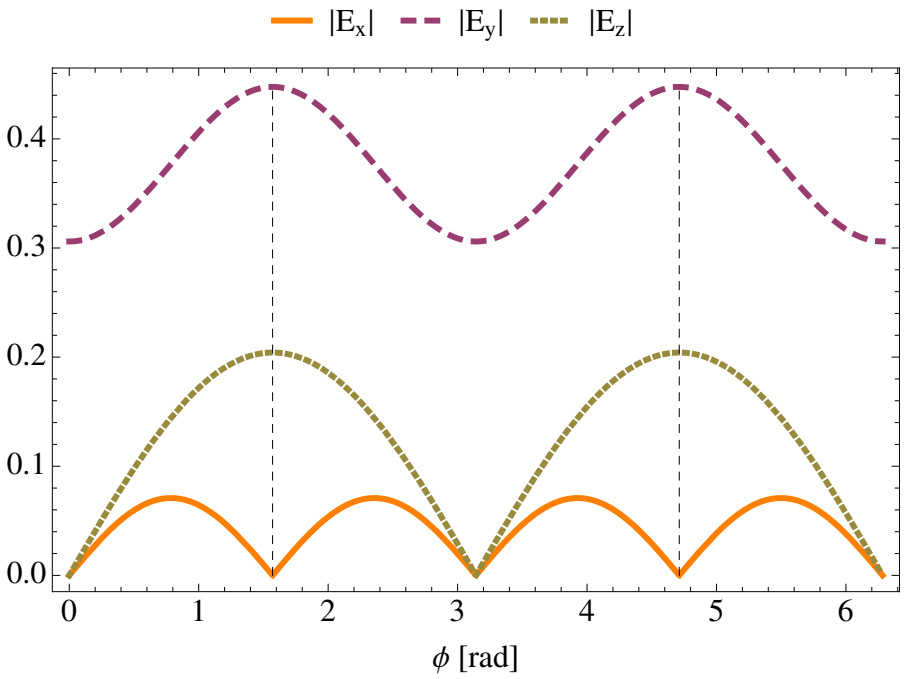

Figure 2.12.: *Electric field components as a function of the aximuthal angle ϕ for a quasi-linearly y-polarized HE$_{11}$ mode. For $\phi = 0, \pi$ the field is completely polarized along y. The vertical dashed lines indicate the position of the potential trap minima of the atoms,* cf. *Section 9.4. All three components are normalized to the value of $|\mathcal{E}_y(\rho = a, \phi = \pi/2)|$. Calculated for the fiber parameters $n_{co} = 1.4469$, $n_{cl} = 1$, $a = 250\,\text{nm}$, and $\lambda = 1057\,\text{nm}$ at $z = 0$ and $\rho = 442\,\text{nm}$ (nominal distance to the atomic trap minima).*

found to be proportional to $\mathbf{E}^{(\text{Cart})} = (0, -0.33i, 0.18)^T$, as written in the Cartesian basis. Upon transformation of this vector to the spherical basis with quantization axis along the x-direction, we have $\mathbf{E}^{(\text{Sph},x)} = (-0.36i, 0, 0.11i)^T$, *cf.* Appendix B for details on the spherical basis with x as the quantization direction. We then find that

$$\left| E^{(\text{Sph},x)}_{q=-1} \right|^2 / \left| \mathbf{E}^{(\text{Sph},x)} \right|^2 = 92\,\%\,, \tag{2.24a}$$

$$\left| E^{(\text{Sph},x)}_{q=+1} \right|^2 / \left| \mathbf{E}^{(\text{Sph},x)} \right|^2 = 8\,\%\,. \tag{2.24b}$$

The field is thus seen to be almost entirely left-handed circularly polarized around the x-axis. Similarly, the polarization on the other side of the TOF, at $\phi = 3\pi/2$, is found to be nearly right-handed circularly polarized.

In order to obtain a more in-depth understanding of the behavior of the quasi-linear HE$_{11}$ running wave (RW) mode in the TOF, we also show a selection of field line plots for different times during an oscillation period. We start by considering the somewhat trivial[14] case for

14 And quite surprising I should perhaps add, as we here have something simple for the otherwise rather complex field mode.

the time-evolution of the transverse components as shown in Fig. 2.13. During the course of time, the light field is simply found to oscillate back and forth between positive and negative y-values, fairly similar to a linear polarization field in free-space. Of course, this plot reveals

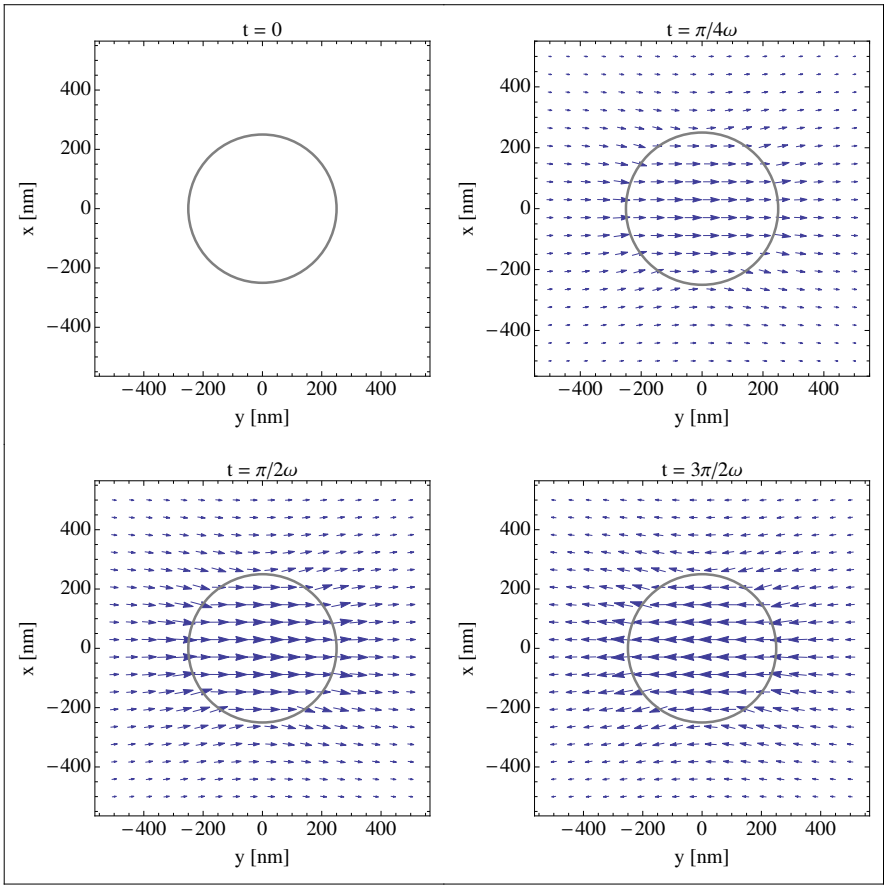

Figure 2.13.: *Transverse electric field distribution in the xy-plane at $z = 0$ for a quasi-linearly y-polarized HE_{11} mode. The gray circle indicates the fiber edge. Calculated for the parameters $n_{co} = 1.4469$, $n_{cl} = 1$, $a = 250\,\text{nm}$, $\lambda = 1057\,\text{nm}$.*

nothing about the non-negligible longitudinal component along the propagation direction of the field. For this we turn to the more interesting Fig. 2.14. For a given position along the fiber axis, the field vector is clearly observed to rotate with time. One could say, that the linear polarization travels along the fiber.

2.5.1 *Standing wave*

Finally, we conclude this chapter by showing the field mode distribution for a standing wave (SW). The time-evolution in the yz-plane is shown in Fig. 2.15. In contrast to the RW shown in Fig. 2.14, the field is no longer circular in this plane. Instead, it is everywhere lin-

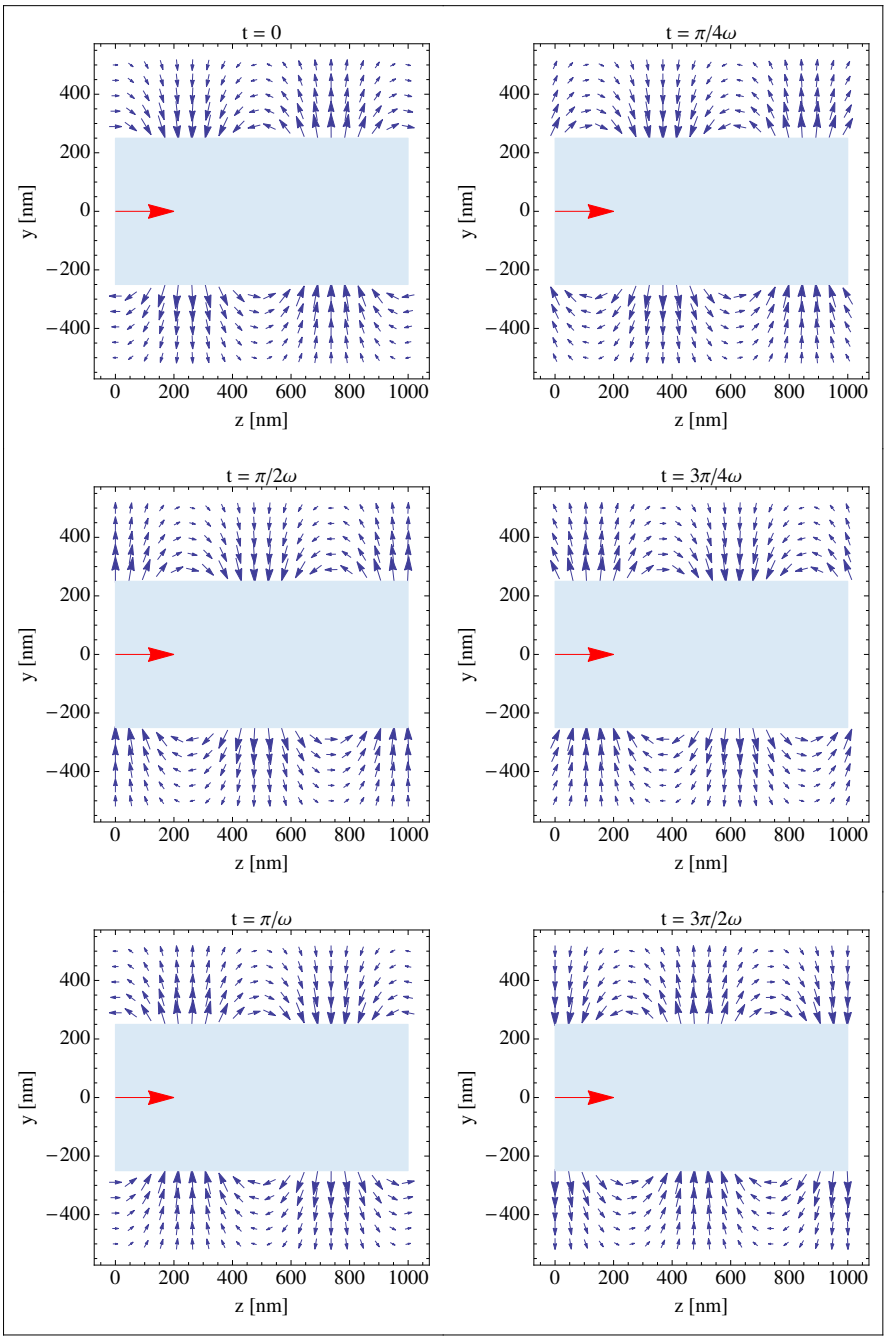

Figure 2.14.: *Electric field distribution in the yz-plane at* $x = 0$ *for a quasi-linearly y-polarized* HE_{11} RW *mode. The fiber is indicated by the shaded region. Calculated for the parameters* $n_{co} = 1.4469$, $n_{cl} = 1$, $a = 250\,\text{nm}$, *and* $\lambda = 1057\,\text{nm}$.

early polarized, albeit oriented along different directions in the plane depending at the location along the fiber axis. At every half wavelength of the field, the longitudinal component thus cancels and the resulting stationary field is found to be purely polarized along the y-axis. This is also evident in Fig. 2.16(a) where the real part of the

electric field components is shown as a function of z. As we shall see in Chapter 9 the atomic trap minima are located in the yz-plane at the positions where the longitudinal field cancels.

As mentioned, the axial component $\mathcal{E}_z$ is $\pi/2$ out of phase with the two transverse components $\mathcal{E}_x$ and $\mathcal{E}_y$. Evidently from Fig. 2.15, this means that the SW in the yz-plane can actually be thought of at two superimposed SWs that are $\pi/2$ out of phase with each other, and where one is polarized along the y-axis while the other is polarized along the z-axis. In Fig. 2.16(a), we thus see that the nodes of the y-polarized SW coincides with the anti-nodes of the z-polarized SW, and vice versa. Of course, in between the nodes and anti-nodes, the field is linearly polarized along some other direction, as we already mentioned. We emphasize, that this configuration means that the resulting intensity of the SW in the yz-plane is never found to be zero, as opposed to a SW wave in free-space, and hence severely degrades the resulting fringe contrast. The intensity distribution of a SW evaluating in the yz-plane as well as the xz-plane can be found in Fig. A.2 in Appendix A.

Since, we already saw, from the RW solution of the electric field, that the longitudinal component $\mathcal{E}_z$ is zero in the xz-plane, when the field is quasi-linearly y-polarized, it is not surprising that the SW display the same results, that is, all electric field components are zero but $\mathcal{E}_y$. We thus see, that the SW in the perpendicular plane to the quasi-linear polarization has full fringe visibility, although the intensity maxima are about half as big as for the in-plane SW, which reduces the coupling to the atoms.

SUMMARY

In the preceding sections we have introduced important concepts, such as the propagation constant and the notion of adiabatic tapers, and established the foundation for later discussions of the TOF as a waveguide platform for light-atom interaction. We have graphically analyzed the solution for the electric field obtained from Maxwell's equations bounded by the cylindrical two-layer fiber geometry. The striking features of the electric field that we have discussed are absolutely vital to consider when exploiting the evanescent field for atom trapping, manipulation, and probing, and we will refer back to the important results given here several times throughout the thesis.

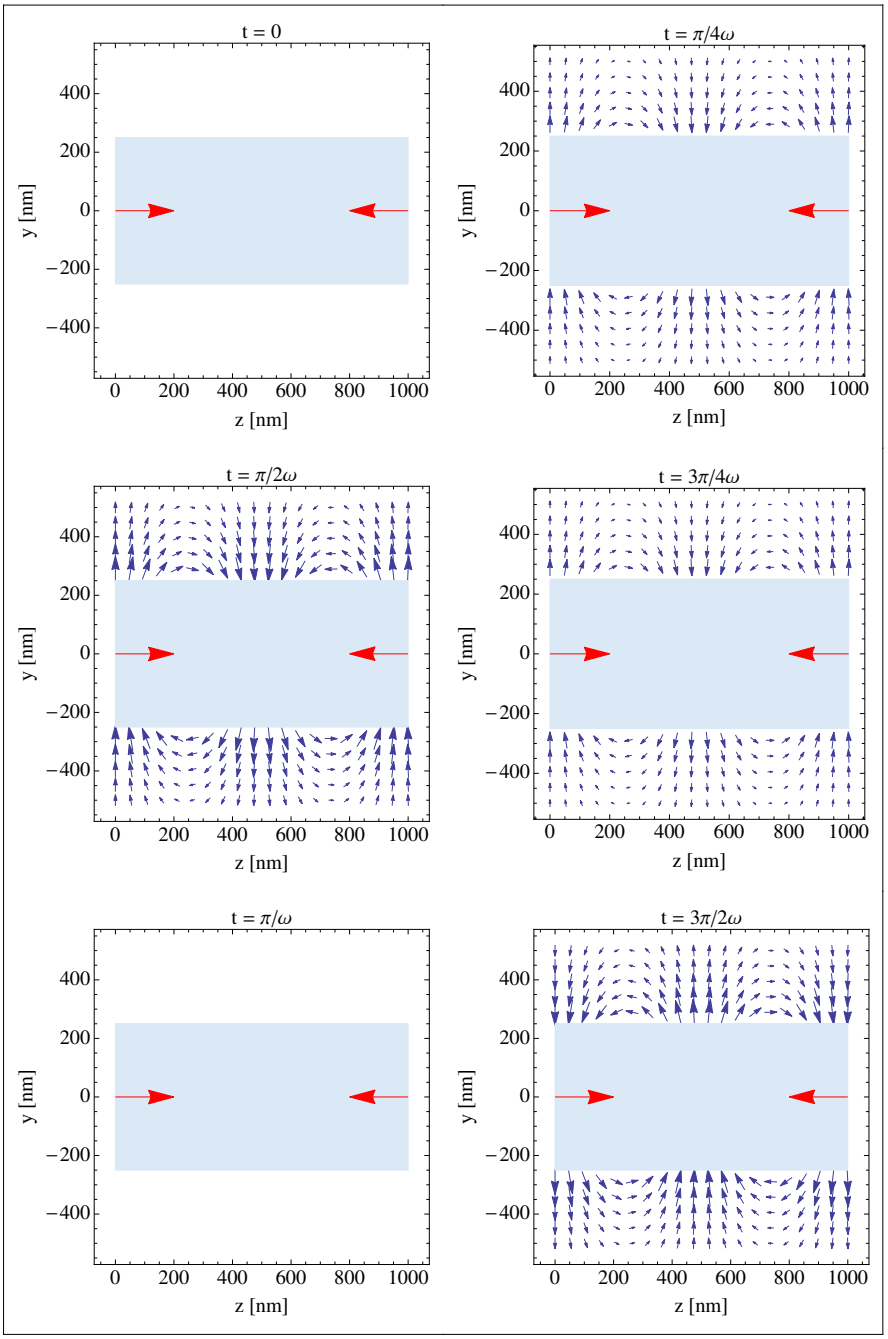

Figure 2.15.: *Electric field distribution in the yz-plane at $x = 0$ for a quasi-linearly y-polarized HE$_{11}$ SW mode. The fiber is indicated by the shaded region. Calculated for the parameters $n_{co} = 1.4469$, $n_{cl} = 1$, $a = 250\,\text{nm}$, and $\lambda = 1057\,\text{nm}$.*

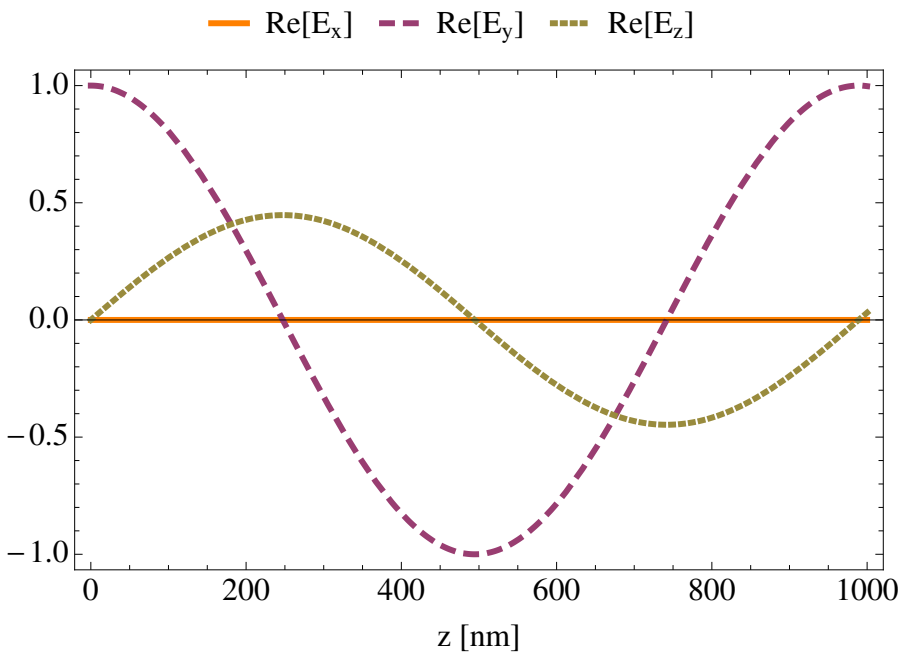

(a) Evalutated in the same plane as the field polarization, *i.e.*, the yz-plane, with $x = 0$ and $y = 442\,\text{nm}$ corresponding to the radial distance of the atomic trap sites to the TOF.

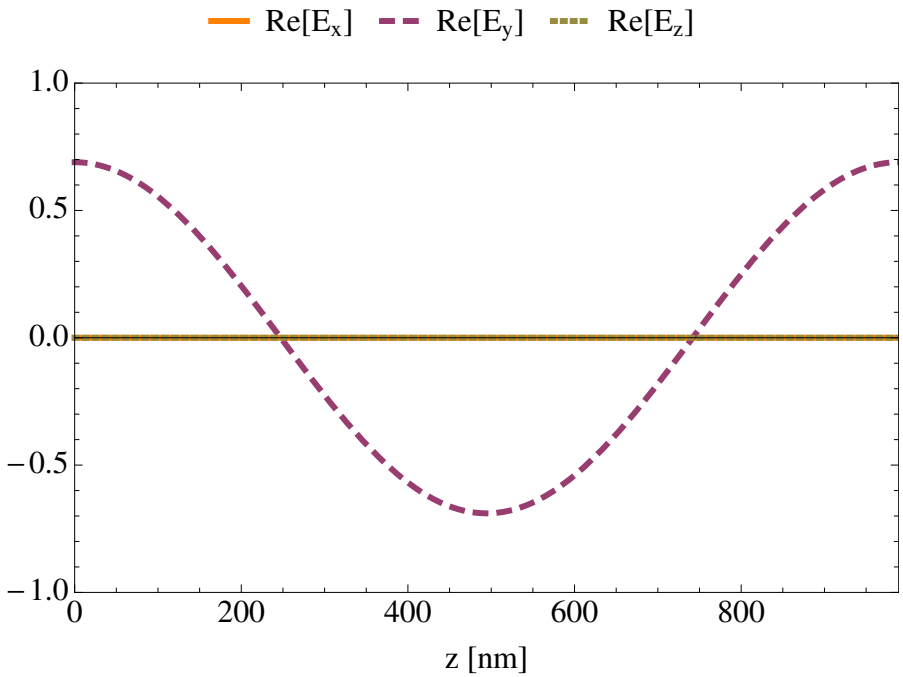

(b) Evalutated in the plane perpendicular to the field polarization, *i.e.*, the xz-plane, with $y = 0$ and $x = 442\,\text{nm}$ corresponding to the radial distance of the atomic trap sites to the TOF.

Figure 2.16.: *Electric field components as a function of z for a quasi-linearly y-polarized HE_{11} SW mode. Evaluated at $t = \pi/2\omega$, normalized to $\text{Re}\,\mathcal{E}_y(x = 0, y = 442\,\text{nm}, z = 0)$, and calculated for the parameters $n_{co} = 1.4469$, $n_{cl} = 1$, $a = 250\,\text{nm}$, $\lambda = 1057\,\text{nm}$. The total intensity of the parallel and perpendicular fields can be found in Fig. A.2 in Appendix A.*

3

EXPERIMENTAL CONTROL OF THE POLARIZATION

In this chapter we describe how we measure and fix the light polarization at the tapered section of the TOF. As we shall see later in Section 9.4, atoms can be confined in a TOF-based dipole trap formed by the evanescent field of two orthogonally polarized guided modes. In order to turn the TOF into an efficient quantum interface between light and atoms, it is therefore of uttermost importance to be able to control the polarization of the guided modes. To do so, we have utilized the method developed by Vetsch *et al.* [2012], where they showed that the polarization at the TOF can be inferred by analyzing the Rayleigh scattered light from a guided mode. For practical reasons, we have extended this method by the use of Jones vectors and matrices.

3.1 STRESS-INDUCED POLARIZATION CONTROL

The TOF is produced from a nonpolarization maintaining (NPM) SIF as described in Chapter 4. Due to the slight (unavoidable) asymmetry in the fiber cross section, both ordinary SIFs and TOFs are birefringent, and the light polarization hence transforms in an unknown (uncontrolled) way upon propagation.

Like in all other materials, the index of refraction of optical fibers depends on both temperature and on induced or built in stress. In

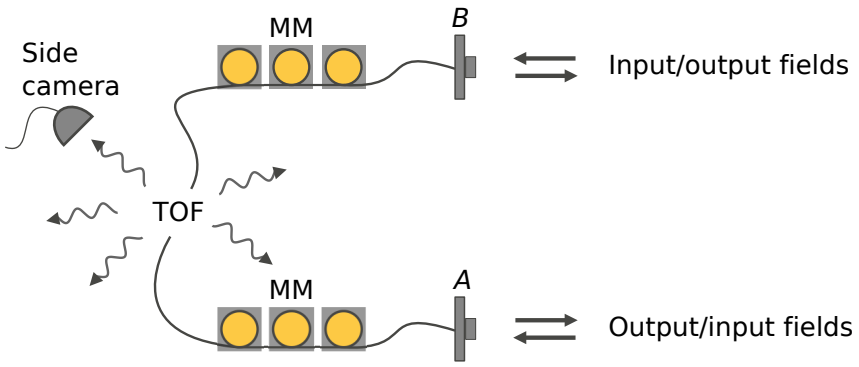

Figure 3.1.: *The TOF setup, as viewed from above, with inserted MM to change the polarization inside the fiber by induced stress. The side camera measures the Rayleigh scattered light explained in Section 3.2 (also see Fig. 3.2). Both port A and B are used as input/output ports.*

order to change the guided mode polarization, we have therefore implemented two 3-paddle fiber controllers[1], in lab-jargon known as the Mickey-Mice (MM) for reasons obvious from their shape as illustrated in Fig. 3.1.

The MM are inserted at an unstretched section of the TOF, on either side of the tapered part, and consists of three paddles with a spool, around which the fiber is wrapped to induce stress from bending. Each paddle effectively works as a waveplate (WP) where the retardation is set by the fiber loop diameter (fixed by the spool diameter), the number of fiber loops per spool, and the wavelength of the guided light mode. To have complete control over the polarization, such that the whole Poincaré sphere can be reached, we have configured the three paddles of each MM such that they behave[2] as quarter-wave plates (QWPs) and half-wave plates (HWPs) in the sequence QWP–HWP–QWP.

Having a tool to change the polarization of a TOF-mode, is of course only worth something if we can actually measure what the resultant polarization is at the TOF waist. This is the objective of the next two sections.

3.2 RAYLEIGH SCATTERING

The method to measure the polarization of a TOF-guided mode, as laid out by Vetsch *et al.* [2012], relies on Rayleigh scattering from inhomogeneities in the silica and surface imperfections of the TOF. Assuming that these defects can be treated as point-scatterers amounts to an isotropic description of the medium in which the induced dipole moments oscillate in the same direction as the local electric field. The basic idea is then to infer the (transverse) electric field polarization by analyzing the emission pattern of the induced dipoles which goes as $I(\phi) \propto \sin^2(\phi)$, where ϕ is the angle spanned between the orientation of the dipole and the position vector from the dipole to the point in space where the scattered intensity $I(\phi)$ is evaluated [Hecht, 2002].

In order to do so, we have installed two CMOS cameras[3] to record the scattered light intensity, placed below and beside the TOF as shown in Fig. 3.2 (also *cf.* Fig. 3.1). In front of each camera is mounted an $f = 50\,\text{mm}$ lens to enlarge the image of the fiber, and a polarizer (Pol.) to ensure that mainly the polarization components transverse

1 *FPC030 – Fiber Polarization Controller, 3 Small Paddles* from Thorlabs.
2 Note, that this is only true for a specific wavelength of the input field. Here, we have configured the MM for $\lambda_{\text{probe}} = 852\,\text{nm}$.
3 *Firefly FFMV-03M2M (Firewire, IEEE 1394)* from Point Grey.

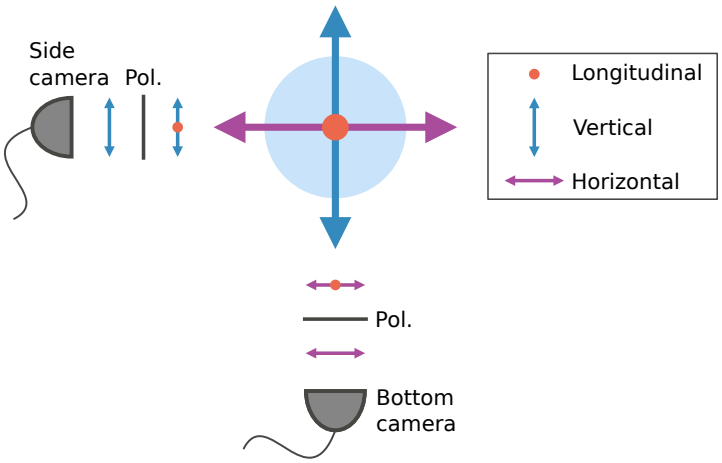

Figure 3.2.: *Setup for imaging the scattered light off the* TOF*, viewed as a transverse cross-section of the fiber,* i.e.*, the fiber axis is in and out of the plane. The legend entries refer to the different polarization components. Pol. is short for polarizer.*

to the fiber axis of the scattered field are measured[4]. The latter is necessary to be able to minimize the intensity on either camera for a given quasi-linear polarization, which would be difficult if the longitudinal component is not suppressed. For the experimental setup shown in Fig. 3.2, the side camera measures the vertical (V) polarization component along the x-axis, while the bottom camera measures the horizontal (H) polarization component aligned to the y-axis. An example of an image of the guided light scattered off the TOF is shown in Fig. 3.3.

Using input light that is either V or H polarized, we adjust the MM paddles while monitoring the scattered intensity. The goal is then to maximize the scattered intensity on one of the two cameras while minimizing it on the other camera. The main challenge is not so much to find a setting of the MM paddles that supports the mapping of external linear polarization to quasi-linear polarization in the TOF for a monochromatic input field, but to find a setting that does this for *three* separate input modes comprised of vastly different wavelengths. As we will see later, in Section 9.4, these wavelengths are given by $\lambda_{\text{blue}} = 780\,\text{nm}$ and $\lambda_{\text{red}} = 1057\,\text{nm}$ for the blue- and red-detuned trapping fields used for the TOF-based dipole trap, and $\lambda_{\text{probe}} = 852\,\text{nm}$ for the probe field near-resonant with the caesium-133 (Cs) D2 line.

In order to find a global setting of the MM, for all three colors, we perform an iterative adjustment of the paddles, interchanging between the red and blue input fields as these hold the extremal values of

4 Due to space issues, the bottom camera is not entirely in level but slightly tilted. As a consequence, some fraction of the longitudinal component is measured alongside the transverse H polarization component of the scattered electric field.

Figure 3.3.: *Image taken with the bottom camera of the TOF using the red trap beam ($\lambda_{red} = 1057\,\mathrm{nm}$) as input light with optical power $P_{red} = 1.5\,\mathrm{mW}$. The background, taken as the average pixel value over a $(50 \times 50)\,\mathrm{pixel}^2$ window in the upper left corner (blue box), is subtracted from each pixel which are afterwards normalized to the maximum pixel value (intensity) to enhance the contrast. The pixel values inside the red box, enclosing the TOF, are integrated to yield the scattered intensity (in arbitrary units).*

the three wavelengths. This is a somewhat tedious task with a big parameter space (three paddles that can each be turned in an angle of 180°) which is further complicated by the fact that it is hard to reproduce a setting, since the paddles are unmarked. When only judging from the stream of camera images, it is also hard to tell how much the scattered intensity changed when turning one of the paddles, and especially if an intensity minimum found on one camera for a given setting of the paddles is greater or smaller than that found previously for the same camera. To ease the task a bit, we have written a graphical user interface (GUI) where the integrated intensities measured by each camera, are plotted in real-time next to the camera images[5].

When a setting has been found that is believed to rotate the polarization of the differently colored input fields, such that they are all quasi-linearly polarized at the TOF, we make a full polarization map for each input as described in the following section.

Before moving on, we point out that for the procedures described here and the next section to work properly, the input field of course has to be stable in terms of power and strong enough that sufficient scattering takes place and illuminate the cameras. However, one should be careful that it is not too strong such that the cameras saturate, as any changes in the scattered intensity are then not resolved.

5 As I am sure this will be helpful for future students in the lab I point you to the script: `livecam_gui_v4.py` which can be found in the Python folder on `kahuna`.

About a milliwatt, a bit more a bit less depending on the wavelength, has proven to be appropriate for our setup.

3.3 POLARIZATION MAPS

The emission pattern radiated by the dipoles is mapped out by recording the scattered intensity on the two CMOS cameras for various orientations of the input field polarization. From each image, a value for the scattered intensity is extracted by integrating the pixels over a box sized such that is covers the TOF as illustrated in Fig. 3.3.

The input field polarization is rotated by using two motorized and computer-controlled WPs placed between the input fiber coupler and a polarizer, as shown in Fig. 3.4. Both WPs are mounted on rubber pads, to minimize vibrations from the motors mediated to the TOF via the optical table. It is important that the set of motorized WPs and polarizer is placed right in front of the input port to the TOF, in order to keep the optical input power at the same level throughout the measurement.

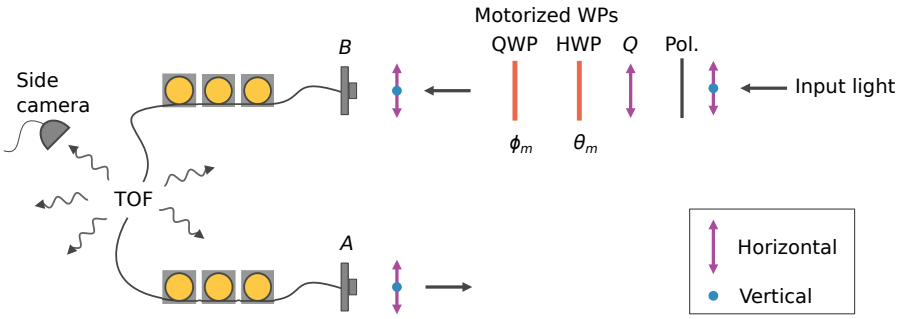

Figure 3.4.: *Setup, as viewed from above, for mapping out the transverse polarization inside the TOF as a function of the input polarization set by the two WPs. The polarizer (Pol.) is set to transmit H-polarized light. The scattered intensity is recorded by the two cameras placed beside and below (not shown) the TOF.*

By interchangeably turning either WPs by 5°, and saving the recorded images by the two cameras[6], we obtain a two-dimensional (2D) polarization map as a function of the angles ϕ_m, θ_m between the horizontal axis and the fast axis of the QWP and HWP, respectively. A typical example of such a map is shown in Fig. 3.5. As expected from the calculated maps in Fig. 3.5(c),(d), the measured intensity maxima/minima for the two polarization components, Fig. 3.5(a),(b), are seen to be out of phase such that the side camera measures maximum (minimum) intensities whenever the bottom camera measures minimum

6 The program for this is `MoveWPandTakeImg4.py` likewise found on `kahuna`.

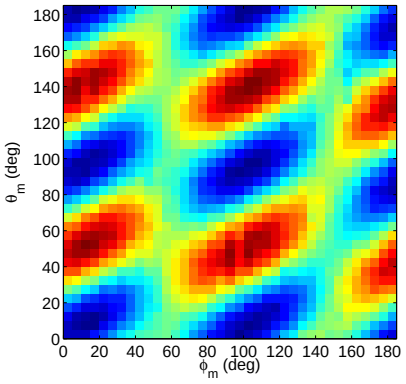

(a) Side camera (measures V).

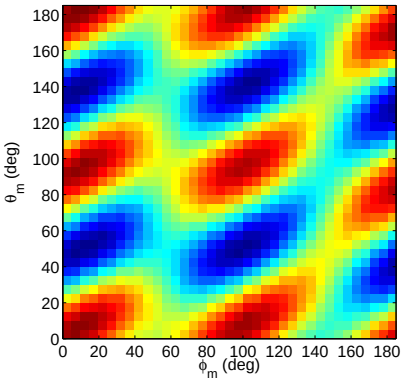

(b) Bottom camera (measures H).

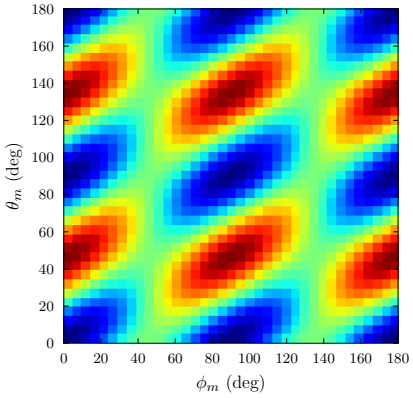

(c) Calculated intensity of V component.

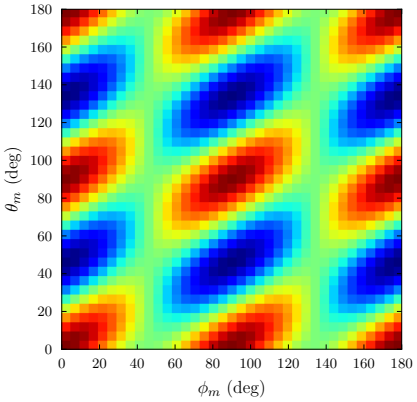

(d) Calculated intensity of H component.

Figure 3.5.: *Polarization maps of the TOF for the probe with free-space wavelength* $\lambda_{probe} = 852\,\text{nm}$. *The angles on the axes refers to the fast axis of the WPs with respect to the horizontal axis. The colorbar scales with the integrated intensity detected by the cameras, using* red *for maximum intensity and* blue *for minimum intensity. The mild distortions in the experimental data, in (a) and (b), are most likely due to the motorized WPs being slightly tilted.*

(maximum) intensities. The calculated polarization maps have been produced by using the Jones matrices for the HWP and QWP given by

$$J_{\text{h}}(\theta) = \begin{pmatrix} \cos 2\theta & \sin 2\theta \\ \sin 2\theta & -\cos 2\theta \end{pmatrix}, \tag{3.1a}$$

$$J_{\text{q}}(\theta) = \begin{pmatrix} \cos^2\theta + i\sin^2\theta & (1-i)\sin\theta\cos\theta \\ (1-i)\sin\theta\cos\theta & \sin^2\theta + i\cos^2\theta \end{pmatrix}, \tag{3.1b}$$

with θ being the angle between the fast axis of the WP and the horizontal axis. The Jones vector for H-polarized light is defined as $\mathbf{H} = (1, 0)^T$, and the resultant polarization $\mathbf{X}$ after the two WP is then simply calculated as $\mathbf{X} = J_{\mathrm{q}}(\phi_m) J_{\mathrm{h}}(\theta_m)\mathbf{H}$.

For the specific data set shown in Fig. 3.5, belonging to a particular setting of the MM, we see that the free-space input polarization transform nearly to the same (transverse) polarization in the TOF. It is, strictly speaking, not necessary to have the MM configured such that this is the case. But it certainly does make it comprehensively easier if the polarization of an input beam, as measured on the optical table, transforms to the same transverse polarization in the TOF.

In principle, it is also not necessary to map out the large range of angles that we do in Fig. 3.5, from 0° to 180° for each WP. But it can be very helpful to see if there is a more optimal setting of the input polarization, being elliptical if that is what it takes, that transform into a more pure quasi-linear mode in the TOF. Making the whole map from 0° to 180° thus tells us if the maximum or minimum that we found, from adjusting the MM while monitoring the scattered intensity, was only a local extremum or if we can do better.

3.4 JONES CALCULUS

The polarization maps presented in Fig. 3.5(a)(b) takes $\sim$ half an hour to measure, without including the preparation time in setting up the motorized WPs and the initial adjustments of the MM paddles, which can amount to hours. It it often necessary to perform several maps, one for each color for each new setting of the MM, making the whole procedure a rather long and tedious task.

As it turns out, it is also quite hard to obtain a global setting for the MM that, for *linearly-polarized* input light, maps all three colors to a quasi-linearly polarized mode in the TOF. Often, we were able to find a setting that would work decently for two of the colors, but then be completely off for the third color. A solution in this case, could be to leave the MM setting as it is and use external WPs for the last color. This is in principle a nice solution, which we also used for a while. Unfortunately, exterior changes to the setup, such as changes in the lab temperature or (especially) an accidental bump of the MM paddles, imply that one occasionally needs to perform a polarization map to make sure that all settings are still appropriate and make according adjustments where needed.

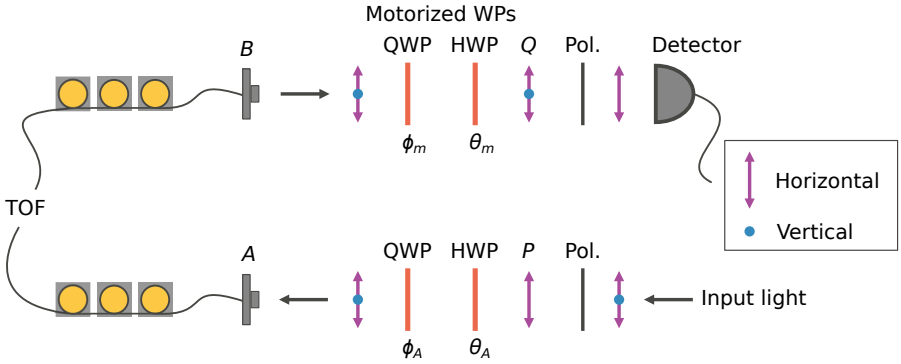

Figure 3.6.: *Illustration of Method I for setting the WPs on the A side such that any input light is either mapped to quasi-linear H or V polarization in the TOF. Both polarizers (Pol.) are set to transmit H-polarized light.*

In the end, we therefore resorted to a different (and more expensive) solution and now use external WPs for all three colors[7]. The benefit is two-fold: (i) the WPs can be locked, or at least the settings can be written down such that they can be reproduced. And (ii) it is faster, as it suffices to make a *single* polarization map for each color (without first trying to adjust the MM paddles), from which the settings of *all* the external WPs can be found, *i.e.*, including input fields to both port A and B into the TOF). In the following we discuss two methods that we have used to set the external WPs.

3.4.1 *Setting the waveplates – Method I*

The objective is to find the two settings of the WPs in front of port A, *i.e.*, the angles ϕ_A and θ_A of the WPs' fast axes with respect to an arbitrary (fixed) axis, that maps the H input polarization, at P, to either a quasi-linearly H- or V-polarized mode at the TOF, see Fig. 3.6. These two WPs and the polarizer are thus integrated parts of the setup, whereas all the elements in front of input port B are only temporarily in the setup to aid finding the values for ϕ_A and θ_A.

The strategy to find the setting of the A WPs that maps the input light to, say, quasi-linearly V-polarized light mode in the TOF is as follows:

1. Make a polarization map from $B \to A$, as described in the previous section, and pick the values for ϕ_m and θ_m that maximizes the intensity on the side camera while minimizing it on the bottom camera, *i.e.*, that maps B input light onto a V-mode in the TOF.

7 Currently, we have not taken the MM out of the setup, so the TOF polarization is still prone to unwanted changes from incautious actions near the two input ports to the TOF. Perhaps removing the MM, and resetting all the WPs, would be a nice start-up project for a new student in the lab?

2. With ϕ_m and θ_m fixed at these values, we know that H-polarized light at Q maps to V in the TOF. This means, that the opposite is also true: V in the TOF maps to H at Q when light propagates from $A \rightarrow B$.
3. Now, we send in light that propagates in the opposite direction, that is, from $A \rightarrow B$.
4. Using the WPs on the A side to maximize the transmission though the polarizer on the B side, we find the angles ϕ_A, θ_A that maps input light to port A to V in the TOF.
5. As a final step, one can use the two cameras to measure whether the intensities of light scattered off the TOF are minimized/maximized as expected.

When the values of ϕ_A, θ_A have been found for both polarization modes (H and V), all the elements on the B side as sketched in Fig. 3.6 (*i.e.*, the motorized WPs, the polarizer, and the detector), can be taken out. The procedure is then repeated to find the settings of a pair of mounted WPs on the B side by using the mounted WPs on the A side to play the role of the motorized WPs.

Experimentally in polarization analysis, it is more robust to identify a minimum rather than a maximum in detected intensity. The procedural steps 4 and 5 can easily take advantage of this fact by simply rotating θ_m by 45° between step 2 and 3.

So far, we have not mentioned any other optical elements that might be present in the TOF setup. What we have mentioned though, is that we will have three different colored modes simultaneously inside the TOF. This effective means that there are quite a few optical elements, such as a dichroic mirror (DM) and beam samplers (BSs), between the input ports and the WPs. Unfortunately, the transmission to reflection ratio for these elements depends strongly on the polarization of the incident beam. For example, after the WPs, the 852 nm input beam passes through a nominal 90:10 BS[8] where 17 % of the light gets transmitted when it is H-polarized, but only 3.1 % when it is V-polarized[9].

These additional optical elements, then, both introduce polarization-dependent losses in the optical path from the WPs to the TOF input port, and rotate the polarization of the optical field when it is not purely H- or V-polarized. This, obviously, makes it harder to use the described procedure to minimize the output on the B side hitting the detector – did the power decrease because the polarization became more vertically polarized at the position before the polarizer? Or, did

8 *BSX11 – Ø1" 90:10 (R:T) UVFS Plate Beamsplitter, Coating: 700-1100 nm, t = 5 mm* from Thorlabs.

9 10 % actually gets transmitted for *unpolarized* light, so in this respect the part name lives up to its reputation.

the power decrease because more light were lost before entering the input port A?

On top of that, for the 852 nm input beams, we usually have only very little light available to begin with, at most a few hundred microwatt at the TOF input ports. This makes things even harder as the detector might not resolve such low powers (when minimizing the output) and step 5 cannot be realized. It also adds to the difficulty of adjusting the MM while monitoring the scattered light intensity as described in Section 3.2 (this was also part of the reason why we typically chose to optimize for the other two wavelengths, 780 nm and 1057 nm). However, for the polarization maps, as shown in Section 3.3, the contrast is acceptable after subtracting the background light and normalize to maximum intensity.

To circumvent these complications we have developed another method, robust against polarization-dependent losses, to set the polarization in the TOF as described in the following.

3.4.2 *Setting the waveplates – Method II*

The objective is still to find the two sets of angles, ϕ_A and θ_A, that maps an H-polarized input beam at P to either a quasi-linearly H- or V-polarized mode at the TOF, see Fig. 3.7. As in Method I, this scheme relies on the ability to initially have a guided mode in the TOF known to be polarized as either quasi-linear V or H. In the following, we will assume that this requirement is met.

We consider the specific case where the polarization in the TOF is known to be V, such that it is described by the Jones vector $\mathbf{V}_{\text{tof}}$. We further assume that ϕ_A and θ_A are set such that this mode maps to V at P, $\mathbf{V}_P = (0,1)^T$, via the expression:

$$\mathbf{V}_P = J_{\text{qh}} J_{\text{bs}} J_{\text{tof}} \mathbf{V}_{\text{tof}} \,, \tag{3.2}$$

where we have introduced the Jones matrix for the combined set of a HWP and a QWP,

$$J_{\text{qh}}(\theta,\phi) \equiv J_{\text{h}}(\theta) J_{\text{q}}(\phi) \,, \tag{3.3}$$

and the Jones matrix for the reflection or transmission through a BS[10]:

$$J_{\text{bs}}(\beta) \equiv \begin{pmatrix} \beta_{\parallel} & 0 \\ 0 & \beta_{\perp} \end{pmatrix} , \tag{3.4}$$

for $\beta_i = r_i, t_i$ with r (t) being the reflection (transmission) coefficient of the BS, and the subscript $i = \parallel, \perp$ referring to the polarization component being either parallel ($\parallel$) or perpendicular ($\perp$) to the plane of incidence. The last Jones matrix J_{tof} yields the polarization transform

10 The Jones matrix for a chain of beam splitters has the same form with $\beta_i = \prod_k \beta_{k,i}$ for $i = \parallel, \perp$.

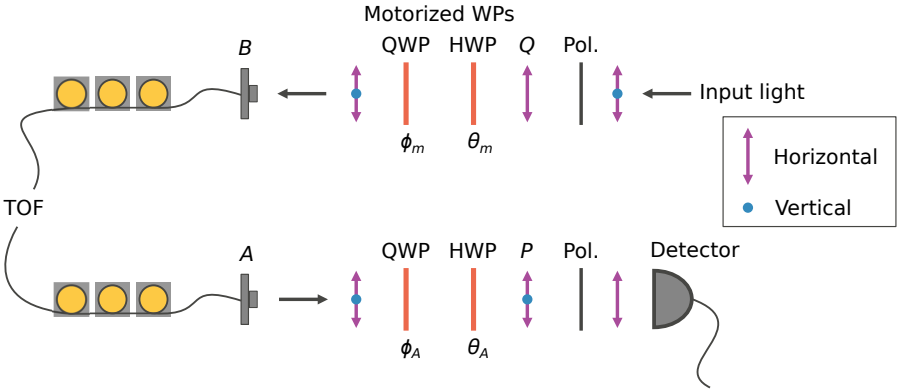

Figure 3.7.: *Illustration of Method II for setting the WPs on the A side such that any input light (from this side) is either mapped to quasi-linear H or V polarization in the TOF. Both polarizers (Pol.) are set to transmit H-polarized light.*

of the light propagating out of the TOF, *i.e.*, from TOF to A in Fig. 3.7, which is assumed to behave as a WP with no losses.

Common to these three Jones matrices, is that they are all invertible: $J_i J_i^{-1} = \mathbb{1}$, for $i =$ qh,bs,tof. Furthermore, both J_{qh} and J_{tof} are unitary: $J_k^* = J_k^{-1}$, for $k =$ qh,tof. The BS Jones matrix can never be unitary by definition, since the light field incident to a BS couples into two different output modes, and the J_{bs} effectively describes a loss process from the incident field to the single output mode that we consider.

As we are interested in the TOF polarization, we isolate $\mathbf{V}_{\text{tof}}$ in Eq. (3.2):

$$\mathbf{V}_{\text{tof}} = J_{\text{tof}}^{-1} J_{\text{bs}}^{-1} J_{\text{qh}}^{-1} \mathbf{V}_P \,. \tag{3.5}$$

In general, if the three Jones matrices would be known, we could calculate the (transverse) polarization of a guided TOF-mode resulting from an arbitrarily polarized input field $\mathbf{a}$, by simply evaluating the expression $J_{\text{tof}}^{-1} J_{\text{bs}}^{-1} J_{\text{qh}}^{-1} \mathbf{a}$. Unfortunately, J_{tof} is not known to us. However, since we only care about quasi-linearly polarized TOF-modes there is a workaround to this. Let us say, that the input field at P is H-polarized such that it is described by the Jones vector $\mathbf{H}_P = (1,0)^T$. The polarization in the TOF is then (formally) given by

$$\mathbf{X}_{\text{tof}} = J_{\text{tof}}^{-1} J_{\text{bs}}^{-1} J_{\text{qh}}^{-1} \mathbf{H}_P \,. \tag{3.6}$$

We now want to calculate the projection of the unknown polarization vector $\mathbf{X}_{\text{tof}}$ onto the quasi-linearly V-polarized TOF-mode: $\mathbf{X}_{\text{tof}}^* \cdot \mathbf{V}_{\text{tof}}$. Taking the conjugate transpose of Eq. (3.6) we have

$$\mathbf{X}_{\text{tof}}^* = \mathbf{H}_P^T J_{\text{qh}} (J_{\text{bs}}^{-1})^* J_{\text{tof}} \,, \tag{3.7}$$

from which we obtain

$$\begin{aligned} \mathbf{X}_{\text{tof}}^* \cdot \mathbf{V}_{\text{tof}} &= \mathbf{H}_P^T J_{\text{qh}} (J_{\text{bs}}^{-1})^* J_{\text{tof}} J_{\text{tof}}^{-1} J_{\text{bs}}^{-1} J_{\text{qh}}^{-1} \mathbf{V}_P \\ &= \mathbf{H}_P^T J_{\text{qh}} \left| J_{\text{bs}}^{-1} \right|^2 J_{\text{qh}}^{-1} \mathbf{V}_P \,. \end{aligned} \tag{3.8}$$

where we have inserted Eq. (3.5) for $\mathbf{V}_{\text{tof}}$. In order to proceed, we need to make the assumption that $\beta_\perp \approx \beta_\parallel$, *i.e.*, that the reflection and transmission coefficients for the two different polarization components are approximately equal[11], we then have:

$$\left| J_{\text{bs}}^{-1} \right|^2 = \begin{pmatrix} |\beta_\parallel|^2 & 0 \\ 0 & |\beta_\perp|^2 \end{pmatrix} \approx |\beta_\perp|^2 \begin{pmatrix} 1 & 0 \\ 0 & 1 \end{pmatrix}. \tag{3.9}$$

Within this approximation we find for Eq. (3.8):

$$\begin{aligned} \mathbf{X}_{\text{tof}}^* \cdot \mathbf{V}_{\text{tof}} &\approx |\beta_\perp|^2 \, \mathbf{H}_P^T J_{\text{qh}} J_{\text{qh}}^{-1} \mathbf{V}_P \\ &= |\beta_\perp|^2 \, \mathbf{H}_P^T \mathbf{V}_P = 0\,, \end{aligned} \tag{3.10}$$

which means that $\mathbf{X}_{\text{tof}}$ necessarily has to be orthogonal to $\mathbf{V}_{\text{tof}}$, that is, quasi-linearly H-polarized. This is a very interesting result, as it gives us a new recipe for setting the angles ϕ_A and θ_A of the WPs for mapping input light a port A to either $\mathbf{V}_{\text{tof}}$ or $\mathbf{H}_{\text{tof}}$. The procedure for doing so, such that, say, input light at A maps to $\mathbf{H}_{\text{tof}}$, goes as follows:

1. Find a setting of the motorized WPs for ϕ_m and θ_m in Fig. 3.7 that maps input light at B to $\mathbf{V}_{\text{tof}}$, for example by running a polarization map from $B \to A$ as described in Section 3.3.
2. With the polarization in the TOF now given by $\mathbf{V}_{\text{tof}}$, turn the WPs on the A side such that the power on the detector is minimized, *i.e.*, such that the light polarization at P becomes V-polarized. Fix ϕ_A and θ_A at this setting. The transformation of the polarization at P to the TOF can now be described by Eq. (3.5).
3. If the propagation direction is now reversed, such light that enters the TOF via port A, we have from Eq. (3.6) that the polarization at the TOF is given by $\mathbf{X}_{\text{tof}}$, since the polarization at P is always H-polarized (for light propagating from $P \to A$). Furthermore, we have from Eq. (3.10) that $\mathbf{X}_{\text{tof}}$ must be quasi-linearly H-polarized and our job is completed.

The procedure to set the A WPs and how to operate them is summarized in Table 3.1. The left column gives the values obtained for the WP angles, ϕ_A, θ_A, as found from the above procedure. The right column shows how these settings for ϕ_A, θ_A should be used in order to get either of the two quasi-linearly polarized modes in the TOF.

With the more rigorous treatment given here, on how the polarization is mapped between an exterior light beam and a TOF-guided mode, we have now also justified the procedure given in Method I. In fact, Method I turns out to be more robust than Method II, in the sense that

11 We have already seen, that there can be a quite big difference between the two quantities, but for a moment we shall ignore that.

CONFIGURING				OPERATING			
Dir.	$\mathbf{X}_{\text{tof}}$	ϕ_A, θ_A	$\mathbf{X}_P$	Dir.	$\mathbf{X}_P$	ϕ_A, θ_A	$\mathbf{X}_{\text{tof}}$
B $\rightarrow$ A	**H**	ϕ_1, θ_1	**V**	A $\rightarrow$ B	**H**	ϕ_1, θ_1	**V**
B $\rightarrow$ A	**V**	ϕ_2, θ_2	**V**	A $\rightarrow$ B	**H**	ϕ_2, θ_2	**H**

Table 3.1.: *Overview of the overall procedure to configure and operate the WPs on the A side in Fig. 3.7 in order to obtain a quasi-linearly polarized guided mode in the TOF.*

no additional optical elements are present between the TOF and the motorized WPs. Which means that the BS Jones matrix is not included in the calculations[12], and hence the approximation made in Eq. (3.9) is avoided. In this respect it is also clear, that the fewer optical elements mounted between the WPs and the TOF input port, the more robust against errors does the procedure becomes.

To the extend possible, we have verified the settings of ϕ_A and θ_A by performing both Method I and Method II, and by inspecting the scattered intensity off the TOF with the two mounted cameras as explained in Section 3.2.

SUMMARY

In this chapter, we have taken a first peak of the TOF setup used for experiments with atoms coupled to the evanescent field of a TOF-guided mode. We have meticulously accounted for how the polarization in the TOF is experimentally controlled and set to either quasi-linear H or V, by analyzing the scattered intensity from the TOF for different input polarization, and, by applying Jones calculus, analyzed the mapping of the polarization through different optical elements.

12 However, the fiber taper itself behaves as a BS with $\sim 4\,\%$ optical losses at each taper.

4

PRODUCING TAPERED OPTICAL FIBERS

The first half part of this PhD was concentrated around building a fiber-pulling rig to produce TOFs. Most of the content in the following sections can therefore be found in a more elaborate form in the progress report [Sørensen, 2013] concluding Part A of this PhD study and a subsequent published paper [Sørensen *et al.*, 2014]. In this chapter we briefly review the main results accomplished during this period, starting with a description of the setup and some of the experimental results. This is followed by a presentation of a numerical model developed for the prediction of the resulting fiber shape after a pulling run.

4.1 EXPERIMENTAL SETUP

The experimental setup consists of two main parts: the fiber-pulling rig where the TOF are produced and smaller surrounding setups to characterize the outcome.

4.1.1 *Fiber-pulling rig*

To produce a TOF we have build a fiber-pulling rig, Fig. 4.1, consisting of two stacked motorized linear translation stages[1] and an electric ceramic microheater[2], from here on denoted as either the oven or the heater. The stacked solution of the stages provides improved stability compared to stages placed in succession of each other [Warken *et al.*, 2008]. By only moving the bottom stage, the fiber can easily be translated (without stretching it) with respect to the sidewards stationary oven.

The oven is mounted on a motorized rail and can be driven out of the setup between consecutive pulls. This is obviously useful when inserting and removing fibers, but it also makes it possible to place a CCD camera at the oven position, that is used to check the fibers for dust particles and for imaging the resultant TOF shape after a pulling run.

1 *PMT-160-150-DC05-R* and *PMT-160-050-DC38-R* from Steinmeyer FMD.
2 *CMH-7019* from NTT Advanced Technology Corporation.

During a pull, the bottom stage moves the right end of the fiber with velocity v_+, whereas the combined motion of the top and bottom stages moves the left end with velocity v_-. In [Sørensen, 2013] it was

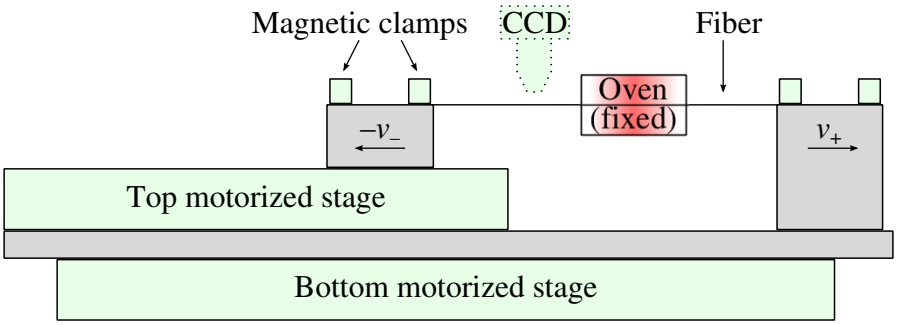

Figure 4.1.: *Schematic drawing of the fiber-pulling rig. The CCD camera can only be inserted when the oven is removed from the setup. From [Sørensen et al., 2014].*

confirmed that identical TOF shapes can be reproducible produced when driving the oven with electrical heating powers[3] in the range 97 W to 103 W. It was also confirmed that the resultant shape only depends on the ratio of the pull speeds v_+/v_-, rather than on their absolute value. This is a consequence of Newtonian fluid flow and remains valid as long as the speeds are sufficiently low that the fiber does not slip underneath the magnetic clamps. For a slow quasi-static pull, the fiber shape therefore only depends on the pull lengths on either side of the oven.

4.1.2 *Imaging*

The TOF shape is measured by imaging it with a CCD camera through a 25× microscope objective placed above the fiber (*cf.* Fig. 4.1). The imaging is non-destructive, fast, and *in situ*: the full fiber shape is obtained by repeatedly recording an image and translating the TOF with the bottom stage. The individual images are joined, and a typical example of 300 merged images is displayed in Fig. 4.2. The green curves indicate the fiber edges found by an edge-detection algorithm specially developed for this purpose. It works by calculating the convolution of each image column with a template kernel. From this the position of the edges is located by the outermost local minimum/maximum values that are significant enough to exceed a certain threshold level, as indicated in Fig. 4.3. Introducing this threshold prevents de-

3 The heating powers has been increased in more recent work that were performed after moving the fiber-pulling rig. This might be a consequence of the re-alignment of the oven with respect to the fiber or a degrade of the oven performance over time. Consult [Knudsen *et al.*, 2014] and [Pedersen, 2015] for the most recent parameters of the fiber-pulling rig.

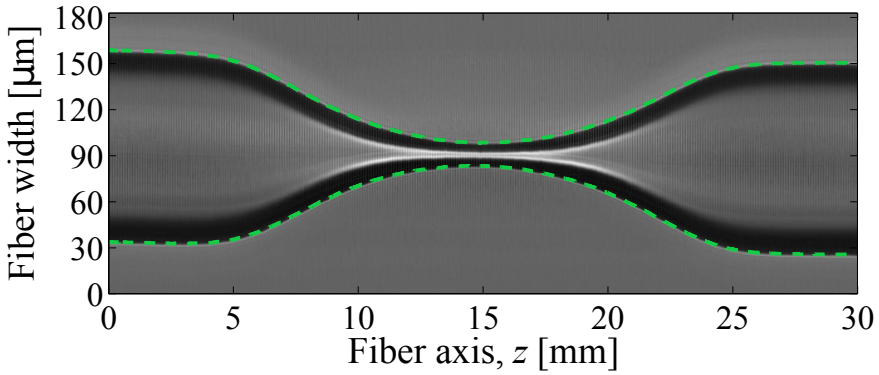

Figure 4.2.: $\sim$ 300 *joined* CCD *images of a* TOF*, symmetrically elongated by* $l = 15\,\mathrm{mm}$*. The waist diameter is measured to* $d_{waist} = 15\,\mu\mathrm{m}$*. The aspect ratio is not to scale. From [Sørensen* et al.*, 2014].*

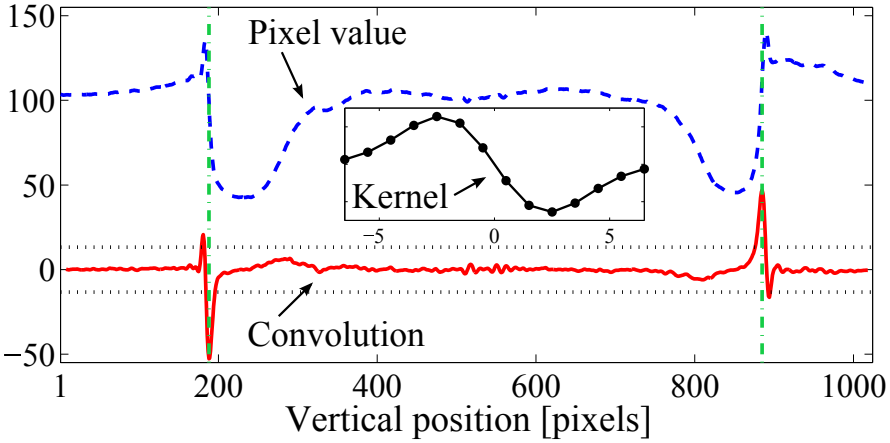

Figure 4.3.: *Edge-detection algorithm. Dashed blue line: Pixel values along the image column at* $z = 5\,\mathrm{mm}$ *in Fig. 4.2. Solid red line: Convolution. Dotted horizontal black lines: Threshold levels* ($= \pm 13$)*. Dashed-dotted vertical green lines: Located edge positions. Inset: Edge-detection kernel. From [Sørensen* et al.*, 2014].*

tection errors caused by the narrow, bright features close to the fiber axis; its value is set to 25 % of the extremal convolution values found in the unstretched fiber. As template kernel the derivative of a Gaussian is used with a width chosen such that the kernel models the pixel values observed at the edges of the unstretched fiber.

The precision of the diameter detection is estimated in two ways: (i) By running the edge detection algorithm over 10^5 image columns of an unstretched 125 µm fiber, a width of 694 pixels with a 1 pixel uncertainty in every column is obtained. (ii) Additionally, after stretching the fiber by 15 mm, similar to the fiber shown in Fig. 4.2, only a relative change of the fiber volume $< 10^{-3}$ is observed compared to that

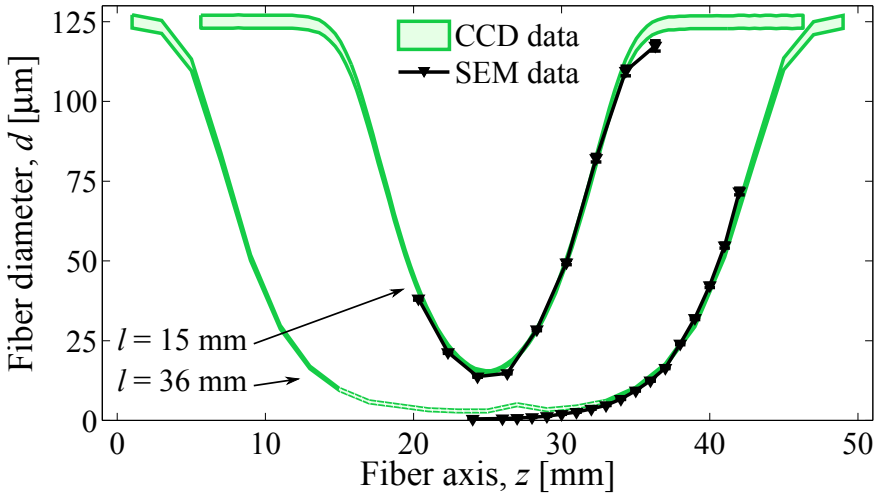

Figure 4.4.: *Comparison of fiber-diameter measuring methods. At several selected positions the fiber diameter is determined both using the CCD imaging and the SEM. For fiber diameters* $< 10\,\mu m$ *diffraction effects limit the accuracy of the CCD method (indicated by the dashed lines), whereas the SEM method fails for large fibers due to space-charge buildup. From [Sørensen* et al., *2014].*

of an unstretched fiber[4]. The dominating contribution to the uncertainty is thus given by how well the diameter of the unstretched fiber is known, nominally given by $(125 \pm 2)\,\mu m$ for the fibers used in this work[5].

Because the edge detection is limited by the optical imaging resolution, diffraction effects, and the fiber bending out of the focal plane, only TOFs with waist diameters larger than $\sim 10\,\mu m$ can be measured. The validity of the fiber shape model, presented in Section 4.2, is confirmed also for thinner TOFs by the additional use of a scanning electron microscope (SEM) to measure the diameter at selected axial positions, as shown in Fig. 4.4.

4.1.3 *Light transmission and adiabaticity*

Using a $\lambda = 852\,nm$ single-mode external cavity diode laser (ECDL) source, the light transmission through the fiber is continuously measured while tapered, in order to quantify the resulting optical losses in the tapers. In [Sørensen, 2013] transmissions of 91 % were reported

4 When comparing the relative volume change before and after a pull, the waist of the resulting TOF should preferable be as thin as possible to make the error estimation more valid, as this reveals more features in the imaging. The $l = 15\,mm$ (symmetrically) stretched fiber results in $d_{waist} = 15\,\mu m$ close to the resolution limit of the imaging setup.

5 LEIKKI^{TM} Passive-6/125.

for TOFs with sub-wavelength waist diameters $d_{\text{waist}} = 0.5\,\mu\text{m}$ that display typical transmission signal (blue curve) as shown in Fig. 4.5. This is far from a record value as evident from Table 4.1 where a selection of reported transmissions through TOFs are collected. Two

GROUP	$\mathcal{T}$ [%]	λ [nm]	d_{waist}/d_0 [µm]	l [mm]
Rauschenbeutel 2011	98.7	850	0.5/125	N/A
Polzik 2013	91	852	0.5/125	36
Rolston 2014	99.95	780	0.53/125	84
Aoki 2014	99.7	852	0.6/62.5	23
Chormaic 2014	99	780	1.1/125	30

Table 4.1.: *Selection of reported light transmissions through TOFs.*

main ingredients enter the successful production of adiabatic TOFs: (i) Optimize the tapers according to the adiabatic criterion, *cf.* Section 2.4.1. In the group of Rauschenbeutel they have achieved this by developing an analytical pulling algorithm. With this they can produce sub-wavelength TOFs with tapers comprised of three linear sections that closely follow the shape in Fig. 2.8(b) [Warken, 2007; Stiebeiner *et al.*, 2010][6]. As an aid to reach low-loss tapers, one can also reduce the cladding to core radius of the initial unstretched fiber, since this makes it easier to fulfill the adiabatic criterion [Frawley *et al.*, 2011]. Finally, (ii), the stripped fiber should be cleaned thoroughly from dust particles and remaining residues of the initially surrounding buffer layer [Hoffman *et al.*, 2014; Ward *et al.*, 2014]. Perhaps a rather trivial point, but nevertheless important.

As already discussed, power loss from the fundamental mode can be assigned to the excitation of higher order cladding-modes. When identifying which modes are excited in the tapers and successively lost, it is helpful to consider the approximative LP modes instead of the exact modes. If the tapers are axisymmetric, only modes with the same azimuthal symmetry can be excited [Love *et al.*, 1991]. Coupling to the higher order modes with LP_{0m} are therefore expected to dominate, with the highest coupling being that to the nearest mode LP_{02}, *i.e.*, the mode with the smallest difference in propagation constant with respect to the fundamental mode. Of course, if the fiber is bending, thus breaking the axial symmetry, coupling to other higher modes can also take place.

6 I apologize for the reference to a PhD thesis written in German, but this is the closest I have gotten to their pulling algorithm so far.

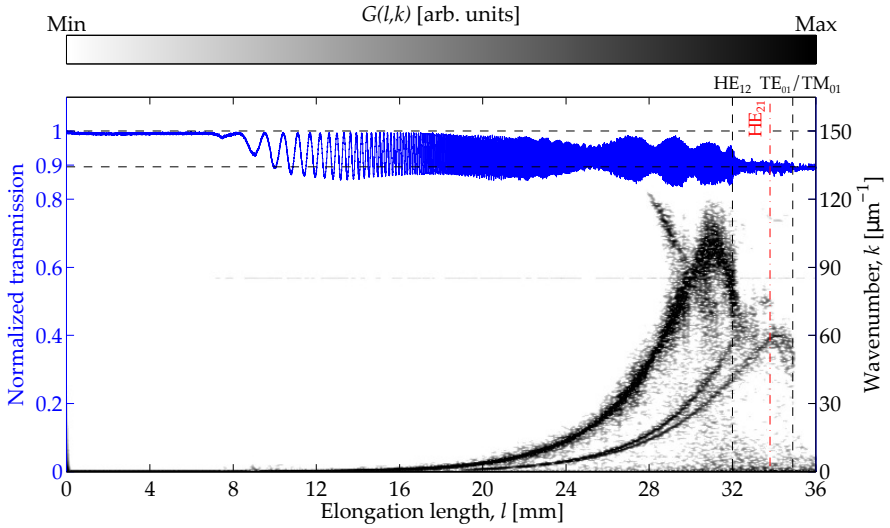

Figure 4.5.: *Transmission signal together with according Gabor transform. The vertical lines indicate the inferred radiative loss of higher order modes. From [Sørensen, 2013].*

In Fig. 4.5, the loss and identification of higher order modes are inferred both from the transmission signal $\mathcal{T}(l)$ and from a frequency analysis performed by applying the Gabor transform to $\mathcal{T}(l)$ [Ding *et al.*, 2010]:

$$G(l,k) = \int_{-\infty}^{\infty} e^{-\alpha(l-z)^2} e^{ikz}\, \mathcal{T}(z)\, dz\,, \tag{4.1}$$

where the free parameter α adjusts the resolution, l is the fiber elongation length, and $k = 2\pi\nu_{\text{beat}}/(v_+ - v_-)$ is the wave number equivalent of the beat note frequency ν_{beat}. Eq. (4.1) is nothing more than a short-time Fourier transform of the transmittance $\mathcal{T}$ with a Gaussian window[7].

Two frequency components are seen to arise after elongating the fiber by about $l = 15\,\text{mm}$ and $l = 20\,\text{mm}$, respectively. The first component then suddenly vanishes at 32.0 mm, while the second component splits into two, which thereafter vanish at 33.8 mm and 34.9 mm, respectively (indicated in Fig. 4.5 by the vertical lines). The disappearance of the three frequency components is assigned to the loss of three bounded modes in the TOF, which is supported by the two black dashed lines coinciding with observed decreases in the oscillation amplitude of the transmission signal.

From Fig. 2.6 and the calculated cut-off diameters of the higher order modes, given in Table 2.2, the excited higher modes are identified

7 This short-time Fourier analysis is used instead of the conventional Fourier transform because the frequency components change during the pull. The Gabor transform thus shows which frequency components are present at a given time and, more importantly for our application, when they are lost, which in the end, tells us when the TOF becomes single-mode

as the HE_{12} mode with a cut-off at $l = 32.0\,\text{mm}$; the HE_{21} mode with a cut-off at $l = 33.8\,\text{mm}$; and the TE_{01} and TM_{01} modes with a cut-off after 34.9 mm symmetric pulling at which the TOF becomes single-mode.

The main reason for our rather low transmission, is that we so far have not done any serious effort in improving it. The transmission signal in Fig. 4.5, and the correspondingly reported transmission of 91 %, belongs to one of the most simple pull trajectories that can be implemented, namely that of pulling both fiber-ends by the same speed, which we shall refer to as a symmetric pull. In Fig. 4.6 we show how the taper angle of such a pull (blue curve), for our experimental parameters and pulling boundary conditions[8], compares with the limiting taper angle from the adiabatic criterion (red curve), *cf.* Fig. 2.8(a). The red and blue solid lines have been calculated for

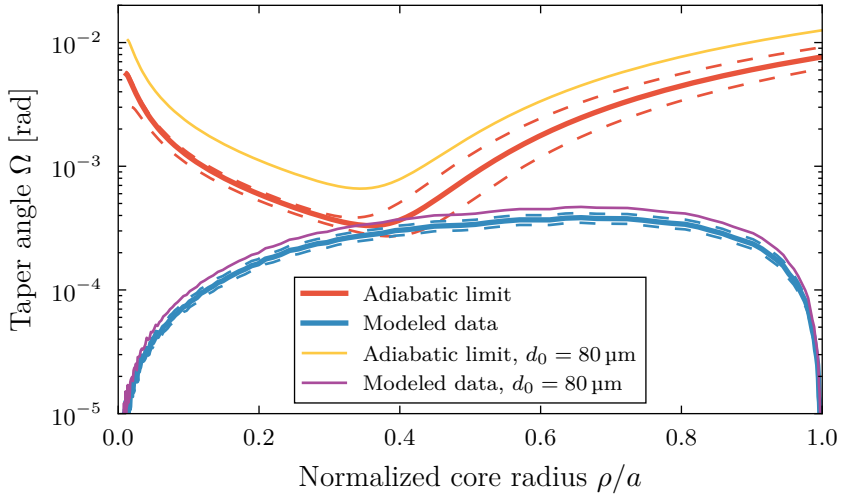

Figure 4.6.: *Comparison of the limiting taper angle as a function of the core radius, to the symmetrically pulled fibers that we have produced (using modeled data, described in Section 4.2). The red and blue curves have been calculated for the parameters* $NA = 0.115$, $n_{cl} = 1.452$, $d_0 = 125\,\mu\text{m}$, *and* $2a = (5.5 \pm 0.5)\,\mu\text{m}$, *while the yellow and purple curve have been obtained for* $NA = 0.16$, $n_{cl} = 1.452$, $d_0 = 80\,\mu\text{m}$, *and* $2a = 4.3\,\mu\text{m}$.

an initial SIF with cladding diameter $d_0 = (125 \pm 2)\,\mu\text{m}$ and core diameter $2a = (5.5 \pm 0.5)\,\mu\text{m}$. Evidently, there is quite a big uncertainty on the core diameter. Taking this into account yields the upper and lower limits for the calculated taper angles indicated by the dashed curves. Our modeled data are observed to just slightly cross the adiabatic limit near $\rho/a = 0.45$. Although, there is only a minimal overlap with the non-adiabatic region, this seems to be sufficient to cause the 10 % loss that we observe in the light transmission through the TOF.

8 The numerical model used to produce this data is given in Section 4.2.

For completeness, we also show the calculated limiting taper angle for a SIF with initial cladding diameter of 80 µm (yellow curve), for which the cladding to core radius is reduced compared to the standard 125 µm diameter SIF that we have used in this work[9]. Interestingly, it appears that if we would just replace our current SIF with the one that has a reduced cladding to core radius (purple curve), we should be able to produce low-loss fibers even when implementing the simple symmetric pull procedure[10].

4.2 MODELING THE FIBER SHAPE

Closely following [Sørensen *et al.*, 2014], we now present a short summary of a numerical model for the prediction of the resulting fiber shape after a performed pull with known boundary conditions, *i.e.*, pull speeds, heating profile *etc*. A more elaborate description including finer details can be found in [Sørensen, 2013].

4.2.1 *Boundary conditions*

We set the stage by writing down a few useful relations. Outside the heated section of the fiber, bounded by $z_\pm$ as illustrated in Fig. 4.7, the fiber is frozen. In these regions, the fiber therefore moves uniformly

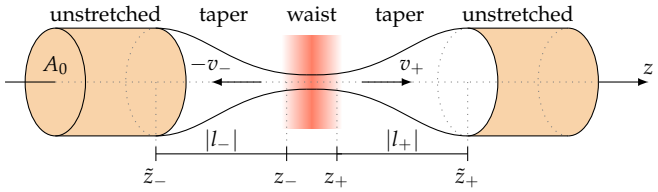

Figure 4.7.: *Boundary conditions during the fiber pulling procedure. From [Sørensen, 2013; Sørensen* et al., *2014].*

with the velocities set by the respective fiber holders, *cf.* Fig. 4.1. For the axial fiber flow $v(z,t)$, at position z and time t, we then have

$$v(z,t) = v_-, \quad \text{for } z < z_-\,, \tag{4.2a}$$
$$v(z,t) = v_+, \quad \text{for } z > z_+\,, \tag{4.2b}$$

where the sign of $v_\pm$ follows the direction of the pull. Inside the heated zone, $v(z,t)$ is described by an unknown function that depends on the pull speeds, the momentary fiber shape contained in

9 Using the specs for the *SM800G80* SIF from Thorlabs with mean values NA $= 0.16$, $d_0 = 80\,\mu\text{m}$, and $2a = 4.3\,\mu\text{m}$.

10 For the modeled data it is assumed that the ratio between the initial core and cladding radii is kept constant during the tapering.

the position- and time-dependent cross-sectional area $A(z,t)$, and the axial viscosity distribution of the fiber, resulting from the axial temperature profile of the heater (when neglecting any transverse variation).

The boundary between each taper and the unstretched fiber is denoted by $\tilde{z}_\pm$. Outside the tapered sections ($z < \tilde{z}_-$ or $z > \tilde{z}_+$), the cross-sectional area corresponds to that of the initially uniform fiber, $A(z,t) = A_0$. We introduce the following convenient abbreviations:

$$v_\infty \equiv v_+ - v_- \,, \tag{4.3a}$$

$$l_\pm = v_\pm t = \tilde{z}_\pm - z_\pm \,, \tag{4.3b}$$

$$A_\mathrm{n}(z,t) \equiv \frac{A(z,t)}{A_0} \,, \tag{4.3c}$$

where v_∞ denotes the overall stretching speed, $l_\pm$ denote the elongated lengths of the fiber on either side of the heated section, and $A_\mathrm{n}(z,t)$ denotes the normalized cross-sectional area.

In the following, we restrict ourselves to cases where the fiber is never compressed, *i.e.*, where $v_+ - v_- > 0$.

4.2.2 *Fiber shape*

The evolution of the fiber shape during the tapering procedure can be described by two coupled differential equations for the normalized cross-sectional area $A_\mathrm{n}(z,t)$ and the axial velocity profile of the fiber $v(z,t)$ [Geyling, 1976; Dewynne *et al.*, 1989]. The continuity equation

$$\frac{\partial}{\partial t} A_\mathrm{n}(z,t) + \frac{\partial}{\partial z}\Big(A_\mathrm{n}(z,t)\, v(z,t)\Big) = 0 \tag{4.4}$$

governs mass conservation, and a simplified equation describes axial momentum conservation:

$$\frac{\partial}{\partial z}\Big(\eta(z) A_\mathrm{n}(z,t) \frac{\partial}{\partial z} v(z,t)\Big) = 0 \,, \tag{4.5}$$

where $\eta(z)$ is the axial viscosity of the fiber fluid. Equation Eq. (4.5) is derived by solving the Navier-Stokes equations for an axisymmetric incompressible Newtonian fluid in the limit of Stokes flow, neglecting body forces (such as gravity, which is negligible compared to viscous forces), and by Taylor-expanding the equations to lowest order in the radial variable [Eggers *et al.*, 1994]. Since the fiber is thin, and its heat conductivity is poor compared to that of the much bigger surrounding oven, the temperature along the fiber (and hence $\eta(z)$) is a function of the axial position within the oven alone. Additionally, we ensure that each mass element of the fiber is in thermal equilibrium with the surroundings by asserting slow motion of the fiber.

In order to solve Eq. (4.4) and Eq. (4.5) numerically, it is necessary to know the axial viscosity $\eta(z)$. Often, this is simply approximated by a uniform distribution such that it is infinite outside the heated region of the fiber and finite and constant inside [Dewynne *et al.*, 1989; Birks *et al.*, 1992; Baker *et al.*, 2011]. In [Xue *et al.*, 2007] they measure the temperature distribution of their heater and use the Arrhenius model for the viscosity dependence on the temperature to indirectly deduce $\eta(z)$. In [Pricking *et al.*, 2010] $\eta(z)$ is heuristically model by a flattened Gaussian profile.

In the following we show how $\eta(z)$ instead can be easily inferred experimentally by measuring the resultant fiber shape after a short symmetric ($-v_- = v_+$) pull. We thereby avoid cumbersome temperature-viscosity calibrations and measurements of the temperature profile inside the heater.

4.2.3 *Fiber fluidity*

The main challenge in solving for the fiber flow in order to obtain the shape, is really the time-dependency (or rather the fiber shape dependency) of the axial velocity in the continuity equation Eq. (4.4). In [Sørensen, 2013] we showed that if $v(z,t)$ had been independent of time, an analytic solution can be obtained for $A(z,t)$ in Eq. (4.4). However, as experimentally confirmed in both [Sørensen, 2013; Pricking *et al.*, 2010] the axial velocity depends on the fiber shape as expressed in Eq. (4.5). We therefore wish to obtain an expression for the variation of $v(z,t)$ while performing a pull.

As mentioned earlier, it was also experimentally confirmed in [Sørensen, 2013] that the TOF shape depends on the ratio of the velocities, and not on the individual velocities. Therefore, only a dependence on the pull lengths $l_\pm = v_\pm t$ remains (and not on t), which makes it more convenient and intuitive to express the axial velocity profile and the cross-sectional area in terms of the total elongation length

$$l = l_+ - l_- = v_\infty t \tag{4.6}$$

instead of time, such that $v(z,t) \to v(z,l)$ and $A_\mathrm{n}(z,t) \to A_\mathrm{n}(z,l)$.

In order to arrive at an expression for $v(z,t)$, we notice that Eq. (4.5) almost screams for being integrated over z, from which we obtain

$$\eta(z) A_\mathrm{n}(z,l) \frac{\partial}{\partial z} v(z,l) = C(l), \tag{4.7}$$

where the integration constant $C(l)$ is spatially constant but may depend on the elongation length. Solving Eq. (4.7) for $\frac{\partial}{\partial z} v(z,l)$ and

integrate once more over z, starting at an arbitrary position z_0, we find

$$v(z,l) = v(z_0,l) + v_\infty \cdot \frac{\int_{z_0}^{z} \frac{f(\zeta)}{A_\mathrm{n}(\zeta,l)}\,\mathrm{d}\zeta}{\int_{z_-}^{z_+} \frac{f(\zeta)}{A_\mathrm{n}(\zeta,l)}\,\mathrm{d}\zeta}\,, \tag{4.8}$$

for the axial velocity profile. Here the integration constant

$$C(l) = \frac{v_\infty}{\int_{z_-}^{z_+} \frac{1}{\eta(\zeta)A_\mathrm{n}(\zeta,l)}\,\mathrm{d}\zeta} \tag{4.9}$$

has been fixed by requiring continuity at the boundaries $v(z_\pm,l) = v_\pm$, details can be found in [Sørensen, 2013]. In Eq. (4.8) we have also introduced a new variable $f(z)$ for the normalized fiber fluidity:

$$f(z) = \frac{\frac{1}{\eta(z)}}{\int_{-\infty}^{\infty} \frac{1}{\eta(\zeta)}\,\mathrm{d}\zeta}\,. \tag{4.10}$$

Since the viscosity $\eta(z)$ necessarily only takes on finite values inside the heated section, $f(z)$ accordingly only differs from zero in this region, bounded by $z_\pm$

4.2.4 *Short pull approximation*

In the following, we show how $f(z)$ can be experimentally inferred from a short symmetric pull where the fiber elongation length l is much smaller than the heated section. In this limit, the spatial variation of the normalized fiber cross-sectional area $A_\mathrm{n}(z,l)$ over regions with non-zero $f(z)$ can be neglected and Eq. (4.8), describing the axial velocity profile, simplifies significantly. If z_0 is chosen outside the heat-softened section, such that $v(z_0,l)$ is constant, we find, from Eq. (4.8) and Eq. (4.10),

$$v(z,l) \approx v(z) = v(z_0) + v_\infty \int_{z_0}^{z} f(\zeta)\,\mathrm{d}\zeta \tag{4.11}$$

to be constant in l during the whole pulling process. From this, the fiber fluidity can be readily approximated by

$$f(z) \approx \frac{\mathrm{d}}{\mathrm{d}z}\frac{v(z,l)}{v_\infty}\,. \tag{4.12}$$

The short pull of the fiber can thus be thought of as providing a snapshot of axial fluidity profile from which the heater is essentially calibrated. Since the axial velocity profile is now independent of the elongation length, the continuity equation Eq. (4.4) can be solved analytically to yield an explicit form for the normalized fiber cross-sectional area:

$$A_\mathrm{n}(z,l) = \frac{\partial}{\partial z}\Big(q^{-1}\big(q(z)-l\big)\Big) \tag{4.13a}$$

$$\text{with } q(z) \equiv \int_{z_*}^{z} \frac{v_\infty}{v(\zeta)}\,\mathrm{d}\zeta\,, \tag{4.13b}$$

as can be directly verified by differentiation, i.e., by inserting Eq. (4.13a) and Eq. (4.13b) into Eq. (4.4). $q^{-1}(\cdot)$ denotes the inverse function of $q(z)$, and z_* is an arbitrarily chosen position. We integrate both sides of Eq. (4.13a) from $\tilde{z}_\pm$ and define a new variable

$$y(z,l) \equiv q^{-1}\big(q(z) - l\big), \text{ so that} \tag{4.14a}$$

$$y(z,l) = \int_{\tilde{z}_\pm}^{z} A_\mathrm{n}(\zeta,l)\, \mathrm{d}\zeta + z_\pm. \tag{4.14b}$$

The second term in Eq. (4.14b) follows from choosing $z_* = z_\pm$ in Eq. (4.13b). The expression $z - y(z,l)$ can be interpreted as the distance that a fiber volume element at position z has moved during the pulling process.

We now apply $q(\cdot)$ to both sides of Eq. (4.14a) and differentiate with respect to z. Using Eq. (4.14b) to express $\frac{\partial y}{\partial z}$ and Eq. (4.13b) to express $\frac{\mathrm{d}q}{\mathrm{d}z}$ in the result, we obtain a recursion formula for the axial velocity profile of the fiber:

$$v\big(y(z,l)\big) = A_\mathrm{n}(z,l)\, v(z)\,. \tag{4.15}$$

Both $A_\mathrm{n}(z,l)$ and $y(z,l)$ are known from a shape measurement of the fiber after the short pull (the latter via Eq. (4.14b)). On the left side of the oven $y(z,l) > z$. Starting from $z = \tilde{z}_-$, using Eq. (4.15), we can now calculate $v(y(z,l))$ from $v(z)$, which lies further to the left, until $y(z,l)$ approaches z. The same can be done from the other side starting from $z = \tilde{z}_+$, since there $y(z,l) < z$. Pseudo-code illustrating the algorithm for calculating $v(z)$ can be found in Appendix C.

4.2.5 *Calibration*

To calibrate our heater, we symmetrically elongate a fiber by $l = 2\,\mathrm{mm}$ with speeds $v_\pm = \pm 50\,\mu\mathrm{m\,s^{-1}}$ and subsequently measure the shape $d(z,l) = 2\sqrt{A(z,l)/\pi}$. By applying the recursion formula (4.15), we infer the axial velocity profile $v(z,l)$ shown in Fig. 4.8(a). Also depicted is a simplifying model which was introduced in the seminal paper by Birks and Li [Birks *et al.*, 1992]. This is commonly used to describe flame-brushing fiber processing [Kenny *et al.*, 1991], and approximates $v(z)$ inside the heated section by interpolating linearly between the exterior pull velocities $v_\pm$ over an "effective hot-zone length" $L_0 = v_\infty \big/ \frac{\mathrm{d}v}{\mathrm{d}z}\Big|_{v=0}$.

The effective hot-zone length L_0 can be found from the waist diameter d_waist using Birks' and Li's formula:

$$d_\mathrm{waist}(l) = d_0 \exp\left(-\frac{l}{2L_0}\right). \tag{4.16}$$

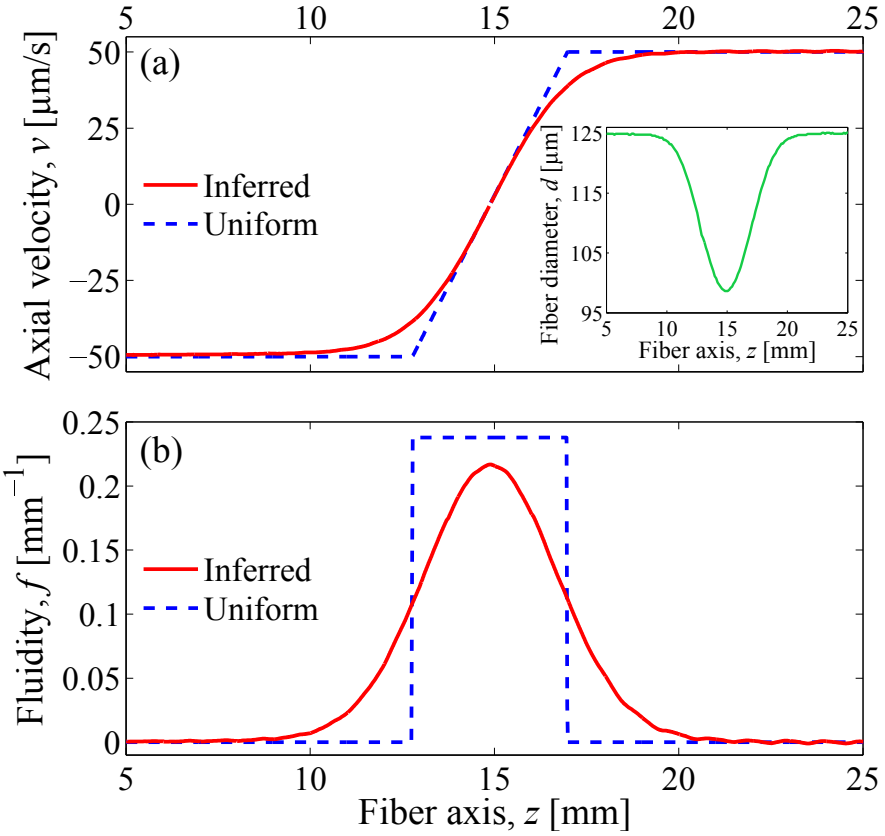

Figure 4.8.: *(a) Axial velocity profile. Inset: measured fiber diameter of an* $l = 2\,\mathrm{mm}$ *stretched fiber used to infer* $v(z,l)$*. (b) Axial fluidity profile, inferred by applying Eq. (4.12) to (a). Red solid lines depict data inferred with the presented algorithm. Blue dashed lines depict data corresponding to a uniform fluidity profile with* $L_0 = 4.2\,\mathrm{mm}$*, which results in an identical waist diameter. From [Sørensen* et al.*, 2014].*

The $l = 2\,\mathrm{mm}$ elongation of a TOF, with an initial diameter $d_0 = 125\,\mu\mathrm{m}$, results in a final waist diameter measured to $d_{\mathrm{waist}} = 98\,\mu\mathrm{m}$, which yields $L_0 = 4.2\,\mathrm{mm}$.

The curves for $v(z)$ in Fig. 4.8(a) agree in value and slope at the oven center and at the ends by construction but they deviate substantially at the edges of the heated section. The difference is even more pronounced in $f(z)$, which is depicted in Fig. 4.8(b). This strongly suggests that the assumption of a uniform temperature distribution does not describe our setup.

4.2.6 *Symmetric pull*

Given the inferred fiber fluidity $f(z)$ we numerically solve the system of equations Eq. (4.4) and Eq. (4.8), using the `MATLAB` function `ode45` with a relative error tolerance of 10^{-6}. For thin TOFs with diameters below $\approx 1\,\mu\mathrm{m}$, numerical instabilities can occur, which necessitates

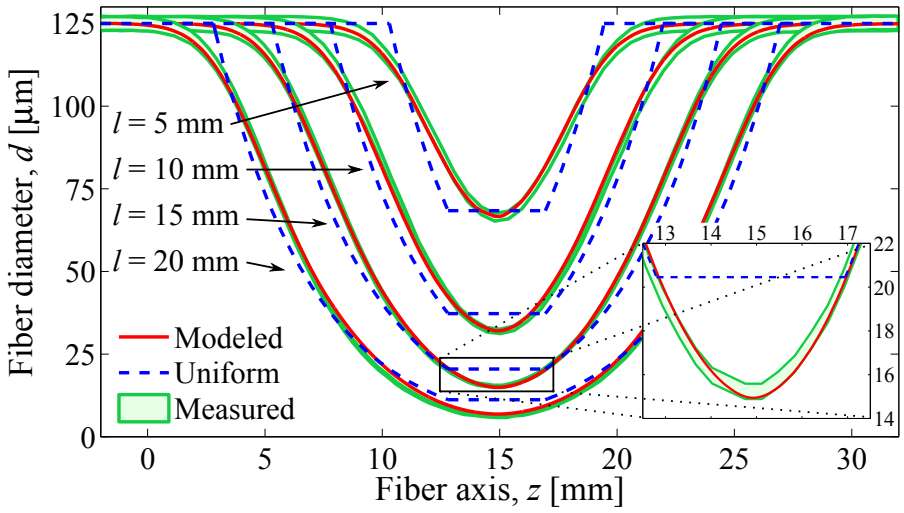

Figure 4.9.: *Fiber diameter of four different symmetrically pulled fibers with various elongation lengths l. Solid red line: Model. Green lines enclosing shaded area: Fiber diameter as measured with CCD camera with measurement uncertainty. Dashed blue line: Fiber shape prediction using an $L_0 = 4.2\,\mathrm{mm}$ uniform fluidity profile. The inset shows a zoom of the waist of the fiber stretched by $l = 15\,\mathrm{mm}$. From [Sørensen et al., 2014].*

decreasing the relative and absolute error tolerances further. Alternatively, by adding a term $D\frac{\partial^2 A_n(z,t)}{\partial z^2}$ to the right-hand side of Eq. (4.4), using a small "diffusion coefficient" D such that $2\sqrt{Dl/v_\infty} \ll L_0$, we can effectively eliminate the numerical stiffness of the problem without introducing a significant change to the solution.

In Fig. 4.9, we present the modeling of four symmetrically stretched fibers, which were elongated by $l = 5, 10, 15, 20\,\mathrm{mm}$ with speeds $v_\pm = \pm 50\,\mu\mathrm{m\,s^{-1}}$. We observe very good agreement between the measured and modeled diameter with only a 1 % discrepancy at the waist of the $l = 5\,\mathrm{mm}$ and $l = 10\,\mathrm{mm}$ streched fibers, and 2 % for the $l = 15\,\mathrm{mm}$ fiber. For the longer $l = 20\,\mathrm{mm}$ stretched fiber the discrepancy is 13 %, however, here the waist is so thin, $d_{\mathrm{waist}} \approx 6\,\mu\mathrm{m}$, that the CCD imaging starts to fail.

For reference, we also show the predicted TOF shape using a uniform profile for the fluidity with $L_0 = 4.2\,\mathrm{mm}$, which (by definition) predicts the waist correctly for $l = 2\,\mathrm{mm}$. For this $f(z)$ it is evident that the waist size is increasingly overestimated for longer pull lengths. As can also be observed by numerically solving Eq. (4.5), this implies that the effective hot-zone length L_0 Eq. (4.16) of the fiber shrinks during the pull (*i.e.*, for smaller fiber diameters) in agreement with similar observations made in [Pricking *et al.*, 2010]. This shape-dependency makes it impossible to predict the waist for arbitrary pull lengths using a constant-width box-profile for the fluidity, as it fails to reproduce qualitative features of the TOF shape. Especially the prediction

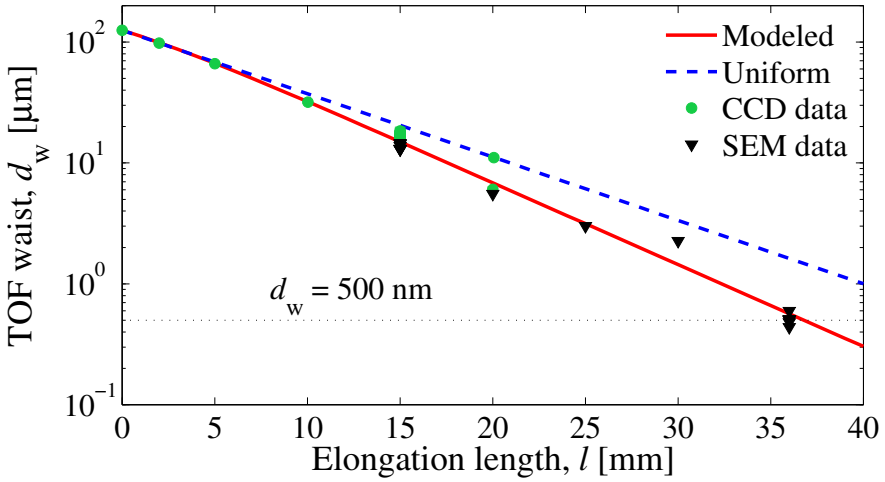

Figure 4.10.: *TOF waist of symmetrically elongated fibers. Note the log scale on the y-axis. From [Sørensen* et al.*, 2014].*

of a homogeneous waist with length L_0 is absent in the data. This necessitates non-symmetric pulling procedures for producing TOFs with long homogeneous waists.

In Fig. 4.10, for symmetric pulls, we compare the predicted fiber waist diameter resulting from our calibration method with experimental data and the simplified prediction (4.16). Whereas the latter overestimates the waist for longer pull lengths, our simulations display good agreement with the data even for very thin TOFs, where the initial diameter has been reduced by a factor of 250 from 125 µm to about 500 nm. In trying to fit (4.16) to the data shown in Fig. 4.10 by determining an *effective* L_0 [Kenny *et al.*, 1991; Ward *et al.*, 2006; Ding *et al.*, 2010], one would compromise on the predicted corresponding shape of the tapers instead.

4.2.7 *Asymmetric pull*

The fiber shape model is not only restricted to symmetric pulls, where $-v_- = v_+$, but can be applied to any combination of pull speeds. This is extremely useful as it makes it possible to test various pulling procedures without actually performing them.

In Fig. 4.11 the measured and modeled diameter of the resulting TOF is shown, for the extreme situation where the two fiber ends are moved in the same direction such that the fiber is being pushed into the oven from one side while being pulled out on the other side with a greater speed, *i.e.*, $0 < v_- < v_+$. Here, an elongation of 15 mm is obtained by push and pull speeds $v_- = 10\,\mu\mathrm{m\,s^{-1}}$ and $v_+ = 100\,\mu\mathrm{m\,s^{-1}}$. The modeled curve predicts the data very closely with only a 3 % dis-

crepancy at the waist and well within the uncertainty of the CCD data. This demonstrate that especially in a situation where the axial fiber

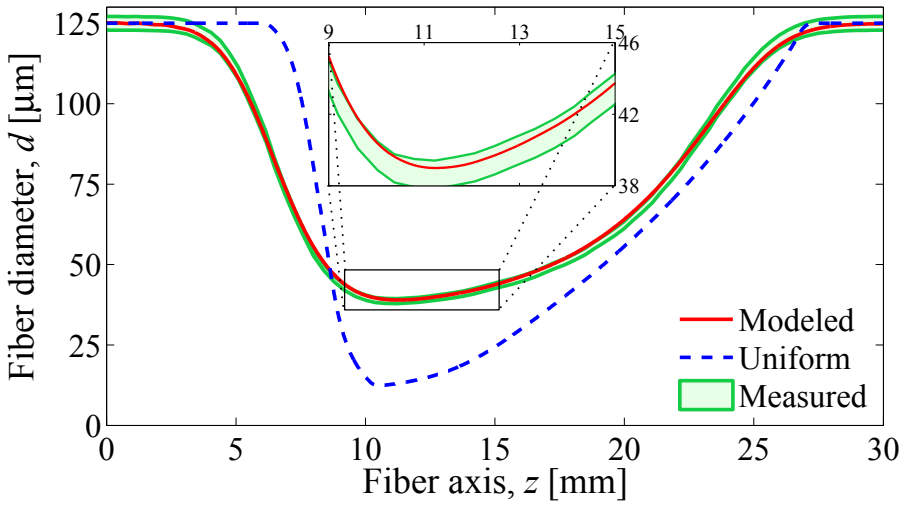

Figure 4.11.: *Shape of a TOF, asymmetrically elongated by* $l = 15\,\mathrm{mm}$. *Red solid line: Predicted fiber shape using the inferred fluidity profile depicted in Fig. 4.8. Green lines enclosing shaded area: CCD measured diameter. Blue dashed line: Solution to Eq. (4.4) and Eq. (4.8) using a uniform fluidity profile with* $L_0 = 4.2\,\mathrm{mm}$. *The inset shows a zoom of the TOF waist. From [Sørensen* et al., *2014].*

diameter changes strongly within the heated zone, accurate modeling of the viscosity profile leads to a significant improvement of the fiber shape prediction.

SUMMERY

Starting with a description of the fiber-pulling rig, we have showed how the TOF can be non-destructively imaged in order to measure the resulting fiber shape after a pulling run. For a symmetric pulling procedure we observe 91 % light transmission through the fiber after tapering down to $d_{\mathrm{waist}} = 0.5\,\mu\mathrm{m}$, when the initial fiber diameter is $125\,\mu\mathrm{m}$. This loss in optical power can be ascribed to non-adiabatic coupling in the tapers. Calculations show that similarly produced TOFs but with an initial reduced cladding to core radius should yield adiabatic coupling in the tapers, and thus improve the light transmission. Finally, we have presented a numerical model for the prediction of the TOF shape. By performing an initial short simple pull, the axial fluidity profile of the fiber within the heater can be inferred. Using this in a set of two coupled differential equations the fiber flow can be modeled during a pull from which we obtain the resulting TOF shape.

Part II

LIGHT-ATOM INTERACTION

5

SCHRÖDINGER'S EQUATION

Everything in quantum mechanics boils down to solve the Schrödinger equation of the particular system under investigation. The field of quantum optics is no exception. However, after a while of considering the (same) different variants of light-atom Hamiltonians and their respective (approximative) solutions, one tends to forget where it all started. We have therefore devoted this chapter to the Schrödinger equation, which we will apply to solve for the dynamics of a two-level atom interacting with a classical light field.

5.1 UNITARY EVOLUTION

We will jump right into it and immediately write down what all the fuzz is about – we here present the Schrödinger equation[1] [Sakurai, 1994]:

$$i\hbar|\dot{\psi}(t)\rangle = \hat{H}|\psi(t)\rangle\,. \tag{5.1}$$

This famous wave equation consists only of the imaginary number $i^2 = -1$, Planck's reduced constant $\hbar = h/2\pi$, the wave function state ket $|\psi(t)\rangle$ representing the physical state under consideration, and the Hamiltonian $\hat{H}$ which originates from classical mechanics as the generator of time evolution. Innocent looking, the Schrödinger equation is by no means easy to solve. In fact, all the solutions given in this thesis will be approximative obtained by careful considerations of the system under investigation.

The state dynamics can be considered by introducing the unitary[2] time-evolution operator $\hat{U}(t, t_0)$ such that an initial state $|\psi(t_0)\rangle$ evolves according to

$$|\psi(t)\rangle = \hat{U}(t, t_0)|\psi(t_0)\rangle. \tag{5.2}$$

Inserting this expression into Eq. (5.1) we obtain the Schrödinger equation for the time-evolution operator:

$$i\hbar\dot{\hat{U}}(t, t_0) = \hat{H}\hat{U}(t, t_0)\,. \tag{5.3}$$

It now becomes clear what we mean when we say that the Hamiltonian is the time-evolution generator, since solving Eq. (5.3) yields

$$\hat{U}(t, t_0) = \mathrm{e}^{-i\hat{H}(t-t_0))/\hbar}\,. \tag{5.4}$$

1 In the following we will make use of the widely known shorthand notation $\dot{x} = \frac{\mathrm{d}x}{\mathrm{d}t}$.
2 Unitary meaning that it fulfills the condition $\hat{U}\hat{U}^\dagger = \hat{U}^\dagger\hat{U} = \hat{I}$.

Knowing $\hat{U}(t, t_0)$ and the initial state of the system is thus all we need. Unfortunately, this is easier said than done. First of all we note that the solution for $\hat{U}(t, t_0)$, Eq. (5.4), is only valid when $\hat{H}$ is independent of time[3]. This is certainly not the case for the Hamiltonian governing light-atom interactions as we shall see in a moment. Generally, in that case, one needs to resort to perturbation theory in order to solve for the dynamics of the system, and only, in the simplistic case of a two-level system exact solutions can be found.

5.1.1 *Isolated atom*

Although, far from the dynamics involved when interacting with light, it can be instructive to consider the evolution of an isolated atom, in order to establish some of the formalism used later. An unperturbed atom can be described by the complete set of basis kets, $\{|b\rangle\}$, containing all the information of the state. The initial wave function for an atom in its most general state is then given by the linear combination

$$|\psi(0)\rangle = \sum_b c_b |b\rangle \,, \tag{5.5a}$$

with the completeness relation

$$\sum_b |b\rangle\langle b| = \hat{I}, \tag{5.5b}$$

where $\hat{I}$ is the unity operator. Similarly, we have for the time-independent atomic Hamiltonian

$$\hat{H}_{\text{atom}} = \sum_b \hbar\omega_{ba} |b\rangle\langle b| \tag{5.6a}$$

$$= \sum_g \hbar\omega_{ga} |g\rangle\langle g| + \sum_e \hbar\omega_{ea} |e\rangle\langle e| \,, \tag{5.6b}$$

where $\hbar\omega_{ba} = \hbar(\omega_b - \omega_a)$ is the eigenenergy of the state $|b\rangle$ with respect to the state $|a\rangle$. In the second equality we have explicitly separated the sum over all atomic states into that of all the ground $|g\rangle$ and exited $|e\rangle$ states. Using Eq. (5.2) we find for the wave function at a later time t:

$$|\psi(t)\rangle = \sum_{b,n} c_n \mathrm{e}^{-i\omega_{ba}|b\rangle\langle b|t} |n\rangle = \sum_b c_b \mathrm{e}^{-i\omega_{ba}t} |b\rangle \,. \tag{5.7}$$

Acting with the eigenstate $\langle a|$ from the left on Eq. (5.7) we obtain the probability to find the system in the state $|a\rangle$ at time t:

$$p_a(t) \equiv |\,\langle a|\psi(t)\rangle\,|^2 = |\,c_a\,|^2 \,. \tag{5.8}$$

3 If $\hat{H} = \hat{H}(t)$ one has to be careful when solving Eq. (5.3) as to whether the $\hat{H}$'s at different times commute or not.

From the latter equality it is clear why the coefficients of the state expansion in Eq. (5.5a) is commonly denoted as the probability amplitudes. One important thing to note for the dynamics described by the atomic Hamiltonian is that once an initial state is given, the probability to find the system in a given state stay fixed. The states in Eq. (5.7) are thus referred to as stationary states, since the only time evolution is given by a simple exponential phase factor. It becomes clear that such an *isolated* description of the atom is not adequate to describe a real system. In fact, no atom is ever truly isolated. At the very least, the interaction with the (quantized) vacuum field should be included, as this causes the atom to undergo transitions by spontaneously emitting a photon. Later in Chapter 6, this inherently quantum mechanical effect is dealt with in a semiclassical treatment using the density operator $\hat{\rho}$.

5.2 SEMICLASSICAL LIGHT-ATOM HAMILTONIAN

In the semiclassical treatment of light-atom interactions, *i.e.*, where the atom is treated as a quantum mechanical particle whereas the light field is treated classically, the Hamiltonian is divided into an unperturbed atomic term, given by Eq. (5.6), and an interaction term:

$$\hat{H} = \hat{H}_{\text{atom}} + \hat{H}_{\text{int}} \,. \tag{5.9}$$

The oscillating electric field drives the electron of the atom and the interaction is therefore described by the electric dipole Hamiltonian:

$$\hat{H}_{\text{int}} = -\hat{\mathbf{d}} \cdot \mathbf{E}(\mathbf{r}, t) \,, \tag{5.10}$$

where $\hat{\mathbf{d}} = e\hat{\mathbf{r}}$ is the electric dipole moment operator of the atom with electron coordinate $\hat{\mathbf{r}}$ and $\mathbf{E}(\mathbf{r}, t)$ is the classical drive field given by [Milonni *et al.*, 1988]

$$\mathbf{E}(\mathbf{r}, t) = \frac{1}{2} \sum_{\mathbf{k}} \left(\mathbf{u}_{\mathbf{k}} \mathcal{E}_{\mathbf{k}}(\mathbf{r}, t) \mathrm{e}^{-i(\omega_{\mathbf{k}} t - \mathbf{k}\cdot\mathbf{r})} + c.c. \right) , \tag{5.11}$$

here $\mathbf{u}_{\mathbf{k}}$ is the unit polarization vector, $\mathcal{E}_{\mathbf{k}}$ is the slowly-varying[4] amplitude of the electric field light mode with corresponding wavevector $\mathbf{k}$ and angular frequency $\omega_{\mathbf{k}}$.

Eq. (5.11) is often simplified by applying the electric dipole approximation; $|\,\mathbf{k} \cdot \mathbf{r}\,| \ll 1$, which is valid when the wavelength of the electromagnetic radiation (for near-infrared wavelengths we have $\lambda = 2\pi/k \sim 1\,\mu\text{m}$) is large compared to the size of the atom $\sim 0.1\,\text{nm}$. In the case of a quasi-monochromatic light field propagating in the z-direction we then have

$$\mathbf{E}(\mathbf{r}, t) = \frac{1}{2} \left(\mathbf{u} \mathcal{E}(\mathbf{r}, t) \mathrm{e}^{-i\omega t} + c.c. \right) . \tag{5.12}$$

4 With respect to the rapid oscillations of the carrier waves $\mathrm{e}^{-i(\omega_{\mathbf{k}} t - \mathbf{k}\cdot\mathbf{r})}$.

As for the atomic Hamiltonian, Eq. (5.6), it is useful to write $\hat{H}_{\text{int}}$ in terms of the ground and exited states of the atom. This can be done by using that the unperturbed eigenstates of the atom form a complete set, Eq. (5.5b). We then find for the dipole operator projected onto the orientation of the electric field

$$\begin{aligned}
\hat{\mu} &= \hat{\mathbf{d}} \cdot \mathbf{u}_{\mathbf{k}} && \text{(5.13a)}\\
&= \sum_{a,b} |a\rangle\langle a|e\hat{\mathbf{r}} \cdot \mathbf{u}_{\mathbf{k}}|b\rangle\langle b| && \text{(5.13b)}\\
&= \sum_{a,b} \mu_{ab}|a\rangle\langle b| && \text{(5.13c)}\\
&= \sum_{e,g} \mu_{eg}|e\rangle\langle g| + \mu_{ge}|g\rangle\langle e| && \text{(5.13d)}\\
&= \sum_{e,g} \mu_{eg}\hat{\sigma}_{eg} + \mu_{ge}\hat{\sigma}_{ge}\,, && \text{(5.13e)}
\end{aligned}$$

where we have used that ground (exited) states do not couple because of parity, and introduced the atomic operator

$$\hat{\sigma}_{eg} \equiv |e\rangle\langle g|\,, \tag{5.14a}$$

with commutation relation

$$\left[\hat{\sigma}_{eg}, \hat{\sigma}_{e'g'}\right] = \delta_{ge'}\hat{\sigma}_{eg'} - \delta_{g'e}\hat{\sigma}_{e'g}\,, \tag{5.14b}$$

as well as the convenient short hand notation for the dipole matrix element[5],

$$\begin{aligned}
\mu_{eg} &\equiv \langle e|e\hat{\mathbf{r}} \cdot \mathbf{u}_{\mathbf{k}}|g\rangle\,. && \text{(5.15a)}\\
\mathbf{d}_{eg} &\equiv \langle e|e\hat{\mathbf{r}}|g\rangle\,. && \text{(5.15b)}
\end{aligned}$$

5.3 TWO-LEVEL ATOM IN THE ROTATING FRAME

At this point it is instructive to solve the Schrödinger equation (5.1) for a two-level atom as illustrated in Fig. 5.1. Using the ground state $|g\rangle$ as the reference level for zero energy, the general wave function is given by

$$|\psi(t)\rangle = c_g(t)|g\rangle + c_e(t)\mathrm{e}^{-i\omega_{eg}t}|e\rangle\,. \tag{5.16}$$

The Hamiltonian for a two-level atom interacting with a classical drive field, Eq. (5.12), is given by

$$\hat{H} = \hbar\omega_{eg}|e\rangle\langle e| - \frac{1}{2}\Big(\mathbf{d}_{eg}|e\rangle\langle g| + \mathbf{d}_{ge}|g\rangle\langle e|\Big)\Big(\mathbf{u}\mathcal{E}\mathrm{e}^{-i\omega t} + \mathbf{u}^*\mathcal{E}^*\mathrm{e}^{i\omega t}\Big)\,. \tag{5.17}$$

This Hamiltonian contains the dynamics of both the unperturbed atom and that caused by the interaction with light. As we are only

5 We caution the reader to be aware that $\mu_{eg} \neq \mu_{ge}^*$, since the polarization vector $\mathbf{u}_{\mathbf{k}}$ can in general be complex.

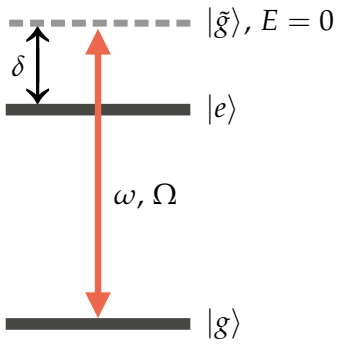

Figure 5.1.: *Two-level atom.* $|\tilde{g}\rangle$ *illustrates the ground state level in the rotating frame with the arbitrary energy reference set to zero. The "tilde" has been omitted in the main text to ease notation.*

interested in the latter, we will perform the so-called rotating frame transformation. In words, this means that we transform the coordinates of the stationary lab frame, containing the atom, into a new set of coordinates rotating with the light field frequency. In math language, one applies the transformation according to the unitary operator (see Appendix D)

$$\hat{U} = \mathrm{e}^{i\omega|e\rangle\langle e|t} \,. \tag{5.18}$$

Defining $\delta \equiv \omega - \omega_{eg}$ for the detuning of the drive field frequency from atomic resonance, we obtain for the transformed wave function

$$\begin{aligned} |\tilde{\psi}(t)\rangle &= \hat{U}|\psi(t)\rangle && \text{(5.19a)} \\ &= c_g(t)|g\rangle + \tilde{c}_e(t)|e\rangle \,, && \text{(5.19b)} \end{aligned}$$

where we have introduced the transformed coordinate

$$\tilde{c}_e(t) = c_e(t)\mathrm{e}^{i\delta t} \,. \tag{5.20}$$

For the transformed Hamiltonian we have in the rotating-wave approximation (RWA)[6]

$$\hat{H}_{\mathrm{rot}} = -\hbar\delta|e\rangle\langle e| - \frac{\hbar}{2}\Big(\Omega_{eg}|e\rangle\langle g| + \Omega_{eg}^{*}|g\rangle\langle e|\Big) \,, \tag{5.21}$$

where the Rabi frequency[7]

$$\Omega_{eg} \equiv \frac{\mu_{eg}\mathcal{E}}{\hbar} \,, \tag{5.22}$$

has been introduced.

6 Meaning that only energy preserving terms are kept in the Hamiltonian, and we thus neglect the rapidly oscillating terms $\mathrm{e}^{\pm 2i\omega t}$.

7 In writing Ω_{eg}^{*} the complex conjugate is meant to be taken of the electric field part of the Rabi frequency.

5.3.1 *Solutions*

To solve the transformed Schrödinger equation:

$$i\hbar|\dot{\tilde{\psi}}(t)\rangle = \hat{H}_{\text{rot}}|\tilde{\psi}(t)\rangle\,, \tag{5.23}$$

we act with $\langle g|$ ($\langle e|$) from the left on both sides, from which we obtain the coupled first-order differential equations

$$i\dot{c}_g = -\frac{\Omega^*}{2}\tilde{c}_e(t)\,, \tag{5.24a}$$

$$i\dot{\tilde{c}}_e = -\delta\tilde{c}_e(t) - \frac{\Omega}{2}c_g(t)\,, \tag{5.24b}$$

in which we have omitted the subscripts on the Rabi frequency for ease of notation. By taking the time-derivative of these equations and rearranging the terms, they can be cast into two uncoupled second-order differential equations for which exact solutions exist given the initial conditions. Taking the Rabi frequency to be real[8] and treating the case where the atom is initially in the ground state; $c_g(0) = 1$, $\tilde{c}_e(0) = 0$, the solutions are given by[9]

$$c_g(t) = \left(\cos\frac{\Omega' t}{2} - \frac{i\delta}{\Omega'}\sin\frac{\Omega' t}{2}\right)e^{i\delta t/2}\,, \tag{5.25a}$$

$$\tilde{c}_e(t) = \left(\frac{i\Omega}{\Omega'}\sin\frac{\Omega' t}{2}\right)e^{i\delta t/2}\,, \tag{5.25b}$$

where Ω' is the generalized Rabi frequency defined as

$$\Omega'(\delta) \equiv \left(\Omega^2 + \delta^2\right)^{1/2}. \tag{5.26}$$

In this respect Ω should be considered as the on-resonance the Rabi frequency. From Eq. (5.25) we see that the effect of the classical light field is to drive the atom between the two states $|g\rangle$ and $|e\rangle$. Noteworthy is the so-called π-pulse, where applying a light pulse with $\delta = 0$ and $\Omega' t = \pi$, coherently drives the atomic state initially in $|g\rangle$ to $|e\rangle$.

The two-level Hamiltonian in Eq. (5.21) can be represented as a matrix with elements given by $H_{ij} = \langle i|\hat{H}_{\text{rot}}|j\rangle$:

$$\hat{H}_{\text{rot}} \doteq -\frac{\hbar}{2}\begin{pmatrix} 0 & \Omega^* \\ \Omega & 2\delta \end{pmatrix}. \tag{5.27}$$

8 This can always be done by a suitable phase choice for the electric fields.

9 For notational convenience, the "tilde" used to distinguish transformed quantities from their original basis will be omitted in the remainder of the thesis, and it should be apparent from the context whether a transform to the rotation frame has taken place or not. The results are of course unaffected.

This matrix can be diagonalized to find the new eigenenergies of the atom (dressed in light) from which we obtain

$$E_g = -\frac{\hbar}{2}(\delta - \Omega')\,, \tag{5.28a}$$

$$E_e = -\frac{\hbar}{2}(\delta + \Omega')\,. \tag{5.28b}$$

In the far-detuned limit; $\Omega \ll |\,\delta\,|$, where absorption is negligible, the shift in the energy levels are found to be

$$\Delta E_g \approx \frac{\hbar\Omega^2}{4\delta}\,, \tag{5.29a}$$

$$\Delta E_e \approx -\frac{\hbar\Omega^2}{4\delta}\,. \tag{5.29b}$$

This is the well-known result for the AC Stark shift of the atomic levels, also known as the light shift, see Fig. 5.2.

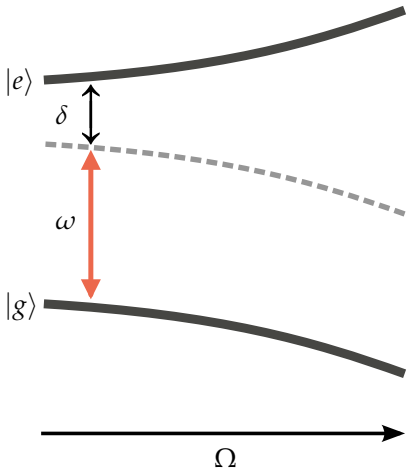

Figure 5.2.: *Illustration of the light induced AC Stark shifted levels. Inspired by [Foot, 2005, Fig. 7.9].*

The formalism presented so far, do not include effects such as decay and dephasing from spontaneous emission and coupling to the environment. The limits of validity are reached at small detuning $|\delta|$ where the excited state population becomes non-negligible and, on the opposite side large detunings $|\delta| \simeq \omega$, where the RWA ceases to be appropriate. A more complete treatment needs to include also the multi-level nature of atoms and naturally leads to a proper perturbation theory. Coupling to all (also empty) radiation modes, which leads to excited state decay, level shifts and dephasing, will be taken into account in later chapters employing density matrix techniques.

5.4 FULLY QUANTIZED LIGHT-ATOM HAMILTONIAN

The generic Hamiltonian for the light-atom interactions where the light field is now quantized is given by

$$\hat{H} = \hat{H}_{\text{atom}} + \hat{H}_{\text{light}} + \hat{H}_{\text{int}} \,. \tag{5.30}$$

As before $\hat{H}_{\text{atom}}$ is given by Eq. (5.6), but now we have also included the Hamiltonian describing the dynamics of the isolated light system:

$$\hat{H}_{\text{light}} = \sum_{\mathbf{k}} \hbar\omega_{\mathbf{k}} \left(\hat{a}^{\dagger}_{\mathbf{k}} \hat{a}_{\mathbf{k}} + \frac{1}{2} \right) \tag{5.31}$$

where $\hat{a}_{\mathbf{k}}$ and $\hat{a}^{\dagger}_{\mathbf{k}}$ are the annihilation and creation operators following the usual commutation relation

$$\left[\hat{a}_{\mathbf{k}}, \hat{a}^{\dagger}_{\mathbf{k}'} \right] = \delta_{\mathbf{k}\mathbf{k}'} \,, \tag{5.32}$$

with δ_{ij} being the Kronecker delta. The light-atom interaction is still described by the electric dipole Hamiltonian:

$$\hat{H}_{\text{int}} = -\hat{\mathbf{d}} \cdot \hat{\mathbf{E}}(\mathbf{r}) \,, \tag{5.33}$$

but now the electric field is quantized and given by the operator [Grynberg *et al.*, 2010]

$$\hat{\mathbf{E}}(\mathbf{r}) = \sum_{\mathbf{k}} i \mathbf{u}_{\mathbf{k}} \mathcal{E}_{\mathbf{k}} \left(\hat{a}_{\mathbf{k}} e^{i\mathbf{k}\cdot\mathbf{r}} - \hat{a}^{\dagger}_{\mathbf{k}} e^{-i\mathbf{k}\cdot\mathbf{r}} \right) , \tag{5.34a}$$

with

$$\mathcal{E}_{\mathbf{k}} \equiv \sqrt{\frac{\hbar\omega_{\mathbf{k}}}{2\epsilon_0 V}} \,, \tag{5.34b}$$

being the classical field amplitude with energy corresponding to a single photon in mode $\mathbf{k}$ defined in the quantization volume V.

We shall use the fully quantized version of the Hamiltonian in Chapter 19 where we derive expressions for the reflection and transmission coefficients for atoms coupled to a one-dimensional (1D) waveguide.

6

DENSITY OPERATOR

As we saw have just seen, using the approach of solving the Schrödinger wave equation to obtain the dynamics of the atom under influence of a classical drive field, lacks a natural inclusion of decay and dephasing mechanisms. In order to appropriately account for these effects one should apply the density operator formalism instead.

Since the (pure) state $|\psi(t)\rangle$ of a system is generally not given to us, the density operator formalism further has the advantage that it is equally well suited to treat pure states as well as mixed states, which is also not possible using the Schrödinger equation (5.1).

In quantum mechanics a mixed ensemble of states is described by the (probability) density operator [Sakurai, 1994]

$$\hat{\rho} \equiv \sum_a p_a |\psi_a\rangle\langle\psi_a| \,, \tag{6.1}$$

where $p_a > 0$ is the probability to find the system in the pure state[1] $|\psi_a\rangle$ and $\sum_a p_a = 1$ since the probability to find the system in any of the possible states naturally has to add to unity.

If the system can be described by a pure state $|\psi\rangle$ the density matrix is simply given by the projector operator

$$\hat{\rho} = |\psi\rangle\langle\psi| \,. \tag{6.2}$$

As an example of a pure state, we can use the state expansion given in Eq. (5.7) from which we find the density operator:

$$\hat{\rho} = \sum_{a,b} c_a(t) c_b^*(t) |a\rangle\langle b| \,. \tag{6.3}$$

If the basis $\{|b\rangle\}$, used for the state expansion, contains in total n eigenstates, $\hat{\rho}$ can be represented by an $n \times n$ (density) matrix with the elements given by

$$\rho_{ab} \equiv \langle a|\hat{\rho}|b\rangle = c_a c_b^* \,, \tag{6.4}$$

and from which we see that $\hat{\rho}$ is Hermitian; $\rho_{ab} = \rho_{ba}^*$. Taking the trace of the density matrix we find

$$\mathrm{tr}\,(\hat{\rho}) \equiv \sum_a \rho_{aa} = \sum_a |\, c_a \,|^2 = 1 \,, \tag{6.5}$$

1 That is, it has $\mathrm{tr}\,(\rho^2) = 1$. Any state with $\mathrm{tr}\,(\rho^2) < 1$ is a statistical mixture.

due to the normalization of the wavefunction, $\langle\psi|\psi\rangle = 1$. In Eq. (5.8) we already saw that the coefficients c_a are directly related to the probability to find the system in a given state $|a\rangle$; $p_a = |\,c_a\,|^2$, and it is no surprise that this is recovered in the density matrix formalism. It is common practice to refer to the probabilities in the diagonal of the density matrix as the population of a given state.

The off-diagonal elements of the density matrix ρ_{ab} contains the relative phase[2] between the two states $|a\rangle$ and $|b\rangle$, and we thus refer to these elements as the coherences between the levels. This becomes apparent if we consider the expectation value of the dipole operator $\hat{\mathbf{d}}$, using Eq. (5.15b) and Eq. (5.19b) we have

$$\langle\,\hat{\mathbf{d}}\,\rangle = \rho_{eg}\mathbf{d}_{ge} + \rho_{ge}\mathbf{d}_{eg}\,, \tag{6.6}$$

The off-diagonal elements of the density matrix are thus directly linked to the displacement of the electron, *i.e.*, the induced dipole moment, and ρ_{eg} can be regarded as its complex amplitude.

Finally, we note that the expectation value of a general operator $\hat{O}$ can be found via the density matrix operator as [Sakurai, 1994]

$$\begin{aligned}
\langle\,\hat{O}\,\rangle &= \sum_a p_a \langle\psi_a|\hat{O}|\psi_a\rangle && \text{(6.7a)}\\
&= \sum_a \langle\psi_a|\hat{\rho}|\psi_a\rangle\langle\psi_a|\hat{O}|\psi_a\rangle && \text{(6.7b)}\\
&= \sum_a \langle\psi_a|\hat{\rho}\hat{O}|\psi_a\rangle && \text{(6.7c)}\\
&= \mathrm{tr}\left(\hat{\rho}\hat{O}\right). && \text{(6.7d)}
\end{aligned}$$

6.1 TWO-LEVEL ATOM INCLUDING DECAY

We now continue the study of the two-level atom started in Section 5.3. Using the density matrix formalism we will include the impact of spontaneous emission and collision events in the description of the atomic evolution. We start out by writing the differential equations in (5.24), giving the time variation of the probability amplitudes, in terms of the density matrix by applying Eq. (6.4). For the populations we then obtain

$$\dot{\rho}_{gg} = -\frac{i}{2}\left(\Omega\rho_{ge} - \Omega^*\rho_{eg}\right), \tag{6.8a}$$

$$\dot{\rho}_{ee} = \frac{i}{2}\left(\Omega\rho_{ge} - \Omega^*\rho_{eg}\right), \tag{6.8b}$$

2 This was already hinted at in the way we wrote the state ket for the two-level atom in Eq. (5.16).

while for the coherences we get

$$\dot{\rho}_{eg} = i\delta\rho_{eg} - i\frac{\Omega}{2}\left(\rho_{ee} - \rho_{gg}\right), \tag{6.9a}$$

$$\dot{\rho}_{ge} = -i\delta\rho_{ge} + i\frac{\Omega^*}{2}\left(\rho_{ee} - \rho_{gg}\right). \tag{6.9b}$$

As a sanity check we confirm that $\dot{\rho}_{eg} = \dot{\rho}^*_{ge}$ and $\dot{\rho}_{gg} + \dot{\rho}_{ee} = 0$ as required from the Hermiticity and conservation of probability for a closed system. The most intuitive way to include spontaneous emission, is by recognizing that the effect is to transfer population from the exited state to the ground state. This can readily be described in the two rate equations for the populations, Eq. (6.8), by adding/subtracting the term $\gamma\rho_{ee}$, where γ is the spontaneous emission rate, see Fig. 6.1. However, for the coherences, Eq. (6.9), we have to be a bit more careful. To see how to add dephasing, caused by spontaneous emission, we will therefore first consider the impact done by inelastic collisions.

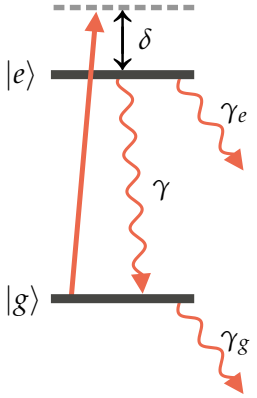

Figure 6.1.: *Two-level system with decay γ from the excited state $|e\rangle$ to the ground state $|g\rangle$, and decay out of the system by γ_g and γ_e.*

Similar to spontaneous emission, inelastic collisions cause a reshuffling of the level populations. If we use γ_a for the collisional decay rate out of level $|a\rangle$ to an unspecified level[3], we obtain the modified rate equations for the populations:

$$\langle\, \dot{\rho}_{gg} \,\rangle = -\gamma_g\rho_{gg} + \gamma\rho_{ee} - \frac{i}{2}\left(\Omega\rho_{ge} - \Omega^*\rho_{eg}\right), \tag{6.10a}$$

$$\langle\, \dot{\rho}_{ee} \,\rangle = -(\gamma_e + \gamma)\rho_{ee} + \frac{i}{2}\left(\Omega\rho_{ge} - \Omega^*\rho_{eg}\right), \tag{6.10b}$$

Since γ_g, γ_e, and γ yields the average rates for the atom to undergo a transition, the rate equations should now be regarded as governing the dynamics of the "average" atom, symbolized by the use of $\langle\,\cdot\,\rangle$[4].

3 Note then, that the system is no longer closed.

4 The density matrix elements on the RHS of Eq. (6.10) should of course also be treated as averaged quantities. We have omitted the brackets for notational convenience.

In order to obtain the impact on the coherences, we use that

$$|\,\rho_{ab}\,| = \left(|\,c_a c_b^*\,|^2\right)^{1/2} = \left(\rho_{aa}\rho_{bb}\right)^{1/2}. \tag{6.11}$$

If there is no drive field, $\Omega = 0$, the solutions to Eq. (6.10) is easily obtained and we find (neglecting spontaneous emission for a moment):

$$\rho_{aa}(t) = \rho_{aa}(0)\mathrm{e}^{-\gamma_a t}, \tag{6.12}$$

for $a = g, e$. We then have for the coherence:

$$\begin{aligned} |\,\rho_{eg}(t)\,| &= \left(\rho_{gg}(t)\rho_{ee}(t)\right)^{1/2} && (6.13)\\ &= |\,\rho_{eg}(0)\,|\,\mathrm{e}^{-(\gamma_g+\gamma_e)t/2}. && (6.14) \end{aligned}$$

Perhaps not so surprising, inelastic collision events is seen to also cause a decay of the coherence terms, *i.e.*, a dephasing of the atomic dipole, but at half the rate as that of the population decay out of the levels. Making the conjecture that spontaneous emission will give rise to the same behavior, we arrive at the modified rate equations for the coherences:

$$\langle\,\dot{\rho}_{eg}\,\rangle = -(\Gamma - i\delta)\rho_{eg} - i\frac{\Omega}{2}\left(\rho_{ee} - \rho_{gg}\right), \tag{6.15a}$$

$$\langle\,\dot{\rho}_{ge}\,\rangle = -(\Gamma + i\delta)\rho_{ge} + i\frac{\Omega^*}{2}\left(\rho_{ee} - \rho_{gg}\right), \tag{6.15b}$$

with:

$$\Gamma \equiv \frac{1}{\tau} + \frac{1}{2}(\gamma_g + \gamma_e + \gamma), \tag{6.15c}$$

used for the total decay rate. For completeness, we have also added the contribution arising from elastic collisions occurring at the average rate $1/\tau$ [Milonni *et al.*, 1988]. Together with Eq. (6.10), the equations in (6.15) constitute what is known as the optical Bloch equations.

6.2 STEADY-STATE SOLUTION FOR A CLOSED SYSTEM

The rate equations, (6.10) and (6.15), given for the density matrix can, save special cases, only be solved numerically. It is, nevertheless, useful to obtain analytically solutions in the steady-state limit, as these contain valuable information of the system dynamics valid for timescales much longer than that set by the damping rate in the optical Bloch equations, *i.e.*, for times $t \gg \Gamma^{-1}$. We will here treat the case for a closed system with negligible collisions, *i.e.*, the only relaxation term present is the one given by the spontaneous emission.

Setting the time derivatives equal to zero in the optical Bloch equations and rearranging terms we arrive at the steady-state solutions[5]:

$$\bar{\rho}_{ee} = \frac{s}{2(1+s)} = \frac{s_0/2}{1+s_0+4(\delta/\gamma)^2}\,, \tag{6.16a}$$

$$\bar{\rho}_{eg} = \frac{i\Omega}{2(\gamma/2-i\delta)(1+s)}\,, \tag{6.16b}$$

where we have introduced the saturation parameter s defined as

$$s \equiv \frac{s_0}{1+4(\delta/\gamma)^2}\,, \tag{6.17a}$$

as well as the on-resonance saturation parameter:

$$s_0 \equiv \frac{2\,|\,\Omega\,|^2}{\gamma^2}\,. \tag{6.17b}$$

In the following we will give some important relations that can be derived from the steady-state solutions (6.16). Since these results will constitute some of the most used concepts used in this thesis, and when dealing with light-matter interaction in general, they have each been granted their own small section.

6.3 SATURATION

We first consider the saturation parameter given in Eq. (6.17). It is common practice to rewrite the on-resonance saturation parameter in terms of the light intensity $I = \frac{1}{2}c\epsilon_0\,|\,\mathcal{E}\,|^2$ such that we have

$$s_0 = \frac{I}{I_{\text{sat}}}\,. \tag{6.18}$$

In combination with Eq. (5.22) for the Rabi frequency, we find the saturation intensity to be given by

$$I_{\text{sat}} \equiv \frac{c\epsilon_0\gamma^2\hbar^2}{4\,|\,\mu_{eg}\,|^2}\,. \tag{6.19}$$

This can be further simplified, such that we get rid of the dipole matrix element μ_{eg}, Eq. (5.15a), by using that the spontaneous emission rate is given by [Foot, 2005]

$$\gamma = \frac{\omega_{eg}^3}{3\pi\epsilon_0\hbar c^3}\frac{g_g}{g_e}\,|\,\mu_{eg}\,|^2\,, \tag{6.20}$$

where g_a is the degeneracy[6] of the atomic level $|a\rangle$. We then find

$$I_{\text{sat}} = \frac{\pi hc\gamma}{3\lambda^3}\,. \tag{6.21}$$

5 $\bar{\rho}_{gg}$ and $\bar{\rho}_{ge}$ follows trivially from the relations $\bar{\rho}_{gg}+\bar{\rho}_{ee}=1$ and $\bar{\rho}_{ge}=\bar{\rho}_{eg}^*$.

6 The ratio g_g/g_e is of course equal to one for the simple two-level atom considered here. But for the general multilevel atom it should be taken into account.

For a low intensity light beam; $s \ll 1$, the excited state population $\bar{\rho}_{ee}$, Eq. (6.16a), increases linearly with the light intensity, while for a high intense beam; $s \gg 1$, it is seen to saturate at half[7] the total population; $\bar{\rho}_{ee} \to ½$. This is in stark contrast with the solutions, Eq. (5.25), obtained for the populations when neglecting any decay mechanisms of the atom. It is, however, possible to recover full population inversion in the two-level system if the Rabi frequency is much bigger than the damping rate in the optical Bloch equations; $\Omega \gg \Gamma$. Alternative, an additional metastable third level in the atom can be used to obtain full population inversion.

6.4 SCATTERING RATE AND POWER BROADENING

The effect of saturation becomes, perhaps, even more clear when considering the scattering rate γ_{sc}. Using that the excitation and decay rates are equal in the steady-state we have:

$$\gamma_{\text{sc}} = \gamma\bar{\rho}_{ee} = \frac{s_0}{1+s_0}\frac{\gamma/2}{1+4(\delta/\gamma')^2}\,, \tag{6.22}$$

when written in terms of the power-broadened linewidth of the atomic transition:

$$\gamma' \equiv \gamma(1+s_0)^{1/2}\,. \tag{6.23}$$

The scattering rate is shown in Fig. 6.2 for various values of the on-resonance saturation parameter. In the saturation limit; $s_0 \gg 1$, γ_{sc} intuitively approaches $\gamma/2$, since for a high intense light field the amount of available photons are sufficient to keep re-exciting the atom whenever it has relaxed to its ground state. The factor of two difference between γ_{sc} and the spontaneous emission rate γ arises from the fact that the photons also cause the atom to undergo stimulated emission. In contrast to a spontaneously emitted photon, a photon created by stimulated emission adds to the same mode as the input field and is thus indistinguishable from the original input flux of photons.

In Fig. 6.2 it is also evident that the scattering rate broadens for higher light intensities. This can be thought of as an effective broadening of the atomic transition and motivates the introduction of the power-broadened linewidth γ'.

6.5 OPTICAL DEPTH

We continue the discussion of the input light beam. For each scattering event a photon with energy $\hbar\omega$ is lost. Knowing the scat-

7 Evidently, population inversion cannot be reached in steady-state with two-level atoms as required for lasing.

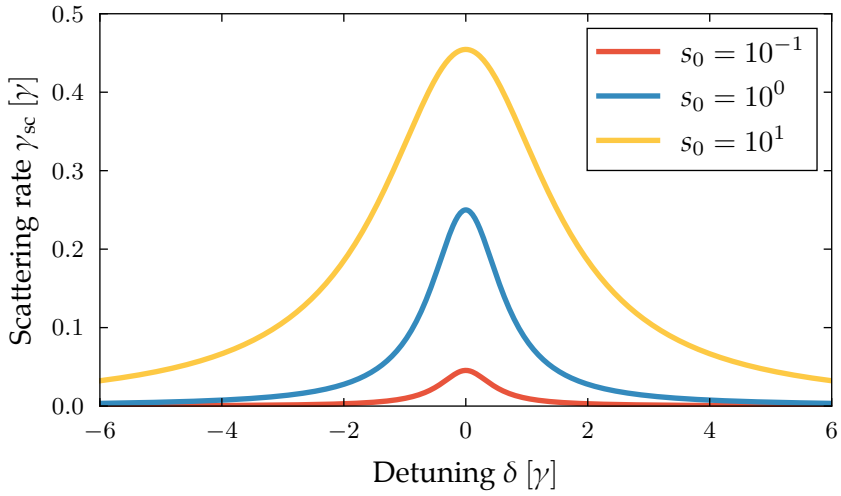

Figure 6.2.: *Scattering rate as a function of the detuning for different saturation parameters.*

tering rate for a single atom, γ_{sc}, the attenuation of a laser beam with intensity I passing through a cloud with atom number density $\mathcal{N} = N_{atom}/V$ can be described by [Metcalf *et al.*, 1999]

$$\frac{dI}{dz} = -\hbar\omega\gamma_{sc}\mathcal{N}\,. \tag{6.24}$$

Inserting Eq. (6.22) into Eq. (6.24) and using $s_0 = I/I_{sat}$ we find

$$\frac{dI}{dz} = -\frac{\hbar\omega\mathcal{N}}{I_{sat}}\frac{\gamma/2}{1 + I/I_{sat} + 4(\delta/\gamma)^2}\,I\,. \tag{6.25}$$

In the limit of negligible saturation; $I \ll I_{sat}$, the non-linear differential equation for I reduces to the linear differential equation

$$\frac{dI}{dz} \approx -\sigma(\delta)\mathcal{N}I\,, \tag{6.26}$$

where we have introduced the atomic cross section for a single atom:

$$\sigma(\delta) = \frac{\hbar\omega\gamma}{2I_{sat}}\frac{1}{1 + 4(\delta/\gamma)^2} = \frac{\sigma_0}{1 + 4(\delta/\gamma)^2}\,, \tag{6.27}$$

with on-resonance scattering cross section given by

$$\sigma_0 \equiv \frac{\hbar\omega\gamma}{2I_{sat}} = \frac{3\lambda^2}{2\pi}\,. \tag{6.28}$$

The solution to Eq. (6.26) is a simple exponential decay, well known as the Lambert-Beer's law:

$$I(z) = I_0 e^{-\sigma(\delta)\mathcal{N}z} = I_0 e^{-d}\,, \tag{6.29}$$

where d is the optical depth (OD). From this we can define the OD per atom as

$$\alpha(\delta) \equiv \frac{d}{N_{\text{atom}}} = \frac{\sigma(\delta)}{A_{\text{eff}}} = \frac{\alpha_0}{1+4(\delta/\gamma)^2}\,, \tag{6.30}$$

where A_{eff} is the effective mode area of the light beam and $\alpha_0 = \sigma_0/A_{\text{eff}}$ is the on-resonance OD per atom. From this definition it is clear that α is a direct measure of the light-atom coupling strength. As such, this parameter plays a vital role in quantum optics experiments with atomic ensembles, and a great effort is made to increase the OD per atom as much as possible. Basically two strategies exists: either (i) the atomic cross section is increased, *e.g.*, by using Rydberg atoms, or (ii) the light field mode area is minimized, *e.g.*, by using a tightly focused beam. In contrast to a free-space light beam where a strong focus is at the expense of a greater divergence, a TOF provides an excellent interface for the atoms to interact with the tightly confined evanescent field. In comparison, only $\sim 10^3$ atoms are needed in our current TOF-setup to achieve the same OD as we had in our old free-space setup with $\sim 10^5$ atoms [Christensen, 2014; Béguin, 2015].

We now consider the highly saturated regime; $I \gg I_{\text{sat}}$. Here the RHS of Eq. (6.25) can be approximated by the constant prefactor, $-\hbar\omega\gamma\mathcal{N}$, from which the solution for the beam intensity is simply given by a linear decay as it propagates through the sample. In other words,

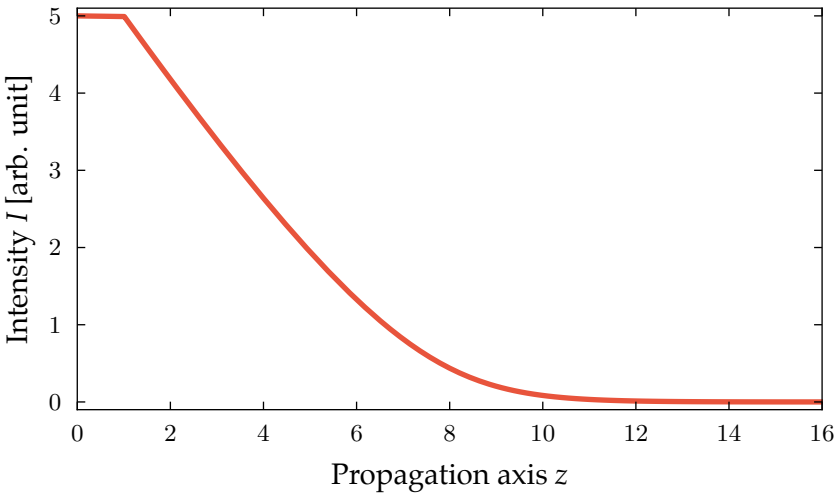

Figure 6.3.: *Numerical solution for $I(z)$ in Eq. (6.25) when entering a homogeneous density sample at $z = 1$ with an initial intensity $I_0 = 5I_{\text{sat}}$.*

now the number of photons lost from the initial input flux scales with the number of available scatteres $\mathcal{N}$. This is illustrated in Fig. 6.3 for an input beam with initial intensity $I_0 = 5I_{\text{sat}}$. Entering the sample at $z = 1$, the intensity linearly decreases until there are so few photons left in the beam that it enters the low-saturation regime (near $z = 7$)

where it then starts to decay exponentially as described by Lambert-Beer's law.

As an experimentalist it is often more useful to work with optical powers P than optical intensities I. For completeness, we therefore give here the following expressions which can be derived using $I = P/A_{\text{eff}}$, the above expressions, and by making the definition of the saturation intensity more general, *i.e.*, frequency dependent $s(\delta) = I/I_{\text{sat}}(\delta)$:

$$s_0 = \frac{P}{P_{\text{sat}}}\,, \tag{6.31a}$$

$$P_{\text{sat}}(\delta) = \frac{\hbar\omega\gamma}{2\alpha_0}\left(1 + 4(\delta/\gamma)^2\right). \tag{6.31b}$$

6.6 LINEAR SUSCEPTIBILITY – ABSORPTION AND DISPERSION

When an atom is driven by an electric field it becomes polarized. If we have $\mathcal{N}$ atoms per unit volume the polarization can be obtained by evaluating the expression

$$\mathbf{P} = \mathcal{N}\langle\,\hat{\mathbf{d}}\,\rangle. \tag{6.32}$$

In Eq. (6.6) we already saw how the expectation value of the induced dipole moment is intimately linked with the off-diagonal elements of the density matrix, *i.e.*, the coherences. In the following we will assume that the induced dipole is parallel to the field[8]. We then have for the polarization [Grynberg *et al.*, 2010]

$$P = \mathcal{N}\,\langle\,\hat{\mu}\,\rangle = \mathcal{N}\left(\rho_{eg}\mu_{ge} + c.c.\right). \tag{6.33}$$

In addition, we recall Eq. (2.5) were the linear susceptibility χ were defined such that

$$\mathcal{P} = \epsilon_0\chi\mathcal{E}\,, \tag{6.34}$$

where $\mathcal{P}$ is the complex amplitude of the polarization when written as

$$\mathbf{P}(\mathbf{r},t) = \frac{1}{2}\left(\mathbf{u}\mathcal{P}(\mathbf{r},t)\mathrm{e}^{-i\omega t} + c.c.\right), \tag{6.35}$$

similar to the classical electric field in Eq. (5.12). Inserting the steady-state solution for ρ_{eg}, Eq. (6.16b), into Eq. (6.33) we find for the linear susceptibility

$$\chi = \frac{\mathcal{N}}{\epsilon_0\hbar}\frac{|\,\mu_{eg}\,|^2}{(\delta + i\gamma/2)(1+s)}\,. \tag{6.36}$$

8 We then have $\hat{\mathbf{r}}\cdot\mathbf{u} = \hat{r}\mathbf{u}\cdot\mathbf{u} = \hat{r}$, which means that $\mu_{eg} = \mu_{ge}^*$.

Taking the real and imaginary part of χ we obtain the well-known equations for the dispersion and absorption respectively:

$$\text{Dispersion:} \quad \mathrm{Re}\,\chi = -\mathcal{N}\frac{|\,\mu_{eg}\,|^2}{\epsilon_0\hbar}\frac{\delta}{\delta^2+(\gamma'/2)^2}\,, \tag{6.37a}$$

$$\text{Absorption:} \quad \mathrm{Im}\,\chi = \mathcal{N}\frac{|\,\mu_{eg}\,|^2}{\epsilon_0\hbar}\frac{\gamma/2}{\delta^2+(\gamma'/2)^2}\,, \tag{6.37b}$$

where we have used the expression for the power-broadened linewidth, Eq. (6.23). In Fig. 6.4 the real and imaginary part of the susceptibility are plotted as a function of the detuning of the drive field frequency from atomic resonance. As the associated names suggests, the imaginary part of the atomic dipole response is responsible for the attenuation of the electric drive field via scattering events, while the real part is related to the phase shift an off-resonant beam will acquire when passing through a cloud of atoms. This relation is apparent

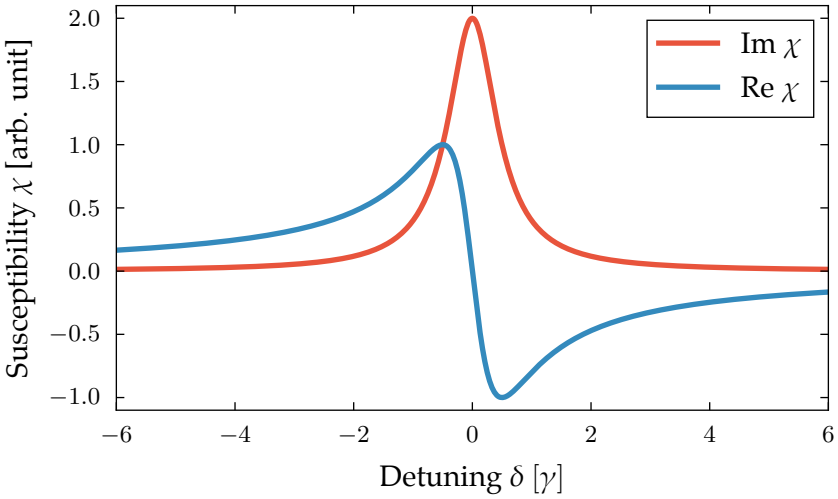

Figure 6.4.: *Real and imaginary part of the atomic susceptibility.*

from the definition of the electric displacement field **D** in Eq. (2.4) in combination with the expression for the polarization, Eq. (2.5), from which we have:

$$n^2(\omega) = 1+\chi\,, \tag{6.38a}$$

$$n(\omega) \approx 1+\frac{\chi}{2}\,, \tag{6.38b}$$

with the approximation being valid for a dilute medium; $|\,\chi\,| \ll 1$. When solving the wave equation (2.6) for a monochromatic electric field one finds the well-known relation for the wavenumber:

$$k^2 = n^2(\omega)\frac{\omega^2}{c^2} = n^2(\omega)k_0^2\,. \tag{6.39}$$

Inserting this into the general expression for a monochromatic field propagating in the z-direction

$$E(\mathbf{r},t) = \frac{1}{2}\left(\mathcal{E}\mathrm{e}^{-n''k_0 z}\mathrm{e}^{-i(\omega t - n'k_0 z)} + c.c.\right), \tag{6.40}$$

with

$$n' \equiv 1 + \frac{\mathrm{Re}\,\chi}{2} \quad \text{and} \quad n'' \equiv \frac{\mathrm{Im}\,\chi}{2}, \tag{6.41}$$

we find the electric field to decay with n'' as anticipated, while it acquires a phase shift proportional to n'.

An important feature to note about the susceptibility, is that while the absorption falls of as δ^{-2}, the dispersion decreases slower as δ^{-1}. This makes it possible to measure the state of an atomic cloud via the phase shift acquired by an off-resonant light probe in a minimally destructive manner, that is, in the sense of causing only very few scattering events on average.

6.7 LIGHT FORCE

The force $\mathbf{F}$ (on any quantum mechanical system) is defined as the expectation value of the force operator $\hat{\mathbf{F}}$, which can be derived from the momentum operator $\hat{\mathbf{p}}$ [Metcalf *et al.*, 1999]:

$$\mathbf{F} = \langle\, \hat{\mathbf{F}} \,\rangle = \frac{\mathrm{d}}{\mathrm{d}t} \langle\, \hat{\mathbf{p}} \,\rangle\,. \tag{6.42}$$

From Ehrenfest's theorem we have [Grynberg *et al.*, 2010]

$$i\hbar \frac{\mathrm{d}}{\mathrm{d}t} \langle\, \hat{\mathbf{p}} \,\rangle = \langle\, [\hat{\mathbf{p}}, \hat{H}] \,\rangle\,, \tag{6.43}$$

and so the force on the atom is directly related to its Hamiltonian. For the force exerted by a classical light field we thus find

$$\mathbf{F} = \frac{1}{i\hbar} \langle\, [\hat{\mathbf{p}}, \hat{H}_{\mathrm{int}}] \,\rangle\,. \tag{6.44}$$

With the usual definition of the momentum operator $\hat{\mathbf{p}} = -i\hbar\boldsymbol{\nabla}$ in the r representation, the force on the atom is found to be given by

$$\mathbf{F} = -\langle\, \boldsymbol{\nabla}\hat{H}_{\mathrm{int}} \,\rangle\,. \tag{6.45}$$

Using Eq. (5.10) for the semiclassical light-atom interaction we have [Grynberg *et al.*, 2010]

$$\mathbf{F} = \boldsymbol{\nabla} \langle\, \hat{\mu} E(\mathbf{r},t) \,\rangle = \langle\, \hat{\mu} \,\rangle\, \boldsymbol{\nabla} E(\mathbf{r},t)|_{\mathbf{r}_{\mathrm{atom}}}\,. \tag{6.46}$$

In the last equality it has been assumed that the atomic wave packet is highly localized at $\mathbf{r}_{\mathrm{atom}}$ and has an extension much smaller than the

wavelength of light, in essence this corresponds to a classical treatment of the atomic position. The expectation value of the atomic dipole moment operator $\langle \hat{\mu} \rangle$, was evaluated in the previous section, where the linear susceptibility was derived from the definition of the polarization of the atom P Eq. (6.32). Using the results obtained in Section 6.6 we can therefore write

$$\langle \hat{\mu} \rangle = \frac{1}{2}\epsilon_0 \chi \mathcal{E}(\mathbf{r}_{\text{atom}}, t) + c.c. \tag{6.47}$$

With the electric field given by

$$E(\mathbf{r}, t) = \frac{1}{2}\mathcal{E}(\mathbf{r}, t)\mathrm{e}^{i(\mathbf{k}\cdot\mathbf{r}-\omega t)} + c.c. \tag{6.48}$$

the light force on the atom is straightforward to calculate. In the RWA we thus find

$$\mathbf{F} = \frac{\epsilon_0}{4}\,\mathrm{Re}\,\chi \boldsymbol{\nabla}\mathcal{E}^2|_{\mathbf{r}_{\text{atom}}} + \frac{\epsilon_0}{2}\,\mathrm{Im}\,\chi \mathbf{k}\,\mathcal{E}^2(\mathbf{r}_{\text{atom}}, t)\,. \tag{6.49}$$

The light force on the atom is seen to be given by two terms. The first term is directly proportional to the real part of the susceptibility, given in Eq. (6.37a), which is the dispersive response of the atomic dipole to the light field, whereas the second term contains the imaginary part of χ, given in Eq. (6.37b), responsible for the absorption. The two contributions to the total light force on the atoms thus governs two different physical processes, which we shall treat individually in the next two sections.

6.7.1 *Radiation pressure force*

Starting with the second force term in Eq. (6.49), this is commonly referred to as the dissipative force[9]. Using the definition of the imaginary susceptibility for the absorption as given in Eq. (6.37b), together with the definitions of the Rabi frequency $\Omega = \hat{\mu}\mathcal{E}/\hbar$ in Eq. (5.22) and the saturation parameter s in Eq. (6.17a), the expression for the dissipative force can be written as

$$\mathbf{F}_{\text{dissipative}} = \frac{\epsilon_0}{2}\,\mathrm{Im}\,\chi \mathbf{k}\,\mathcal{E}^2(\mathbf{r}_{\text{atom}}, t) = \hbar\mathbf{k}\frac{\gamma}{2}\frac{s}{1+s}\,. \tag{6.50}$$

Being proportional to the wavevector of the light field and $\mathrm{Im}\,\chi$, expression (6.50) can be understood to originate from the momentum or recoil kick that is delivered to the atom every time it scatters a photon. As expected from the absorption profile in Fig. 6.4, the force takes on its maximum value when the light is on-resonance with the atom. For an intense light field, $s \gg 1$, the atom saturates and the

9 As well as the scattering force and the radiation pressure force.

maximum force that can be given to the atom by the dissipative force is

$$\mathbf{F}^{\max}_{\text{dissipative}} = \hbar \mathbf{k} \frac{\gamma}{2} . \tag{6.51}$$

$\mathbf{F}_{\text{dissipative}}$ is thus ultimately limited by the lifetime of the atom: $\tau_{\text{atom}} = 1/\gamma$ and not by the light field intensity. As a final remark, we note that the dissipative force is not a conservative field since it relies on spontaneous emission – an inherently irreversible mechanism. This means that atoms cannot be trapped with this force while at the same time having optical, hyperfine or Zeeman coherences kept unperturbed. With $\mathbf{F}_{\text{dissipative}}$ being a dissipative force it can, however, efficiently[10] be used to slow atoms, a mechanism for two-level atoms referred to as Doppler cooling. To see this in expression Eq. (6.50), one should remember to make the replacement $\delta \to \delta - \mathbf{k} \cdot \mathbf{v}$, where $\mathbf{v}$ is the velocity of the atom.

6.7.2 *Dipole force*

The first force term in Eq. (6.49) is known as the dipole force:

$$\mathbf{F}_{\text{dipole}} = \frac{\epsilon_0}{4} \operatorname{Re} \chi \boldsymbol{\nabla} \mathcal{E}^2 |_{\mathbf{r}_{\text{atom}}} . \tag{6.52}$$

Following the dispersive profile in Eq. (6.4), the dipole force is seen to be zero on atomic resonance contrary to the dissipative force. Inserting the expression for the dispersion $\operatorname{Re}\chi$, given in Eq. (6.37a), into Eq. (6.52), the $\mathbf{F}_{\text{dipole}}$ can be restated as

$$\mathbf{F}_{\text{dipole}} = -\frac{\hbar \delta \boldsymbol{\nabla} \Omega^2}{4\delta^2 + \gamma^2 (1 + s_0)} . \tag{6.53}$$

In the far-detuned limit with small saturation, $|\delta| \gg \gamma, \Omega$, this reduces to

$$\mathbf{F}_{\text{dipole}} = -\frac{\hbar \boldsymbol{\nabla} \Omega^2}{4\delta} = -\boldsymbol{\nabla}(\Delta E_g) , \tag{6.54}$$

where we, in the last equality, have used expression (5.29a) for the AC Stark shift of the atomic ground state ΔE_g. Evidently, $\mathbf{F}_{\text{dipole}}$ is a conservative force field which originates from a potential very much related to the energy shift experienced by the atom when placed in a light field. The dipole force is seen to be oriented along the gradient of the light field. For a red-detuned field, $\delta < 0$, the atom is thus attracted towards high intensity regions, whereas it is repelled for a blue-detuned field with $\delta > 0$. This will be opposite for excited states, where the AC Stark shift is opposite of that of the ground states.

10 That is, as long as the atomic lifetime is short enough, since otherwise the atom can essentially drift out of the light field before it is again in its ground state ready to scatter yet another photon.

As we already noticed for the dispersion and absorption profiles in (6.37), Re χ falls of as δ^{-1}, while Im χ falls of much faster as δ^{-2}. For a light field far-off resonance, the dipole force will therefore dominate over the dissipative force, which is really what makes it possible to trap atoms in the conservative optical dipole potential. Indeed, this is also how we confine atoms in our experimental setup, which will be the main subject in Chapter 9. For any further notion on slowing and trapping atoms, the reader is referred to the very nice textbook by Metcalf *et al.* [1999] on the topic in general, and to the paper by Grimm *et al.* [2000] on optical dipole traps in particular.

6.8 MASTER EQUATION

We conclude this chapter with a remark concerning the treatment for the inclusion of atomic state decay mechanisms. So far, we dealt with it in a phenomenological way by adding relaxation terms to the optical Bloch equations by hand. Strictly speaking, one should use the master equation, governing the time-evolution of the density operator, to meticulously account for dissipative processes [Lukin *et al.*, 2011]:

$$\dot{\hat{\rho}} = -\frac{i}{\hbar}[\hat{H}, \hat{\rho}] + \mathcal{L}(\hat{\rho})\,. \tag{6.55}$$

Here the first term[11] contains only the coherent or unitary evolution of the state generated by the Hamiltonian $\hat{H}$ as described in Section 5.1, which, in the case of a two-level atom interacting with a single-mode light field, we saw results in the equations (6.8) and (6.9) for the dynamics of $\hat{\rho}$. The last term, then, contains all decay and dephasing mechanisms of the state described by the Lindblad superoperator:

$$\mathcal{L}(\hat{\rho}) = -\frac{1}{2}\left(\hat{C}^\dagger\hat{C}\hat{\rho} + \hat{\rho}\hat{C}^\dagger\hat{C} - 2\hat{C}\hat{\rho}\hat{C}^\dagger\right), \tag{6.56}$$

where the operator $\hat{C}$ contains all the mechanisms causing the state to undergo decay events or dephasing. For example, to account for spontaneous emission where the atom decays from $|e\rangle$ to $|g\rangle$ at a rate γ, we would have $\hat{C} = \sqrt{\gamma}\hat{\sigma}_{ge}$, which reproduces the results we found in Eq. (6.10) and Eq. (6.15) when evaluating Eq. (6.55).

When only including the first term in Eq. (6.55), it is often referred to as the Liouville equation, which, in fact, is the density operator equation of motion equivalent to the Schrödinger equation (5.1).

11 This is not to be confused with the Heisenberg equation of motion, which for a time-dependent operator $\hat{O}(t)$ is given by $i\hbar\dot{\hat{O}}(t) = [\hat{O}(t), \hat{H}]$.

SUMMARY

Starting with a brief review of the Schrödinger equation and how to solve the dynamics for a two-level atom driven by a single-mode classical light field, we continued to the density operator formalism where decay and dephasing mechanisms were included in the description for the atomic evolution. Thus considering a simplistic two-level system we have in this chapter introduced some of the most vital concepts when dealing with light-atom interactions. This includes, *e.g.*, the OD, the scattering rate, the linear susceptibility, and the dipole force, just to mention a few. These concepts will be referred to extensively throughout the thesis and this chapter, together with Chapter 2 for the description of TOFs, thus constitutes a broad foundation for the remaining chapters.

7

REAL ATOMS—A MULTILEVEL SYSTEM

The two-level atom considered so far, is an idealized system that serves well for a fundamental understanding of light-atom interactions, but in practice does not comply with real physical systems. In particular, we work with neutral caesium-133 (Cs) atoms, which most definitely should be considered as a multi-level atom. Before moving on to Part iii, where we present our experimental setup, we therefore give here a general introduction to Cs, followed by a discussion in the next chapter on some interesting and important features that emerge when an atom is placed in the evanescent field of a TOF.

7.1 CAESIUM

As apparent from the small portion of the rich level structure of Cs, shown in Fig. 7.1, we are dealing with a highly multi-level atom containing in total 16 groundstates. Being an alkali atom Cs has a single unpaired valence electron [Foot, 2005], which makes it possible to treat it as a hydrogen-like atom. Due to the spin-orbit interaction, *i.e.*, the coupling between the magnetic moment of the valence electron (proportional to its spin $\mathbf{S}$, with $S = 1/2$) and the magnetic field (proportional to its orbital angular momentum $\mathbf{L}$), arising from the electron moving through the electrostatic potential of the nucleus, the atomic energy levels are split into several sub-levels. This is known as the fine structure and characterized by the total angular momentum of the electron $\mathbf{J} = \mathbf{L} + \mathbf{S}$, with quantum number J restricted to the range $|L - S| \leq J \leq |L + S|$ (in integer steps).

For the ground state, where the electron is in the s shell, we have $L = 0$ such that $J = S = 1/2$. The ground state thus remains a single energy level and is written as $n^{2S+1}L_J = 6^2S_{1/2}$, where n is the principal quantum number. The first exited state has $L = 1$ (p shell), and is therefore split into the two levels, $6^2P_{1/2}$ and $6^2P_{3/2}$, also known as the fine structure doublet[1]. The ground state is connected to these states via the so-called D1 and D2 transition lines as shown in Fig. 7.1. In this thesis we have exclusively worked with transitions on the D2 line and any later references to the atomic exited state should be understood to govern the $6^2P_{3/2}$ level only.

1 With the two levels being separated by 17 THz the fine structure splitting in Cs is really not that fine again as pointed out by Foot [2005].

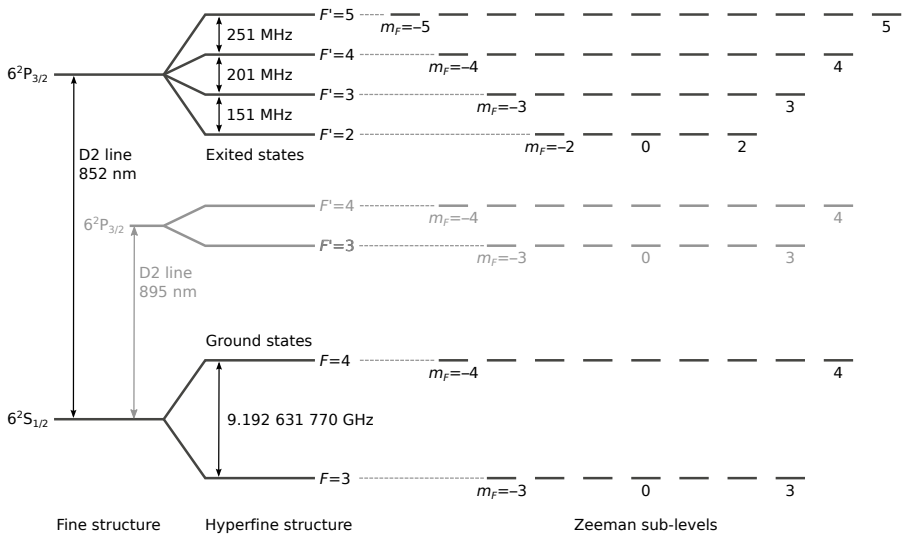

Figure 7.1.: *Level diagram of the hyperfine state architecture of the ground and first exited state in Cs.*

The interaction between the magnetic moment of the nucleus (proportional to its spin $\mathbf{I}$) and the magnetic flux density of the valence electron (approximately proportional to $\mathbf{J}$) gives rise to a further division of the atomic energy levels into the hyperfine structure, *cf.* Fig. 7.1. To represent these levels a new quantum number is introduced for the total angular momentum: $\mathbf{F} = \mathbf{I} + \mathbf{J}$, with quantum number F and, as J, it is restricted to be within the range $|I - J| \leq F \leq |I + J|$. With $I = 7/2$ for Cs, the ground state thus splits into two hyperfine states:

$$6^2\mathrm{S}_{1/2} \rightarrow \begin{cases} 6^2\mathrm{S}_{1/2}, F = 3\,, \\ 6^2\mathrm{S}_{1/2}, F = 4\,, \end{cases} \tag{7.1}$$

while the highest level of the first exited state splits into four hyperfine states:

$$6^2\mathrm{P}_{3/2} \rightarrow \begin{cases} 6^2\mathrm{P}_{3/2}, F' = 2\,, \\ 6^2\mathrm{P}_{3/2}, F' = 3\,, \\ 6^2\mathrm{P}_{3/2}, F' = 4\,, \\ 6^2\mathrm{P}_{3/2}, F' = 5\,. \end{cases} \tag{7.2}$$

Here we have employed the commonly used notation, where exited states are explicitly referred to by adding a prime to the quantum number. Each hyperfine level has $2F + 1$ Zeeman degenerate sublevels, denoted by m_F, that are lifted by any externally applied magnetic fields, including the earth magnetic field. The somewhat ab-

stract representation of an atomic state given in Eq. (5.7) can now be made more concrete using the F and m_F quantum numbers:

$$|\psi(t)\rangle = \sum_g c_g(t)|g\rangle + \sum_e c_e(t)|e\rangle \tag{7.3a}$$

$$= \sum_{F,m_F} c_{F,m_F}(t)|F\, m_F\rangle + \sum_{F',m'_F} c_{F',m'_F}(t)|F'\, m'_F\rangle\,. \tag{7.3b}$$

In the remainder of the thesis, we will represent the atomic states by their F and m_F quantum numbers as either $|F\, m_F\rangle$ or $|F\rangle$ in cases where an isotropic distribution in the Zeeman sublevels are considered.

7.2 DIPOLE TRANSITIONS FROM INTERACTION WITH LIGHT

As described in Section 5.2, the ground and exited states are coupled via electric dipole transitions when the atom is driven by an near-resonant electromagnetic field. The strength of these transitions is contained in the dipole matrix element given formally in Eq. (5.15a). In terms of the F and m_F quantum numbers we have

$$\mu_{eg} = \langle F'\, m'_F|e\hat{\mathbf{r}}\cdot\mathbf{u}_\mathbf{k}|F\, m_F\rangle\,. \tag{7.4}$$

7.2.1 *Spherical basis*

When dealing with light-atom interactions, the most convenient coordinate frame is given by the spherical basis $\{\mathbf{u}_q\}$ with $q = -1, 0, +1$, as this greatly simplifies the evaluation of μ_{eg} which will become apparent in a moment. In the spherical basis frame the position operator $\hat{\mathbf{r}}$ takes the form of a spherical tensor of rank 1, $T^{(1)}_q$, written as

$$\hat{\mathbf{r}} = \sum_q r_q \mathbf{u}_q\,. \tag{7.5}$$

Similarly, we have for the unit polarization vector in Eq. (7.4)

$$\mathbf{u}_\mathbf{k} = \sum_q \varepsilon_{\mathbf{k}q}\mathbf{u}_q\,, \tag{7.6}$$

where $\varepsilon_{\mathbf{k}q}$ yields the distribution of the light field polarization among the three basis vectors fulfilling $\sum_q \varepsilon_{\mathbf{k}q} = 1$. If the quantization axis is chosen along the unit vector $\mathbf{u}_z$ in the Cartesian basis $\{\mathbf{u}_i\}$ with $i = x, y, z$, we have [Normand *et al.*, 1982]

$$\mathbf{u}_{-1} = \frac{+\mathbf{u}_x - i\mathbf{u}_y}{\sqrt{2}}\,, \tag{7.7a}$$

$$\mathbf{u}_0 = \mathbf{u}_z\,, \tag{7.7b}$$

$$\mathbf{u}_{+1} = \frac{-\mathbf{u}_x - i\mathbf{u}_y}{\sqrt{2}}\,. \tag{7.7c}$$

When relating the light field polarization to the atomic system, it is common practice to refer to it as π-polarized when it is parallel to the quantization axis, *i.e.*, along $\mathbf{u}_0$, and σ-polarized when it is perpendicular (senkrecht in German) to the quantization axis, *i.e.*, given by a linear combination of $\mathbf{u}_{-1}$ and $\mathbf{u}_{+1}$. In the special case where the light field is circularly polarized with respect to the quantization axis, and hence oriented along either $\mathbf{u}_{-1}$ or $\mathbf{u}_{+1}$, it is denoted as σ_- and σ_+ polarized light, respectively.

7.2.2 *Selection rules*

Writing the dipole matrix element, Eq. (7.4), in the spherical basis we have

$$\mu_{eg} = \sum_q \varepsilon_{\mathbf{k}q} \langle F' \, m'_F | e r_q | F \, m_F \rangle \, . \tag{7.8}$$

In order to calculate the transition elements between the ground and excited states, we, in principle, have to evaluate the matrix element in Eq. (7.4) $3 \times (2F'+1) \times (2F+1)$ times, since there is 3 polarization components, $2F'+1$ excited states, and $2F+1$ ground states (for just a single hyperfine excited state and ground state F' and F). Fortunately, it is possible to derive a set of selection rules that greatly reduces the number of evaluations. This is the main motivation for working in the spherical basis, since the position operator in this coordinate frame satisfies the following commutation relations with the angular momentum components[2] [Sakurai, 1994]

$$[F_z, r_q] = \hbar q r_q \, , \tag{7.9a}$$

$$[F_\pm, r_q] = \hbar \sqrt{(1 \mp q)(2 \pm q)} r_{q\pm 1} \, . \tag{7.9b}$$

Using Eq. (7.9a) it is straightforward to obtain the m_F selection rule (the derivation can be found in Appendix E):

$$\langle F' \, m'_F | e r_q | F \, m_F \rangle = 0 \, , \quad \text{if } m'_F \neq m_F + q \, . \tag{7.10}$$

This selection rule directly reflects the conservation of angular momentum. When an atom, initially described by the m_F quantum number, absorbs a photon carrying spin angular momentum $q\hbar$, the new internal state of the atom must have quantum number $m'_F = m_F + q$ in order for the system to have the same total angular momentum before and after the absorption event.

2 Spherical tensors are in general irreducible operators, in contrary to Cartesian tensors, and the following the commutation relations

$$[J_z, T^{(k)}_q] = \hbar q T^{(k)}_q \, , \; [J_\pm, T^{(k)}_q] = \hbar \sqrt{(k \mp q)(k \pm q + 1)} T^{(k)}_{q\pm 1} \, ,$$

where $\mathbf{J}$ is any angular momentum operator and $T^{(k)}_q$ is a spherical tensor of rank k, can in fact be regarded as the very definition of spherical tensors [Sakurai, 1994].

From Eq. (7.9b) the following relation can be derived [Sakurai, 1994]:

$$\langle F'\, m'_F|er_q|F\, m_F\rangle = \langle F\, 1\, m_F\, q|F'\, m'_F\rangle\langle F'||e\hat{\mathbf{r}}||F\rangle\,, \tag{7.11}$$

which is known as the Wigner-Eckart theorem. The double-bar notation, in the second factor, denotes a reduced matrix element. The first factor is what really makes the Wigner-Eckart theorem powerful since this is simply the Clebsch–Gordan (CG) coefficient of the dipole transition. In terms of the Wigner 3-j symbol the CG coefficient is given by

$$\langle F\, 1\, m_F\, q|F'\, m'_F\rangle = (-1)^{F-1+m'_F}\sqrt{2F'+1}\begin{pmatrix} F & 1 & F' \\ m_F & q & -m'_F \end{pmatrix}, \tag{7.12}$$

and we readily obtain the following selection rules for the atomic dipole transitions, since the Wigner 3-j symbol is zero unless

$$\Delta m_F = m'_F - m_F = q\,, \tag{7.13a}$$
$$\Delta F = F' - F = 0, \pm 1\,, \tag{7.13b}$$
$$F + F' + 1 = \text{even integer}, \quad \text{if } m_F = m'_F = q = 0\,. \tag{7.13c}$$

These selection rules not only tells us which ground to excited state transitions are allowed, but also relates the light polarization to specific transitions via the spherical basis index q in Eq. (7.13a) (equal to what we found in Eq. (7.10)). We thus see that π polarized light only drives transitions where $\Delta m_F = 0$, whereas $\sigma_\pm$ polarized light are responsible for transitions with $\Delta m_F = \pm 1$. It greatly pays off to learn the selection rules in Eq. (7.13) by heart[3] and I can only recommend future students in the lab to always keep them in mind.

7.2.3 *Reduced matrix element*

The reduced matrix element, $\langle F'||e\hat{\mathbf{r}}||F\rangle$ encountered in the Wigner-Eckart theorem (7.11), can be further factorized and simplified, and in the end, the dipole matrix element μ_{eg}, Eq. (7.4), is actually not that hard to evaluate, albeit a bit tedious. For more details on how to do this, the reader is referred to [Steck, 2003], who has a nice section on this subject as well as tables for all the CG coefficients of the D1 and D2 line transitions in Cs. Here we simply note that since the CG coefficients are essentially just the elements of the transformation matrix connecting the two angular-momentum bases $\{\mathbf{J}^2, \mathbf{J}_1^2, \mathbf{J}_2^2, J_z\}$ and

3 For example, the $|4,0\rangle \to |4',0'\rangle$ transition is found to be forbidden (at least to first order), which on one hand is great, since is makes it possible to purify the atomic ensemble into $|4,0\rangle$, but on the other hand it can be really annoying when atoms are accidentally shelved into the $|4,0\rangle$ state. Remembering the selection rules, such mistakes occur less often.

$\{\mathbf{J}_1^2, J_{1z}, \mathbf{J}_2^2, J_{2z}\}$, they can be readily calculated, although I would suggest[4] to use either the `ClebschGordan` function in *Mathematica* or the Python library `SymPy`.

As a final comment on the reduced matrix element, we note that it is related to the spontaneous emission rate given in Eq. (6.20) for a two-level atoms, and a more precise form of the excited state decay rate is [Steck, 2003]

$$\gamma_e = \frac{\omega_{eg}^3}{3\pi\epsilon_0\hbar c^3}\frac{2J+1}{2J'+1}\left|\langle J'||e\hat{\mathbf{r}}||J\rangle\right|^2 . \tag{7.14}$$

4 Just be cautious about different conventions!

8

ATOMS PLACED IN THE EVANESCENT FIELD

With the main theory concerning the evanescent light field and Cs atoms now established, together with a conceptual introduction to light-atom interactions, we are now ready to consider the behavior of these two physical systems when brought together. This is the main focus of the remainder of this thesis with the exception of a few detours, for example, when describing the detection scheme that we use for probing the atoms in Chapter 10.

Here we give a general overview of a couple of important properties that comes into effect when an atom is placed in the evanescent light field of a TOF-guided mode. In particular, we will discuss how the quasi-linear polarization of the HE_{11} should be interpreted in the atomic frame and how this affects the atomic scattering rate.

8.1 POLARIZATION IN THE ATOMIC FRAME

In what follows, we take a leap ahead and anticipate an ensemble of Cs atoms to be confined in close vicinity to the TOF. Later, in Section 9.4, it is shown how this is accomplished in practice, and that the atoms are formed into two 1D strings positioned along either side of the TOF. This means, that the atoms will be entirely confined within a 2D plane, made up of the two parallel 1D strings, which we shall refer to as the atomic plane. In the lab frame, we have chosen this plane to be horizontal, and with respect to the cylindrical coordinate frame, where the TOF-axis is coinciding with the horizontal z-axis and the transverse x-axis is vertically aligned along the gravity axis, the atomic plane is equivalent to the yz-plane.

As shown in Section 2.5, the evanescent field of a RW TOF-mode with quasi-linear y polarization has a significant longitudinal electric field component in the yz-plane, *i.e.*, parallel to the atomic plane. In Eq. (2.24) this were found to yield a nearly circular polarization at the atomic trap sites. It was also found, that if the field polarization is rotated by 90°, to quasi-linear x polarization, it will be purely x-polarized in the now perpendicular atomic plane[1].

1 Actually, in Section 2.5 we did not rotate the polarization but rather ourselves to the perpendicular axis. In the end, the result is of course the same.

A conceptual sketch of these two situations is shown in Fig. 8.1, with the quantization axis q chosen along the vertical x-axis. For an evanes-

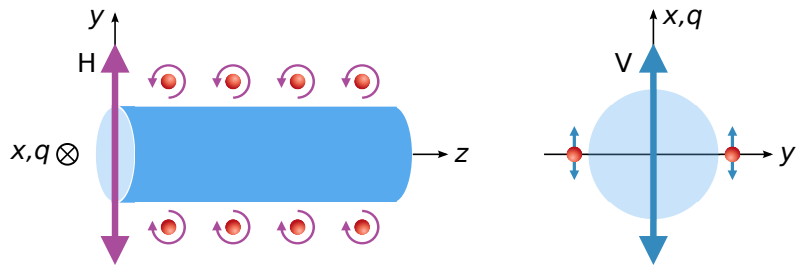

(a) Quasi-linear horizontal polarization is circular at the atoms (red balls) and hence causes $\sigma_\pm$ transitions where $\Delta m_F = \pm 1$.

(b) Quasi-linear vertical polarization is linear at the atoms (red balls) and hence causes π transitions where $\Delta m_F = 0$.

Figure 8.1.: *Illustration of the quasi-linear horizontal (in the atomic plane) and vertical (perpendicular to the atomic plane) polarization modes in the* TOF *evanescent field. The quantization axis is chosen along the vertical x-axis. Also* cf. *Fig. 2.12 and Fig. 2.14.*

cent field mode with quasi-linear horizontal polarization in Fig. 8.1(a), the effective left-handed circular polarization at the atoms positioned on the upper (right) side of the TOF mainly causes σ_- transitions (92 % as found in Eq. (2.24), the remaining 8 % will be σ_+ transitions), while atoms located on the opposite side of the TOF will undergo σ_+ transitions when driven by the right-handed circularly polarized electric field. In contrast, a quasi-linear vertical polarization field will only drive π-transitions in the atoms, since the polarization is now purely linear along x at the location of the atoms, as illustrated in Fig. 8.1(b).

8.2 ANISOTROPIC SCATTERING RATE

When an exited atom, placed in the vicinity of a TOF, decays, the spontaneously emitted photon can either couple to a free-space radiative mode or couple into the TOF as a guided mode. The total scattering rate of the atom γ_{sc} can thus be described as the sum of the two scattering rates of either scenario as

$$\gamma_{sc} = \gamma_{free} + \gamma_{TOF}\,. \tag{8.1}$$

Because we only collect light that couples out of either input-output ports of the TOF, we are mainly concerned about emitted photons coupled into the TOF, and hence γ_{TOF}. Four channels in the TOF are available for the emitted photon. Two for either propagation direction

along the positive $(+)$ or negative $(-)$ z-direction in the TOF, and two for either of the quasi-linear polarization modes x and y. The total scattering rate in either of the two propagation direction can therefore be written as

$$\gamma_{\pm} = \sum_{p=x,y} \gamma_{\pm,p} \,, \tag{8.2}$$

where

$$\gamma_{\pm,p} = \sum_{e,e'} \gamma_{ee'}^{(\pm,p)} \rho_{ee'} \,, \tag{8.3}$$

with the double sum taken over all exited states $|e\rangle = |F'\, m'_F\rangle$. Expression (8.3) is an extension of the two-level atom scattering rate given in Eq. (6.22) to the case of a multi-level atom. It is worth noting, however, that in contrast to a two-level atom, where the spontaneous emission rate only governs the population decay out of the exited state $|e\rangle$, $\gamma = \gamma_{ee}$, now the decay of cross-level coherences $\gamma_{ee'}$ between exited state levels, $|e\rangle$ and $|e'\rangle$, also has to be taken into account [Le Kien *et al.*, 2005].

We previously saw in Eq. (6.20) for a two-level atom, that the spontaneous emission rate is proportional to the norm square of the dipole matrix element projected onto the orientation of the field polarization, $\gamma_{ee} \propto \left|\, \mu_{eg} \,\right|^2$, with μ_{eg} given by Eq. (7.4). A natural extension for the multi-level spontaneous emission rate into the TOF is then something like

$$\gamma_{ee'}^{(\pm,p)} \propto \sum_{g} \mu_{eg}^{(\pm,p)} \left(\mu_{ge'}^{(\pm,p)}\right)^* . \tag{8.4}$$

This expression of course has to be evaluated at the position of the atom with the field orientation given accordingly. To make this circumstance a bit more transparent it might be more appropriate to write $\gamma_{ee'}^{(\pm,p)}$ according to that in [Le Kien *et al.*, 2014], which is given by

$$\gamma_{ee'}^{(\pm,p)} = 2\pi \sum_{g} G_{eg}^{(\pm,p)} \left(G_{e'g}^{(\pm,p)}\right)^* , \tag{8.5a}$$

with

$$G_{eg}^{(\pm,p)} = \sqrt{\frac{\omega_{eg}\beta'}{4\pi\epsilon_0\hbar}}\, \mathbf{d}_{eg} \cdot \boldsymbol{\varepsilon}_{\pm,p}\, \mathrm{e}^{\pm i\beta z} \,, \tag{8.5b}$$

where the shorthand notation $\beta' = \mathrm{d}\beta/\mathrm{d}\omega|_{\omega_{eg}}$ is used for the derivative of the propagation constant β with respect to the field frequency evaluated at the atomic resonance transition frequency ω_{eg}. $\boldsymbol{\varepsilon}_{\pm,p}$ is the field mode profile function of the four available TOF channels, and defined from the complex electric field amplitude in Eq. (2.7) as

$$\boldsymbol{\mathcal{E}}_{\pm,p}(\rho,\phi) = C\boldsymbol{\varepsilon}_{\pm,p}(\rho,\phi) \,, \tag{8.6}$$

where C is a normalization constant containing the field optical power among other things, see Appendix A for the components of $\boldsymbol{\mathcal{E}}(\rho, \phi)$ and note that the sign of the z component depends on the propagation direction, $\mathcal{E}_z \to \pm\mathcal{E}_z$. From Eq. (8.5) it should be clear that the spontaneous emission rate into the TOF not only depends on the internal structure of the atom, but also on its degree of spatial overlap with the available decay channels. The question is thus, if the atom couple equally well to all four channels in the TOF, or if some are preferred over the other?

Le Kien *et al.* [2014] answer this question by calculating the steady-state solution of the optical Bloch equations for a weak (far below saturation) forward $(+)$ propagating probe field, scattering off the $|4\rangle \to |5'\rangle$ transition of a Cs atom placed in the evanescent field. In Table 8.1 we have collected a few of the numerical results they obtained for the scattering efficiency

$$\eta_{\pm,p} = \frac{\hbar\omega\gamma_{\pm,p}}{P_z}, \tag{8.7}$$

into the four TOF-modes, using a quasi-linearly polarized probe field and an atom placed on the y-axis[2] at the rim of the TOF. Perhaps

PROBE FIELD	SCATTERED FIELD			
	$+, x$	$-, x$	$+, y$	$-, y$
$+, x$	4.0	4.0	5.5	5.5
$+, y$	~ 0.01	~ 0.01	130	10

Table 8.1.: *Scattering efficiency $\eta_{\pm,p}$ into the four available decay channels of the TOF, for an atom sitting on the y-axis on the TOF rim,* i.e., *at $\rho, \phi = a, \pi/2$. For an atom placed further out at $\rho = 450\,\text{nm}$ corresponding to the position of the potential trap minima, the table entries are about 30 times lower. The values are read of Fig. 3 and Fig. 4 in [Le Kien* et al., *2014], which were made using the parameters $P_z = 10\,\text{fW}$, $\omega = \omega_{eg}$, $n_{co} = 1.45$, $n_{cl} = 1$, and $a = 250\,\text{nm}$.*

what is first caught by the eye in Table 8.1, is that when the probe polarization is oriented along the y-axis, containing the atom, the atomic radiative decay is one order of magnitude higher into the forward propagation mode than into the backward propagation mode, for the polarization preserving channel. While, for the opposite case, when the probe polarization is perpendicular to the atomic axis, the scattered light couples equally into the forward and backward propagation modes regardless of which of the two polarization channels

2 Actually, in [Le Kien *et al.*, 2014] the atom is placed on the x-axis, but we have rotated the frame by 90° to make it match the coordinate frame used in this thesis.

it couples into. These results can be explained by the presence of the longitudinal electric field component when the field polarization is quasi-linear y, while $\mathcal{E}_z(\rho, \phi = \pi/2) = 0$ when the field polarization is quasi-linear x.

Well, one thing at a time, so let us first try to understand the second row in Table 8.1, where the probe field is aligned with the atom, *i.e.*, quasi-linearly y-polarized. Apart from what we already noticed, it is also found that the scattered light almost exclusively couples into the same polarization mode as the drive field. This can be understood from the fact that Le Kien *et al.* [2014] consider the steady-state solutions of the optical Bloch equations. Because the atom is essentially driven by σ_- polarized light, *cf.* Fig. 8.1(a) in the previous section, it will eventually be optically pumped to the stretched $|4, -4\rangle$ state. For a scattering event into the other polarization channel x to occur, a change in spin angular momentum by $\pm\hbar$ of the scattered photon with respect to the incoming photon is required from the selection rule given in Eq. (7.10). This can only happen in the highly improbable scattering event where the atom is excited to the $|5, -3\rangle$ state by a σ_+ photon. This is not only unlikely to happen due to only 8 % of the light being σ_+ polarized, but also because the transition probability is 45 times weaker for the $|4, -4\rangle \rightarrow |5, -3\rangle$ transition than for the $|4, -4\rangle \rightarrow |5, -5\rangle$ transition. On top of all that, the vacuum field strength for the x-polarized mode is at the same time substantially weaker than for the y-polarized mode, and any scattering into $\pm, x$ is therefore effectively suppressed.

We now turn our attention back to the dominant coupling into the forward propagation mode for the quasi-linearly y-polarized probe. This can also be understood from the nearly circular field driving the atom into the $|4, -4\rangle$ state. As the atom in $|4, -4\rangle$ is mainly excited to the $|5', -5'\rangle$ state, it can only decay back to $|4, -4\rangle$. Again, due to angular momentum conservation, we know the that emitted photon then has to be σ_- polarized. Since we know, that the electric field distribution is such that a forward propagating mode consist of 92 % σ_- polarized light while only 8 % is σ_+ polarized, we also have that a backward propagating mode, at the same positions, must consist of 92 % σ_+ polarized light and only 8 % σ_- polarized light. Accordingly, 92 % of the σ_- light scattered of the atom into the TOF should couple into the forward propagating mode and only 8 % into the backward propagating mode, which matches perfectly with the ratio $10/130 = 8\,\%$.

We now consider the first row in Table 8.1, where the probe field is quasi-linearly x-polarized. Here the calculations by Le Kien *et al.* [2014] predict a stronger coupling into the orthogonal polarization mode in stark contrast to what we have just found for the y-polarized probe. Somewhat counter-intuitive at first, this can be explained by

the stronger vacuum field strength at the atom for the quasi-linear y polarization mode than for the quasi-linear x polarization mode, as evident in Fig. 2.10 to Fig. 2.12. Since, the initially isotropic atom are now driven exclusively by π polarized light, the steady-state distribution of the population in the $|4, m_F\rangle$ levels will be symmetric around $|4, 0\rangle$, and hence no directionality is built into the scattering.

To gain further insight of the anisotropic scattering rate, we show in Fig. 8.2 the ratio between the scattering rates into the forward and backward propagation modes in the TOF, as calculated for a two-level atom placed on the positive y-axis near the TOF. For this simplified

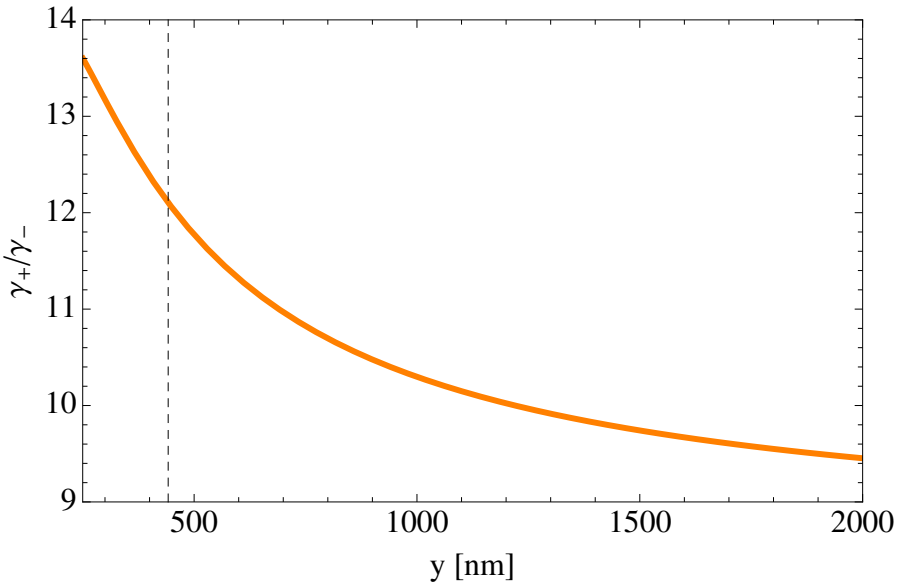

Figure 8.2.: *Ratio between the forward γ_+ and backward γ_- scattering rate into a TOF-guided mode of a two-level atom placed near the TOF on the same axis as the quasi-linear polarization field driving the atom. The nominal distance between the atomic trap site and the TOF is indicated by the dashed line.*

system, consisting of only a single ground and exited state, the spontaneous emission rate into the guided modes, given in Eq. (8.5), simplifies to

$$\gamma^{(\pm,p)} \propto \left| \mathbf{d}_{eg} \cdot \boldsymbol{\varepsilon}_{\pm,p} \right|^2 . \tag{8.8}$$

Considering a probe field with quasi-linear y-polarization, the ratio between the forward and backward scattering rates evaluated on the positive y-axis (with $\phi = \pi/2$) are simply given by [Le Kien *et al.*, 2014]

$$\frac{\gamma_+}{\gamma_-} = \left(\frac{|\varepsilon_r| + |\varepsilon_z|}{|\varepsilon_r| - |\varepsilon_z|} \right)^2 , \tag{8.9}$$

where $\varepsilon_r, \varepsilon_z$ are the radial and axial components of $\boldsymbol{\varepsilon}_{\pm,y}$, respectively. As in Table 8.1 the forward scattering rate into the TOF is seen to dominate the backward scattering rate by more than a factor of ten.

Evidently, the anisotropy decreases further away the atom is located from the TOF, but as indicated by the dashed line for the nominal position of the atom, there is still one order of magnitude difference between the two coupling rates and this effect can and should therefore not be neglected.

SUMMARY

After the introduction of Cs as the atomic species used in this work, we peaked into some of the features that has to be taken into account when such an atom is made to interact with the evanescent field of a TOF-guided mode. Especially important is the electric field polarization at the position of the atoms depending on whether it is aligned parallel with the atomic plane, also later referred the to as oriented along the strong coupling axis (SCA), or perpendicular to the atomic plane and thus along a weak coupling axis (WCA) with the atoms. This is important for the atomic Bragg mirror experiment, where also the anisotropy of the scattering rate has to be taken into account when back-scattering off the atoms is considered.

Part III

A ONE-DIMENSIONAL ATOMIC CRYSTAL

9 CONFINING ATOMS

The feasibility of confining atoms is, perhaps needless to say, required for the serious study of light-atom interactions, whether it being a physical confinement of atoms inside a sealed glass container or atoms confined in the conservative potential of an optical dipole trap. In our group, we have chosen the latter option and hold atoms in the evanescent field of two light modes guided by a TOF. In this chapter an overview of the principles behind the 1D crystallized spatial confinement of atoms is given.

9.1 MAGNETO-OPTICAL TRAP

As a second generation PhD-student working in the "fiber group" at QUANTOP, I have greatly benefited from the large amount of work done by Jean-Baptiste Béguin in designing, building, and mounting most parts on the optical table supporting the TOF-setup. Great many details on the magneto-optical trap (MOT), in large part of practical notion, can be found in his PhD thesis [Béguin, 2015]. I will not claim that it is a trivial task to build a MOT, with all its requirements to electronic control, an appropriate vacuum chamber, laser light sources, and magnetic fields, but it is certainly not hard to operate as soon as the effort of implementing it has been overcome. As MOTs by now has become a basic ingredient in many quantum optics labs around the world working with cold atoms, and the basic work principles behind it is already covered in several theses and textbooks, *e.g.*, [Metcalf *et al.*, 1999], I will resort to only briefly mention a few details regarding our setup in particular.

We implement a 3D MOT inside a cylindrical glass cell, see Fig. 9.1, connected to a vacuum system. This is done using as a standard 6-beam configuration for the two laser sources required to cool and repump the atoms, denoted the cooler and repumper in the following. The magnetic field gradient is provided by a set of anti-Helmholtz coils build around the glass cell. In additional, three compensation coils is mounted around the setup to cancel the static background magnetic field arising from the local earth magnetic field and other stray magnetic fields in the lab.

Two Cs dispensers are mounted near the entrance of the glass cell from which a vapor of Cs atoms inside, the otherwise evacuated, glass

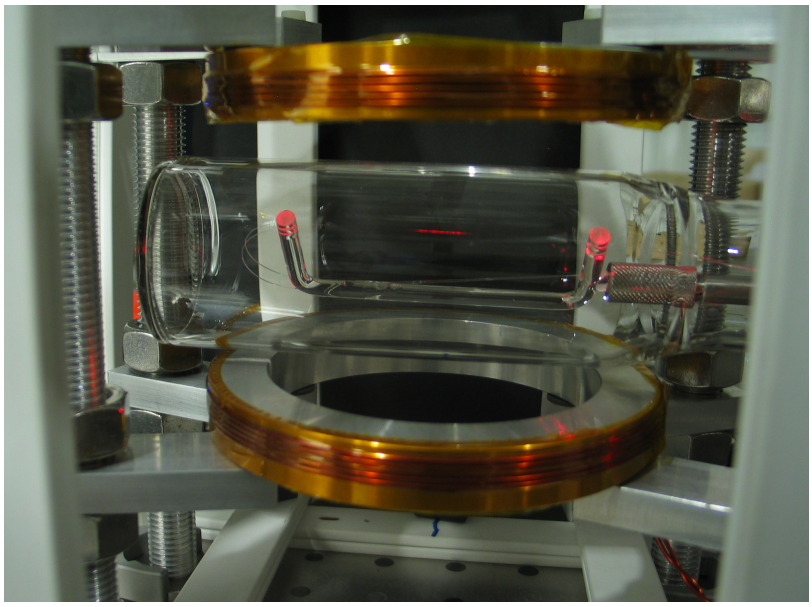

Figure 9.1.: TOF *inside an evacuated glass cell surrounded by a pair of anti-Helmholtz coils. The* 35 mm *long tapered section of the* TOF*, in the center of the image, is lit up from guided light (provided by a He-Ne laser pen coupled into the fiber) scattered off impurities in the* TOF*.*

cell can be established. Via the dissipative light force, described in Section 6.7.1, the atoms are Doppler cooled using the cycling transition $|4\rangle \rightarrow |5'\rangle$ of the D2 line, see Fig. 9.2. Even though the decay

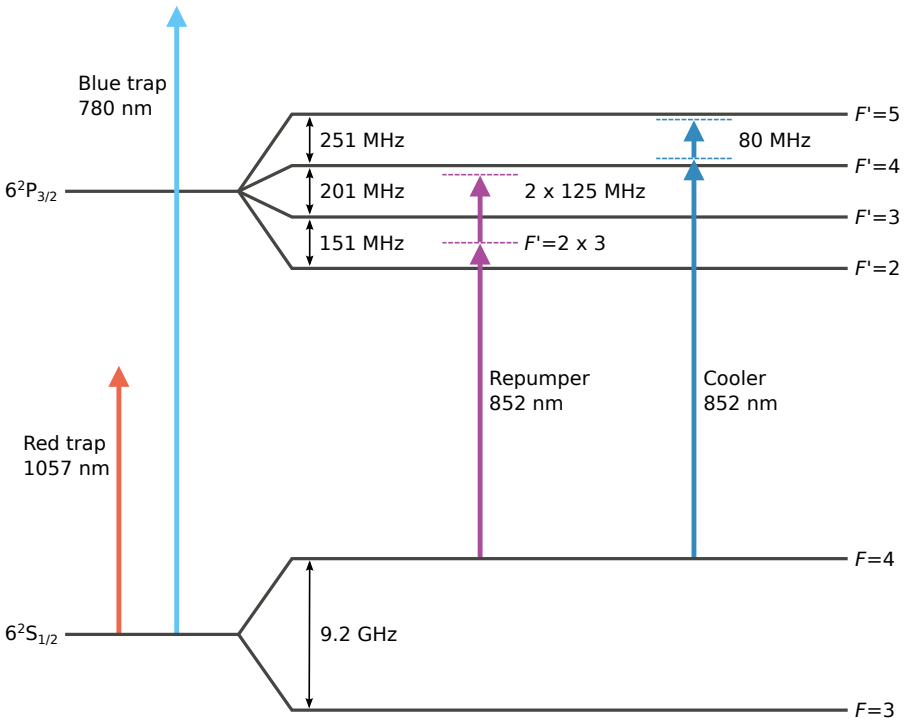

Figure 9.2.: Cs *level diagram together with the trap lasers.*

from $|5'\rangle$ to $|3\rangle$ is a forbidden transition, the atoms eventually end up in (the transparent state) $|3\rangle$ due to off-resonant excitation of the $|4'\rangle$ level. To prevent these atoms from drifting away, an additional laser, the repumper, optically pumps them from $|3\rangle$ back into $|4\rangle$ via the $|3\rangle \rightarrow |4'\rangle$ transition.

The coldest atomic cloud attainable with plain Doppler cooling is limited by the Doppler temperature: $T_D = \hbar\gamma/2k_B = 125\,\mu K$ for the Cs D2 line. Unfortunately, this temperature is too high for efficient loading of atoms into the dual-color dipole trap, and an additional 15 ms sub-Doppler cooling stage of the atoms, employing a blue Sisyphus cooling technique, is therefore performed after the initial 2 s Doppler cooling. Further details can be found in [Béguin, 2015], here it suffices to say that this method works and to advise the reader that the atoms are left in $|3\rangle$ and not in $|4\rangle$ after the two cooling stages.

9.2 LASER LOCKING

Both the cooler and the repumper are 852 nm 150 mW single-mode home build ECDLs in Littrow configuration, see *e.g.*, [Riehle, 2006]. For the laser cooling to work efficiently both lasers are frequency stabilized.

9.2.1 *Doppler-free polarization spectroscopy*

For the repumper the frequency stabilization is implemented by performing Doppler-free polarization spectroscopy [Wieman *et al.*, 1976], see Fig. 9.3. As in standard Doppler-free absorption spectroscopy, a saturating beam and a probe are sent through a vapor cell, with the main difference being that the saturating beam is now circularly polarized. This induces an anisotropy in the atomic sample that basically turns into a birefringent medium, and leads to a polarization rotation of a weak linearly polarized probe field passing through the sample. Even small changes in polarization are easily detectable by sending the probe output through a polarizer which translates the polarization change into an alteration of the intensity, which are then measured by a highly sensitive differential detection scheme. An advantage of the polarization spectroscopy over the ordinary saturation spectroscopy, is that the measured probe intensity resembles a dispersive signal when the probe frequency is varied over the atomic resonances, and, in a sense, the error-signal thus comes for free. Using this signal, the repumper is frequency stabilized onto the $F = 3 \rightarrow F' = 2 \times 3$ crossover by fast control of the laser supply current.

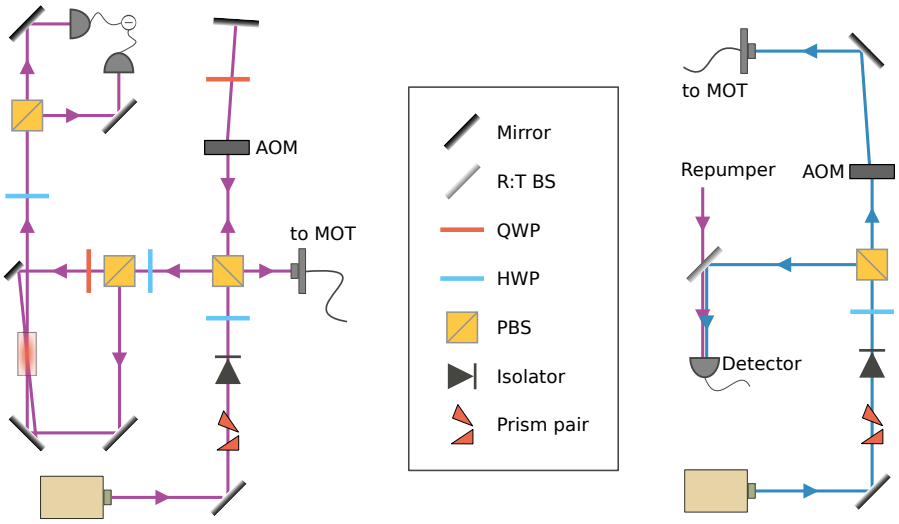

Figure 9.3.: *Simplified sketch of the optical setup of the repumper (left) and cooler (right).*

Before being sent into a 6-port fiber beam-splitter, providing the 6 beams for the MOT, the repumper is frequency-shifted by about $2 \times 125\,\mathrm{MHz}$ by using the first order beam diffracted off a double-pass acousto optical modulator (AOM). This also enables fast switching of the repumper light.

9.2.2 *Phase-locked loop*

The cooler (as well as the other 852 nm single-mode ECDLs that are introduced later) is frequency stabilized against the repumper via a phase-locked loop (PLL) developed by Appel, MacRae, *et al.* [2009]. Using a fast photodiode the beat note frequency ν_{beat} resulting from interfering the cooler with the repumper is recorded. The cooler frequency can then be adjusted and tuned by referencing ν_{beat} with a target frequency. Using a single-pass AOM allows for the fast switching of the cooler before it is coupled into the same 6-port fiber beam-splitter as the repumper.

9.3 CLOSE ENCOUNTER BETWEEN A COLD ATOMIC CLOUD AND A HOT GLASS WIRE

As already shown in Fig. 9.1, the TOF is stretched out and hold by a U-shaped glass rod placed inside the same evacuated glass cell in which the MOT is implemented. In it by no means obvious that a cold cloud of atoms confined in a MOT can be brought close to a hot macroscopic object like a TOF. It nevertheless works surprising well as seen from

the pictures displayed in Fig. 9.4. In the top panel, Fig. 9.4(a), the

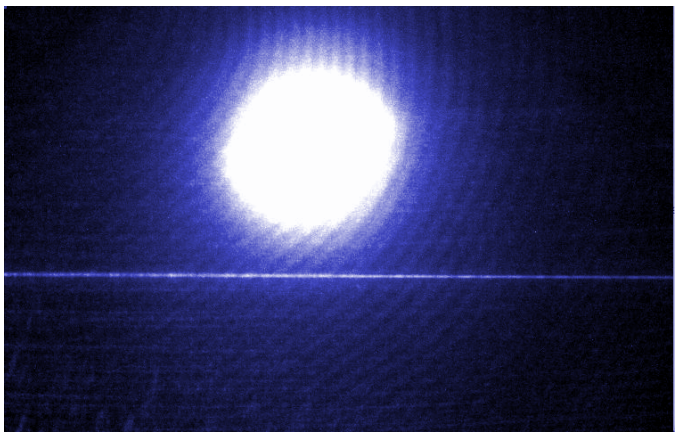

(a) Positioned above the TOF.

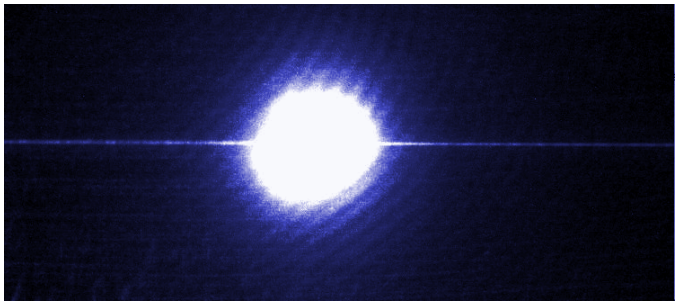

(b) Positioned on the TOF.

Figure 9.4.: *Images of the fluorescence from Cs atoms confined in a MOT. The* 500 nm *thin TOF is seen as the thin horizontal line. The image width corresponds to about* 2 mm*. Photo credit: Jean-Baptiste Béguin.*

fluorescence of the cold atoms in the MOT is seen as the bright "sun" in the center of the image. Right underneath it, the TOF is seen as the thin illuminated horizontal line. Using the MOT coils, the position of the MOT can be steered by moving the position of the B-field zero point. With this, the MOT center is made to overlap[1] with the TOF, as shown in the bottom panel, Fig. 9.4(b). The MOT size, evidently, shrinks when placed on top of the TOF, due to atoms being heated out of the trap from collisions with the hot glass wire. Still, this MOT provides a sufficiently cold atomic reservoir in the vicinity of the TOF, that 10^3 atoms can be efficiently loaded into the TOF-based dual-color dipole trap, which is the subject of the next section.

1 We use the same cameras for imaging the MOT as for configuring the polarization of a TOF-mode as described in Chapter 3. These two cameras image the MOT along two different axes both orthogonal to the TOF, which enables us to precisely place the MOT center on the TOF.

9.4 DUAL-COLOR OPTICAL DIPOLE TRAP

The Doppler cooling used for implementing the MOT, works by scattering red-detuned light off the atoms, which, in simple terms, effectively carries away the excess energy between absorbed and emitted photons. It is thus clear that the cold atoms spend a lot of their time in the exited state which is very impractical for most quantum optical experiments. We therefore seek a different way of confining the atoms. This can be done by implementing an optical dipole trap, where the atoms are trapped in a conservative light potential, and was first experimentally realized by [Chu *et al.*, 1986] for the alkali sodium using a tightly focused Gaussian laser beam.

For a far-off resonance trapping field with $|\delta| \gg \gamma, \Omega$, where only negligible fluorescence emission occurs, we saw in Section 6.7.2 that the dipole potential can be approximated by the AC Stark shift experienced by atoms in a light field, Eq. (6.54):

$$\mathbf{F}_{\text{dipole}} = -\boldsymbol{\nabla} U_{\text{dipole}} \approx -\boldsymbol{\nabla}(\Delta E_g)\,. \tag{9.1}$$

Using a perturbative treatment of the multi-level atomic system to second order, the AC Stark shift for ground $|g\rangle$ and exited $|e\rangle$ states can found to be given by [Grimm *et al.*, 2000], *cf.* Eq. (5.29):

$$\Delta E_g = \hbar \sum_e \frac{|\,\Omega_{eg}\,|^2}{4\delta_{eg}}\,, \tag{9.2a}$$

$$\Delta E_e = -\hbar \sum_g \frac{|\,\Omega_{eg}\,|^2}{4\delta_{eg}}\,, \tag{9.2b}$$

where $\Omega_{eg} = \mu_{eg}\mathcal{E}/\hbar$ is the Rabi frequency as defined in Eq. (5.22) and $\delta_{eg} = \omega - \omega_{eg}$ is the detuning between the light field frequency ω and the atomic resonance frequency ω_{eg} between the two levels $|g\rangle$ and $|e\rangle$. In short, all levels that a given state connects to, via the optical laser field, have to be taken into account in order to calculate the effective energy shift of the considered state. Cs has a very rich level structure, *cf.* Fig. 7.1, and in principle the sum in Eq. (9.2a) should be evaluated by calculating all the dipole matrix elements, Eq. (7.4):

$$\mu_{eg} = \langle F'\, m_F' | e\hat{\mathbf{r}} \cdot \mathbf{u}_{\mathbf{k}} | F\, m_F \rangle\,, \tag{9.3}$$

for a given ground state $|F\, m_F\rangle$. However, if the trapping field is so far detuned from atomic resonance, that the hyperfine splitting cannot be resolved, $|\delta| \gg \omega_{\text{hfs}}$, with $\omega_{\text{hfs}} = 2\pi \times 9.2\,\text{GHz}$ for the two hyperfine ground states, the sum can be greatly reduced to only contain the nearest fine structure exited states [Grimm *et al.*, 2000].

From Eq. (9.1) and Eq. (9.2a) it is obvious that the trapping laser field should be red-detuned ($\delta < 0$) in order to attract atoms to high

intensity regions[2]. This is especially true for the free-space implementation, using a tightly focused Gaussian laser beam, where atoms are confined in the volume effectively spanned by the waist radius and the Rayleigh range around the focal point.

In [Ovchinnikov *et al.*, 1991] it was proposed to trap atoms in the evanescent field arising from the total internal reflection of light at a dielectric-vacuum interface. Again, a red-detuned trapping beam is used to supply the attractive force on atoms. However, since the evanescent field monotonically decays away from the dielectric, and thus has it maximum field strength at the surface, an attractive red-detuned trapping beam would end up smashing the atoms into the dielectric. Therefore, a blue-detuned ($\delta > 0$) trapping beam is added to (elastically) repel the atoms from the surface. This works only because the penetration depth is inversely proportional to the field frequency, *cf.* Eq. (2.23), and hence the repulsive blue-detuned field decays faster than the attractive red-detuned field. By balancing the powers properly, the blue-detuned field will then dominate close to the dielectric and act as a soft barrier, whereas further out, the total field will mainly consist of the red-detuned field in which the atoms can be held. We shall refer to this configuration as a dual-color dipole trap.

A decade later, the optical fiber technology had developed to a point where low-loss sub-wavelength TOFs could be fabricated as demonstrated in [Tong *et al.*, 2003]. This catalyzed [Balykin *et al.*, 2004; Le Kien, Balykin, *et al.*, 2004] to extend the original proposal in [Ovchinnikov *et al.*, 1991], to use TOFs as the dielectric-vacuum interface. Experimentally, Cs atoms were confined in a TOF-based dual-color dipole trap for the first time in [Vetsch *et al.*, 2010] and then later in [Goban *et al.*, 2012; Béguin *et al.*, 2014]. Recently, it was also realized in [Lee *et al.*, 2015] for rubidium-87 (Rb) atoms.

9.4.1 *Trap potentials*

The effective trapping potential for the dual-color dipole trap is given by the sum of the individual light potentials for each trapping beam and the van der Waals potential:

$$U_{\text{trap}} = U^{\text{blue}}_{\text{dipole}} + U^{\text{red}}_{\text{dipole}} + U_{\text{vdW}} \,. \tag{9.4}$$

The individual dipole potentials are given by, *cf.* Eq. (6.52),

$$U_{\text{dipole}} = \frac{\epsilon_0}{4} \operatorname{Re} \chi(\omega) \, | \, \mathcal{E}(\mathbf{r}) \, |^2 \,, \tag{9.5}$$

2 In principle, one could also use a blue-detuned ($\delta < 0$) field, where atoms seek towards low-intensity regions. It is, of course, somewhat impractical that all the space where no light field is present is also a low-intensity region.

where $\mathcal{E}(\mathbf{r})$ is the HE_{11} electric field mode in the TOF with quasi-linear polarization, *cf.* Appendix A. For the real part of the susceptibility we use the (classically derived) expression given in [Le Kien, Balykin, *et al.*, 2004]:

$$\operatorname{Re}\chi = 2\pi c^3 \sum_e \frac{g_e}{g_g} \frac{\gamma_e(1-\omega^2/\omega_{eg}^2)}{(\omega_{eg}^2-\omega^2)^2+\gamma_e^2\omega^2}\,, \tag{9.6}$$

where $g_i = 2J_i + 1$ is the multiplicity of the state $|i\rangle$ with quantum number J_i. The ratio $(2J_e+1)/(2J_g+1)$ is thus the weighted strength of the different line transitions, *cf.* Eq. (6.20) and Eq. (7.14).

Using the free-space wavelengths $\lambda_{\text{red}} = 1057\,\text{nm}$ and $\lambda_{\text{blue}} = 780\,\text{nm}$ for the red- and blue-detuned trapping fields[3], it is sufficient to only evaluate the sum in Eq. (9.6) over the four exited states given in Table 9.1 with relevant parameters.

LEVEL	λ_{eg} [nm]	$\gamma_e/2\pi$ [MHz]
$6^2P_{1/2}$	894.347	4.575
$6^2P_{3/2}$	852.113	5.234
$7^2P_{1/2}$	459.317	0.126
$7^2P_{3/2}$	455.528	0.293

Table 9.1.: *The four excited states used to calculate the TOF-based dual-color dipole trap potential. $\lambda_{eg} = c/2\pi\omega_{eg}$ is the free-space wavelength. The values were taken from [A. Kramida* et al., *2015].*

In order to create a 3D confinement of the atoms, the red trap is configured as a SW with quasi-linear y polarization, whereas the blue trap is simply a RW with quasi-linear polarization oriented along the vertical x-axis, and thus rotated by 90° with respect to the red trap. With these settings, we obtain the TOF-based dual-color dipole trap potential as shown in Fig. 9.5(a),(b) for the transverse and longitudinal cross sections of the TOF respectively. The minima of the potential are clearly seen to be located on the horizontal y-axis close to the fiber surface, and separated by $\lambda_{\text{red}}^{\text{TOF}}/2$ along the fiber axis as expected for a SW which has nodes and antinodes repeating every half wavelength. In this configuration the dipole trap becomes a 1D optical lattice, consisting of two periodic atomic strings aligned parallel to the TOF.

Because the atoms are only confined in the yz-plane, we see that we have three options for the orientation of the probe field: (i) quasi-linearly polarized parallel to the atomic plane, (ii) quasi-linearly polarized perpendicular to the atomic plane, (iii) everything in between.

3 From now on, these fields are simply referred to as either the red (blue) trap, trapping field, beam, laser, *etc.*

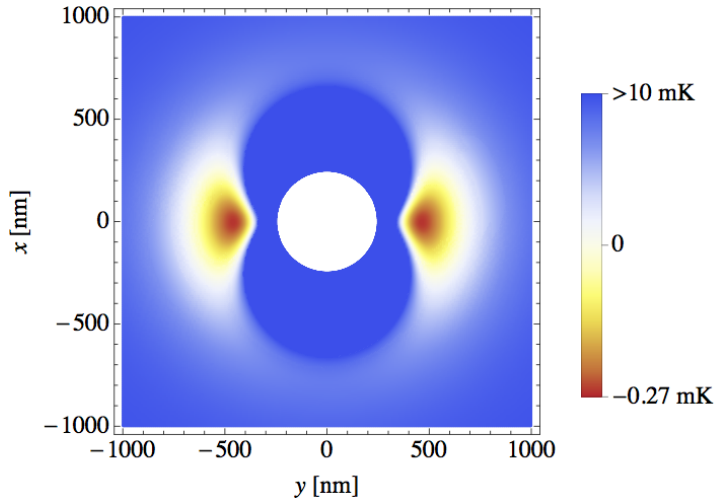

(a)

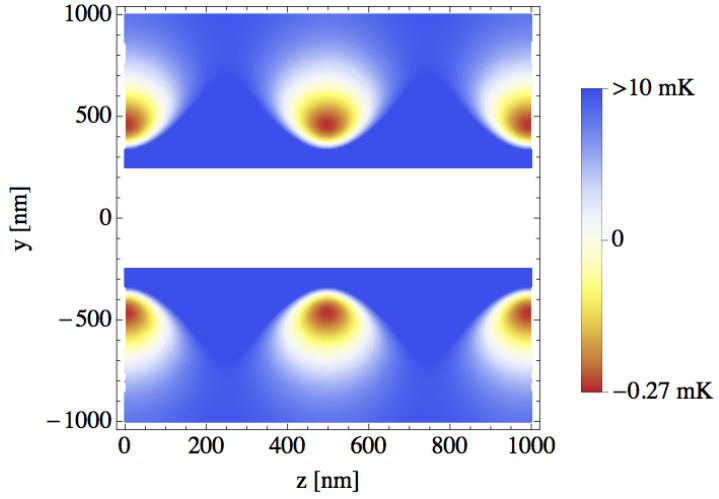

(b)

Figure 9.5.: *2D plot of the TOF-based dual-color dipole trap potential for (a) the transverse xy-plane and (b) the longitudinal yz-plane of the TOF. The colorbar represent the value of $U_{trap}(\mathbf{r})$, with red colors used for $U_{trap}(\mathbf{r}) < 0$ (attractive potential) and blue colors are used for $U_{trap}(\mathbf{r}) > 0$ (repulsive potential). The white area indicates the TOF. Calculated for $n_{co} = 1.45732$, $n_{cl} = 1$, $a = 250\,\text{nm}$, $P_{blue} = 14\,\text{mW}$, and $P_{red} = 1.3\,\text{mW}$, which are all typical values used in the lab.*

In order to distinguish between the first two options, we will occasionally refer to (i) as probing along the strong coupling axis (SCA), and (ii) as probing along the weak coupling axis (WCA).

The potential gradient between the minima and the fiber surface is observed to be quite steep, due to the blue trap repulsive barrier, whereas it is more shallow on the other side of the minima facing away from the TOF. This is more evident in Fig. 9.6, where the solid yellow curve is the trap potential U_{trap} along the y-axis for $x = z =$

0. Together with U_{trap} is also shown the individual trap potentials U_{dipole} for the red SW (red dashed curve) and the blue RW (dotted blue curve). Fig. 9.6(b) is just a zoom of Fig. 9.6(a) to make the shape of U_{trap} more clear. The trap minimum is observed to be located about 210 nm from the TOF surface and has a potential depth of $U_{\text{min}} = -0.27$ mK corresponding to an AC Stark shift of 35 MHz.

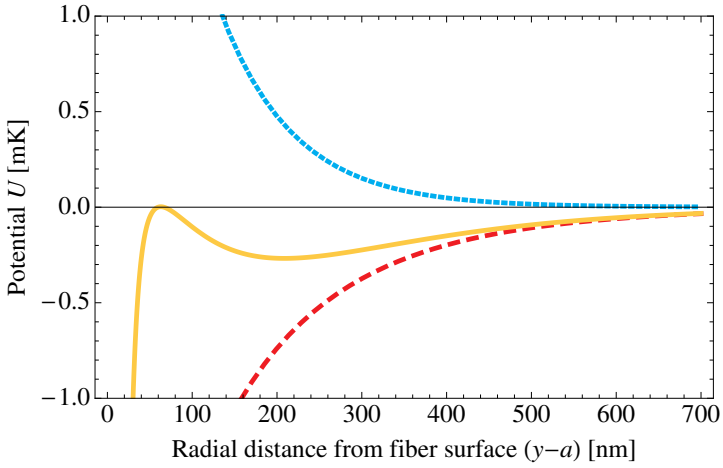

(a)

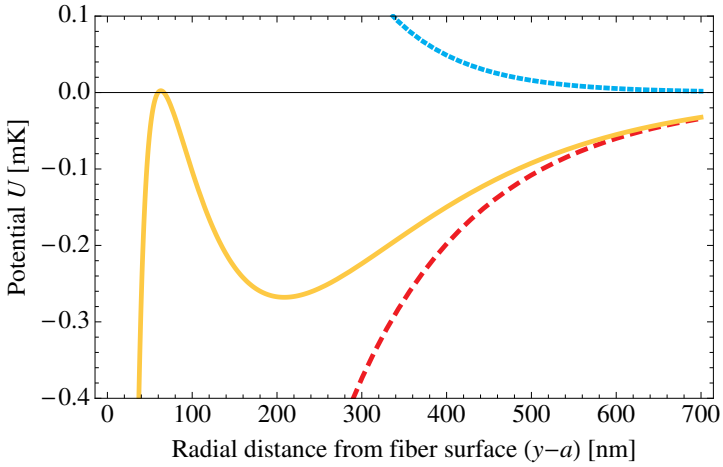

(b) Zoom of (a).

Figure 9.6.: *(a) TOF-based dual-color dipole trap potential as a function of the radial distance from the TOF surface. Blue dotted curve: Repulsive dipole potential provided by the blue-detuned trapping field. Red dashed curve: Attractive dipole potential provided by the red-detuned trapping field. Yellow solid curve: Effective dipole potential with contributions from the blue- and red-detuned trapping fields as well as the van der Waals force near the fiber surface. Calculated for the same TOF parameters as in Fig. 9.5 at $x = 0$ and $z = 0$. (b) Zoom in on potential minimum presented in (a).*

9.4.2 *Collisional blockade*

In order to efficiently load atoms into the potential minima, MOT cooling near the trap sites is required to provide a sufficiently cold reservoir of atoms that can fall into the potential wells. In this respect, the very small volume of the evanescent field dipole trap sites, with a characteristic length scale of $\sim 100\,\mathrm{nm}$, adds an extra layer of complexity. In [Schlosser *et al.*, 2002] it was found that the average number of atoms loaded into a very small dipole trap depends strongly on the loading rate R and three regimes were identified. In particular, the collisional blockade regime has caught much attention in the community working with TOF-based dipole traps, and is reached when the loading rate is within the range

$$\frac{\gamma_{\mathrm{one}}}{2} < R < \frac{\gamma_{\mathrm{two}}}{4}, \tag{9.7}$$

with γ_{one} denoting the one-body loss rate of dipole trapped atoms from collisions with the hot background vapor, and $\gamma_{\mathrm{two}} \propto V_{\mathrm{trap}}^{-1}$ denoting the light-assisted two-body collisional loss rate inversely proportional to the volume of the trap sites [Kuppens *et al.*, 2000]. The collisional blockade regime is characterized by an average occupation of 0.5, and as consequence each trap site will either be empty or contain a single atom only.

Operating with a TOF-based dipole trap for Cs, similar to our setup, [Vetsch *et al.*, 2012] estimated their trap parameters to be described by Eq. (9.7). However, as pointed out by Béguin [2015], it is often taken for granted that a TOF-based dipole trap is automatically characterized by Eq. (9.7), which is of course not true. We will, nevertheless, assume for the remainder of this thesis, that our setup is characterized by the collisional blockade regime. With each trap thus only occupied by at most a single atom at the time, this has the striking effect that the confined atoms are spatially arranged as two truly 1D dilute crystals.

9.4.3 *Laser setup*

Both the red and blue trapping fields are derived from home-build single-mode ECDL in the Littrow configuration operated well above threshold. The red trap laser is split into two beams via a polarizing beam-splitter (PBS) in order to form a SW in the TOF, as illustrated in Fig. 9.7. Before coupled into the two input ports, A and B, to the TOF, each arm of the red SW passes through a pair of WPs in order to make it quasi-linearly y-polarized in the TOF. The power ratio between the two arms is balanced using a HWP before the PBS. The blue trap laser, configured as a RW, only enters the TOF at input port

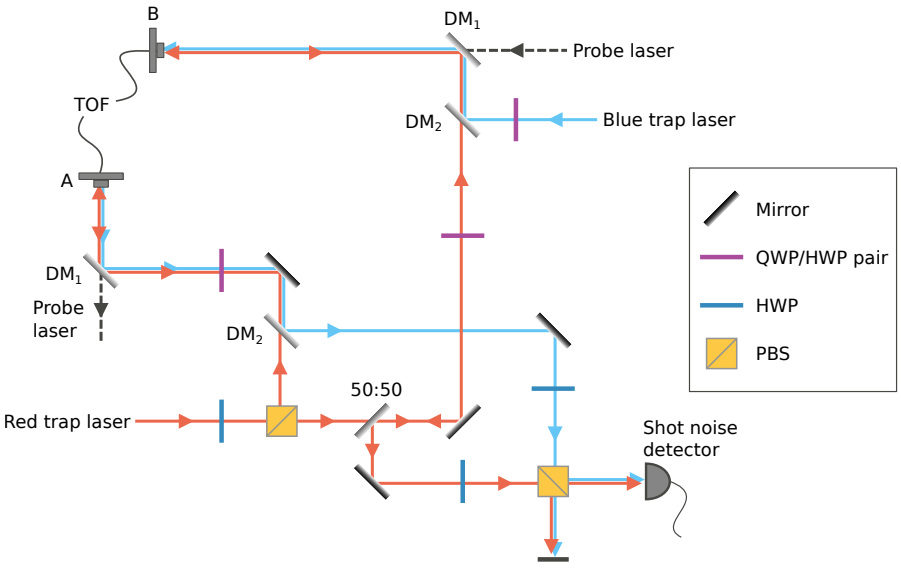

Figure 9.7.: *Dual-color dipole trap laser setup.* DM_1 *is a customized dichroic mirror which efficiently transmits* 852 nm *light (used for probing) and reflects the* 780 nm *and* 1057 nm *light fields for trapping.* DM_2 *is a dichroic mirror for reflecting* 780 nm *light and transmitting* 1057 nm *light (DMLP950 from Thorlabs).*

B. It is overlapped with the red trap laser on a DM after having passed through at set of WPs that makes it quasi-linearly x-polarized in the TOF.

Immediately before entering input port B, both trapping fields are combined with the $\lambda_{\text{probe}} = 852\,\text{nm}$ probe field on yet a DM. Similarly, when the trapping fields exit through port A, they are again separated from the probe beam on a dichroic mirror. The reverse is of course true for the counter propagating red beam.

The blue trap, leaving the TOF at output A, and the arm of the red trap exiting through B, are both directed to a photodetector connected to a spectrum analyzer[4], by which the intensity noise of the two fields can be monitored while running experiments.

In Fig. 9.7 the probe is configured to enter via input B, but we point out that the setup is versatile and the probe can also be made to enter the TOF at input A.

4 *E4405B ESA-E* (9 kHz to 13.2 GHz) from Agilent.

9.4.4 *Laser intensity noise*

In contrast to the repumper and the cooler, neither of the two trap lasers are frequency-stabilized[5]. To have an efficient trap it is, nevertheless, required that they are stable in frequency and intensity. In particular the latter is extremely important, since the effective trap potential (Fig. 9.6) results from a very delicate balancing of the power ratio between the red and blue trapping fields, and even slight changes in this ratio has a dramatic effect on the shape of U_{trap}. It is less severe, if the trap powers change together, that is, if their power ratio is kept constant. In this case the shape of U_{trap} is more or less preserved, with the main influence being how deep the trap is. To this end, it could be helpful to split a small fraction of light from the two trapping beams in order to monitor any changes in their optical power. Having a computer controlled motorized HWP in front of a PBS in the optical path of, say, the blue trap beam, would make it possible to change its optical power according to any detected changes in either the blue or red optical powers due to, *e.g.*, mode jumps or slow drifts over the course of the experiment. At the very least, it would be beneficial to record any changes in the optical power of the two trapping fields while performing measurements, since this would allow for to post-selection of data depending on whether the trapping field intensities were stable or not.

As mentioned, the intensity noise on the two trap lasers are monitored with a spectrum analyzer while conducting measurements. An example of the resulting power spectrum for the blue trap laser with large intensity fluctuations is shown as the blue trace in Fig. 9.8(a). The yellow trace is the electronic noise of the detector and the magenta trace is the intensity noise from an ordinary flashlight hitting the detector and producing the same DC photocurrent. Being a thermal light source, one would naively expect the flashlight to yield a thermal distribution in the intensity noise. However, the flashlight is also highly multi-mode. In fact, it emits light into so many modes, that the probability of each mode to be occupied by more than a single photon is much smaller than one. The thermal distribution therefore resembles that of a Poisson distribution and the flashlight can be regarded as a shot noise reference.

The magenta trace in Fig. 9.8(a) for the flashlight, therefore gives a baseline for the shot noise corresponding to a given DC power mea-

5 The $\lambda_{\text{blue}} = 780\,\text{nm}$ trap laser could in principle be locked to the Rb D2 line via Doppler-free polarization spectroscopy in the same manner as the repumper. For the $\lambda_{\text{red}} = 1057\,\text{nm}$ trap laser it is a bit more tricky to find a vapor cell containing a sample with the right transition frequency. It is also not possible to frequency stabilize against any of the other lasers in the lab via a PLL since the frequency difference is simply too high. The best option for the red trap is most likely a cavity lock.

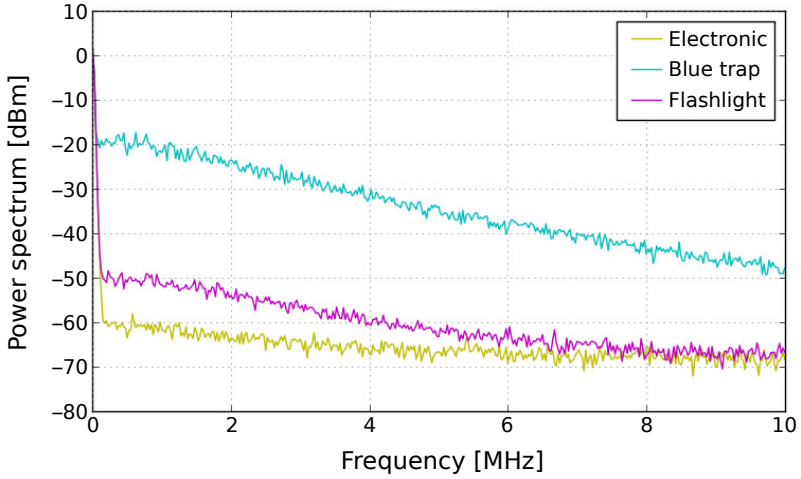

(a) High intensity noise on the blue trap laser. $P_{\mathrm{DC}} = 1.58\,\mathrm{V}$.

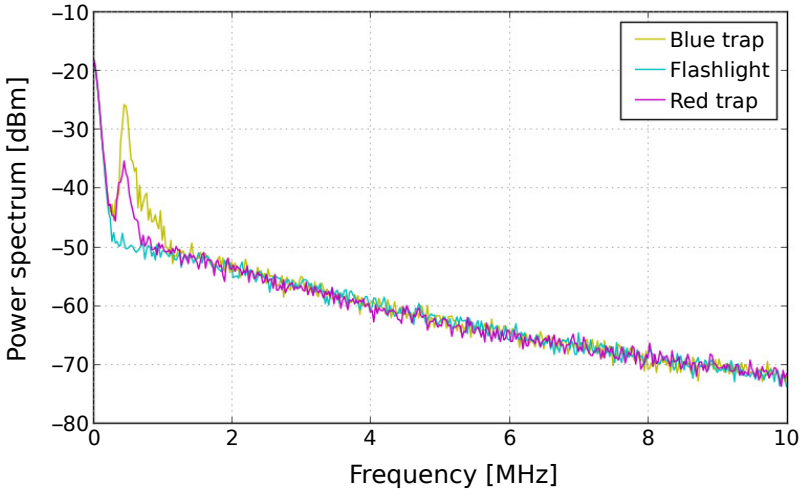

(b) Shot noise limited blue and red trap lasers.

Figure 9.8.: *Laser intensity noise before (a) and after (b) changing the blue trap laser.*

sured at the same time[6]. If a laser source is shot noise limited it should thus give rise to the same power spectrum as that given by a flashlight with an equivalent DC power. This is clearly not the case for the blue trace in Fig. 9.8(a), recorded for the blue trap laser with DC power matched to that of the flashlight, but seen to have intensity fluctuations more than 20 dB above the shot noise level. This trace stems from a previous home-build free-running diode laser source that we used to have for the blue trapping field, but which we ultimately

6 The detector as two output ports, one giving the measured DC power which can be directly plugged into, for example, a voltmeter, and an AC port, containing the measured power fluctuations, and connected to the spectrum analyzer.

replaced[7] due to the large amount of intensity noise as observed in Fig. 9.8(a).

As evident in Fig. 9.8(b), the work in replacing the free-running blue trap laser with an ECDL certainly payed off. With the blue trace now being that of the DC equivalent shot noise from a flashlight, both the red and blue lasers are indeed seen to be shot noise limited. The two peaks near 300 kHz, observed in both the yellow and red traces for the power spectrum of the trapping fields, are currently believed to be caused by a torsional vibration mode in the TOF. Having measured the intensity noise of the lasers before entering the TOF, we have a least confirmed that they are absent before passing through the TOF. The peaks are also absent if the power spectrum is measured before any polarizing optical element after passing through the TOF, which suggest that the intensity noise rises from fluctuations in the polarization of the TOF output beams.

During measurements, the red and blue laser noise are simultaneously detected and displayed on the spectrum analyzer. This yields a trace slightly above the magenta and yellow traces in Fig. 9.8(b), from the higher total optical power hitting the detector, but otherwise it is the same, see Section F.1. If any of the two trapping fields starts to mode jump, it should be noted by the attentive PhD student as an increase in the power spectrum signal and dealt with by appropriately changing the laser current or, as a last resort, the temperature[8].

9.5 THE SMOKING GUN – EVIDENCE OF TRAPPED ATOMS

Although, we have not yet discussed the detection scheme used to probe the atomic state, we would like to show here the absorption signal arising from atoms confined in the dual-color dipole trap. In all our measurements, the two trapping lasers are present at all time in the TOF. To observe if any atoms have been loaded into the dipole trap, an absorptive measurement is performed by the evanescent field of a $\lambda_{\text{probe}} = 852\,\text{nm}$ probe on-resonance with the $|4\rangle \rightarrow |5'\rangle$ hyperfine transition. The resulting signal is shown in Fig. 9.9. Before commenting on the difference between the individual traces, we first present a few general remarks about the three signals and how they where obtained.

After the (presumed) loading of Cs atoms into the dipole trap, the MOT lasers, *i.e.*, the cooler and the repumper, and the MOT coils are turned off. A 10 ms waiting time is then imposed before starting the absorption measurement, in order to ensure that only a negligible

7 For internal use: this was done on April 17 2015.
8 Of course, only after identifying which of the trapping lasers is the noisy one!

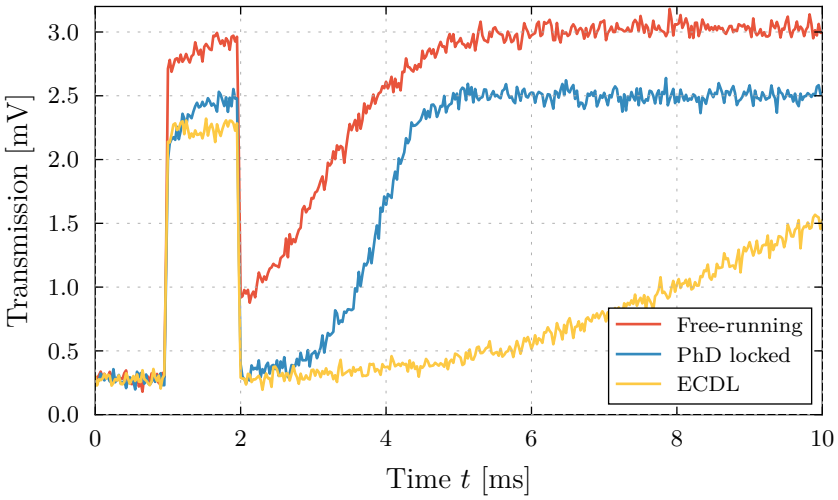

Figure 9.9.: *Probe absorption signal* 10 ms *after loading the dual-color dipole trap and turning off the* MOT *laser beams, obtained for probing along the* SCA *with power* $P_{probe} \approx 3\,\mathrm{pW}$ *below saturation. Measured with the spectrum analyzer in zero span mode and centered at* $\nu = 62.5\,\mathrm{MHz}$, cf. *Chapter 10*.

amount of MOT atoms are probed[9]. In the first millisecond of the measurements in Fig. 9.9, the probe is turned off in order to establish a background level, which is found to be 0.3 mV. As previously mentioned, the atoms will be in the hyperfine ground state $|3\rangle$ after the sub-Doppler cooling. Turning the probe on at $t = 1\,\mathrm{ms}$ thus give a reference signal for full transmission until $t = 2\,\mathrm{ms}$, at which the (external[10]) repumper is turned on, in order to optically pump the atoms from $|3\rangle \rightarrow |4\rangle$. With the probe now on-resonance with the atoms, it is expected to be absorbed, which is clearly observed as the drastic decrease in all three signals at $t = 2\,\mathrm{ms}$. Hereafter, the probe transmission steadily increases as the atoms are either heated out of the trap.

By simply blocking either of the blue or red trapping fields, while keeping all other experimental conditions the same, full transmission of the probe is detected from $t = 1\,\mathrm{ms}$ to $t = 10\,\mathrm{ms}$ (not shown in Fig. 9.9). Hence, absorption only occurs when the trapping fields are present in the TOF, verifying that the three signals in Fig. 9.9, from $t = 2\,\mathrm{ms}$ to $t = 10\,\mathrm{ms}$ must be caused by the absorption of light by atoms confined in the dual-color dipole trap and not simply in the MOT. Elaborate details on the probing of MOT atoms and the different

9 Alone from free fall in the gravity field, the atoms (at rest) should have moved a distance $\Delta x = gt^2/2 \approx 0.5\,\mathrm{mm}$.

10 External in the sense that it is not a guided TOF mode. It is provided by the six fiber couplers for the MOT beams.

characteristics measured for MOT versus dipole trapped atoms can be found in the PhD thesis by Béguin [2015].

We now turn our attention to the differences between the three traces shown in Fig. 9.9. As the figure legend suggests, the red and the yellow signals are obtained for the blue trapping field provided by either the free-running diode laser or the ECDL, respectively. Changing the high intensity noise laser source to a shot noise limited source thus has a tremendous impact on the trap lifetime, as seen from the much slower decay of the yellow trace as compared to the red trace. The light-atom coupling is also greatly enhanced when using the quiet laser source, as observed from the much higher OD of the yellow (ECDL) trace compared to the red (free-running) trace.

The blue signal were acquired with the free-running blue trap laser while monitoring the intensity noise on a spectrum analyzer, *cf.* Fig. 9.8, and, at the same time, keeping it stable by manually tweaking the laser current, which is essentially a semi-automatic PhD lock. This clearly improves both the lifetime and the OD. Ultimately, this indisputable revelation on how destructive a laser source with substantial fluctuations in the intensity is, lead to the decision of changing the free-running diode laser to a more stable ECDL source.

SUMMARY

In this chapter we have presented the optical setup that we use for cooling and trapping atoms. We have introduced the dual-color configuration for the TOF-based dipole trap in which atoms are confined as two 1D crystals along the TOF and only $\simeq 210\,\mathrm{nm}$ away from the hot surface. From intensity noise measurements of the trapping fields, compared to the resulting lifetime of the trapped atoms and the coupling strength to a guided probe field, we have (not surprisingly) seen that the trap quality depends critically on the stability of the trapping fields.

10

DETECTION SCHEME

We utilize a optical heterodyne technique for all the measurements presented in the following chapters. Although, originally designed to exploit the mapping of phase modulations to amplitude modulations, such that any phase shift imprinted on the probe light by the atomic ensemble can be measured, the main focus in this thesis has been to extract the number of photons impinging on our detectors. As we shall see, the heterodyne detection technique is also extremely useful in this respect as very small signals from only a few photons can be resolved.

10.1 OPTICAL HETERODYNE DETECTION

An optical heterodyne measurement utilizes linear mixing of two light fields, a signal beam and a local oscillator (LO) beam, at a BS and subsequent square-law detection (*i.e.*, nonlinear in the field) of the output beam with a photodetector.

10.1.1 *Experimental setup*

In Fig. 10.1 the interferometric setup that we employ for the detection is shown. Both the signal beam and the LO are derived from the same source, loosely referred to as the probe, such that any common mode noise fluctuations cancel in the heterodyne detection. The probe laser is a single-mode $\lambda_{\text{probe}} = 852\,\text{nm}$ home build ECDL operated well above threshold, similar to the cooler and the repumper used for the MOT, described in Section 9.4.3. The laser is frequency stabilized near the $|4\rangle \rightarrow |5'\rangle$ transition exactly like the cooler, *i.e.*, via a PLL using the repumper as a frequency reference (*cf.* Section 9.2). The arms in the Mach-Zehnder interferometer (MZI) are carefully been made to match in length, such that the interferometer is operated at the white light position, in order to reduce frequency and phase noise from the broad emission background of the laser diode.

Unlike in more commonly known optical homodyne technique, the two beams, signal and LO do not share the same carrier frequency. After the probe has been separated from the LO at the entrance of the MZI, it is thus shifted in frequency by $\Omega = 2\pi \times -62.5\,\text{MHz}$,

using an AOM, before sent onto the atoms confined in the TOF-based dipole trap. In practice, we use a HWP and a PBS, instead of a BS, when recombining the output signal from the TOF and the LO, in order to maintain as much of the signal beam as possible. For this reason, it is necessary with the additional pair of HWP and PBS in front of the detector, such that the two fields are mapped onto the same polarization mode as necessary for interference. Again, in order to

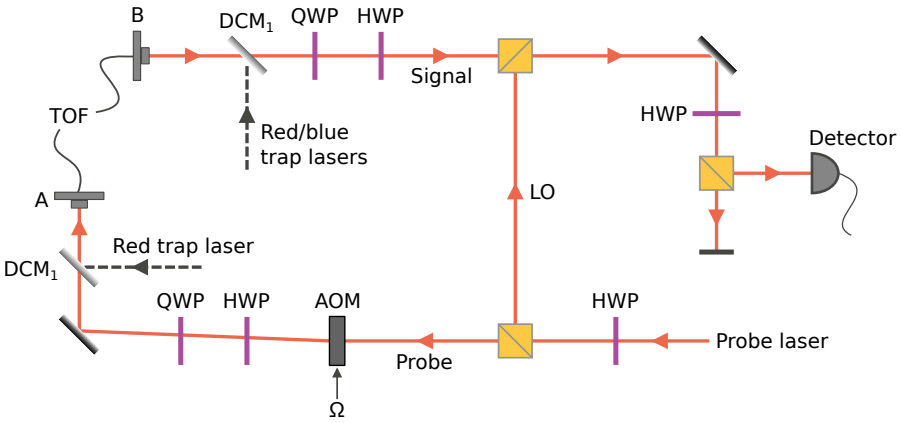

Figure 10.1.: *Simplified illustration of the MZI used to perform optical heterodyne measurements.*

maximize the signal beam, this last HWP is set to reflect $\sim 95\,\%$ of the signal beam (in expense of the LO).

Assuming that the individual field amplitudes and phases are both slowly varying in time and space and thus constant over an optical oscillation period, the two individual fields fields in front of the detector can be written as[1]

$$E_{\mathrm{LO}}(\mathbf{r},t) = \frac{1}{2}\mathcal{E}_{\mathrm{L}}(\mathbf{r})\mathrm{e}^{-i(\omega_{\mathrm{L}}t+\phi)} + c.c. \tag{10.1a}$$

$$E_{\mathrm{signal}}(\mathbf{r},t) = \frac{1}{2}\mathcal{E}_{\mathrm{s}}(\mathbf{r})\mathrm{e}^{-i(\omega_{\mathrm{L}}-\Omega)t} + c.c. \tag{10.1b}$$

Here $\mathcal{E}_i$ denotes the electric field amplitudes, ω_{L} the optical (angular) frequency by which the fields oscillates, ϕ the phase difference between the two fields and Ω the small radio frequency (RF) difference between the LO and the signal field. The resulting field and power ($\propto |\, E_{\mathrm{det}}(\mathbf{r},t)\,|^2$) in front of the detector are then given by

$$E_{\mathrm{det}}(\mathbf{r},t) = E_{\mathrm{LO}}(\mathbf{r},t) + E_{\mathrm{signal}}(\mathbf{r},t) = \frac{1}{2}\mathcal{E}_{\mathrm{d}}(\mathbf{r},t) + c.c.\,, \tag{10.2a}$$

$$|\, E_{\mathrm{det}}(\mathbf{r},t)\,|^2 = \frac{1}{4}\left(\mathcal{E}_{\mathrm{d}}^2(\mathbf{r},t) + \mathcal{E}_{\mathrm{d}}^{*2}(\mathbf{r},t) + 2\,|\,\mathcal{E}_{\mathrm{d}}(\mathbf{r},t)\,|^2\right), \tag{10.2b}$$

with

$$\mathcal{E}_{\mathrm{d}}(\mathbf{r},t) = \mathcal{E}_{\mathrm{L}}(\mathbf{r})\mathrm{e}^{-i(\omega_{\mathrm{L}}t+\phi)} + \mathcal{E}_{\mathrm{s}}(\mathbf{r})\mathrm{e}^{-i(\omega_{\mathrm{L}}-\Omega)t}\,. \tag{10.2c}$$

1 Here we have dropped the vector notation since the two fields reaching the detector are necessarily in the same polarization mode after reflecting off the PBS.

In the following we will drop the explicit notation of the spatial dependence in the field amplitudes and simply set $\mathcal{E}_i = \mathcal{E}_i(\mathbf{r})$.

10.1.2 *Detector response*

Driven well below saturation we can assume the detector output $y(t)$ to be a linear map of the input power $P(t)$ (further details on the linearity are given in next section). We can therefore use the well established theory of linear time-invariant (LTI) systems and express the detector output as the convolution of the input signal and the detector response h (also known as the linear response function) [Hobbs, 2009]:

$$y(t) = (h * P)(t) = \int_{-\infty}^{\infty} h(t')P(t-t')\,\mathrm{d}t'\,. \tag{10.3}$$

Using the convolution theorem

$$\mathcal{F}\{(f*g)(t)\} = \mathcal{F}\{f(t)\}\cdot\mathcal{F}\{g(t)\}\,, \tag{10.4}$$

with $\mathcal{F}\{\cdot\}$ denoting the Fourier transform[2]

$$f[\omega] = \mathcal{F}\{f(t)\} \equiv \frac{1}{\sqrt{2\pi}}\int_{-\infty}^{\infty} f(t)\mathrm{e}^{-i\omega t}\,\mathrm{d}t\,, \tag{10.5a}$$

$$f(t) = \mathcal{F}^{-1}\{f[\omega]\} = \frac{1}{\sqrt{2\pi}}\int_{-\infty}^{\infty} f[\omega]\mathrm{e}^{i\omega t}\,\mathrm{d}\omega\,, \tag{10.5b}$$

we see that Eq. (10.3) can equally well be expressed in the frequency domain known as the transfer function:

$$h[\omega] = \frac{y[\omega]}{P[\omega]}\,. \tag{10.6}$$

Before solving Eq. (10.3) let us first consider the input power given in Eq. (10.2). We see that the first two terms of $|\,E_{\mathrm{det}}(\mathbf{r},t)\,|^2$ entirely consist of rapidly oscillating terms; $\mathcal{E}_{\mathrm{d}}^2 \propto \mathrm{e}^{-2i\omega_{\mathrm{L}}t}$. At present time, no detectors are able to track the extremely fast oscillations of optical fields ($\omega_{\mathrm{L}} \sim 2\pi\times 10^{14}\,\mathrm{Hz}$) and the transfer function necessarily equates to zero at these frequencies. Consequently, we only need to treat the last term in the response function such that:

$$y(t) \propto \frac{1}{2}\int_{-\infty}^{\infty} h(\tau)\,|\,\mathcal{E}_{\mathrm{d}}(t-\tau)\,|^2\,\mathrm{d}\tau\,. \tag{10.7}$$

From Eq. (10.2c) we have

$$\begin{aligned}|\,\mathcal{E}_{\mathrm{d}}(t)\,|^2 &= \left|\,\mathcal{E}_{\mathrm{L}}\mathrm{e}^{-i(\omega_{\mathrm{L}}t+\phi)} + \mathcal{E}_{\mathrm{s}}\mathrm{e}^{-i(\omega_{\mathrm{L}}-\Omega)t}\,\right|^2 \\ &= |\,\mathcal{E}_{\mathrm{L}}\,|^2 + |\,\mathcal{E}_{\mathrm{s}}\,|^2 + \mathcal{E}_{\mathrm{L}}\mathcal{E}_{\mathrm{s}}^*\mathrm{e}^{-i(\Omega t+\phi)} + \mathcal{E}_{\mathrm{L}}^*\mathcal{E}_{\mathrm{s}}\mathrm{e}^{i(\Omega t+\phi)}\,.\end{aligned} \tag{10.8}$$

2 In general the Laplace transform $H[s] = \mathcal{L}\{h(t)\} \equiv \int_0^{\infty} h(t)\mathrm{e}^{-st}\,\mathrm{d}t$ is used in LTI theory. This can be extended to the bilateral Laplace transform, *i.e.*, extending the lower limit in the integral to $-\infty$ from causality reasoning ($h(t<0)=0$), which, since we are only dealing with sinusoidal signals, reduces to the usual Fourier transform with $H[s] = H[i\omega] = h[\omega]$.

The output signal is thus comprised of both direct current (DC) (first two terms) and alternating current (AC) components. By inserting a band-pass filter at the detector output centered around Ω we easily filter out the DC terms as well as unwanted frequencies from potential noise sources. Inserting the remaining AC terms into Eq. (10.7) we obtain the detector output as

$$\begin{aligned} y(t) \propto \mathcal{E}_L \mathcal{E}_s^* \int_{-\infty}^{\infty} h(\tau) e^{-i(\Omega(t-\tau)+\phi)} \, d\tau \\ + \mathcal{E}_L^* \mathcal{E}_s \int_{-\infty}^{\infty} h(\tau) e^{i(\Omega(t-\tau)+\phi)} \, d\tau \\ = \mathcal{E}_L \mathcal{E}_s^* e^{-i(\Omega t+\phi)} \int_{-\infty}^{\infty} h(\tau) e^{i\Omega\tau} \, d\tau \\ + \mathcal{E}_L^* \mathcal{E}_s e^{i(\Omega t+\phi)} \int_{-\infty}^{\infty} h(\tau) e^{-i\Omega\tau} \, d\tau \end{aligned} \tag{10.9}$$

Using the definition of the Fourier transform, Eq. (10.4), we see that we can write the last equality in terms of the response function $h[\Omega]$.

$$y(t) \propto h[\Omega]^* \mathcal{E}_L \mathcal{E}_s^* e^{-i(\Omega t+\phi)} + c.c. \tag{10.10}$$

Additionally, we can rewrite the complex response function in terms of its magnitude $|\, h[\Omega] \,|$ and argument $\theta = \arg h[\Omega]$, and identify the former quantity as the gain function $G(\Omega)$ and the latter as the phase lag between input and output signal. We then finally arrive at

$$y(t) \propto G(\Omega) \mathcal{E}_L \mathcal{E}_s^* e^{-i(\Omega t+\phi+\theta)} + c.c. \tag{10.11}$$

It is thus clear that the output signal will bear all the important information from the input power, here especially the signal field amplitude, that we are interested in for the analysis in the following chapters.

10.1.3 *Photocurrent*

More specifically, we use a homebuild detector[3] designed to have a low electronic noise floor at the beat note frequency Ω. The photodiode[4] is a semiconductor operated in the photoconductive mode, where the arrival of a photon triggers an ionization process by which an electron-hole pair is created and carried away from the depletion region in a characteristic time τ_{min}. The generated stream of photoelectrons is formulated as a photocurrent described by [Grynberg *et al.*, 2010]

$$\langle\, i(t) \,\rangle = e \,\langle\, \Phi_e(t) \,\rangle \,, \tag{10.12}$$

3 Designed by Jürgen Appel.
4 Hamamatsu S5971.

where e is the charge of the electron and the photoelectron flux is given by the number of electrons n_e released per unit time:

$$\langle \Phi_e(t) \rangle = \frac{\mathrm{d} \langle n_e \rangle}{\mathrm{d}t} . \tag{10.13}$$

In practice, of course, the detector has a finite bandwidth $B = 1/2\tau$ and we measure a time average over a time τ of the photocurrent (denoted by an overbar):

$$\langle \bar{i} \rangle = \frac{e \langle \bar{n}_e \rangle}{\tau} . \tag{10.14}$$

The probability of a photon to fire a photoelectron is given by the quantum efficiency of the detector η. In the case where η is close to unity the noise statistics of an arriving photon flux $\Phi_{\mathrm{ph}}(t)$ can be directly carried over to the generated electron flux. The $\langle \cdot \rangle$, in the above equations, is thus to remind us that the photocurrent should be considered as a statistical ensemble average due to the intrinsic fluctuations present in the photon flux arising from its probabilistic quantum nature[5] [Milonni *et al.*, 1988; Milonni *et al.*, 2010].

The input light is, as mentioned earlier, derived from a laser source operated well above threshold. It is thus well described as a coherent state where the photon number n_{ph} is Poissonian distributed bearing the root mean square (RMS) deviation $\delta n_{\mathrm{ph}} = \sqrt{\langle n_{\mathrm{ph}} \rangle}$. Carrying the photon number noise statistics directly over to display a similar distribution for number of photoelectrons, we find for the fluctuations on the photocurrent

$$\delta i = \frac{e \delta n_e}{\tau} = \sqrt{2e \langle \bar{i} \rangle B} , \tag{10.15}$$

most likely familiar to the reader as the shot noise.

It should be mentioned that the light shot noise is not the only contribution to the photocurrent fluctuations. For example, false detection events, caused by background light, give rise to a dark current leading to shot noise similar to that in Eq. (10.15). Also the finite temperature of the detector will add a contribution known as the Johnson-Nyquist noise[6]. Fortunately, all these noise sources are independent of each other and thus add in quadrature. We can therefore get around by grouping them into a single noise variable, embracing all noise contributions but the light shot noise, and simply label it the electronic noise; δi_{en}.

5 In the case where $\eta \ll 1$ the photocurrent still has to be treated as an ensemble average. However, in this case, the inherent fluctuations are caused by the quantized detection resulting in a random sampling of the input flux thus obeying Poisson statistics [Grynberg *et al.*, 2010].

6 For more elaborate details, including more noise sources or photodetection in general, the reader is referred to almost any quantum optics textbook, *e.g.*, [Bachor *et al.*, 2004], or to previous work done in our group, *e.g.*, [Béguin, 2015].

Before returning to the resulting photocurrent for the optical field of interest, Eq. (10.2), we conclude this section by making the following observation. Since the shot noise describes the independent arrival of photons its frequency spectrum is inherently white. Recognizing this as a stochastic process we can linearize the ensemble average of the photocurrent $\langle\, i(t) \,\rangle$ around its mean value such that it is given by

$$\langle\, i(t) \,\rangle = \langle\, i \,\rangle + \delta i(t) \tag{10.16a}$$

with the total noise given by

$$\delta i(t)^2 = \delta i_{\text{en}}^2 + \delta i_{\text{sn}}^2 \,. \tag{10.16b}$$

In this way, both $\langle\, i \,\rangle$ and $\delta i(t)$ are treated as random variables drawn from independent distributions; the former with zero variance and mean value $\langle\, i \,\rangle$ and the latter with zero mean, $\langle\, \delta i(t) \,\rangle = 0$, and variance given by the total noise $\delta i(t)^2$, *i.e.*, including contributions from both the electronic noise[7] and the shot noise, henceforth denoted as δi_{sn}.

10.1.4 *Impinging photon flux*

Relating the measured photocurrent[8] to the impinging photon flux Φ_{ph} we have

$$\langle\, i \,\rangle = e \int \frac{\langle\, \Phi_{\text{ph}} \,\rangle}{\pi w^2(z)} S(r)\, \mathrm{d}^2 r \,, \tag{10.17}$$

where the integration is to be carried out over the sensitive area of the photodiode hit by the beam spot with cross-sectional area $\pi w^2(z)$. In the following, we will assume that $S(r)$, characterizing the spatial dependence of the sensitivity of the detector, gives a flat response over the physical detector area, and that the beam spot size is matched well within this area. $\pi w^2(z)$ is then effectively integrated out and left is the photocurrent directly linked to the overall photon flux

$$\langle\, i \,\rangle = e\eta \,\langle\, \Phi_{\text{ph}} \,\rangle \,. \tag{10.18}$$

It should be well understood, however, that any mismatch lowers the detection sensitivity; (i) If the beam waist is too big compared to the area of the photodiode we obviously loose photons and the input flux

7 Although the electronic noise in general has a non-trivial representation in the frequency domain, this treatment is allowed as long as the LO is strong enough that it dominates the noise, that is to say, the detection is shot noise limited. In practice, one might need to decrease the detection bandwidth to enter this regime.

8 In principle, we do not measure the current directly, but rather the voltage drop over a resistor in series with the photodiode (which is of course proportional to the photocurrent). However, this is not important for the following analysis and we will keep the discussion in terms of the photocurrent. For a nice discussion on this matter we encourage to consult [Béguin, 2015].

will consist of a random sampling of the actual photon flux. This is known as clipping and not only lowers the overall detected signal but also removes any quantum signatures present in the noise statistics. (ii) A beam focused too hard onto the detector, illuminating only a small fraction of the photosensitive area, results in a high density of the photocurrent. This leads to a decrease of the electric field in the depletion region thereby enhancing the electron-hole recombination and slowing the drift. Overall, the detector response becomes non-linear and slow [Hobbs, 2009].

We can rewrite Eq. (10.18) in terms of the optical power using the well known relation

$$\langle \Phi_{\text{ph}} \rangle = \frac{\langle P \rangle}{\hbar\omega} . \tag{10.19}$$

From the discussion in Section 10.1.2 it is clear that the power we should insert is the one given by the beat note between the signal beam and the LO. From Eq. (10.8) we have for the equivalent optical power of the beat note[9]:

$$P_{\text{b}} = 2\sqrt{P_{\text{L}} P_{\text{s}}} \cos(\Omega t + \phi) . \tag{10.20}$$

Trivially derived by writing the complex electric field amplitudes in terms of their magnitude and phase; $\mathcal{E}_i = |\mathcal{E}_i| e^{i\phi_i}$, such that $P_i \propto |\mathcal{E}_i|^2$. The individual phase contributions, as well as the added phase lag from the detector response in Eq. (10.11), have then all been absorbed into a new global phase ϕ.

10.1.5 *Visibility*

As mentioned earlier, the photocurrent should be considered as the ensemble average over all possible light states hitting the detector. In this regard we need to evaluate $\langle P_{\text{b}} \rangle$. For reasons that will become clear later, it is beneficial to consider the ensemble average of the complete input signal, *i.e.*, Eq. (10.8) including the trivial DC terms:

$$\begin{aligned} \left\langle |\mathcal{E}_{\text{d}}(t)|^2 \right\rangle = \left\langle |\mathcal{E}_{\text{L}}|^2 \right\rangle + \left\langle |\mathcal{E}_{\text{s}}|^2 \right\rangle \\ + 2\,\text{Re}\left[\left\langle \mathcal{E}_{\text{L}}^* \mathcal{E}_{\text{s}} e^{i\phi_{\text{noise}}(t)} \right\rangle \right] \cos(\Omega t + \phi) . \end{aligned} \tag{10.21}$$

In writing this expression, we have expanded the global phase into a constant contribution ϕ and a stochastic noise contribution $\phi_{\text{noise}}(t)$ which stems from laser phase noise and path length noise (also known as acoustic noise) in the MZI. As mentioned earlier, the laser phase noise can effectively be suppressed by operating the MZI at the white light position. Furthermore, since we in this work mainly use a coherent averaging time on the sub-millisecond scale, much faster than

9 P_{b} should be understood as the deviation from the (much bigger) average power incident on the detector, and, as such, can of course also become negative.

any acoustic noise processes, only a minimal phase noise influence is expected on the photodetected signal.

Eq. (10.21) can be rewritten using the first-order normalized mutual coherence function[10] [Milonni *et al.*, 1988]:

$$\gamma^{(1)}(\tau_l) = \frac{\left\langle \mathcal{E}_\mathrm{L}\mathcal{E}_\mathrm{s}^* e^{i\phi_\mathrm{noise}(\tau_l)} \right\rangle}{\sqrt{\left\langle |\mathcal{E}_\mathrm{L}|^2 \right\rangle \left\langle |\mathcal{E}_\mathrm{s}|^2 \right\rangle}}, \tag{10.22}$$

with $\tau_l = (l_\mathrm{L} - l_\mathrm{s})/c$ used for the temporal difference between the two fields, which in practice is due to a path length difference in the interferometer. We then have (in terms of optical power)

$$\langle P_\mathrm{d} \rangle = \langle P_\mathrm{L} \rangle + \langle P_\mathrm{s} \rangle + 2\sqrt{\langle P_\mathrm{L} \rangle \langle P_\mathrm{s} \rangle}\, \mathrm{Re}\left[\gamma^{(1)}(\tau_l)\right] \cos(\Omega t + \phi)\,. \tag{10.23}$$

From the definition of the fringe visibility, which describes the degree of overlap between the two field modes, we see that

$$\mathcal{V} = \frac{\langle P_\mathrm{d} \rangle_\mathrm{max} - \langle P_\mathrm{d} \rangle_\mathrm{min}}{\langle P_\mathrm{d} \rangle_\mathrm{max} + \langle P_\mathrm{d} \rangle_\mathrm{min}} = \frac{2\sqrt{\langle P_\mathrm{L} \rangle \langle P_\mathrm{s} \rangle}}{\langle P_\mathrm{L} \rangle + \langle P_\mathrm{s} \rangle}\, \mathrm{Re}\left[\gamma^{(1)}(\tau_l)\right]\,. \tag{10.24}$$

Before running the experiment, we optimize and calibrate the fringe visibility, while having an equal amount of optical power in both arms of the MZI, such that

$$\mathcal{V}_0 = \mathrm{Re}\left[\gamma^{(1)}(\tau_l)\right]\,. \tag{10.25}$$

It is clear from Eq. (10.24), that the genuine visibility $\mathcal{V}$ during the measurement is actually much lower than the calibrated visibility $\mathcal{V}_0$, since the optical power of the signal beam is much weaker than that of the LO; $P_\mathrm{s} \ll P_\mathrm{L}$. Nevertheless, it is fortunately the latter that enters into the expression for the equivalent beat note power, and by inserting Eq. (10.25) into Eq. (10.23) we have

$$\langle P_\mathrm{b} \rangle = 2\mathcal{V}_0\sqrt{\langle P_\mathrm{L} \rangle \langle P_\mathrm{s} \rangle}\cos(\Omega t + \phi)\,. \tag{10.26}$$

10.1.6 *Signal power*

In order to extract the optical signal power, we mix the photocurrent down to baseband, by demodulating[11] it by the beat note frequency Ω, and then time average[12] it over an integer number m of oscilla-

10 In general this is defined as $\gamma^{(1)}(x_1, x_2) = \frac{\langle E^*(x_1)E(x_2)\rangle}{\sqrt{\langle |E(x_1)|^2\rangle\langle |E(x_2)|^2\rangle}}$ for $x_i = \mathbf{r}_i, t_i$. Because the system considered here is a MZI we can set $\mathbf{r}_\mathrm{L} = \mathbf{r}_\mathrm{s}$ and encapsulate the path difference as a time difference given by $\tau_l = (l_\mathrm{L} - l_\mathrm{s})/c$.

11 This can be done either electronically or in the subsequent data analysis. In this work both methods have been used.

12 In the analysis this is carried out as a low-pass filtering, *i.e.*, a boxcar average, by convolving the detector output signal with a normalized uniform distribution with "length" τ.

tion periods; $\tau = 2\pi m/\Omega$ (this effectively determines the detection bandwidth):

$$\begin{aligned}\langle \bar{i} \rangle &= \frac{e\eta}{\hbar\omega}\frac{1}{\tau}\int_0^\tau 2\mathcal{V}_0\sqrt{\langle P_\mathrm{L}\rangle\langle P_\mathrm{s}\rangle}\cos(\Omega t+\phi)\mathrm{e}^{-i\Omega t}\,\mathrm{d}t \\ &= \frac{e\eta\mathcal{V}_0}{\hbar\omega}\sqrt{\langle \bar{P}_\mathrm{L}\rangle\langle \bar{P}_\mathrm{s}\rangle}\,\mathrm{e}^{i\phi}\,. \end{aligned} \tag{10.27}$$

The signal power within the detection bandwidth is then found by taking the modulus square of the photocurrent yielding

$$\langle \bar{P}_\mathrm{s}\rangle = \left(\frac{\hbar\omega}{e\eta\mathcal{V}_0}\right)^2\frac{|\langle \bar{i}\rangle|^2}{\langle \bar{P}_\mathrm{L}\rangle}\,. \tag{10.28}$$

We have previously seen that the photocurrent noise is in direct correspondence to that of the light noise statistics. Exploiting the fact, that the LO is much stronger than the signal; $P_\mathrm{s} \ll P_\mathrm{L}$, we further have that the light shot noise is dominated by the number of LO photons. Using this in the expression for the shot noise, Eq. (10.15), by inserting Eq. (10.18) with the total photon flux replaced by that of the LO, we find

$$\delta i_\mathrm{sn}^2 = e^2\eta\frac{\langle \bar{P}_\mathrm{L}\rangle}{\hbar\omega\tau}\,. \tag{10.29}$$

Together with Eq. (10.16b) we can now use this expression to simplify Eq. (10.28) for the signal power:

$$\langle \bar{P}_\mathrm{s}\rangle = \frac{\hbar\omega}{\tau\eta\mathcal{V}_0^2}\frac{|\langle \bar{i}\rangle|^2}{\delta i^2-\delta i_\mathrm{en}^2}\,. \tag{10.30}$$

The alert reader will notice that $|\langle \bar{i}\rangle|^2$ is not only given by the signal photocurrent but also contains the noise fluctuations as seen from the linearization in Eq. (10.16a). Since the fluctuations on the photocurrent are (mainly) caused by the random arrivals of photons, we can assume that $\delta i(t)$ is ergodic such that a time average of $\langle i(t)\rangle$ equals the ensemble average; $\langle \bar{i}\rangle = \langle i\rangle$. We then have

$$|\langle \bar{i}\rangle|^2 = |\bar{i}|^2 + |\delta i|^2\,. \tag{10.31}$$

To get the true signal power, proportional to the mean value $|\bar{i}|^2$, we should therefore subtract the total noise from the measured photocurrent. We then, finally, end up with the expression

$$\langle \bar{P}_\mathrm{s}\rangle = \frac{\hbar\omega}{\tau\eta\mathcal{V}_0^2}\frac{|\langle \bar{i}\rangle|^2-|\delta i|^2}{\delta i^2-\delta i_\mathrm{en}^2}\,. \tag{10.32}$$

As a final remark, we note that both δi_en and δi are easy measurable, the former by blocking both the signal beam and the LO, the latter by blocking the signal beam only.

10.1.7 *Detector calibration*

In Eq. (10.16b) we gave the detection noise as the sum of the electronic noise of the detector and the light shot noise. In practice there might also be a contribution from additional classical noise on the LO. This adds yet an extra term to the variance, which shall refer to as excess noise. We then have for the total detection noise

$$\delta i^2 = \delta i^2_{\text{en}} + \delta i^2_{\text{sn}} + \delta i^2_{\text{excess}} \,. \tag{10.33}$$

The origin of this extra noise has its roots in several sources. As already mentioned in the beginning of this chapter, the broad emission pattern from the diode laser can lead to fluctuations in the frequency and phase of the laser. Excess noise from this source is suppressed by balancing the MZI such it is operated at the white light position. Another source is laser intensity noise, which we encountered earlier in connection with the blue trap laser, Section 9.4.4. This can be suppressed by doing a balanced detection of the MZI output instead of the "single photodiode" detection can we have sketched so far[13]. And

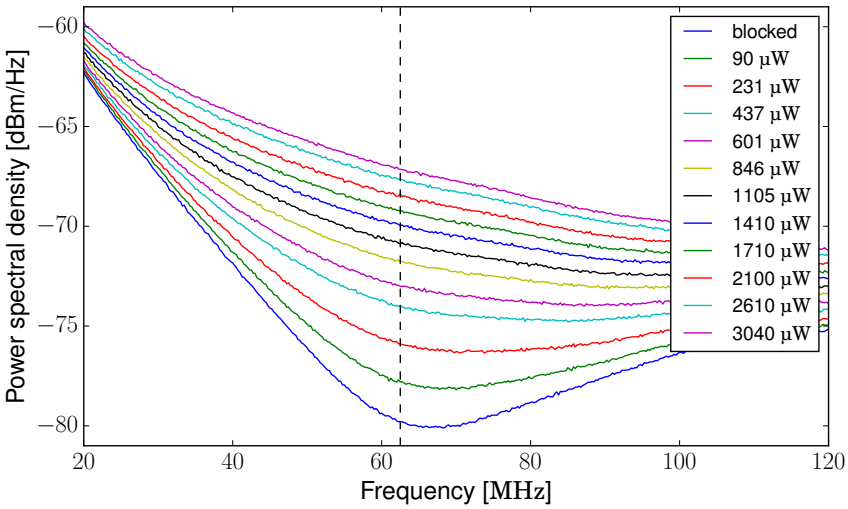

Figure 10.2.: *Power spectral density acquired for a frequency band centered around the beat note frequency* $\Omega = 2\pi \times -62.5\,\text{MHz}$ *indicated by the vertical dashed line. Spectrum analyzer settings: RBW* $=$ *VBW* $=$ $100\,\text{kHz}$, *sweep time* $= 10\,\text{s}$, *each trace is* 10 *power averages.*

then there is the more sketchy acoustic noise contribution, which is essentially everything that affects the path length difference of the MZI. More elaborate details on the three different noise sources mentioned here can be found in the thesis by [Oblak, 2009].

13 For the two detectors used in the atomic Bragg mirror experiment described later, we do balanced detection in the transmission, whereas the reflection detection is as described in this chapter.

Fortunately, these noise sources all have in common that they scale quadratically with the LO power, whereas the shot noise contribution is only linear in the LO power. As such, any excess noise is easy detectable. Before use, we therefore calibrate our detectors to ensure that the photodetection is shot noise limited.

In Fig. 10.2 the power spectral density for one of our balanced photodetectors (used for the transmission detection in the atomic Bragg mirror experiment) is shown for varying optical power of the LO (the signal beam is blocked in all these measurements). The bottom trace

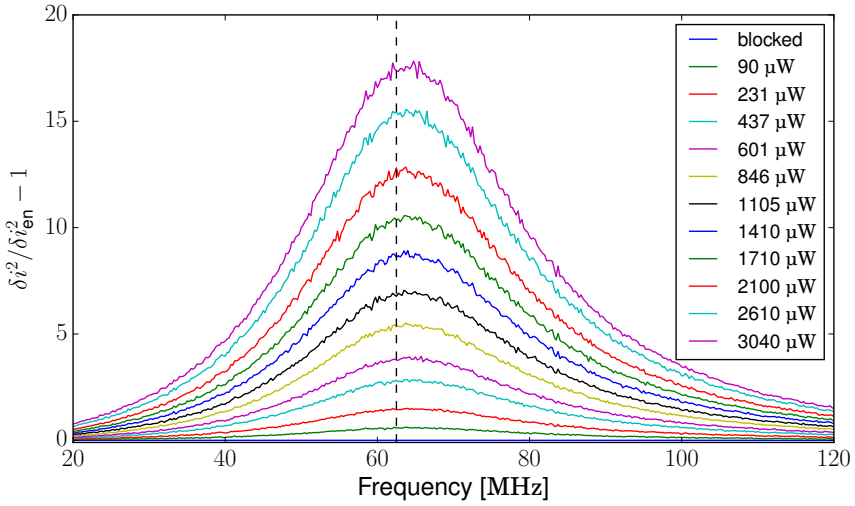

Figure 10.3.: *Scaling analysis of the noise power spectrum. The same data as in Fig. 10.2 after applying Eq. (10.34).*

is the electronic noise obtained when blocking the LO. The photodetector has been designed specially for the detection of the beat note between the signal and the LO, which is evident in the suppressed noise floor near the beat note frequency $\Omega = 2\pi \times -62.5\,\text{MHz}$ (vertical dashed line). To check the scaling of the noise power with the LO power P_L we subtract the electronic noise from the total noise power[14]:

$$\frac{\delta i^2}{\delta i^2_{\text{en}}} - 1 = \frac{\delta i^2_{\text{sn}} + \delta i^2_{\text{excess}}}{\delta i^2_{\text{en}}} = aP_\text{L} + bP_\text{L}^2 \tag{10.34}$$

with

$$\frac{\delta i^2_{\text{sn}}}{\delta i^2_{\text{en}}} \equiv aP_\text{L} \quad \text{and} \quad \frac{\delta i^2_{\text{excess}}}{\delta i^2_{\text{en}}} \equiv bP_\text{L}^2\,. \tag{10.35}$$

Applying Eq. (10.34) to the data in Fig. 10.2 results in Fig. 10.3. Because we are only interested in the frequency component correspond-

14 We recall here the relation

$$x_\text{dBm} = 10\log_{10}\frac{P}{1\,\text{mW}}\,.$$

ing to the beat note, we show in Fig. 10.4 the data in Fig. 10.3 at 62.5 MHz as a function of the LO power. From the linear scaling in

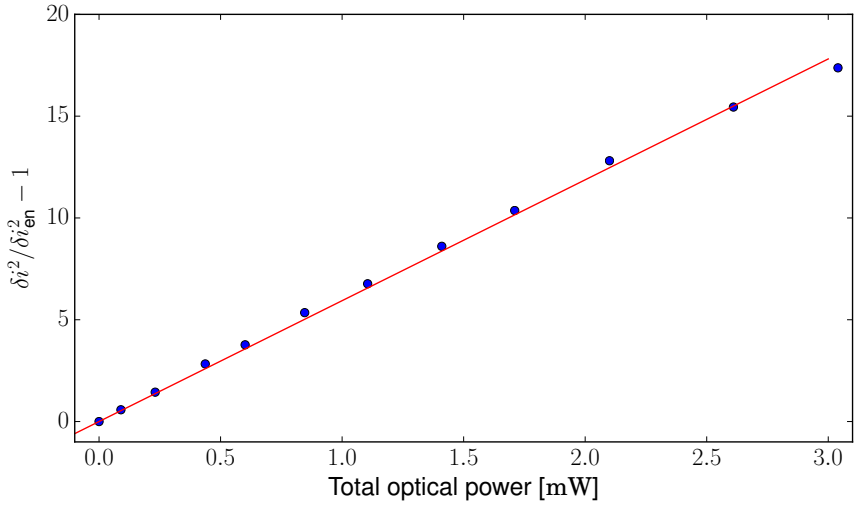

Figure 10.4.: *Scaling analysis of the noise power spectrum at* 62.5 MHz*, same data (blue points) as in Fig. 10.3. Red solid line is a linear fit to the data.*

Fig. 10.4 the photodetector is found to be shot noise limited.

SUMMARY

In this chapter we have presented the optical heterodyne measurement technique used in this thesis work. From a detailed analysis on the measured photocurrent it has been shown how the optical signal power impinging onto the photodiode can be extracted. Finally, we have verified that the detection is shot noise limited by performed a noise scaling analysis.

11

ATOM NUMBER

In this chapter we present our protocol for the determination of the number of trapped atoms confined in the TOF-based dual-color dipole trap, by employing a measurement technique build upon counting the total number of photons scattered off the atoms [Ketterle *et al.*, 1993]. A particularly nice feature of this scheme is that it is insensitive to the light-atom coupling strength and thus provides a robust method for inferring the number of trapped atoms. Elaborate details can be found in the theses by [Christensen, 2014; Béguin, 2015] and in the paper [Béguin *et al.*, 2014], and in the following we therefore restrict ourselves to give only a brief overview of the main concepts in the measurement.

11.1 COUNTING PHOTONS

The measurement protocol utilizes the rate at which atoms, initially in the hyperfine ground state $|4\rangle$, are optically pumped to $|3\rangle$ via the $|4'\rangle$ exited state[1]. Within this simple three-level scheme, we set up a model for the OD as a function of the number of atoms in $|4\rangle$, N_4, while probing on the $|4\rangle \rightarrow |4'\rangle$ hyperfine transition. Due to spontaneous emission events atoms eventually pile up in the $|3\rangle$ state, and N_4 is therefore a dynamical variable during the measurement. As such, it can be related to the input (output) photon flux $\Phi_{\text{in}}(t)$ ($\Phi_{\text{out}}(t)$):

$$\dot{N}_4(t) = -\frac{1}{k}\left(\Phi_{\text{in}}(t) - \Phi_{\text{out}}(t)\right), \tag{11.1}$$

where k is determined from the branching ratio for the radiative decay from $|4'\rangle$ to $|3\rangle$ and $|4\rangle$ given by the CG coefficients. For the two hyperfine transitions the partial decay rates are given by $5\gamma/12$ and $7\gamma/12$, respectively. On average, it thus takes $k = 12/5 = 2.4$ scattering events to transfer an atom from $|4\rangle$ to $|3\rangle$. We stress that this is independent on the initial population distribution in the $|4\rangle$ Zeeman levels, and only depends on the hyperfine line strengths.

The relation between the input and output photon fluxes is given by Lambert-Beer's law, Eq. (6.29):

$$\Phi_{\text{out}}(t) = \Phi_{\text{in}}(t)\mathrm{e}^{-d}, \tag{11.2}$$

1 Quick note: after trap loading the atoms are initially in $|3\rangle$. Here, we have thus assumed that the atoms have already been optically pumped to $|4\rangle$.

where we recall the relation $N_4(t) = \alpha/d(t)$. Inserting this together with Eq. (11.2) into Eq. (11.1) yields the differential equation

$$\dot{d}(t) = -\frac{\alpha}{k}\Phi_{\text{in}}(1 - \mathrm{e}^{-d(t)}) \tag{11.3}$$

for the OD, with solution given by

$$d(t) = \ln\left(1 + \left(\mathrm{e}^{d(t=0)} - 1\right)\mathrm{e}^{-\alpha\Phi_{\text{in}}t/k}\right), \tag{11.4}$$

in assuming a constant input flux. From Eq. (11.4) the transmittance, $\mathcal{T}(t) = \Phi_{\text{out}}(t)/\Phi_{\text{in}}(t) = \mathrm{e}^{-d(t)}$, is easily obtained, and we have

$$\mathcal{T}(t; N_{\text{atom}}, \alpha) = \left(1 + \left(\mathrm{e}^{\alpha N_{\text{atom}}} - 1\right)\mathrm{e}^{-\alpha\Phi_{\text{in}}t/k}\right)^{-1}. \tag{11.5}$$

From a simple time-resolved absorption measurement, we can thus obtain both the initial atom number in $|4\rangle$, $N_{\text{atom}} = \alpha/d(t=0)$, and the OD per atom α.

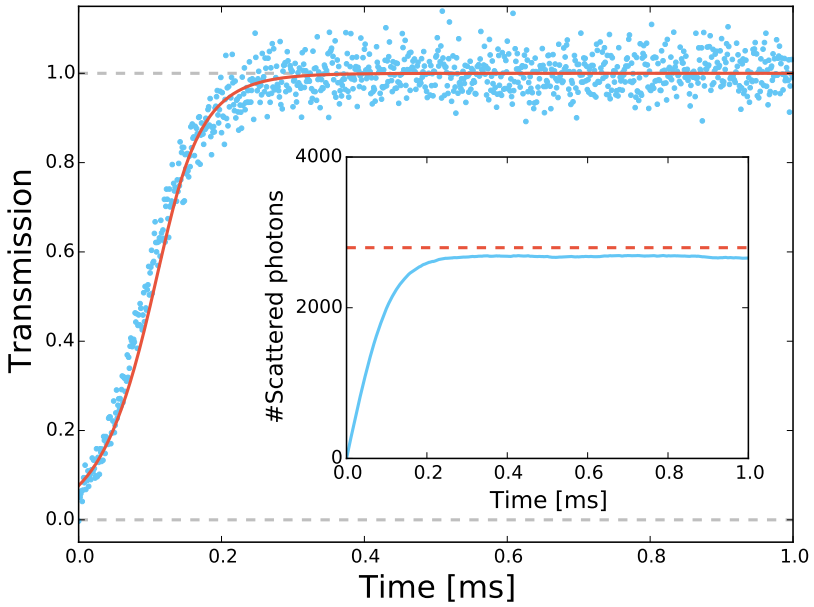

Figure 11.1.: *Blue points: Typical transmission signal average over* $\sim$ 200 *measurement. Red curve: Fitted curve using Eq. (11.5). Acquired with a* 5 pW *resonant probe on the* $|4\rangle \rightarrow |4'\rangle$ *transition aligned along the WCA.*

We typically conduct $\sim$ 200 absorption measurements. Fitting the measurement data with Eq. (11.5), a practical question arises on whether one should fit the average of all the signal traces, shown in Fig. 11.1, or each single transmission signal independently of each other and then afterwards average over the fit parameters N_{atom}, α. Here we have found, that the atom number is rather robust against these two different strategies, whereas significantly different results for the OD

per atom are found when choosing one fitting procedure over the other [Christensen, 2014; Béguin *et al.*, 2014; Béguin, 2015].

The main reason is that systematic effects in the measurement, such as probe detuning and polarization, atomic population distribution in the Zeeman sub-levels, and inhomogeneous broadening of the probe transition by the trapping fields, all influence the speed of the transmission transients from measurement to measurement. When doing a fit to the average transmission signal, these slightly different transients tend to smear out the otherwise sharp transition from almost complete absorption to full transmission. This introduces a bias in the fitted value for α, while N_{atom} is left unaffected, since the number of scattering events required to transfer an atom from $|4\rangle$ to $|3\rangle$ remains the same.

FIT PARAMETERS	SINGLE	AVERAGE	COMMON
N_{atom}	1162	1098	1145
α	0.59 %	0.49 %	0.55 %

Table 11.1.: *Average fit parameters obtained from the three different fit procedures applied to the data shown in Fig. 11.1. The OD per atom α has been extrapolated to the $|4\rangle \rightarrow |5'\rangle$ resonant transition. Histograms of the single trace fit parameters can be found in Section F.2.*

In Table 11.1 we have collected the fitted mean values according to the two different fit procedures applied to the data shown in Fig. 11.1. The relative difference for N_{atom} is seen to be 94 %, whereas it is 83 % for α. The third column yields the results for a combined fit strategy, where α is constrained to take on a global value in all the single trace fits, and only N_{atom} is allowed to vary between measurements. Compared to dispersive phase shift measurements, a discrepancy of ~ 25 % is found for the OD per atom with a tendency towards lower values when inferred from the atom number measurement as described here [Béguin *et al.*, 2014].

In the remainder of the thesis, we will be taking $N_{\text{atom}} = 1300$ and $\alpha_0 = 0.51$ % for the on-resonant OD per atom for the $|4\rangle \rightarrow |5'\rangle$ transition when probing along the WCA, as reference values when estimating saturation intensities and the like.

Part IV

AN ATOMIC MIRROR

12

TURNING A DILUTE ATOMIC STRING INTO A MIRROR

A large part of this PhD study has been centered around Bragg scattering off the atomic crystal confined in the TOF-based dual-color dipole trap. This was originally motivated by a proposal from our (theoretical) colleague Ivan Iakoupov on the implementation of a phase gate in an atomic ensemble coupled to a waveguide by combining Bragg scattering with electromagnetically induced transparency (EIT) [Iakoupov, 2013] (details on how EIT can be used to aid Bragg scattering are given in Appendix G).

Before presenting the experimental results, we here recapture the physics behind Bragg scattering and discuss two different schemes for turning an unstructured atomic ensemble into a Bragg mirror via optical pumping.

12.1 BRAGG SCATTERING

Bragg scattering can be understood by considering the reflection off a string of atoms where each atom behaves as a point scatterer. If the atomic sample is optically thin, and all the atoms couple identically to the incoming light field, the total electric field reflected off the atoms can be described as the sum of all the individually scattered fields having the same amplitude A:

$$E_{\text{ref}} = A\mathrm{e}^{-i\omega t}\sum_{n=0}^{N-1}\mathrm{e}^{i\phi_n}, \tag{12.1}$$

with $\phi_n = \mathbf{k}\cdot\mathbf{r}_n$ being the spatial phase of the field reflected off the n'th atom out of a total of N atoms.

12.1.1 *Randomly spaced atoms*

The intensity of the reflected field is given by the norm squared of Eq. (12.1):

$$\begin{aligned} I &= |A|^2 \sum_{n=0}^{N-1} e^{i\phi_n} \sum_{m=0}^{N-1} e^{-i\phi_m} \\ &= |A|^2 \sum_{n=m}^{N-1} e^{i(\phi_n-\phi_m)} + \sum_{n\neq m}^{N-1} e^{i(\phi_n-\phi_m)} . \end{aligned} \tag{12.2}$$

If the spacing between the atoms is randomly distributed, as illustrated in Fig. 12.1(a), the phases in the last sum will add incoherently and hence equate to zero. We then have

$$I = |A|^2 N . \tag{12.3}$$

That is, for an optical thin sample the reflected intensity scales with the number of scatterers. This result could also have been obtained from Lambert-Beer's law given in Eq. (6.29):

$$\Phi_{\text{out}} = \Phi_{\text{in}} e^{-d} , \tag{12.4}$$

written here in terms of the input and output photon flux, Φ_{in} and Φ_{out}. For the thin optical sample: $d \ll 1$. We can therefore Taylor expand the exponential to first order in the OD, d, from which we find

$$\Delta\Phi = \Phi_{\text{out}} - \Phi_{\text{in}} = -d \propto N . \tag{12.5}$$

The missing number of photons thus scales linearly with the number of scatterers. For isotropic scattering, the back-scattered photon flux

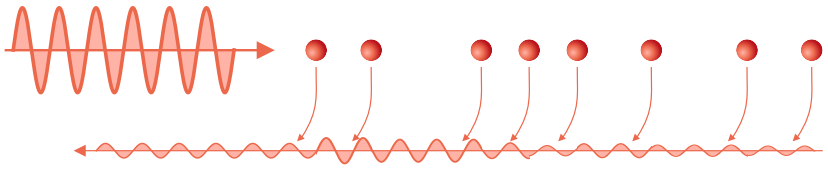

(a) Unstructured atoms. The back-scattered field amplitudes have random phases.

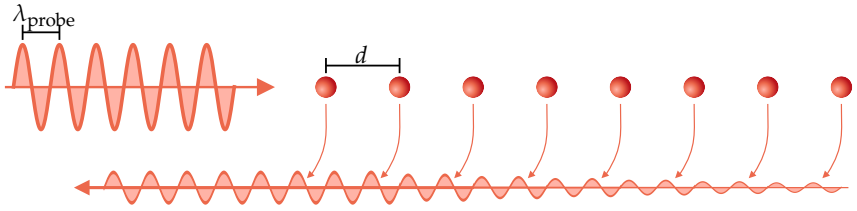

(b) Structured atoms. The back-scattered field amplitudes are in phase.

Figure 12.1.: *Reflection field off a string of atoms (red balls). Left going waves are incident on the atoms. Right going waves are back-scattered off the atoms.*

then likewise scales with N in agreement with the result obtained in Eq. (12.3).

12.1.2 *Regularly spaced atoms*

Let us now consider the case where the atoms are evenly spaced by a distance d. In this case, the reflected field, Eq. (12.1), can we written as

$$E_{\text{ref}} = A\mathrm{e}^{-i\omega t}\sum_{n=0}^{N-1}\mathrm{e}^{in\Delta\phi}\,, \tag{12.6}$$

where

$$\Delta\phi = |k|2x = \frac{2\pi}{\lambda}2d\sin\theta\,, \tag{12.7}$$

is the phase difference between fields reflected off neighboring atoms, and θ is the angle between the incoming wavevector $\mathbf{k}$ with modulus $|k| = 2\pi/\lambda$ and the normal to the line of atoms, *cf.* Fig. 12.2. The

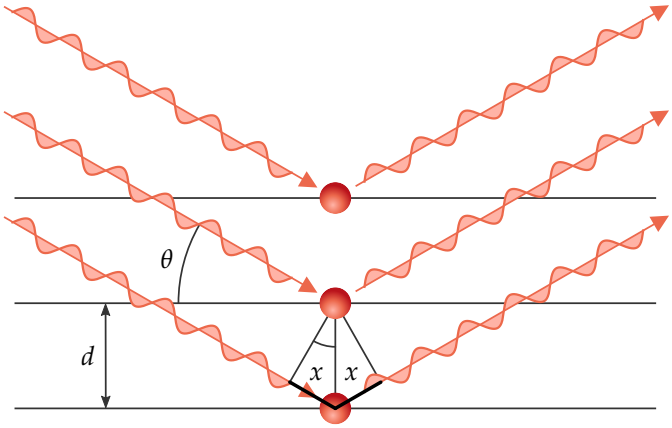

Figure 12.2.: *Reflection off a string of atoms. Wavy lines illustrates the incoming field from the left and the reflected field to the right. Red balls symbolize single atoms separated by a distance d. The accumulated phase of the field reflected off the bottom atom with respect to the field reflected off the middle atom corresponds to the longer travel distance given by $2x$ as indicated by the thick black lines.*

sum is now a geometric series and Eq. (12.6) reduces to [Riley *et al.*, 2006]:

$$\begin{aligned} E_{\text{ref}} &= A\mathrm{e}^{-i\omega t}\frac{\mathrm{e}^{iN\Delta\phi}-1}{\mathrm{e}^{i\Delta\phi}-1} \\ &= A\mathrm{e}^{-i\omega t}\mathrm{e}^{i(N-1)\Delta\phi/2}\frac{\mathrm{e}^{iN\Delta\phi/2}-\mathrm{e}^{-iN\Delta\phi/2}}{\mathrm{e}^{i\Delta\phi/2}-\mathrm{e}^{i\Delta\phi/2}} \\ &= A\mathrm{e}^{-i\omega t}\mathrm{e}^{i(N-1)\Delta\phi/2}\frac{\sin(N\Delta\phi/2)}{\sin(\Delta\phi/2)}\,. \end{aligned} \tag{12.8}$$

Taking the norm squared to obtain the reflected intensity we get:

$$I = |A|^2\frac{\sin^2(N\Delta\phi/2)}{\sin^2(\Delta\phi/2)}\,. \tag{12.9}$$

The reflected intensity is maximized when the reflected fields add in phase, *i.e.*, when $\Delta\phi = 2\pi m$, for integer m, from which we obtain:

$$I_{\max} = |A|^2 N^2 . \tag{12.10}$$

The intensity thus scales quadratically with the number of scatterers when an optically thin sample of atoms are periodically spaced such that the reflected field amplitudes add coherently and interfere constructively, see Fig. 12.1(b). This result is in stark contrast to what we found for a randomly distributed string of atoms, and we see that the intensity can be enhanced by a factor of N in the perfect arrangement. From Eq. (12.7) it follows that the expression

$$d \sin\theta = m\frac{\lambda}{2} \quad \text{for integer } m , \tag{12.11}$$

should be satisfied, which is the well-known Bragg condition.

IN THE TOF GEOMETRY For our inherently 1D system $\theta = \pi/2$ and the Bragg condition (12.11) reduces to

$$d = m\frac{\lambda^{\mathrm{TOF}}_{\mathrm{probe}}}{2} \quad \text{for integer } m . \tag{12.12}$$

The attentive reader will remember that the spacing between the TOF-trapped atoms is given by the red trap wavelength $d_{\mathrm{trap}} = \lambda^{\mathrm{TOF}}_{\mathrm{red}}/2$. With an atomic sample length of $\sim 1\,\mathrm{mm}$ the incommensurate ratio $\lambda^{\mathrm{TOF}}_{\mathrm{red}}/\lambda^{\mathrm{TOF}}_{\mathrm{probe}}$ allows us to treat the atomic crystal as completely unstructured leading to negligible reflection as shown in a previous experiment by [Reitz *et al.*, 2014]. To turn the atoms into an effective Bragg mirror we facilitate the configurable internal spin states to burn a grating via optical pumping. In the following sections we will go through two different schemes that we have employed to create a dilute yet rather efficient atomic mirror.

12.2 VERSATILE SPIN GRATING

Starting with all atoms in the same initial state $|4\rangle$, the key idea is to form a SW along the atomic crystal by sending two counter-propagating beams, derived from the same laser source and with free-space wavelength, $\lambda_{\mathrm{struct}}$, into the TOF. If $\lambda_{\mathrm{struct}}$ is tuned close to an atomic resonance, atoms located at the intensity maxima of the SW, *i.e.*, at the antinodes, are prone to be optically pumped out of their initial level and into the state $|3\rangle$ transparent to the light field[1], see Fig. 12.3. If the atomic sample is afterwards probed by a light field with matching wavelength to that of the SW structuring pulse, $\lambda_{\mathrm{probe}} \approx \lambda_{\mathrm{struct}}$, only atoms left in $|4\rangle$ contributes to the scattering and the Bragg condition, given by Eq. (12.12), is automatically met.

1 Commonly referred to as a dark state.

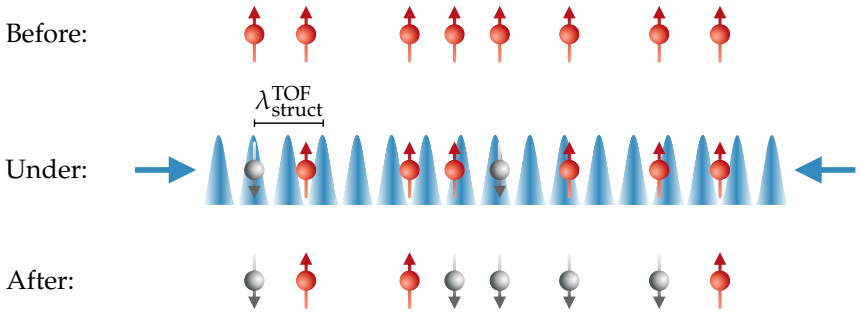

Figure 12.3.: *Internal state of the atoms before, under, and after optical pumping with an SW structuring pulse. Red (gray) balls illustrates atoms in the* $|4\rangle$ $(|3\rangle)$ *state.*

12.2.1 *Experimental considerations on the light fields*

For both the structuring and the probing of the atoms the evanescent field of a guided TOF mode is used. It is therefore necessary to be careful about which polarization to chose for the two fields. Should it be quasi-linear parallel or orthogonal to the atomic plane? In the following, this question is answered first for the SW structure pulse and then for the RW probe.

STRUCTURING FIELD For the Bragg condition (12.12) to be fulfilled, the pitch of the structuring pulse should match the wavelength of the probe, and we therefore have $\lambda_{\text{struct}} = 852\,\text{nm}$ for the free-space wavelength of the structuring field. In Section 2.5.1 we discussed the field mode distribution of a SW mode in the TOF. Here, it became

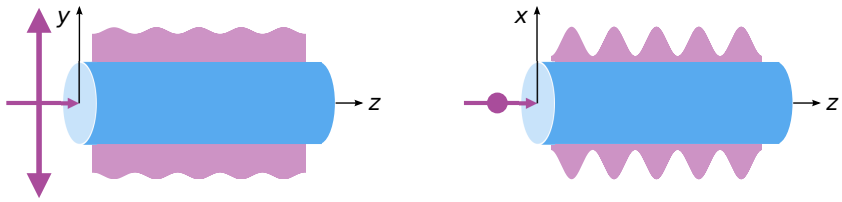

(a) A weakly modulated SW is formed along z for $x = 0$.

(b) A strongly modulated SW is formed along z for $y = 0$.

Figure 12.4.: *Exaggerated sketch of the SW modulation for a quasi-linear polarization mode in the TOF. In the plane where the longitudinal component is present, the net effect is a weakly modulated SW.*

evident that that the fringe contrast of a SW formed in the same plane as the polarization orientation is substantially lower compared to that formed in the perpendicular plane, as illustrated in Fig. 12.4.

For the red SW used in the dual-color TOF-based dipole trap, this is not a problem, since the atoms are confined only at the antinodes of the field, where the longitudinal component vanish. For the structur-

ing pulse, however, a high fringe contrast is needed in order to make sure that atoms sitting in the SW nodes are not optically pumped. In Fig. 12.5 the intensity distribution along the TOF axis, at the radial distance corresponding to the atomic positions, is shown for the red SW trap beam and the SW structuring pulse with quasi-linear polarization either parallel or perpendicular to the red trap. The atoms

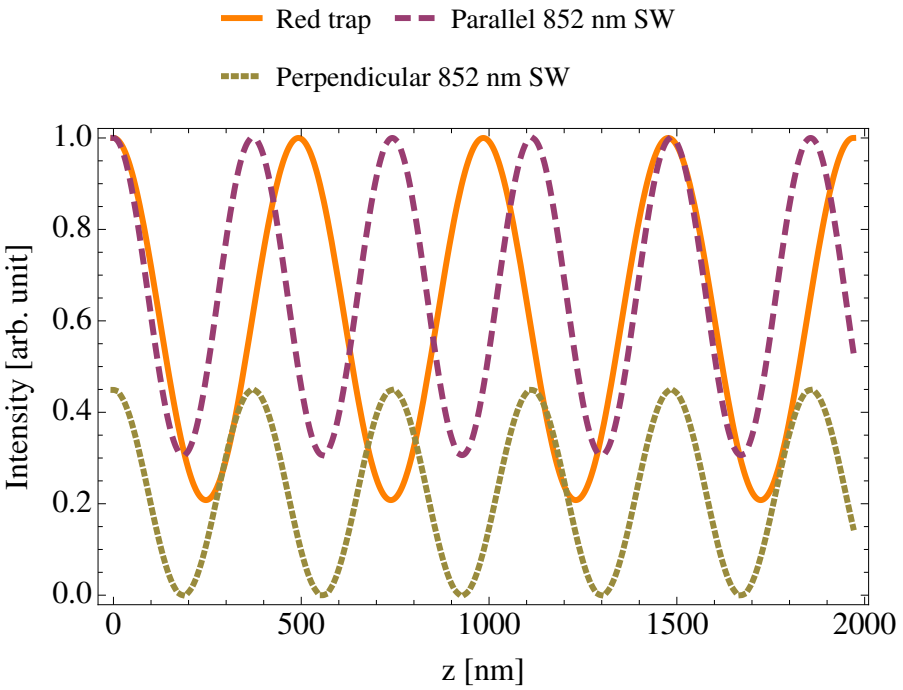

Figure 12.5.: *Intensity distribution along the fiber axis of a quasi-linear HE_{11} SW mode field. Calculated for the parameters $n_{co} = 1.4469$, $n_{cl} = 1$, $a = 250\,\text{nm}$, $x = 0$, $y = 442\,\text{nm}$.*

are trapped at the intensity maxima of the red trap (orange curve). As we already know, the 852 nm SW is incommensurate with the red trap, as seen from the pitch of the purple dashed and dotted green curves compared to the orange curve. For the structuring SW parallel to the red trap the fringe visibility is observed to be only $\mathcal{V} \approx (1 - 0.3)/(1 + 0.3) = 54\,\%$. A significant light field is thus present, even when the minima of the 852 nm parallel SW overlap with the atomic sites, *e.g.*, near $z = 1000\,\text{nm}$. If instead the overall weaker perpendicular SW structuring pulse is considered, the (in principle) 100 % fringe visibility ensures that no atoms are pumped, when its minima overlap with the red trap intensity maxima. For this reason, we chose to configure the structuring field as quasi-linearly x-polarized, and thus perpendicular to the atomic plane.

PROBE FIELD In Section 2.5 it was shown that a RW fundamental mode in the TOF with quasi-linear y polarization, *i.e.*, parallel to the horizontal yz-plane containing the atoms, has a significant longitudi-

nal electric field component at the atomic locations. From the discussion in Section 8.2, we know that this alters the atomic scattering rate such that spontaneous emission into a forward propagating mode is favored over a backward propagating mode. This asymmetry was found in [Le Kien *et al.*, 2014] to yield as much as one order of magnitude difference between the scattering rates into the two modes. It was, however, also found that if the polarization is chosen perpendicular to the atomic plane, where the field is purely vertically polarized at the location of the atoms, *cf.* Fig. 8.1, the scattering rates into either forward or backward propagating modes are equal.

For a measurement, where the sole purpose is to measure an enhancement in the back-reflected photon flux from Bragg scattering off the atoms, Table 8.1 for the scattering rates into the four available TOF modes, seems to suggest that the optimal choice for the probe field polarization is quasi-linear y. It should be kept in mind, however, that these values are calculated in the steady-state regime, and the results might therefore not be representative for the $|4, m_F\rangle$ distribution that we actually have when running the experiment. In fact, in [Reitz *et al.*, 2014] were the back-scattering properties of an unstructured ensemble of Cs atoms, confined in the TOF-based dipole trap similar to ours, were investigated, a higher back-scattering was observed when probing perpendicular to the atomic plane, *i.e.*, using quasi-linearly x-polarized probe light, as compared to parallel probing. These measurement were obtained within the first 200 ns probing, where the atoms can essentially be assumed motionless and only negligible reshuffling of the initial atomic distribution in the Zeeman sub-levels takes place. The contradictory results with respect to that of [Le Kien *et al.*, 2014] can therefore be explained by the different Zeeman distribution of the atoms. In the end, which probe polarization to chose for the most efficient back-scattering rate, therefore depends on the atomic distribution in the Zeeman sub-levels. For all the results presented in the work the probe field was configured as quasi-linearly x-polarized, *i.e.*, perpendicular to the plane containing the atoms.

12.2.2 *Dark scheme*

We have explored two schemes for turning the 1D atomic crystal into a Bragg mirror via optical pumping. These have been termed the *dark* and *bright* schemes, respectively, and are described in the following starting with the dark scheme. The name of choice refers to the atoms being optically pumped from a bright state into a dark state by the SW structuring pulse. Here, the nomenclature bright and dark explicitly refer to the probe laser frequency which is tuned close to resonance with the $|4\rangle \rightarrow |5'\rangle$ transition. The hyperfine ground state $|4\rangle$ is thus regarded as a bright state, whereas the 9.2 GHz lower lying $|3\rangle$

hyperfine ground state is dark in the sense that the probe frequency is too detuned to drive any notable transitions from this state.

All atoms are initially in the dark state, $|3\rangle$, after loading into the TOF-based dipole trap, *cf.* Section 9.4. Before structuring the atoms, the MOT beams are shut off and a $\sim 10\,\mathrm{ms}$ waiting time is imposed to ensure that only lattice trapped atoms are probed. Using the repumper, *cf.* Section 9.2, the atoms are optically pumped for $3\,\mu\mathrm{s}$ from $|3\rangle$ to $|4\rangle$, see Fig. 12.6. Soon after[2], a short, varying between $0.25\,\mu\mathrm{s}$ and $1.0\,\mu\mathrm{s}$,

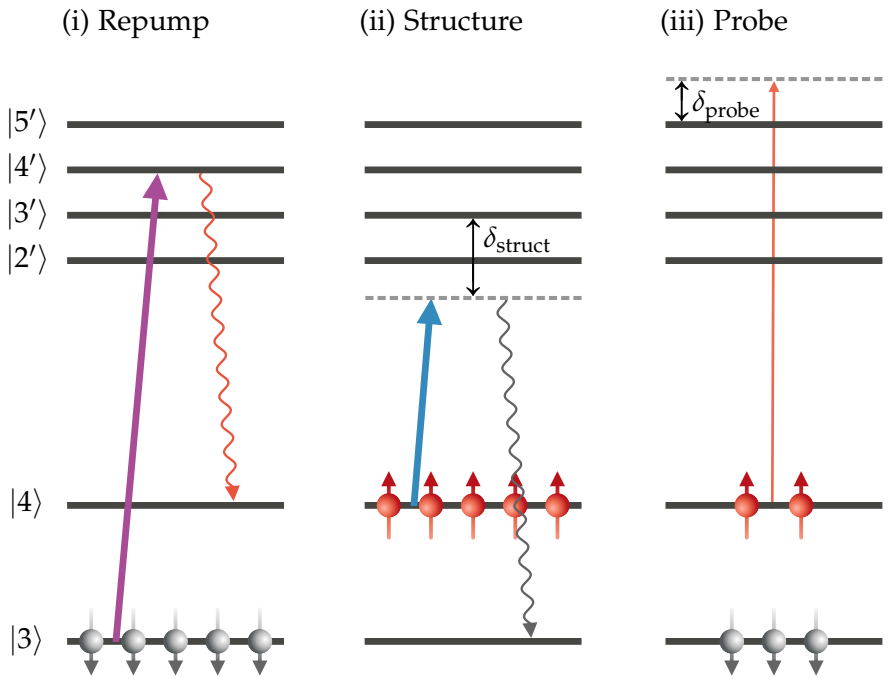

Figure 12.6.: *Dark scheme sequence for creating an atomic Bragg mirror.*

SW structuring pulse is sent onto the now bright atoms. As illustrated in Fig. 12.3, all atoms located near the antinodes of this pulse will be pumped back to the dark state $|3\rangle$, while atoms sitting at a node are left in $|4\rangle$.

With the remaining atoms in the bright state now separated by multiples of half-wavelengths of the structuring pulse, $\lambda^{\mathrm{TOF}}_{\mathrm{struct}}/2 \approx \lambda^{\mathrm{TOF}}_{\mathrm{probe}}/2$, the probe is sent onto the atomic crystal, shortly after the structuring pulse, to measure the reflectance.

It is clear from the discussion in the first part of this chapter (Section 12.1) that the amount of back-scattered light depends very sensitively on how well the atoms are localized as to fulfill the Bragg condition (12.12). Any deviation from the regular half-wavelength spacing leads to a drastic reduction in the reflected intensity which, for an optically thin sample, where found to scale quadratically with

2 The complete time sequence is given in Section 13.2.

the number of atoms for the perfectly arranged ensemble, while for the completely unstructured ensemble it only exhibit a linear scaling with the number of scatterers. In this respect, we would like to make the structuring pump as strong as possible as to ensure that only well-positioned atoms are left in $|4\rangle$. However, this would obviously leave us with less atoms in total to contribute to the coherent back-scattering leading to yet a decrease in the reflected intensity. Apparently, we are facing a situation where we have to choose between many atoms on one side and a high degree of localization on the other side.

We visualize this trade-off by considering the probability p^j_{dark} for an atom, positioned at z_j along the string, to remain in the bright $|4\rangle$ state after the structuring pulse assumed to be in the low-saturation regime:

$$p^j_{\text{dark}} = \mathrm{e}^{-\zeta \cos^2(2\pi z_j/\lambda^{\text{TOF}}_{\text{struct}})}\,, \tag{12.13}$$

with ζ denoting a dimensionless parameter expressing the pumping strength. In Fig. 12.7 this probability is shown for varying ζ resulting in different number of atoms N_4 remaining in the bright state after applying the structuring pulse. Using N_{atom} to denote the total number

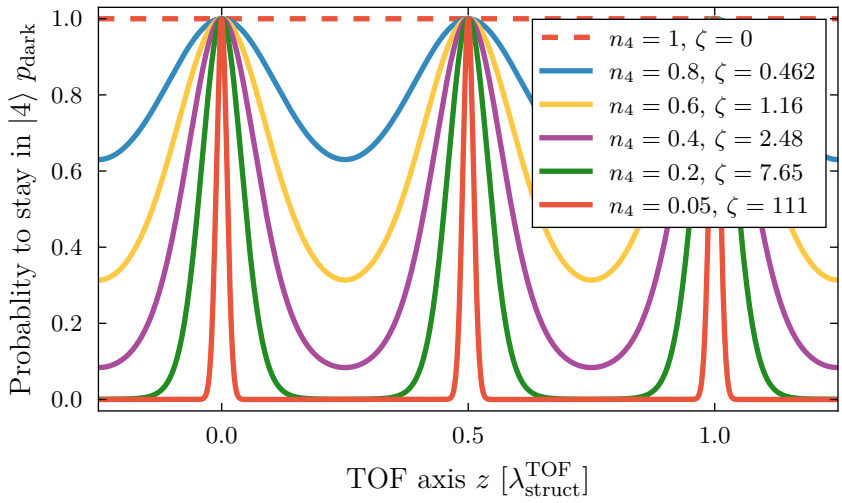

Figure 12.7.: *Probability distribution for an atom to survive the optical pumping into the dark state. The legend states the fraction of atoms remaining in the bright state out of the total number of atoms n_4 and the corresponding pump strength ζ.*

of atoms in $|4\rangle$ before the structuring pulse, we have

$$n_4 = \frac{N_4}{N_{\text{atom}}} \tag{12.14}$$

for the survival fraction of atoms. The values for n_4 in the figure legend are obtained by evaluating the expression

$$n_4 = \frac{\int_{z_0}^{z_1} p^j_{\text{dark}}(\zeta)\,\mathrm{d}z}{\int_{z_0}^{z_1} p^j_{\text{dark}}(\zeta=0)\,\mathrm{d}z}\,, \tag{12.15}$$

for $|z_1 - z_0| > \lambda^{\text{TOF}}_{\text{struct}}/2$. It is seen in Fig. 12.7 that the harder the atoms are pumped into the Bragg structure the more spatial sharp does the survival probability for an atom become to stay in $|4\rangle$, and hence the more localized do the bright atomic wave packets become at the expense of leaving less atoms to contribute to the back-scattering.

As a final remark, before moving on to the bright scheme, we point out that after transferring the atoms into the TOF-based dipole trap, they are distributed among all the nine Zeeman sublevels in $|3, m_F\rangle$ with $m_F = -4, -3, \ldots, +4$. The structuring pulse only couples $|4\rangle$ to the two exited states $|3'\rangle$ and $|4'\rangle$, and since it is quasi-linearly vertically polarized only π transitions, with $\Delta m_F = 0$, are driven. All the Zeeman levels couple differently according to their respective CG coefficients, and especially noteworthy are the stretched levels $|4, m_F = \pm 4\rangle$ that only couple to the $|4'\rangle$ exited state, and $|4, m_F = 0\rangle$ that only couples to the $|3'\rangle$ exited state. Both the power and the frequency of the structuring pulse have been experimentally optimized with respect to the reflectance as shown later in Chapter 15.

12.2.3 *Bright scheme*

We now discuss the bright optical pumping. In this scheme the repumper step is skipped and the atoms are structured by pumping them with the SW directly from the dark state $|3\rangle$ to the bright state $|4\rangle$ as illustrated in Fig. 12.8. Being technical simpler to implement, the disadvantage of this scheme is that it offers less localized atoms. This can be seen by considering the probability for an atom, located at z_j, to be pumped into the bright state. In the low-saturation regime for the SW structuring pump beam this is given by (*cf.* Eq. (12.13))

$$p^j_{\text{bright}} = 1 - \mathrm{e}^{-\zeta \cos^2(2\pi z_j/\lambda^{\text{TOF}}_{\text{struct}})}\,, \tag{12.16}$$

and is plotted in Fig. 12.9 for various pumping strengths ζ. In contrast to the localization offered by the dark pumping scheme in Fig. 12.7, we here have a spatially very broad probability distribution for the atoms to be in $|4\rangle$. For practical purposes we, nevertheless, initially implemented the bright scheme. With the repumper frequency sitting already at the right hyperfine transition, $|3\rangle \to |x'\rangle$, it was straightforward to use this for the SW structuring pulse.

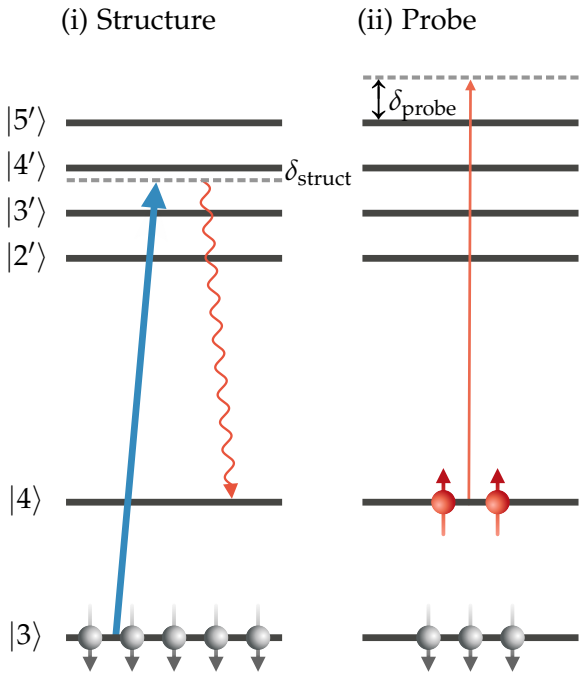

Figure 12.8.: *Bright scheme sequence for creating an atomic Bragg grating.*

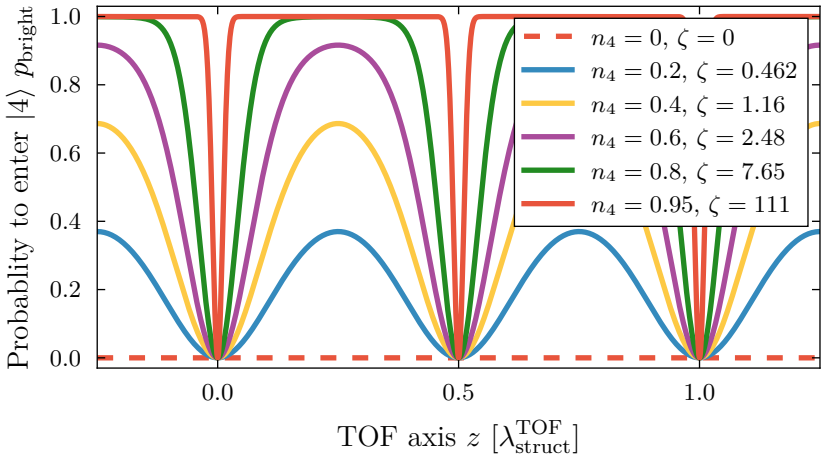

Figure 12.9.: *Probability distribution for an atom to be optically pumped into a bright state. The legend states the fraction of atoms pumped into the bright out of the total number of atoms.*

SUMMARY

In this chapter, we have established the basic physics leading to Bragg scattering and presented two schemes on how to transform a 1D dilute atomic crystal into a Bragg mirror via optical pumping. With the

main theory thus laid out we are ready to continue to the experimental results obtained for the atomic Bragg mirror experiment.

13

EXPERIMENTAL DETAILS

Apart from the structuring, the experimental setup for the bright and dark schemes are identical. In this chapter, we therefore introduce the experimental procedure for preparing and probing the atomic Bragg mirror in general terms that covers both the bright and dark schemes. We start out by describing the setup and the time sequence. Thereafter, we present typical time traces measured of the transmitted and reflected light fields. These signals bear all the information we have about the system and is the foundation of all subsequent analyses presented in the following chapters.

13.1 SETUP

Both the transmitted and reflected light fields are coherently detected[1] by an interferometric heterodyne measurement as described in Chapter 10. Before entering the setup, illustrated in Fig. 13.1, the probe is

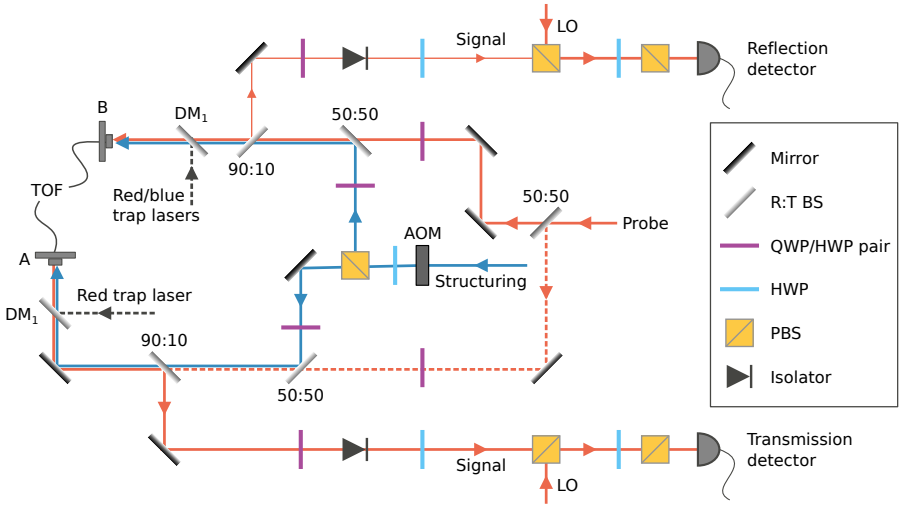

Figure 13.1.: *Illustration of the optical setup for the atomic Bragg mirror experiment.*

therefore split from an LO reference beam and send through an AOM to shift it in frequency by $\Omega = 2\pi \times -62.5\,\mathrm{MHz}$ with respect to the LO frequency.

1 The signal is recorded by a fast oscilloscope: *54832d Infiniium MSO* from Agilent.

With the probe entering the TOF-trapped atomic mirror via input B, the reflected field emerges also via input B. It is then reflected off the probe input path on a 90 : 10 BS. Using a QWP and a HWP in connection with an optical isolator, the reflected field is analyzed[2] either along the V or H component of the quasi-linear polarization in the TOF[3]. The reflected signal field is then combined with the LO on a PBS and send onto the detector. Likewise, the transmitted field, exiting through port A, is detected.

The optical losses from B to the reflection detector is typically given by 50 %. This could be improved by removing the optical isolator which only transmits 70 % of the light. Unfortunately, it is needed to prevent any scattering of the strong LO beam off the detector back onto the atoms. For the atomic mirror experiment, any stray LO photons would most likely not cause severe damage to the quality of the atomic mirror, as the LO is detuned from atomic resonance by ~ 12 linewidths and hence the probability of a scattering event is low. Furthermore, even if an LO photon would enter the TOF and excite an atom in the Bragg grating, it would not cause the atom to undergo a spin flip from the bright state $|4\rangle$ to the dark hyperfine state $|3\rangle$[4]. On top of that, the atomic mirror only depends on the population in the $|4\rangle$ state and not on any coherence between states, and the "only" damage that could be caused by back-scattered LO photons is would thus be to heat atoms out of the trap or the Bragg grating.

The optical isolators were needed in previous measurements and will be needed again in future measurements. For this reason, and for practical purposes, we therefore chose to keep them in the setup. Although not apparent in this thesis, the setup is designed to perform quantum-nondemolition (QND) measurements of the atomic ensemble via the phase shift induced on two light probes passing through the atomic ensemble. In this case, the frequency of the two probe beams are detuned by $\Omega = 2\pi \times \pm 62.5\,\mathrm{MHz}$ from atomic resonance and combined onto a shared LO field *on-resonance* with the atomic transition. The absorption probability of such an LO photon is thus much higher. In addition, if the experiment exploits atomic coherences, the impact of a scattering event is much more damaging than for the atomic mirror measurement, making the need for the optical isolators apparent. For more details on past measurements were the

2 The majority of the measurements presented in this thesis have been obtained while analyzing along V. So unless stated otherwise, this setting should implicitly be assumed in the following.

3 The WPs are set by sending probe light into the TOF at input A (dashed red line in Fig. 13.1). For each of the two polarization modes at the TOF, the analyzer WPs are then turned to minimize the transmission through the optical isolator. The final setting is then obtained by rotating the HWP (mounted between the QWP and the isolator) by 45° to maximize the output.

4 Since we probe on the $|4\rangle \rightarrow |5'\rangle$ transition and the $|3\rangle \rightarrow |5'\rangle$ is a forbidden transition.

dual-color probing was utilized and for future planned experiments please see [Béguin *et al.*, 2014; Béguin, 2015; Christensen, 2014].

The laser used for structuring the atoms is derived from an 852 nm single-mode ECDL, and locked to the repumper via a PLL exactly like the cooler and the probe, *cf.* Section 9.2.2, before sent to the setup. After passing through an AOM, that allows for fast switching, the structuring beam is split into two separate fields on a PBS. With one of the fields entering the TOF at input A and the other at input B a SW is formed at the atoms.

13.2 TIMING

In Fig. 13.2 the general time sequence for a complete experimental run, *i.e.*, cooling, trapping, preparing, and probing a single realization of the atomic Bragg mirror, is shown. The initial MOT loading and sub-Doppler cooling, transferring the atoms into the TOF-based trap, takes $\sim 2\,\mathrm{s}$. Prior to creating the Bragg grating, initial reference measurements of the (fully) transmitted and (zero) reflected fields are established by turning the probe on for a few microseconds while having all the atoms in the transparent state $|3\rangle$. The probe is then turned

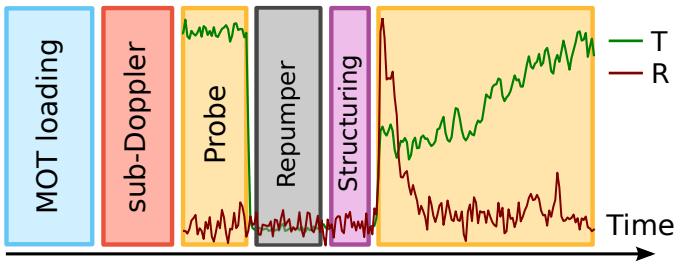

Figure 13.2.: *Time sequence of a single experimental run. Green (red) curve is an illustration of the transmitted (reflected) power (not to scale). The repumper is only present in the dark scheme.*

off and the atoms are structured into a Bragg mirror by either the dark or bright pumping procedure, *cf.* Section 12.2.2 and Section 12.2.3. Immediately after structuring, the probe is turned back on and both the reflected and transmitted fields are continuously measured for up to 40 µs after the SW structuring pulse.

13.3 TYPICAL EXPERIMENTAL SIGNALS

In Fig. 13.3 typical times traces for the reflected and transmitted fields are shown. Each trace is a statistical average of 200 consecutive experimental runs of the photocurrent "intensity", *i.e.*, the square of the photocurrent $\left|\left\langle \bar{i} \right\rangle\right|^2$, obtained within a $B = 1/2\tau = 5.2\,\mathrm{MHz}$ detec-

tion bandwidth[5] (*cf.* Eq. (10.27)). The black curve is the electronic noise, $\delta i_{\text{en}}{}^2$, of the detectors measured by running the experiment while blocking the probe and both LO beams. The blue trace for the

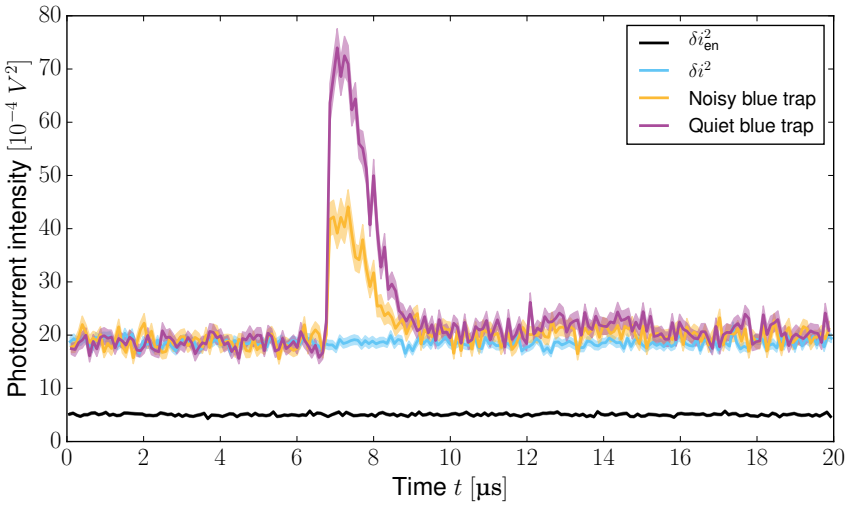

(a) Reflected signal.

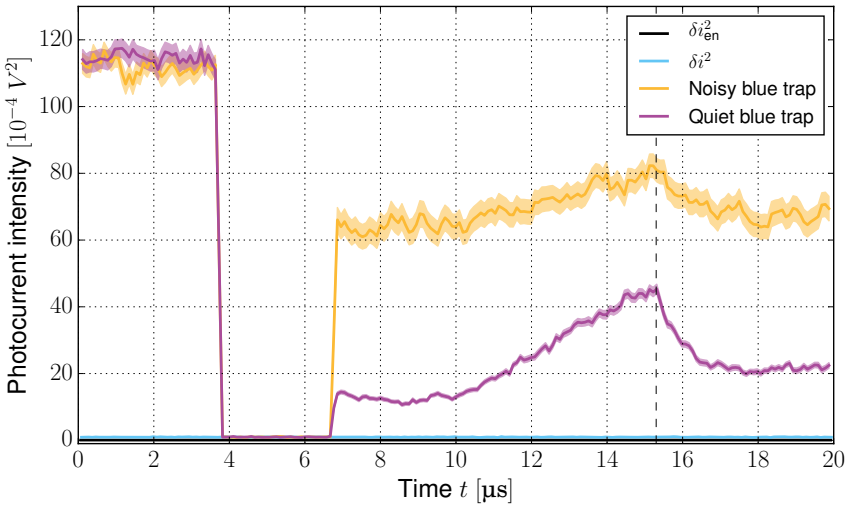

(b) Transmitted signal.

Figure 13.3.: *Simultaneously measured reflected and transmitted signals of light send onto the atomic Bragg mirror as a function of time. The structure were made by employing the bright scheme. The light-colored bands signify the one-sigma uncertainty from the statistical averaging of* 200 *consecutive experimental runs. Measured with a resonant probe with optical power* $P_{probe} = 940\,\text{pW}$.

total noise δi^2 is obtained likewise by blocking the probe beam only. As discussed in Section 10.1.3, the total noise should be dominated

5 Corresponding to a $\tau = 96\,\text{ns}$ boxcar average, or equivalently to 6 oscillation periods of the beat note between the signal beam and the LO.

by the (white) shot noise of the LO as this allows us to linearize the photocurrent around its mean value. In Fig. 13.3(a), for the reflection detector, this is clearly seen to be fulfilled as the total noise is about 6 dB above the electronic noise floor. This level is reached with a typical optical power of the LO given by $P_L \approx 700\,\mu W$. For the transmission detector the total noise is 11.6 dB above the electronic noise floor for $P_L \approx 3.5\,mW$.

The yellow and purple traces are the more interesting ones as they contain the signal of Bragg structured atoms. We will for a moment ignore the yellow trace and concentrate on the purple trace only. As illustrated in Fig. 13.2 for the experimental time sequence, the probe is initially on for 3.7 µs to obtain a reference measurement of the reflected and transmitted fields without resonant atoms. From the transmitted light signal in Fig. 13.3(b) it is clearly the case that this yields a high flat signal as expected for full transmission. For the reflected light, the purple trace is completely buried in the total noise and hence no signal is observed at all in this time interval. This is of course also to be expected, but for the reflected signal one has to be a bit more careful as there could potentially be light reflected off the fiber coupler or other optical elements that could give rise to a background signal. Since this is not the case, we can use the first 6.7 µs of each signal trace in Fig. 13.3(a) (for the reflected signals), as reference measurements for the total noise that is needed in order to calculate the number of detected photons. This is more convenient than using a single total noise measurement (blue trace) since each individual trace automatically keeps track of any drifts in the LO power.

When the probe is turned back on, a clear rise of the purple trace in both the transmitted and reflected signals is observed. The reflected signal peaks close to $75 \cdot 10^{-4}\,V^2$ corresponding to the detection of about $(75-20)/(20-5) = 3.7$ photons on average within the $\tau = 96\,ns$ sample time. To this day, I still find it quite amazing that a detection scheme that relies on adding an extremely weak signal field to a strong reference field can resolve signals on the single photon level. With the extra beauty added to it, that the measurements can be accomplished with all the room lights on and not caring about stray fields from any of the other lasers in the setup. It is true, though, that we need to conduct several experimental runs in order to overcome the signal shot noise with a fractional uncertainty of $\sqrt{3.7}/3.7 = 52\,\%$ in a single shot. The 200 averages used here have proven to be appropriate for most measurements, but 50 to 100 runs are sufficient for quick[6] parameter/configuration checks, although the data is then, of course, somewhat noisier.

After reaching a maximum signal at $t = 7.1\,\mu s$ the light reflected off the atoms quickly decays to nearly zero before it features a small

6 100 measurements takes approximately $100 \times 2\,s = 3.3\,min$.

revival near $t = 14\,\mu s$. A more thorough analysis of the lifetime of the reflectance is carried out in Chapter 16, and we therefore postpone any further discussion on the subject.

Turning our attention back to the transmission signal in Fig. 13.3(b), it rises to only 60 % of its original signal strength when the probe is turned back on at $t = 6.7\,\mu s$, since the light field is now scattered by the atoms. The transmission then first decreases slightly until $t = 8.5\,\mu s$ at which point it starts to increase rather quickly.

The abrupt turning point at $t = 15.3\,\mu s$ is the result of turning on the repumper, which optically pumps the remaining atoms in the dark state $|3\rangle$ to the bright state $|4\rangle$. From this two observations can be made: (i) since the transmission after repumping, near $t = 18\,\mu s$, is higher than that after the reflectance has died out, near $t = 10\,\mu s$, we either have less atoms after repumping, compared to that after the structuring pulse, or the light-atom coupling has decreased over this time interval, (ii) although substantial scattering is evident after repumping the atoms, no notable reflection is observed from these (unstructured) scatterers compared to the significant reflection occurring right after the structuring of the atoms at $t = 6.4\,\mu s$.

We started this section by stating that the signals for the reflection and transmission shown in Fig. 13.3 are typical examples of what we measure. It it certainly true for the reflection signal, but for the transmission signal it is mainly true to the extend that the time sequence for the measurement always follow the recipe given in Fig. 13.2. As it turns out, the temporal dynamics in the transmission signal, after structuring the atoms, is quite rich. A more comprehensive analysis of the dynamics in the system is therefore given separately in Chapter 17 and Chapter 20. This also applies to the reflection off an unstructured ensemble of atoms that will be treated independently in Chapter 14.

13.3.1 *Blue trap laser intensity noise*

Finally, we turn our focus to the yellow trace in Fig. 13.3. What is noteworthy, is that the data belonging to this trace were acquired right before the purple trace data for the exact same experimental parameters. Yet only half the signal is observed in the reflection signal, and in the transmission signal it is clear that much less probe light is scattered off the atoms compared to the purple signal. The reason for this observed difference, can be assigned to the high amount of fluctuations in the free-running blue trap laser intensity, which was still in use when these measurement were conducted. The purple signal in Fig. 13.3 was measured for a intensity noise level of the blue trap laser which lead the blue absorption signal in Fig. 9.9, whereas

the yellow signal in Fig. 13.3 was obtained for a much noisier blue trap intensity, that could not be stabilized by tweaking the laser current while measuring. The yellow signal can thus be related to the same conditions under which the red absorption trace in Fig. 9.9 was acquired.

The free-running blue trap laser was replaced with an ECDL soon after the data in Fig. 9.9 were acquired. Simultaneously with the laser upgrade, we took the opportunity to also modify the setup such that the more promising[7] dark scheme would be used for the optical burning of the Bragg mirror instead of the bright scheme. Therefore, all data acquired under the bright structuring scheme were influenced by the noisy free-running laser source used for the blue trap. For this reason, the bright scheme measurements were not always reproducible even when acquired close in time. This obviously makes it difficult to compare any experimental results obtained within this scheme to other experimental results acquired either with the bright or dark scheme.

For all measurements on the dark scheme, the blue trap ECDL was employed, making the experimental results more reliable and reproducible. When the results are presented in the following chapters it will, however, be apparent that also within the dark scheme the results are not always consistent from day to day. Indeed, during the course of taking data, we got better and better at loading the TOF-based lattice trap and at controlling the polarization of guided TOF modes, which resulted in better and better results, *i.e.*, higher reflections. We will of course let the reader know when results can be compared or not. One thing to notice, however, is that even though the absolute reflectance might not be comparable between measurements taken on different days, relative comparisons can still be made, for example in how the reflectance changes with the frequency of the structuring pulse.

13.4 OPTICAL DEPTH

It can often be instructive to consider the OD since, for example, the OD is directly proportional with the number of scatterers in the low saturation regime as shown in *cf.* Section 6.5. From Lambert-Beer's law, Eq. (6.29), we have

$$\mathcal{T} = \mathrm{e}^{-d}\,, \tag{13.1}$$

where d is the OD, which can then easily be extracted from the transmittance given by

$$\mathcal{T} = \frac{I}{I_0} = \frac{\left|\left\langle \bar{i}_0 \right\rangle\right|^2 - \delta i^2}{\left|\left\langle \bar{i} \right\rangle\right|^2 - \delta i^2}\,, \tag{13.2}$$

7 Compare Fig. 12.7 with Fig. 12.9.

where $\langle \bar{i}_0 \rangle$ is used to denote the reference photocurrent obtained in the first $t = 3.6\,\mu s$ when the reference measurements of the reflection and transmission signals are established. Applying Eq. (13.1) and Eq. (13.2) to the transmission signals shown in Fig. 13.3(b) we obtain Fig. 13.4 for the OD during the measurement. With d being the

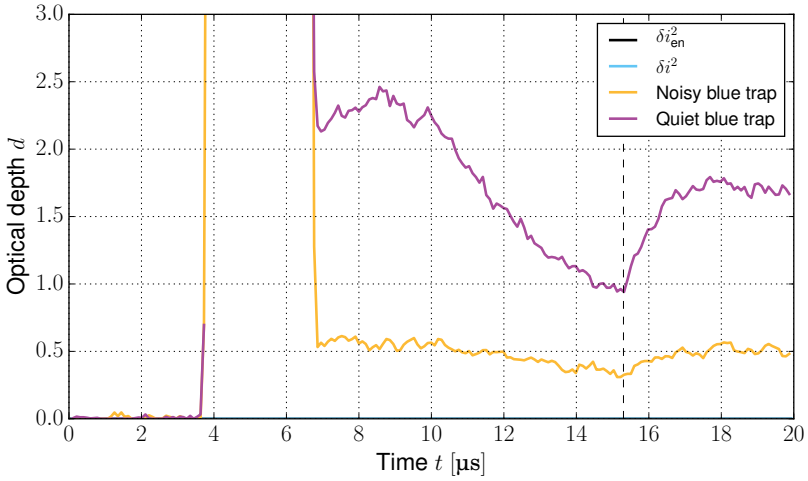

Figure 13.4.: *OD as a function of time. Calculated from the transmission signal in Fig. 13.3(b).*

logarithm of the transmittance, considering the OD also bear the advantage of blowing up small features in the transmitted light, as seen in the purple trace between $t = 7.1\,\mu s$ and $t = 10\,\mu s$. The absence of signal between $t = 3.7\,\mu s$ and $t = 6.7\,\mu s$ when the probe is off, stems from the logarithmic function being undefined at zero. We will leave further discussions on the OD acquired from the Bragg mirror measurements to later, when more careful analysis is carried out. For now, we simply want the reader to be aware that we can extract the OD from the transmission signal and how it is done in practice.

13.5 REFLECTANCE

In order to discuss the efficiency of the created atomic Bragg mirror, we need to calculate the reflectance $\mathcal{R}$, defined as the power ratio between the reflected and incident light onto the atomic crystal:

$$\mathcal{R} \equiv \frac{P_{\text{reflected}}}{P_{\text{incident}}}. \tag{13.3}$$

We have already shown in Eq. (10.32) how the optical power impinging onto the detector can be extracted from the measured photocurrent. Thus, the only thing we need to do, is to take the optical losses l between the atomic crystal and the detector into account in order to obtain $P_{\text{reflected}}$. Typically, we have 50 percent losses between the TOF

output fiber coupler and the detector. In addition to this, 4 % losses from the TOF taper should be included[8]. Using $\epsilon = \eta(1-l)\mathcal{V}_0^2$ for the overall quantum efficiency of the detection, the reflected power is calculated as

$$\langle \bar{P}_{\text{reflected}} \rangle = \frac{\hbar\omega}{\tau\epsilon} \frac{|\langle \bar{i} \rangle|^2 - |\delta i|^2}{\delta i^2 - \delta i_{\text{en}}^2}. \tag{13.4}$$

We remind ourselves that this result for the reflected power depends on the detection noise to be limited by the LO shot noise, *cf.* the discussion around Eq. (10.16) that is used in deriving Eq. (13.4).

13.5.1 *Power calibration*

To validate the results for the reflected power extracted from the measured photocurrent via Eq. (13.4), we have also occasionally performed power calibration measurements of the reflection detector. The main idea is simply to send light with a known optical power onto the detector, and compare the response with that of the reflected signals. Practically, this is done by reversing the probe beam propagation direction, such that it enters the TOF via port A, as illustrated by the red dashed line in Fig. 13.1. The transmitted probe, in this configuration, will now be measured by the reflection detector. The resulting signals, obtained with no trapped atoms, is shown in Fig. 13.5, for varying probe powers in the range 5 pW to 45 pW. The data is col-

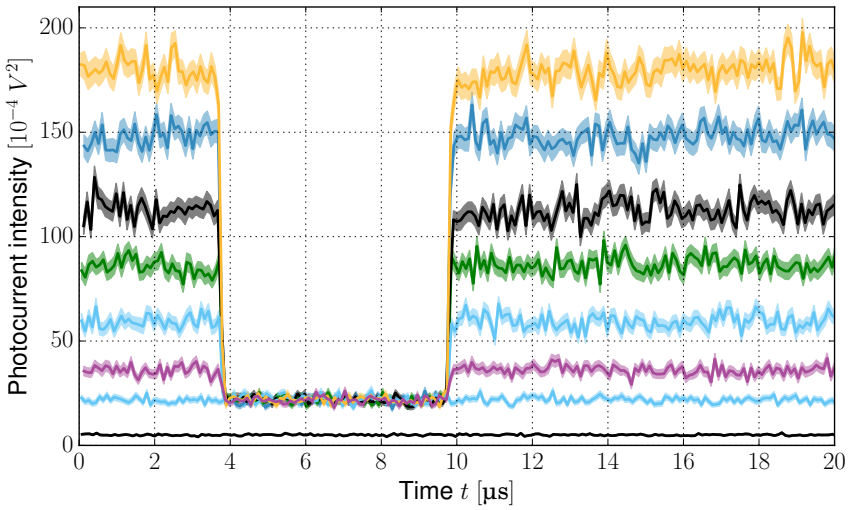

Figure 13.5.: *Power calibration measurements. The lowest two curves are the detector electronic and total noise. Sampled over* $\tau = 96$ ns.

8 In total, the transmission is 92 % through the TOF, from which we assign 4 % to each taper.

lected using the same measurement sequence as before[9], *i.e.*, having the probe initially on yielding a full transmission signal, before turning it off at $t = 3.7\,\mu s$ for measuring the total noise floor after which it is then turned on again at $t = 9.75\,\mu s$. The sequence is of course now completely arbitrary for the information we want to extract[10].

To compare the detector response $\left|\left\langle \bar{i} \right\rangle\right|^2$ for a given optical power, the photocurrent intensity for each signal in Fig. 13.5 is time-averaged from $t = 10\,\mu s$ to $t = 20\,\mu s$ and plotted against P_{calib}, for the corresponding probe power inside the TOF. This is shown in Fig. 13.6(a) using the same color reference as in Fig. 13.5. By doing a linear fit to

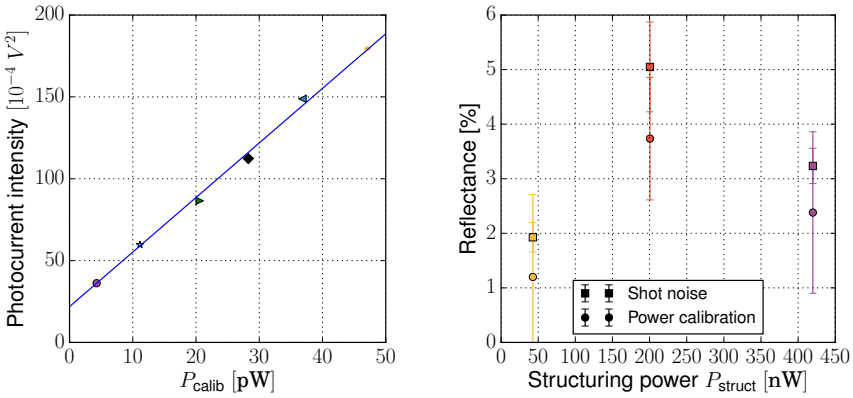

(a) (b)

Figure 13.6.: *(a)* 10 ms *time-averaged photocurrent intensiy* $\left|\left\langle \bar{i} \right\rangle\right|^2$ *from the signals in Fig. 13.5 as a function of the corresponding probe power referenced to the* TOF *waist. The blue line is a linear fit with the slope as the only free parameter. (b) Comparison between the obtained reflectances of the reflection peaks in Fig. 13.7 when extracting* $P_{reflected}$ *by using either Eq. (13.4) (squares) or Eq. (13.5) (circles). The errorbars are obtained as the one-sigma uncertainty from the statistical averaging and a* 5 % *probe power fluctuation during the measurement.*

these six points, while keeping the intersection with the y-axis fixed at the average total noise $\left\langle \delta i^2_{\text{calib}} \right\rangle$ of the six calibration signals, we obtain the simple expression

$$P_{\text{calib}} = \frac{1}{a}\left(\left|\left\langle \bar{i} \right\rangle\right|^2 - \left\langle \delta i^2_{\text{calib}} \right\rangle \right) \tag{13.5}$$

for the optical signal power in the TOF as a function of the detector response, with a being the fitted slope. This method for extracting the

9 The attentive reader will notice, however, that the probe off time is longer than that shown in Fig. 13.3. This is because the dark scheme was implemented for the measurements shown here.

10 As a side remark, we mention that the probe rise and fall time has been extracted from the calibration signals similar to those in Fig. 13.5, and found to be about 80 ns measured within 10 % to 90 % reference levels

reflected power off the atoms, does not rely on any measurements for the overall quantum efficiency ϵ of the detector. The only thing we need to know in order to obtain Eq. (13.5), is the optical probe power in the TOF. Which, in any event, is a parameter that we need to know in all our measurements.

Using both Eq. (13.4), with $\eta = 89\,\%$, $l = 53\,\%$, and $\mathcal{V}_0 = 93\,\%$, and Eq. (13.5) for extracting the maximum reflected power of the three measurements shown in Fig. 13.7, we apply formula (13.3), with $P_{\text{probe}} = 390\,\text{pW}$, to obtain the reflectance. The results are shown in Fig. 13.6(b) as a function of the structuring power which were varied for the particular three measurements used here as example for the power calibration shown in Fig. 13.7. The two methods for obtaining $P_{\text{reflected}}$, *i.e.*, the *shot noise* calibration method and the *power* calibration method, are seen to be in excellent agreement with well overlapped errorbars. For the data shown here, there is however a clear

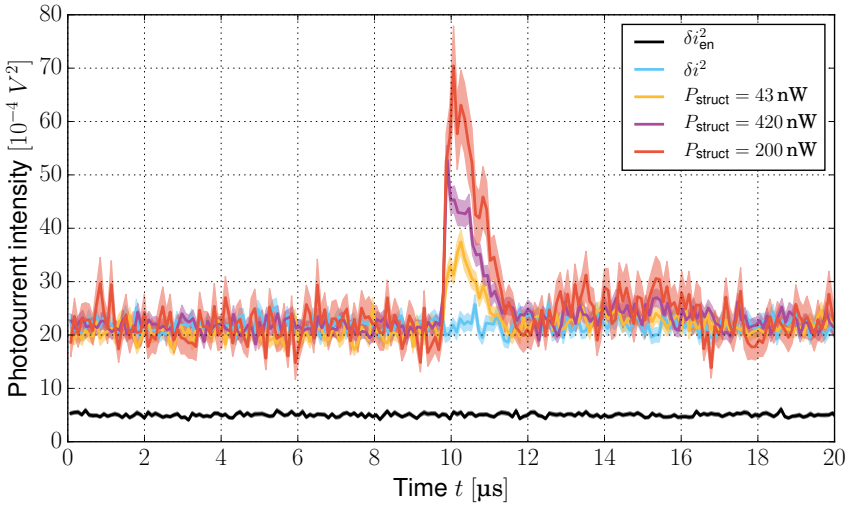

Figure 13.7.: *Reflected signal for three different powers of the structuring pulse* P_{struct} *using the dark scheme. Each curve is a statistical average over* $50 - 250$ *experimental runs and sampled over* $\tau = 96\,\text{ns}$. *Obtained with* $P_{probe} = 390\,\text{pW}$ *and* $\delta_{probe} = 2\pi \times 5\,\text{MHz}$.

bias which tend to yield higher values for the reflectance obtained with the shot noise calibration method, compared to those acquired with the power calibration method.

As a closing remark for this section, we mention that both the probe power P_{probe} as well as the structuring power P_{struct} are varied using a stack of up to three calibrated neutral density (ND) filters. For each beam, these are placed immediately before a single-mode fiber bringing the laser beam to the TOF setup. This can potentially cause a steering of the beams that might decrease the coupling efficiency into the before mentioned fiber. However, judging from Fig. 13.6(a), this

seems to be only a minor effect as all six points are well distributed around the straight line fit. This has been further confirmed for a few of the least absorbing ND filters by simply measuring the output power of the fiber with and without the ND filter. Compared against the expected calibrated value, at most a 5 % deviation was observed. This experimental uncertainty is thus already contained in the 5 % relative power fluctuation of the probe.

13.6 THE TOTAL NOISE

The level of the total noise intensity δi^2 enters in both Eq. (13.4) and Eq. (13.5) for extracting the reflected optical power off the atomic crystal. We therefore present here an estimation of the error on the total noise of the detection.

We first consider a typical time trace of $\left|\left\langle \bar{i} \right\rangle\right|^2 = \delta i^2$, shown in Fig. 13.8(a), which corresponds to the blue traces in both Fig. 13.3(a) and Fig. 13.7. The statistical mean and the standard deviation (std)

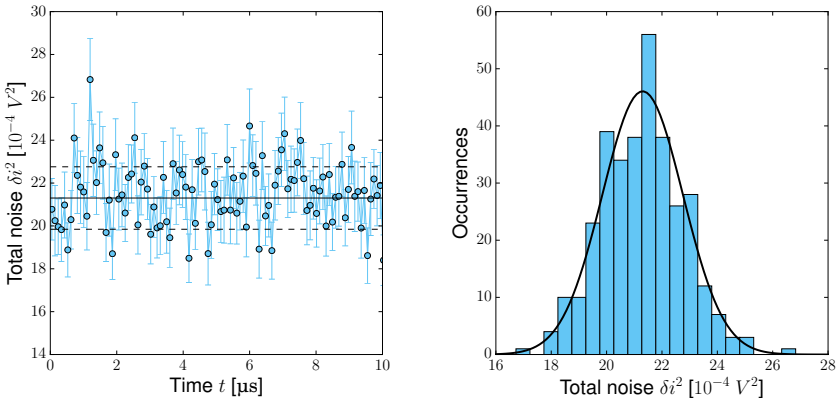

(a) (b)

Figure 13.8.: *Total detection noise reference measurement of the reflection detector. Obtained as the statistical average over* 200 *consecutive experimental runs sampled over* $\tau = 96\,\text{ns}$. *(a) Total noise as a function of the measurement time. Only shown for the first* 10 µs *of a* 32 µs *measurement for visual clarity, the full time trace can be found in Section F.3. Black solid line indicated the statistical mean of the data and the dashed lines the one-sigma uncertainty. (b) Histogram of the (full time trace) data in (a). Black solid line is a Gaussian fit.*

of the (full 32 µs) time trace are indicated in Fig. 13.8(a) by the black solid line for the mean and the dashed lines for the uncertainty band, and yields a total noise given by $\delta i^2 = (21.3 \pm 0.1) \cdot 10^{-4}\,\text{V}^2$, where the error on the mean are calculated as usual: $\text{std}/(N-1)^{1/2}$ with $\text{std} = 1.5 \cdot 10^{-4}\,\text{V}^2$ and $N = 333$. The data points are observed to be

randomly distributed around the mean and with statistical errorbars (from the 200 experimental averages) overlapped well within the std.

In Fig. 13.8(b) the histogram of the (full) time trace in Fig. 13.8(a) is shown together with a Gaussian fit yielding $\delta i^2 = (21.3 \pm 0.1) \cdot 10^{-4}\,\mathrm{V}^2$, in exact correspondence with that of the statistical mean. The total detection noise can thus safely be regarded as Gaussian distributed.

In calculating the peak reflectances shown in Fig. 13.6(b), we do not use an initial reference measurement for δi^2, but instead extract δi^2 from each individual signal trace in Fig. 13.7 by taking the time average over the first 9.75 µs, as mentioned previously. This will off course give a slightly larger error contribution to δi^2, simply because the time average is three times shorter. However, the Gaussian noise is already low enough, that the uncertainty on the total noise barely contributes to the errorbars in Fig. 13.6(b), which have been obtained by applying the well-known error propagation formula for uncorrelated variables. For the square points, obtained by applying Eq. (13.4), the statistical variance from the different experimental realizations is found to be on average 50 times higher than the variance on the Gaussian total noise, regardless of the number of experimental realizations (the maximum point were obtained using 50 consecutive measurements, whereas 250 measurements were used for the other two points). The statistical variance from the different experimental realizations, are also found to dominate the 5 % power fluctuation assigned to the probe beam by a factor of 7 on average for the three square points in Fig. 13.6(b).

13.6.1 *Time drift*

We also consider the drift on the total detection noise over many measurements, as shown in Fig. 13.9. Each measurement yields signal traces similar to those shown in Fig. 13.7, and consists of between 100 and 200 experimental realizations. As before, the total noise δi^2 is obtained as the time average over the first 9.75 µs of each signal trace, and it is these values that are in Fig. 13.9.

The total noise is initially found to be steadily distributed around the same mean value, until it slowly starts to decrease. This can be attributed to a drift in the optical power of the LO, most likely caused by a drift in lab temperature, which influences the laser output mode. Drifting lab temperature does not necessarily change the output power, but can influence the spatial shape and pointing stability of the output beam, which degrades the transmission through the subsequent fiber coupling of the laser source to the TOF setup. Regardless of which of the two caused the LO power to decrease, the net effect is the same, namely to cause a decrease in the detection

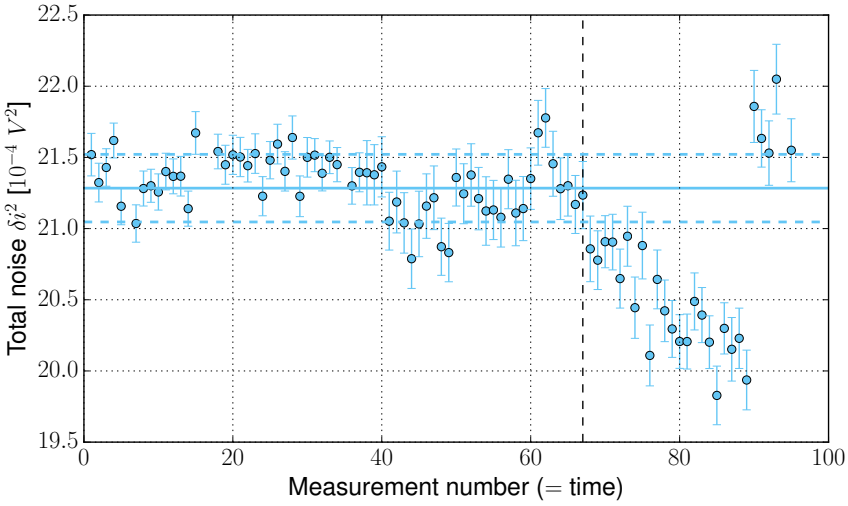

Figure 13.9.: *Time drift of the total detection noise. Each point is a* 9.75 µs *time average of the total detection noise in a single measurement consisting of* 200 *consecutive experimental runs until measurement number* 37*, whereafter only* 100 *runs in each measurement were executed, hence the larger errorbars. The x-axis marks the measurement number of each point and can be used as a proxy for the time at which the measurement were acquired. The vertical dashed line at measurement number* 67 *indicates where the* LO *power starts to drift towards lower optical power.*

efficiency. The total noise of the last five points were obtained after fiber couplings for both the LO and the probe were re-optimized.

The measurements up until number 67 (vertical dashed line) are used to give another estimate of the error of the total noise, and a statistical average yields $\delta i^2 = (21.3 \pm 0.2) \cdot 10^{-4}\,\mathrm{V}^2$ in good agreement[11] with what we found for the reference measurement of the total noise, which belongs to the same data set, see Fig. 13.8.

13.6.2 *But is it shot noise limited?*

In order to estimate if the total noise is shot noise limited, we consider yet again the data shown in Fig. 13.6(b) and Fig. 13.7. The maximum point, with $\mathcal{R} = (5.0 \pm 0.8)\,\%$, corresponds to $n_{\mathrm{ph}} = 2.9 \pm 0.5$ detected photons[12] on average over 50 experimental runs within the $\tau = 96\,\mathrm{ns}$

11 Note, that it is the std that are now used in the assignment of the uncertainty on the total noise, since we want to compare with that found in the individual measurements.

12 The detected number of photons within a sample time of τ is seen from Eq. (13.4) to be given by

$$n_{\mathrm{ph}} = \frac{\left|\left\langle \bar{i} \right\rangle\right|^2 - \left|\,\delta i\,\right|^2}{\delta i^2 - \delta i_{\mathrm{en}}^2}\,. \tag{13.6}$$

coherent averaging time. From this, the relative measurement error is found to be $0.5/2.9 = 16\,\%$. In total, $2.9 \times 50 = 147$ photons were detected during the whole measurement, which should result in a relative error of $\sqrt{147}/147 = 8\,\%$ if the detection is shot noise limited. The relative measurement error is thus found to be twice as high as that expected from the shot noise limit.

In general, a factor of 2 discrepancy is found in all our measurements, although it is slightly smaller for higher reflectances. To exclude that the difference arises from the temporal structure of the reflectance peak, fluctuating atom number or the like that could cause a noisier signal than expected from the shot noise contribution, the finding has been verified using the calibration signals shown in Fig. 13.5.

Nevertheless, we will apply Eq. (13.4), and thus use the shot noise limited extraction of the reflected power off the atomic Bragg mirror, together with Eq. (13.3), for the remaining results on the reflectances presented in this thesis.

14

REFLECTION OFF UNSTRUCTURED ATOMS

We have already demonstrated that we can have at least 5 % of light reflected of the atomic crystal with a Bragg grating burned onto it. But how much light would we actually collect from an unstructured ensemble? In this chapter, this question in answered by considering the experimental results from measurements with unstructured atoms and compare these to measurements with periodically structured atoms.

In Fig. 14.1 the recorded reflections from an unstructured (blue) and Bragg structured (red) atomic ensemble in the TOF-based dual-color dipole trap is shown. By applying Eq. (13.4) and Eq. (13.3), both signals have been converted to reflectances, for which reason the electronic noise and the detection total noise traces are not shown. The

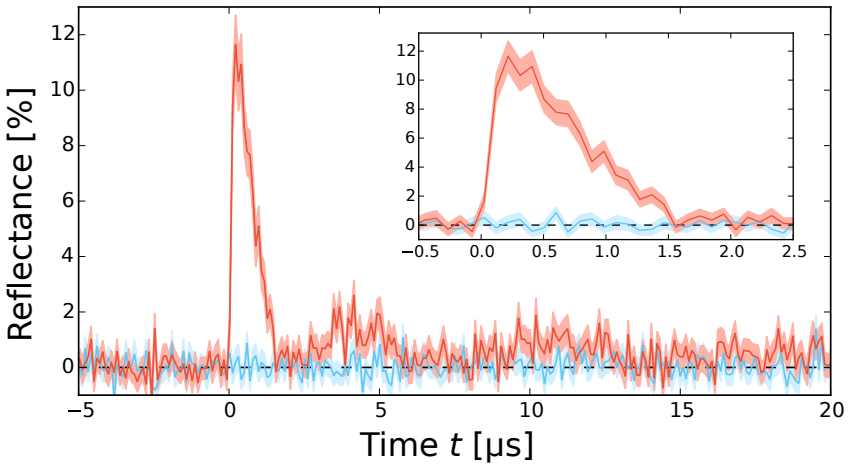

Figure 14.1.: *Reflectance off the atomic crystal sampled over* 96 ns *and using a* 150 pW *probe tuned* 8 MHz *above resonance. Blue: Reflectance off unstructured atoms, average over* 250 *experimental runs. Red: Reflectance off (dark scheme) structured atoms, average over* 200 *experimental runs. Inset: time zoom of the high reflectance peak. Note, that the time axis has been shifted such that the zero point coincides with the onset of the probe, but the timing sequence remains the same,* cf. *Fig. 13.5.*

blue signal for the unstructured ensemble is seen observed to randomly distributed around $\mathcal{R} = 0$ over the whole time trace[1]. Even

1 Obviously, a reflectance cannot be zero. This is simply an artifact from subtracting the total detection noise from the signal. What it means then, is that this signal is completely buried in the noise floor.

from the time zoom near the probe onset time at $t = 0$, no reflectance of the randomly distributed atomic ensemble is observed. This is in accordance with the very weak reflection off an unstructured atomic ensemble, confined in a trap similar to ours, that were reported in [Reitz *et al.*, 2014]. Here they observed (using an SPCM) only a few picowatt power reflection from $\lesssim 10^3$ atoms, when probing with the same optical probe power that we use here, $P_{\text{probe}} = 150\,\text{pW}$. Such low powers can only be measured in our setup when using a long integration time.

For this reason, we show in Fig. 14.2 a time trace of the power reflection off an unstructured ensemble containing ~ 1300 atoms. The

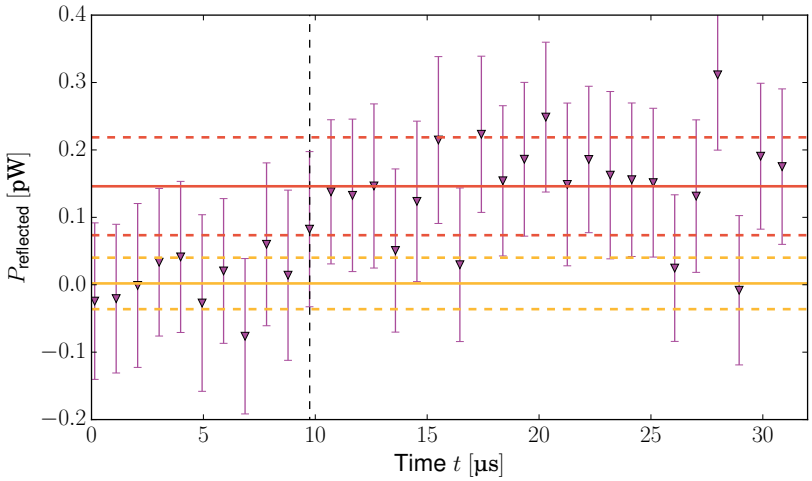

Figure 14.2.: *Purple data points: Reflected power from unstructured atoms as a function of time, using a* 140 pW *probe tuned* 8 MHz *above atomic resonance. Each point is an average over* 1900 MOT *loadings sampled over* $\tau = 96\,\text{ns}$*, and afterwards time averaged over* 960 ns*. The errorbars are given by the statistical one-sigma uncertainty from this last time average. Yellow (Red) lines: Statistical mean (solid) and* 1 std *uncertainty band (dashed) over the data points measured before (after) the probe is turned on at* $t = 9.8\,\mu\text{s}$*. The measurement were also performed with a resonant probe giving similar results, see Section F.4.*

timing sequence is the same as in the previously shown figures, for example see Fig. 13.5: The probe in on for the first 3.7 µs where it is turned off while the atoms are optically pumped from $|3\rangle$ to $|4\rangle$, after which the probe is turned on again at $t = 9.8\,\mu\text{s}$ (black vertical dashed line). The data has been collected from 1900 MOT loadings, and yet the reflected power, observed after $t = 9.8\,\mu\text{s}$, is barely distinguishable from the initial reference points. Before $t = 9.8\,\mu\text{s}$ the reflected power is measured to be on average zero (yellow lines for the

mean and uncertainty band) as expected[2]. After $t = 9.8\,\mu s$ the light reflected off the atoms are observed to be only on the sub-picowatt scale, and results in a reflectance of only $\mathcal{R}_{\text{unstruct}} = (0.10 \pm 0.01)\,\%$ for the 140 pW probe used here[3]. This yields a contrast between reflection of a Bragg structured and unstructured atomic ensemble of $\mathcal{R}_{\text{struct}}/\mathcal{R}_{\text{unstruct}} = 112 \pm 15$, with $\mathcal{R}_{\text{struct}} = (11.6 \pm 1.1)\,\%$ for the maximum atomic mirror reflectance observed in Fig. 14.1.

2 Note, that most of these points have actually be obtained when the probe is off, but as evident from the data, it does not make any real difference whether they are included or not.

3 It would have been beneficial to use a higher probe power for this measurement, but the data presented here were initially taken with for a different purpose where a weak probe were acquired.

15

CREATING AN EFFICIENT MIRROR – A HIKE IN PARAMETER SPACE

In the following sections, we show and discuss how we have optimized the reflectance of the dark scheme atomic mirror, *cf.* Section 12.2.2, by varying the different experimental knobs available in the lab. As it turns out, the parameter space is humongous, and hence took quite a while to explore, although we only managed to cover in detail a small fraction of it.

The four parameters we shall discuss are the optical power of the probe P_{probe}, the probe detuning δ_{probe} with respect to the $|4\rangle \rightarrow |5'\rangle$ transition, the optical power of the SW structuring pulse P_{struct}, and the frequency of the structuring pulse given in terms of its detuning δ_{struct} from the $|4\rangle \rightarrow |3'\rangle$ hyperfine transmission, *cf.* Fig. 12.6. Unless stated otherwise, the pulse length of the Bragg structuring was set to $t_{\text{struct}} = 250\,\text{ns}$ in all the measurements.

15.1 PROBE POWER

We start by considering the probe power. In Fig. 15.1 three different data sets is shown for the number of detected photons n_{ph}, sampled within a detection window of $\tau = 96\,\text{ns}$. The parameters[1] for the three remaining and fixed experimental knobs are displayed in Table 15.1.

All three[2] data sets are clearly observed to saturate with increasing probe power, and accordingly fitted by a simple saturation model:

$$f(P_{\text{probe}}) = n_{\text{ph}}^{\infty}\left(1 - e^{-P_{\text{probe}}/P_{\text{sat}}}\right), \tag{15.1}$$

1 All the reflection signals presented in the thesis have been obtained by analyzing along the same polarization orientation as the probe beam, *i.e.*, along the WCA apart from the May 23 data set presented here for which the analyzer WPs were oriented along the SCA. For the saturation of the reflection signal with the probe power, this has only an negligible effect since the effective scattering cross section for π-light is very similar for a homogeneous Zeeman level distribution compared to the steady-state distribution for π-light. This means that Zeeman pumping due to the probe will not markedly change the transition strength and corresponding saturation power. Also *cf.* Table 8.1.

2 It is a bit hard to claim this for the blue data set, without a data point further out. However, there is no reason to believe that it should not saturate like the two other data sets.

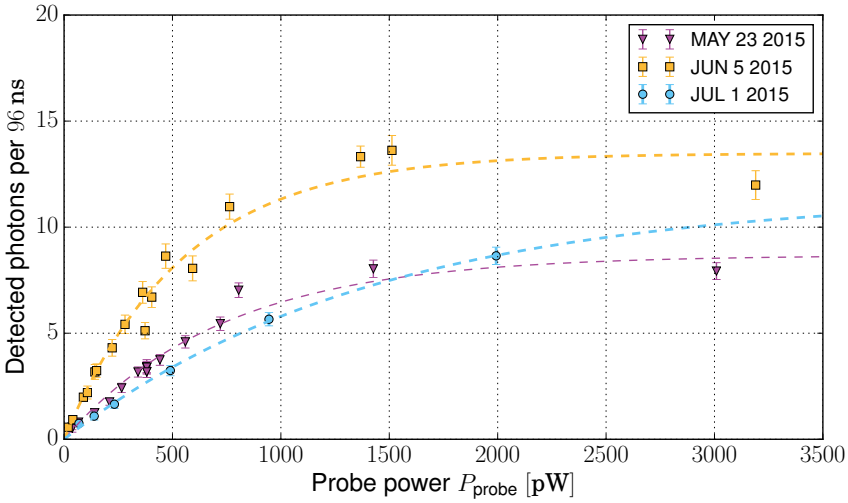

Figure 15.1.: *Detected number of photons n_{ph} within a sample time of $\tau = 96\,\text{ns}$. The experimental parameters used in each data set are given in Table 15.1.*

PARAMETERS	MAY 23 2015	JUN 5 2015	JUL 1 2015
δ_{probe} [MHz]	0	−5	+8
P_{struct} [nW]	150	200	250
δ_{struct} [MHz]	+140	−175	−175
$(n_{\text{ph}}^{\infty}, P_{\text{sat}})$ [(1, pW)]	(8.7, 730)	(13.7, 550)	(12, 1400)

Table 15.1.: *Experimental parameters belonging to the data shown in Fig. 15.1. The probe (structuring) detuning δ_{probe} (δ_{struct}) is given with respect to the $|4\rangle \rightarrow |5'\rangle$ ($|4\rangle \rightarrow |3'\rangle$) transition. P_{struct} refers to the optical power in a single arm of the SW structuring pulse.*

using two free parameters: n_{ph}^{∞} for the saturated number of photons that gets detected, and the effective power P_{sat} at which the reflection saturates. The fitted parameters are listed together with the experimental parameters in Table 15.1.

It is no surprise that the reflected power is observed to saturate with increasing probe power. Having a finite excited state lifetime $\tau_{\text{atom}} = \gamma^{-1} = (2\pi \times 5.23\,\text{MHz})^{-1} = 30.4\,\text{ns}$, an isolated atom in free space features a maximum scattering rate. As shown in Section 6.3, for the always illustrative example of a two-level system, the population in the excited state saturates at 50 % of the total population. This will, of course, also limit how much light the atoms can scatter in the backward direction.

The fitted values for P_{sat} in Table 15.1 are obtained with a phenomenological model different from the two-level atom case described earlier in Eq. (6.31). It is, nevertheless, instructive to calculate the expected P_{sat} and see how it compares. Using an on-resonance OD per atom of $\alpha_0 = 0.5\,\%$, inferred from an atom number measurement as described in Chapter 11, results[3] in $P_{\text{sat}}(\delta = 0) = 750\,\text{pW}$, which is found to be in very good agreement with the data set from May 23 2015.

However, as is already indicated by the distinctly smaller value for the fitted P_{sat} obtained with a probe detuned a linewidth from resonance (June 5), both of the remaining two data sets compare poorly to $P_{\text{sat}}(\delta = 2\pi \times -5\,\text{MHz}) = 3.6\,\text{nW}$ and $P_{\text{sat}}(\delta = 2\pi \times 8\,\text{MHz}) = 7.9\,\text{nW}$, respectively. Neither inhomogeneous broadening nor a global line shift fully explain the observed values. From Table 15.1 the parameters used for the structuring power are quite different for the last two data sets compared to the first data set, especially δ_{struct}. For $\delta_{\text{struct}} = 140\,\text{MHz}$, the structuring pulse sits between the $|4\rangle \rightarrow |3'\rangle$ and the $|4\rangle \rightarrow |4'\rangle$ transitions, whereas $\delta_{\text{struct}} = -175\,\text{MHz}$ places the structuring pulse below the (forbidden) $|4\rangle \rightarrow |2'\rangle$ transition and thus more than 30 linewidths from the nearest allowed dipole transition $|4\rangle \rightarrow |3'\rangle$, *cf.* Fig. 7.1 for the Cs level diagram. The red-detuned structuring pulse can thus cause an alteration of the trap potential due to the induced inhomogeneous AC Stark shift of the atoms. This pulls the atoms toward the TOF into a higher coupling region with the probe, which can effectively lower the saturation power. We will return to the influence of the AC Stark shift from the structuring pulse later in Chapter 20.

As a final remark, we point out that for optimizing the overall reflectance of the atomic Bragg mirror, the probe should be in the linear saturation regime. From Fig. 15.1 this means that P_{probe} should not be chosen any higher than a few hundred picowatt.

15.2 PROBE DETUNING

We now consider how the reflectance varies with the probe detuning δ_{probe}, shown in Fig. 15.2 for three data sets with experimental parameters according to Table 15.2. A clear double-peak structure is visible in all three data sets, with maxima observed to be 1 to 3 linewidths away from atomic resonance. This result can be explained by the presence of delocalized atoms in the 1D atomic mirror string. In order to understand this, it is instructive to first consider the influence of the necessary formation of a SW along the atomic crystal by the counter-propagating incident probe and back-scattered fields.

3 These values refer to probing along the WCA on the $|4\rangle \rightarrow |5'\rangle$ transition.

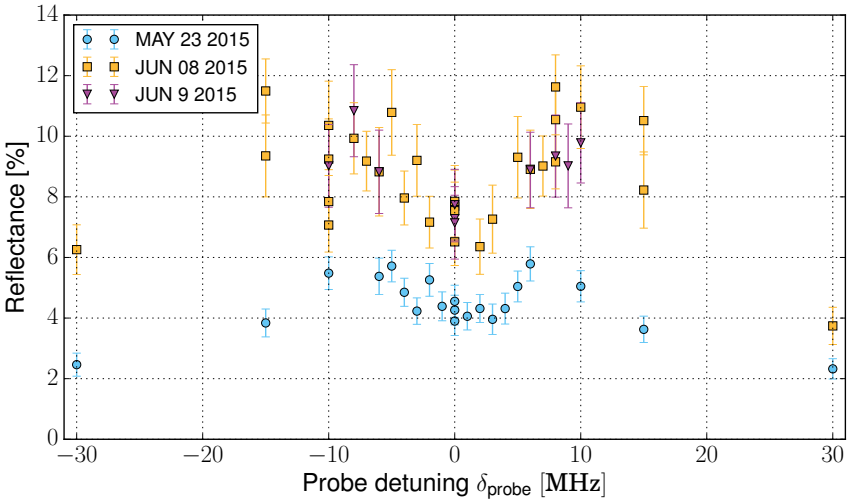

Figure 15.2.: *Reflectance as a function of the probe detuning δ_{probe} with respect to the $|4\rangle \rightarrow |5'\rangle$ transition. time bin of $\tau = 96\,\text{ns}$. The experimental parameters used in each data set are given in Table 15.2*

PARAMETERS	MAY 23 2015	JUN 8 2015	JUN 9 2015
P_{probe} [pW]	380	150	140
P_{struct} [nW]	150	200	200
δ_{struct} [MHz]	+140	−175	−175

Table 15.2.: *Experimental parameters belonging to the data shown in Fig. 15.2. The structuring detuning δ_{struct} is given with respect to the $|4\rangle \rightarrow |3'\rangle$ transition. P_{struct} refers to the optical power in a single arm of the SW structuring pulse.*

By employing the transfer matrix formalism, Slama *et al.* [2006] found that the in the case of perfectly positioned atoms, fulfilling the Bragg condition Eq. (12.12), the SW nodes will adjust such as to coincide with the atomic locations. This effectively suppresses the absorption and allows the probe to propagate further into the atomic sample, which in return increases the number of contributing scatterers to the coherent back-scattering. The reflection spectrum for this scenario is simply a Lorentzian with maximum reflection for a resonant probe coupled strongly to the atoms [Le Kien *et al.*, 2014].

When delocalized atoms are present, diffuse scattering becomes prominent and hence increases the absorption. As a consequence, the penetration depth of the probe into the sample reduces drastically and lowers the number of active scatterers. This can be circumvented by tuning the probe slightly off resonance. Thus reducing the coupling

to the atoms, the probe can propagate further into the sample and accordingly interact with more atoms which add more contributions to the Bragg reflected fields [Birkl *et al.*, 1995]. This description fits very much with what we observe in Fig. 15.2: Starting from $\delta_{\text{probe}} = 0$, the reflectance is at first only observed to increase when moving away from resonance. At some point, the coupling becomes too low for the probe to effectively scatter off the atoms and it is no longer beneficial to detune it any further.

As evident from Table 15.2 the structuring pulse is detuned by tens of linewidths from atomic resonance. This necessarily introduces a phase mismatch between the probe and the Bragg structure imprinted on the atoms. To estimate the effect of this we consider the relative wavelength difference between the probe and the structuring given by $\Delta\lambda/\lambda = (\lambda/c)\Delta\nu = 5 \cdot 10^{-7}$. The two waves thus dephases over a distance of a meter. Compared to the sample length of about a millimeter any effects due to phase mismatch can safely be neglected. This also means that the reflection spectrum should be symmetric around atomic resonance, as verified by the data in Fig. 15.2.

15.3 STRUCTURING FREQUENCY

We next consider how the reflectance depends on the chosen frequency of the structuring pulse. From the Bragg condition Eq. (12.12) it is expected that the frequency should be matched to that of the probe. Of course, in order to ensure that the whole (optically thick) ensemble is equally pumped, it is necessary to detune the structuring pulse from atomic resonance. Here, a rule of thumb is to choose a detuning that correspond to an OD equal to one, where about 37 % of the light makes it through the sample, *cf.* Section 6.5. From Eq. (6.30) we find that if we have $N_{\text{atom}} = 1000$ atoms and an on-resonance OD per atom of $\alpha_0 = 0.5\,\%$ a detuning of one linewidth gives $d = 1$ for the OD. This is, however, not the full story.

When optically pumping atoms from $|4\rangle$ to $|3\rangle$ with π polarized light, *cf.* Section 12.2.1, there is inevitable some challenge in choosing a detuning of the pump beam that couples all the Zeeman levels in $|4\rangle$ more or less equally to the excited states. Noteworthy are the forbidden dipole transition $|4,0\rangle \rightarrow |4',0'\rangle$ and the stretched levels $|4,\pm4\rangle$ which do not couple to $|3'\rangle$. A more homogeneous coupling of all levels can be achieved by tuning midway between the two excited state transitions. Starting at $\delta_{\text{struct}} = 2\pi \times 100\,\text{MHz}$ we performed an absorption measurement of the atoms, and adjusted P_{struct} until we found a setting where about half of the atoms were pumped out of $|4\rangle$. From these initial settings of δ_{struct} and P_{struct} the search for an optimized setting, *i.e.*, yielding a higher reflectance, started.

PARAMETERS	APR 23 2015	JUN 4 2015 A,B	JUN 5 2015
P_{probe} [pW]	950	420	400
δ_{probe} [MHz]	0	$0, +5$	$+5$
P_{struct} [nW]	40	200	200
t_{struct} [µs]	0.5	0.25	0.25

Table 15.3.: *Experimental parameters belonging to the data shown in Fig. 15.3. The probe detuning δ_{probe} is given with respect to the $|4\rangle \rightarrow |5'\rangle$ transition. t_{struct} is the duration of the structuring pulse. P_{struct} refers to the optical power in a single arm of the SW structuring pulse.*

The data presented in Fig. 15.3 illustrates the search in parameter space along the structuring pulse detuning direction. The cluster of red triangular points between 50 MHz and 160 MHz is where we started exploring the dark scheme. Here we take a halt and caution the reader that the probe power used in these measurements was saturating the atoms in order to have as much back-scattered light as possible. This means that the reflectances for this data set look substantially worse compared to the two other data sets, than if the detected power would have plotted instead. For a fair comparison (same effective probe saturation) the April 23 data should be scaled up by a factor two.

Keeping the detuning of the structuring pulse within the two excited states $|3'\rangle$ and $|4'\rangle$ a local maximum at $\delta_{\text{struct}} = 140\,\text{MHz}$ for the most optimal setting with respect the reflectance is found. We worked with this setting for a while, until we, by sheer coincidence[4], became aware of the existence of a more favorable value for δ_{struct}. This made us extend the search for a new frequency setting of the structuring detuning, that soon after ended several linewidths red-detuned to both the excited states at $\delta_{\text{struct}} = 2\pi \times -175\,\text{MHz}$. The blue-detuned side has not been explored (due to time constraints)[5].

4 The frequency lock of the structuring laser had not been activated and after a while the laser mode jumped from its initial position, with $\delta_{\text{struct}} = 140\,\text{MHz}$, to another (unknown) frequency, at which point we suddenly measured twice the reflection signal that we had ever observed.

5 The red-detuned side was chosen because the structuring field is derived from the +1st order mode of an AOM, and we wanted to prevent (potential resonant) leakage from the 0th order mode that distorts the loading into the dipole trap.

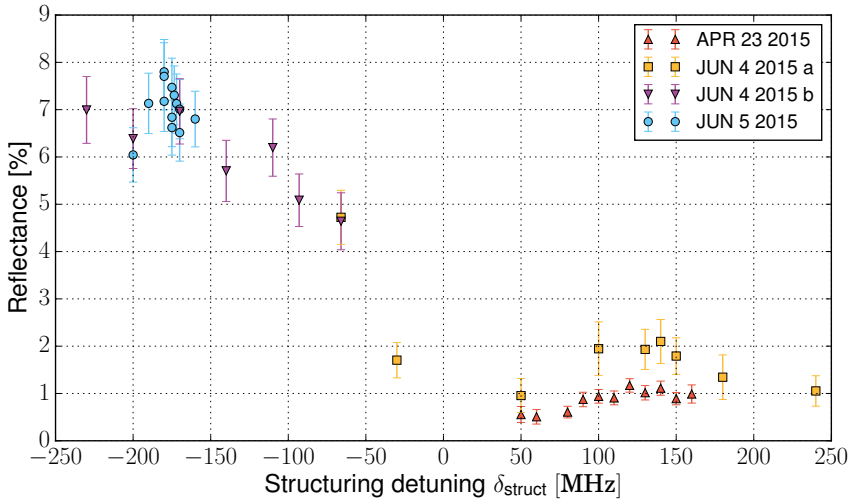

(a)

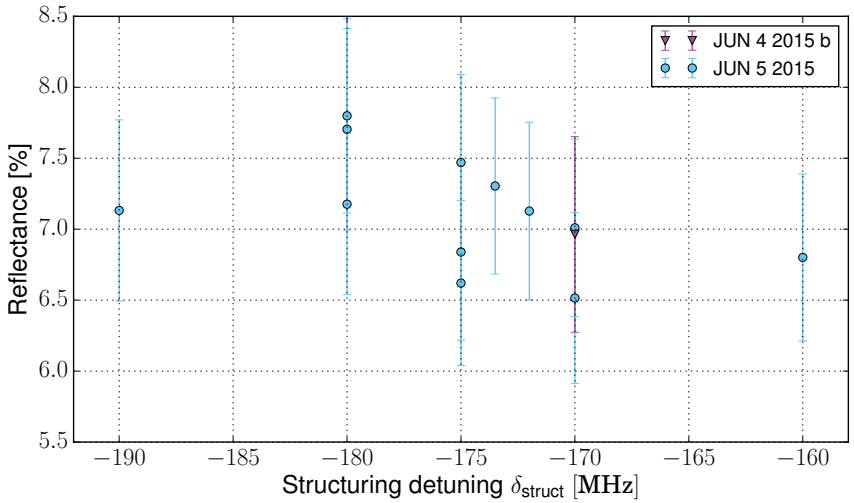

(b) Zoom in of the high reflectance data in (a).

Figure 15.3.: *Reflectance as a function of the detuning δ_{struct} of the SW structuring pump with respect to the $|4\rangle \rightarrow |3'\rangle$ transition. The sample time is $\tau = 96\,\text{ns}$. The experimental parameters used in each data set are given in Table 15.3.*

15.4 STRUCTURING POWER

Finally, we have reached the fourth experimental knob, namely the optical power of the structuring pulse P_{struct}. In Fig. 15.4 we present how the reflectance varies with P_{struct}. Although, the two data sets do

not display the same reflectances[6], they are very similar in shape and peak near the same structuring power at $P_{\text{struct}} = 200\,\text{nW}$. Although, it is a bit hard to tell if the yellow data set actually peaks at slightly higher powers. The dependence of the reflectance on the structuring

PARAMETERS	JUN 3 2015	JUN 9 2015
δ_{probe} [MHz]	+5	+8
P_{probe} [pW]	390	140
δ_{struct} [MHz]	+140	−175

Table 15.4.: *Experimental parameters belonging to the data shown in Fig. 15.4. The probe (structuring) detuning δ_{probe} (δ_{struct}) is given with respect to the $|4\rangle \rightarrow |5'\rangle$ ($|4\rangle \rightarrow |3'\rangle$) transition.*

power can again be understood by a qualitative description of the dynamics of the trapped atoms. As we found for the dependence with the probe detuning, the key element is again delocalized atoms. Before any structuring, the atoms are randomly spaced with respect to the pitch required for efficient Bragg scattering. For a weak structur-

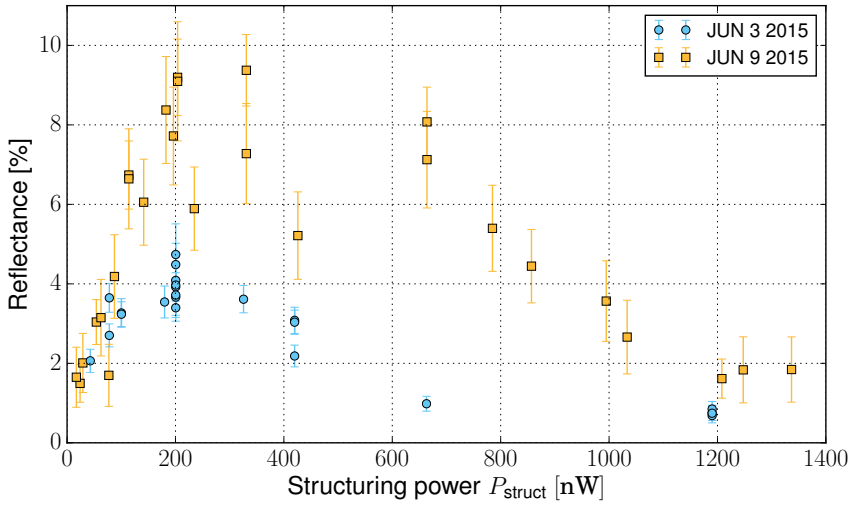

Figure 15.4.: *Reflectance as a function of the optical power in a single arm of the SW structuring pulse. The sample time is $\tau = 96\,\text{ns}$. The experimental parameters used in each data set are given in Table 15.4*

ing pulse, and thus a weak pump efficiency, it is not hard to imagine that there will be a substantial fraction of the atoms left in the wrong spots along the atomic crystal. With only a few atoms removed at

6 It is tempting to again say that this is due to the higher probe power used for the blue data set than for yellow, but here we caution the reader to also take the saturation curves for the probe power into account (Fig. 15.1).

the antinodes of the SW structuring pulse, the Bragg condition will be somewhat meet, but only to a small extend, also *cf.* Fig. 12.7 and Eq. (12.13). So, cranking up the structuring power should remove more atoms from the sites contributing to the destructive interference of the back-scattered waves.

Besides the degree of localization, the number of scatterers of course also enters into the amount of reflected light. This explains why the reflectance does not continue to rise with P_{struct}, since at some point there will simply be too few atoms left.

16

TEMPORAL DYNAMICS IN THE REFLECTION

In Chapter 13 it became clear that the system poses a lot of rich dynamics. Here the lifetime of the atomic Bragg mirror reflectance and its partial revivals are analyzed by considering the dynamics of the atomic wave packets confined in the TOF-based dual-color dipole lattice trap.

16.1 ATOMIC MOTION

The attenuation of Bragg peaks caused by thermal atomic motion are described by the Debye-Waller factor [Birkl *et al.*, 1995]:

$$f_{\mathrm{DW}}(t) = \mathrm{e}^{-K^2\sigma_z^2(t)}\,, \tag{16.1}$$

where $K = 4\pi/\lambda_{\mathrm{probe}}^{\mathrm{TOF}}$ is the momentum transfer in a single back-scattering event with respect to an incoming photon, and σ_z is the position spread of the atomic wave packet along the propagation direction. The Debye-Waller factor was originally introduced in crystallography as a tool to describe and explain the attenuation of x-ray or neutron coherent scattering peaks caused by thermal vibrations in the crystal lattice [Kittel, 2004]. Since atoms confined in an optical lattice poses a strict periodic structure much like a crystallized solid, it was suggested by [Deutsch *et al.*, 1995] that the former system should also display Bragg scattering, but now for optical radiation matched to the much larger length scale given by the wavelength of the lattice beams. This was soon after experimentally confirmed for a three-dimensional (3D) optical lattice in [Birkl *et al.*, 1995], where they also showed that the strength of the Bragg peaks can be parameterized by the temperature of the trapped atoms and thus described by the Debye-Waller factor. Since then, Bragg scattering has been used as a tool to study the properties of optical lattices, for example, to estimate the trap temperature and the extension of the bound atomic wave packets [Weidemüller *et al.*, 1998; Slama *et al.*, 2005].

16.1.1 *Spatial spread of the atomic wave packet*

In order to apply the Debye-Waller factor, Eq. (16.1), for the reflectance lifetime, it is necessary to know the time-dependence for the spread

of the atomic wave packet $\sigma_z(t)$ confined in the dual-color lattice trap. In Fig. 13.3(a) the reflectance was observed to decay to zero in about a microsecond. This is much faster than a full trap oscillation[1] $\omega_{\text{trap}} \approx 2\pi \times 100\,\text{kHz}$ [Vetsch *et al.*, 2010; Goban *et al.*, 2012], which allows us to approximate the time evolution of $\sigma_z^2(t)$ as free ballistic expansion:

$$\sigma_z^2(t) = \sigma_z^2(0) + \frac{\sigma_p^2}{m^2} t^2 \,, \tag{16.2}$$

where m is the atomic mass and σ_p is the momentum spread of the wave packet. Under the assumption that the trap sites can be described as isotropic harmonic oscillator potentials, the momentum spread for a thermal state with temperature T is given by

$$\frac{\sigma_p^2}{m^2} = \frac{\hbar\omega_{\text{trap}}}{2m} \coth \frac{\hbar\omega_{\text{trap}}}{2k_B T} \approx \frac{k_B T}{m} \,, \tag{16.3}$$

with k_B denoting the Boltzmann constant. The second approximate follows the assumption $\hbar\omega_{\text{trap}}/2k_B T \ll 1$, and is valid for $T \gtrsim 10\,\mu\text{K}$. The expected temperature of the trapped atoms is generously bounded from below by the recoil temperature (0.2 µK), and a conservative upper limit is given by the depth of the trap potential (270 µK). The approximation is thus valid within a broad range between these limits.

16.2 DECAY TIME CONSTANT

In Fig. 16.1 the temporal decay of the data presented in Fig. 13.3(a) is fitted by the generic function for the Debye-Waller factor

$$f_{\text{DW}}(t) = f_{\text{DW}}(t_0) \mathrm{e}^{-(t-t_0)^2/2\tau_{\text{DW}}^2} \,, \tag{16.4}$$

with the characteristic time constant

$$\tau_{\text{DW}} = \frac{\lambda_{\text{probe}}^{\text{TOF}}}{4\pi} \left(\frac{m}{2k_B T} \right)^{1/2} \,, \tag{16.5}$$

and t_0 being the time delay between the end of the structuring pulse and beginning of the probing. The delay time to be used in the formula is limited to positive values. In the experiment it is important to take possible delay times between digital control signals and

1 Recently, one of our Master students Kilian Kluge together with Jean-Baptiste Béguin, estimated the radial trap frequency to be 82 kHz: By turning the red trap off for 0.5 µs the atoms receive a radially outward push from the repulsive blue trap. Still confined in the potential well, the atoms are now sloshing in the radial direction. This is done while performing a dispersive measurement. On the measured phase shift, a damped oscillation is observed from the change in the light-atom coupling strength due to the atomic motion, with frequency corresponding to the radial trap frequency.

the controlled action (here the structuring pulse power) into account properly. Due to these delays for the data shown in Fig. 13.3(a) the structuring pulse actually extends 0.2 µs into the probing time interval. The main influence of the overlap between the structuring pulse

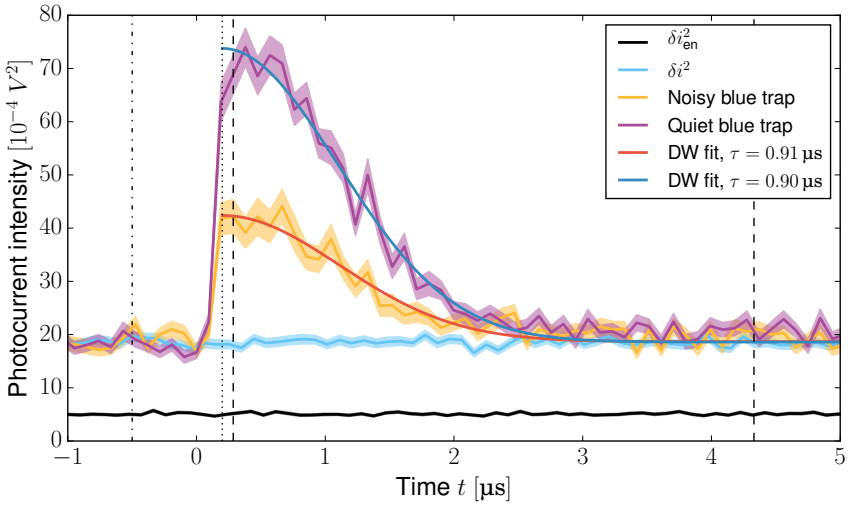

Figure 16.1.: *Zoom in of the same data as shown in Fig. 13.3(a) for the detected light reflected off the atomic Bragg mirorr. Dotted line indicates the end of the structuring pulse. Dashed lines mark the beginning and end of the data to be fitted. The time axis has been shifted by* 6.67 µs *such that the zero point coincides with the onset of the probe.*

and the probe, seems to be a slow initial rise of the probe instead of the 80 ns rise time we mentioned earlier. For the fit procedure, we do therefore not start the fit at $t = 0.08$ µs, but slightly later, at $t = 0.29$ µs (dashed line), when the maximum reflection is reached. As free parameters $f_{\mathrm{DW}}(t_0)$ and τ_{DW} are used, while we set $t_0 = 0.2$ µs.

Strikingly, the fitted time constants for the two curves are found to be nearly identical. For the yellow data, obtained with the noisy blue trap, the fit yields $\tau_{\mathrm{DW}} = (0.91 \pm 0.04)$ µs, while the fit of the purple data, for the quiet trap, yields $\tau_{\mathrm{DW}} = (0.90 \pm 0.02)$ µs. Since, τ_{DW} is directly related to the temperature of the trapped atoms, this suggest that the main effect of a blue trap with substantial intensity noise is to decrease the number of trapped atoms, and thus the number of contributing scatterers for the Bragg reflection.

The fitted time constants yields for the temperature of the atomic wave packets: $T = (34 \pm 3)$ µK and $T = (35 \pm 2)$ µK for the noisy and quiet blue trap signal traces, respectively. This is about eight times lower than the trap well depth of 270 µK, and thus a reasonable result.

For the remaining part of the thesis, only data with no mismatch between programmed and implemented timing of the structuring pulse will be considered.

In Fig. 16.2 we present a histogram of the characteristic time constant τ_{DW}, acquired by fitting several reflectance signals varying in strength with Eq. (16.4). The measurements were conducted over two days and are accordingly divided into two different data set. Both data sets are

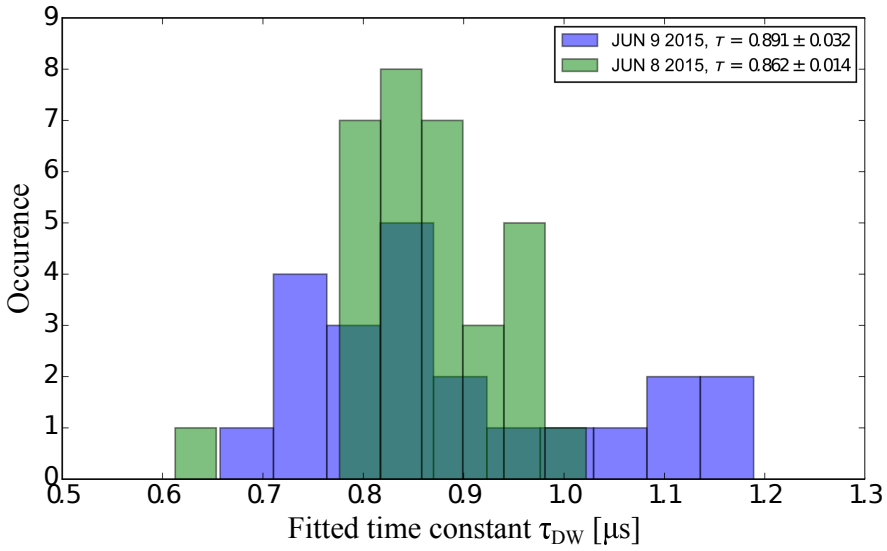

Figure 16.2.: *Histogram of τ_{DW} for two different data sets with $t_0 = -0.3\,\mu s$, i.e., the structuring pulse ended $0.3\,\mu s$ before the probe were turned on. The green data set corresponds to the one shown in Fig. 15.2 and the blue to that shown in Fig. 15.4.*

seen to yield consistent values for τ_{DW} distributed around the same statistical mean value with overlapping errors, see figure legend.

In Section 16.3 below, it will become evident that the blue data set have several entries with very low reflectances, for which the fitting procedure are less robust. This might explain the broader distribution observed for the this data set than for the green, which we, in Section 15.2, shall see only consists of reflectances higher than 3 %.

It is reasonable to conclude that the trap quality is stable[2] for both data sets presented here, resulting in trap temperatures of $T = (35 \pm 3)\,\mu K$ and $T = (38 \pm 1)\,\mu K$ for the blue and green data set, respectively. These results are in agreement with those reported in [Vetsch *et al.*, 2012] and [Reitz *et al.*, 2013] working on a setup similar to ours: By comparing the initial number of atoms trapped in $U_{min} = k_B \times 400\,\mu K$ deep potential wells, to the number of atoms remaining in the trap after the potential is adiabatically lowered to a new depth (done by reducing the optical power of the red trapping field), Vetsch *et al.* [2012] infer the initial temperature of the atoms to be $T = (29.8 \pm 0.9)\,\mu K$. In

2 In the sense, that the temperature of the trapped atoms are consistently the same for different data sets. As we saw in Fig. 16.1, we stress, that one should be careful about not interpreting this as also implying that the loading rate into the dipole trap is stable.

[Reitz *et al.*, 2013], a reported value of $T = (71 \pm 4)\,\mu\text{K}$ was extracted as a fit parameter when modeling experimentally observed Ramsey fringes and Rabi oscillations between two atomic ground states coherently driven by microwave radiation.

The lifetime of the reflectance observed here is also in accordance with that previously reported in [Birkl *et al.*, 1995] using a 3D free-space optical lattice. In their experimental configuration, the optical lattice constant were tuned very close to atomic resonance, only about 5 linewidths below the $|4\rangle \rightarrow |5'\rangle$ transition in Cs. The atoms are thus spatially confined in a Bragg fulfilling structure to begin with. To avoid wave mixing between the probe and the lattice beam mediated by the atoms, they turn off the optical lattice immediately before probing. With the atoms no longer spatially confined, ballistic expansion takes place allowing them to perform an analysis of the reflectance lifetime similar to what we have presented here.

16.3 INITIAL REFLECTANCE

Let us now consider the other fit parameter, $f_{\text{DW}}(t_0)$. We recall, that this fit parameter yields the Debye-Waller factor for the system, right after the structuring of the atomic ensemble into a Bragg grating has ended. Choosing the onset time for the probe as the zero point for the time axis, and taking the peak time of the reflectance $t_{\text{peak}} = 0.2\,\mu\text{s}$ into account[3], the maximum reflectance to be measured according to the fit can be evaluated as[4]

$$f_{\text{DW}}(t = t_{\text{peak}}) = f_{\text{DW}}(t_0)\mathrm{e}^{-(t_{\text{peak}}-t_0)^2/2\tau_{\text{DW}}^2}\,, \tag{16.6}$$

where $t_0 = -0.3\,\mu\text{s}$ is the time where the structuring stopped. Applying Eq. (16.6) to the same data set resulting in the blue histogram in Fig. 16.2, we obtain the purple points in Fig. 16.3, shown together with the corresponding (yellow) data points for the maximum observed reflectances, acquired by applying Eq. (13.4) and Eq. (13.3) to the maximum point of the measured signal. Evidently, the reflectances extracted from the Debye-Waller fit and the peak value of the observed reflection signal tend to agree very well with each other and overlap within the errorbars. There are, however, also some discrepancies. For reflectances below 4 % the purple points are always observed to be lower than the yellow points. This can be understood by considering the reflection signal for these low reflectance points.

3 t_{peak} is thus also the time at which the fit is started.

4 The Debye-Waller factor is of course a dimensionless quantity, but since we apply the fit to data given in units of V^2, f_{DW} of course takes on the same dimension. Afterwards, the procedure described in Section 13.5, can be applied to get f_{DW} in terms of reflectance.

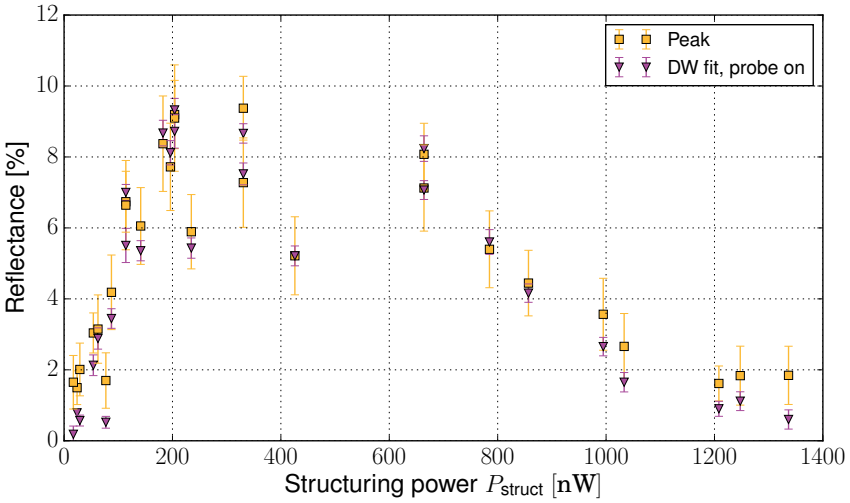

Figure 16.3.: *Difference between the reflectance inferred from the Debye-Waller factor fit $f_{DW}(t_0)$ (purple points), and the maximum experimentally observed value (yellow points). The data are the same as shown in Fig. 15.4 and used for the blue histogram in Fig. 16.2. The errorbars on the purple points are given by the one-sigma fit uncertainty, while the errorbars on the yellow points are the one-sigma uncertainty from the statistical averaging over* 200 *experimental realizations with an added contribution from a* 5 % *power fluctuation of the probe.*

As an example, we take a closer look on the reflection signal obtained with $P_{\text{struct}} = 1210\,\text{nW}$, shown in Fig. 16.4. Here the peak reflectance yields $\mathcal{R}_{\text{peak}} = (1.6 \pm 0.5)\,\%$, whereas the one extracted from the Debye-Waller fit yields $\mathcal{R}_{\text{DW}} = (0.9 \pm 0.2)\,\%$. The yellow signal trace is observed to be almost completely hidden in the detected noise given by the blue trace. With squeezed eyes and knowing what to look for a very small bump is barely visible at t_{peak} right after the probe is turned on. However, it is not higher than the fluctuating point of the total noise observed near $t = -8.5\,\mu\text{s}$, and as such it is not possible to claim any reflectance for this low resolution signal. This is a prime example, that one should always be critical about claiming a signal and make sure to also study the "raw" signals. For such a low signal the fit actually yields a much more reasonable result. Since there is essentially no structure to fit, it simply gives an almost flat line. In this respect, if working with very low reflection signals, we are better off using the fitted values of the Debye-Waller factor, which takes the whole structure into account and not just a single point.

It is interesting to note that the Debye-Waller fit also gives access to what we should measure, if the probe could be started exactly after the structuring pulse had ended. For the highest reflectances in Fig. 16.3, reaching 9 %, the fit parameter $f_{\text{DW}}(t_0)$ is found to be two

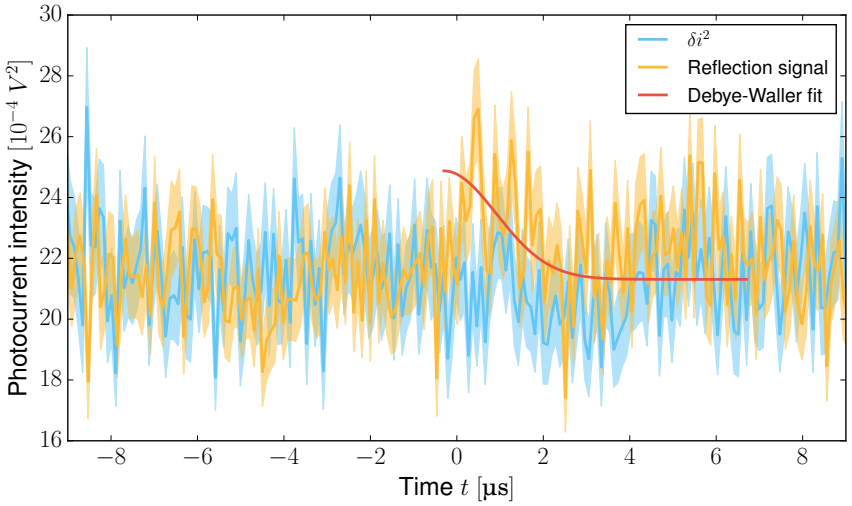

Figure 16.4.: *Reflection signal measured for the point with* $P_{struct} = 1210\,\mathrm{nW}$ *in Fig. 16.3. The electronic noise trace has been omitted for visual clarity. Other experimental parameters:* $P_{probe} = 140\,\mathrm{pW}$, $\delta_{probe} = 2\pi \times 8\,\mathrm{MHz}$ *with respect to the* $|4\rangle \rightarrow |5'\rangle$ *transition, and* $\delta_{struct} = 2\pi \times -175\,\mathrm{MHz}$ *with respect to the* $|4\rangle \rightarrow |3'\rangle$ *transition.*

percentage points higher, and thus more than 10 % of the incident probe is reflected off the atomic Bragg mirror.

16.4 PROBE INFLUENCE

Even though we have seen that the Debey-Waller fit yields consistent values for the temperature of the trapped atoms with those reported in the literature [Birkl *et al.*, 1995; Vetsch *et al.*, 2012; Reitz *et al.*, 2013], and as such reveals a good explanation for the rapid decay of the reflectance that we observe, it is good scientific practice to perform additional checks. Could the probe, for example, induce heating out of the trap? It is unlikely on this time scale, but to be sure, we performed a series of measurements for increasing delay between the structuring pulse and the probe, as shown in Fig. 16.5. If the reflectance lifetime is mainly dominated by an influence of the probe, the peak height if the reflection signal is not expected to change significantly by delaying the probe further with respect to the structuring pulse, and as such the whole reflection structure should just simply be delayed.

This is not the case in Fig. 16.5. Instead, the delayed reflection signals are observed to follow the blue curve, which is the Debye-Waller fit to the first (black) reflection signal. Evidently, the probe can only have a negligible effect on the temporal shape of the reflected light, that is, the dephasing of the imprinted Bragg grating.

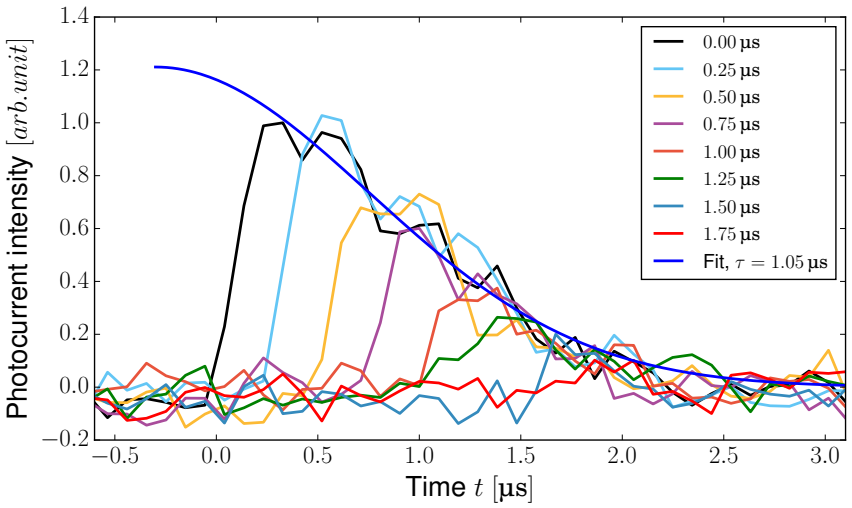

Figure 16.5.: *Result of the reflection measurements with delayed probe pulse. The uncertainty band is omitted for visual clarity, and the curves are normalized to the peak height of the first (black) curve. Each curve is an average over 100 consecutive experimental runs obtained for a* 150 pW *on-resonant probe and sampled over* $\tau = 192$ ns. *Corresponding data showing the transmitted power is given in Fig. F.5.*

16.5 BUT WHY DOES IT DECAY?

One could justifiably ask why the reflection signal decays in the first place. After all, the atoms are still confined in the conservative trap potential after structuring. In order to answer this question, we refer back to Section 12.2.1, specifically to Fig. 16.6. We recall, that the atoms are confined at the anti-nodes, or equivalently, at the intensity maxima of the red trap. For the dark scheme, atom sitting in the low intensity regions of the $\lambda_{\text{struct}} = 852$ nm SW structuring pulse, are left in the $|4\rangle$ state.

Let us consider, what could happen for an atom located at the trap site near $z = 1000$ nm in Fig. 16.6. It will not spend all its time exactly at the trap minima, but oscillates back and forth in the potential well with the trap frequency. If it appears to be located close to the right edge at the time the structuring pulse is turned on, it will be exposed to a higher intensity of the structuring pulse, than if it would instead had been making a turn at the left edge of the trap site. As such, all the surviving atoms in $|4\rangle$ actually becomes highly localized within the trap sites. Or put in another way, the atomic wave packets become squeezed in their spatial coordinate, much more than what they already are from being confined in the potential wells. When the structuring pulse is turned off again, a localized atomic wave packet will start to dephase back to a state with a broader spatial extension,

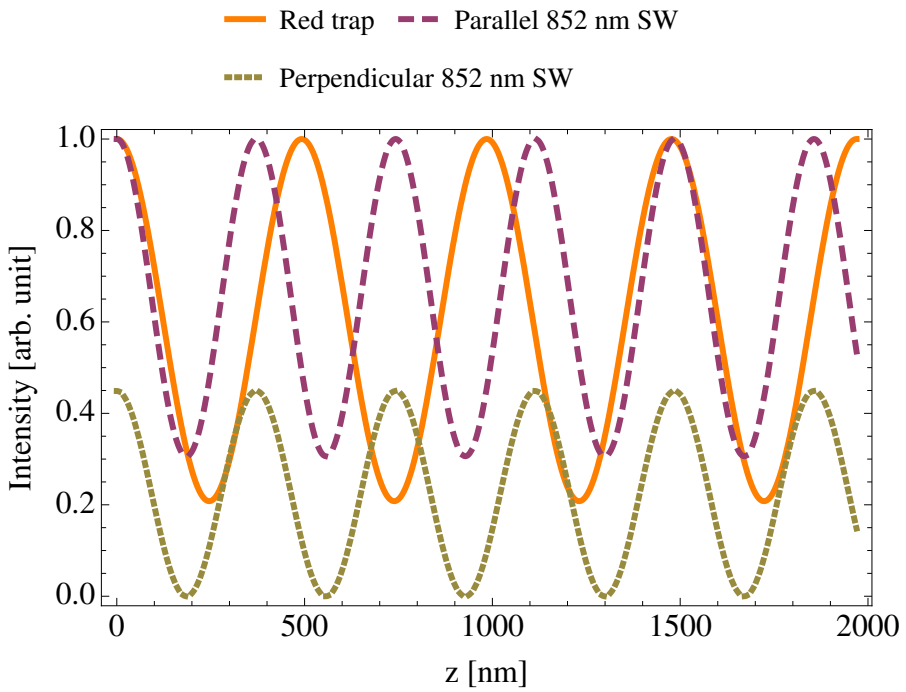

Figure 16.6.: *Intensity distribution along the fiber axis of a quasi-linear* HE_{11} *SW mode field. Calculated for the parameters* $n_{co} = 1.4469$, $n_{cl} = 1$, $a = 250\,\text{nm}$, $x = 0$, $y = 442\,\text{nm}$.

while continuing sloshing in the well, and thus moving in and out of a high coupling region with the probe.

16.5.1 *Partial revivals*

For a perfect simple harmonic oscillator potential, where an atomic wave packet rotates uniformly in phase-space, a full revival of the reflectance would have been expected. Clearly, in the reflection signals presented so far, only a fractional revival is present if at all. This can be accounted for by the trap potentials being neither truly harmonic nor isotropic. It is as such reasonable to assume that the atomic wave packet will dephase back to a thermal state.

For the red reflection signal[5] in Fig. 16.7, two revivals can be observed to appear after roughly 4 µs and 11 µs of the probe onset at $t = 0$. The peak reflectance of these small bumps are $\mathcal{R} = (2.6 \pm 0.5)\,\%$ and $\mathcal{R} = (1.9 \pm 0.6)\,\%$, respectively. The revival at 11 µs corresponds well to a trap frequency of $\omega_{\text{trap}} = 2\pi \times 100\,\text{kHz}$, which we previously used for estimating the temperature of the trapped atoms. It is also reasonable close to a radial trap frequency of $\omega_\rho = 2\pi \times 82\,\text{kHz}$ that

5 We point out that this is in fact our record signal, showing a high reflectance reaching nearly 12 %.

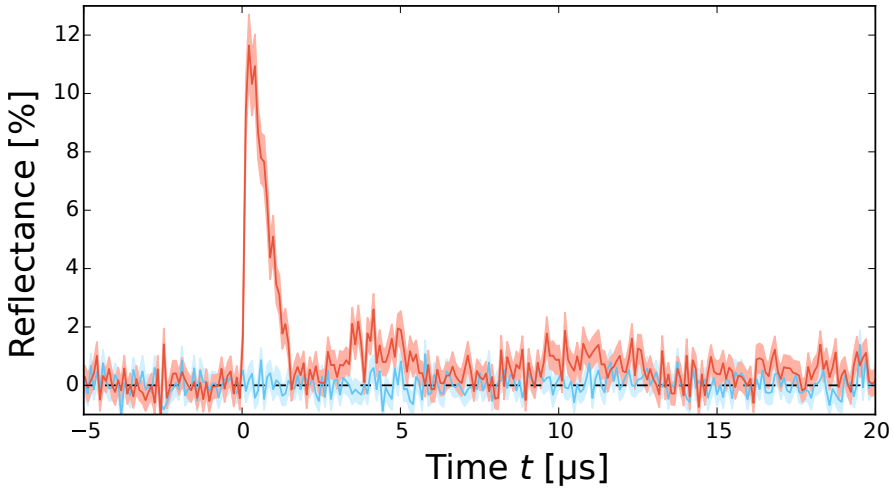

Figure 16.7.: *Reflection signal with substantial revivals. Achieved with the experimental parameters* $P_{probe} = 150\,\mathrm{pW}$, $\delta_{probe} = 2\pi \times 8\,\mathrm{MHz}$, *with respect to the* $|4\rangle \rightarrow |5'\rangle$ *transition,* $P_{struct} = 200\,\mathrm{nW}$, $\delta_{struct} = 2\pi \times -175\,\mathrm{MHz}$ *with respect to the* $|4\rangle \rightarrow |3'\rangle$ *transition.*

was recently measured in our setup [Kluge, 2015]. An axial trap frequency of $\omega_z = 2\pi \times 315\,\mathrm{kHz}$ is calculated in [Vetsch *et al.*, 2010] for experimental parameters similar to ours, and would agree with the revival appearing after 4 µs.

17

MIRROR QUALITY

Creating an atomic Bragg mirror by burning the spatial structure onto the internal states of the atoms should allow for a versatile system that can be turned on and off on demand. In this chapter we therefore investigate the ability making more than a single realization of the atomic spin grating with the same batch of atoms.

17.1 REPEATABLE MIRROR

To see if the atoms can be restructured into a Bragg mirror after the first reflection signal has faded out, we simply extend the timing sequence for the measurement. After the final yellow slot in Fig. 17.1,

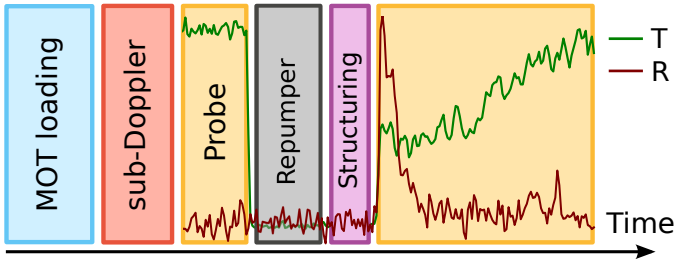

Figure 17.1.: *Time sequence of a single experimental run. Green (red) curve is an illustration of the transmitted (reflected) power (not to scale).*

we turn off the probe again and add the three last slots, repumper, structuring, probe, repeatedly to the sequence. In this way, atoms that are pumped to the hyperfine level $|3\rangle$ by the first structuring pulse are repumped to $|4\rangle$ and then structured again, after which the probe is turned back on. In Fig. 17.2 we show the resulting reflection and transmission signals of this looping sequence for periods of 8 µs, 20 µs, 40 µs and 60 µs. Quite disappointingly, the strength of the second mirror reflection, Fig. 17.2(a), is always 3 to 4 times lower than the first, and only for the 8 µs repetition time is it possible to resolve the third reflection above the noise level. The conclusion must be that the atoms are either badly structured or simply not there. If we consider the transmission signal in Fig. 17.2(b), the latter argument seems to be the case. As before, the first few microseconds are a reference signal for the empty trap transmission. The looped transmission signal are observed to decay faster towards full transmission for shorter repetition rates. This suggests, that either the Bragg preparation se-

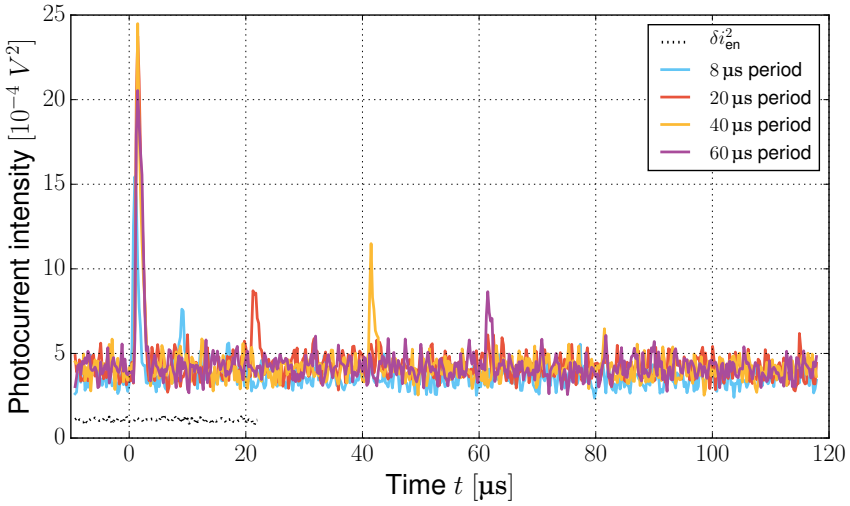

(a) Reflection signal.

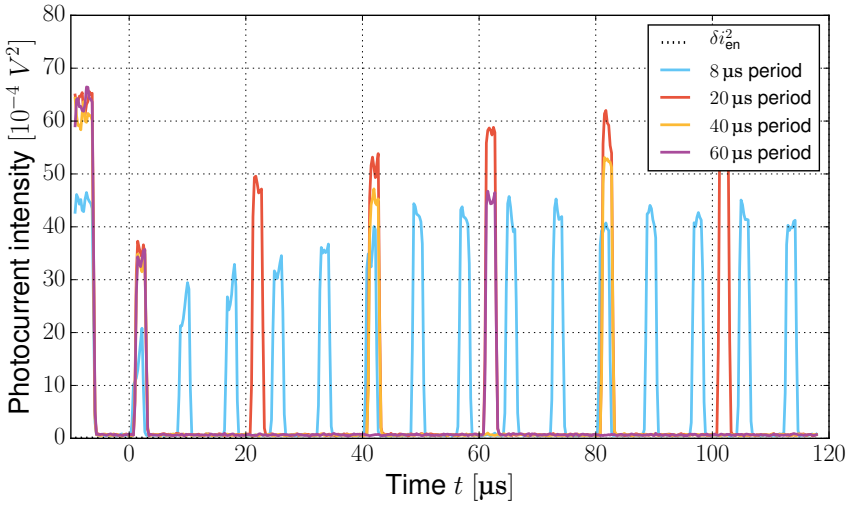

(b) Transmission signal.

Figure 17.2.: *Looping reflection and transmission signal. The uncertainty band has been omitted for visual clarity. Each curve is an average over* 50 *consecutive experimental runs obtained with* $P_{probe} = 150\,\text{pW}$, $\delta_{probe} = 8\,\text{MHz}$, $P_{struct} = 2 \times 200\,\text{nW}$, $\delta_{struct} = 2\pi \times -175\,\text{MHz}$, *and using a* $\tau = 496\,\text{ns}$ *running average.*

quence or the probing causes the atoms to heat out of the trap. As we have already verified, in Section 16.4, that the probe has negligible influence on the decay of the reflection signal, it is the repumping or, more likely, the structuring that is destructive.

17.2 DECAY SOURCE

Following our findings in the previous section, we investigate here the impact of the repumper and the structuring pulse on the mirror quality. The idea is a follows: First, we delay the usual sequence of repumper, structuring and final probing, *i.e.*, the last three slots in Fig. 17.1, by about 20 µs as seen in Fig. 17.3 where the reflection and transmission signals now appear later than $t = 0$. For the blue signal, this is it, and nothing has happened apart from an overall delay. As such, this signal serves as our reference for the reflection and transmission signal taken under these conditions (probe power *etc.*).

Next, we add an extra single (3 µs as usual) repump pulse at $t = 0$, to see whether this influences the signals or not. This is the yellow signal and no difference with respect to the blue reference can be observed. As a side remark, we note that this also confirms that the 3 µs repumping is sufficient to bring all the atoms from $|3\rangle$ to $|4\rangle$.

Adding now both the repumper and the structuring at $t = 0$, purple curve, amounts to prepare the atomic Bragg grating twice, but without probing in between as in Fig. 17.2. Clearly, this substantially degrades the reflection signal making it more than four times weaker than the reference. Also, in transmission, a shortage in signal is evident. It becomes even more apparent when making a quick estimation of the OD, where we have $d \approx \ln(70/35) = 0.7$ for the blue reference signal and $d \approx \ln(70/53) = 0.3$. Since $d \propto N_{\text{atom}}$ we find that less than half of the number of atoms are contributing to the purple signal as compared to the reference.

Finally, we also add the structuring pulse only at $t = 0$ (red curve). At this point in time, all the atoms should be in $|3\rangle$, and the far-detuned (9.2 GHz) structuring pulse is not expected to have any influence on the atoms. From Fig. 17.3 this is indeed observed to be the case, with this signal completely coinciding with the blue reference.

The only reasonably conclusion from all the signals in Fig. 17.3, must be that the structuring pulse besides from shaping the atomic crystal into a Bragg grating, also exerts a destructive fingerprint on the atoms. Since we have seen that the rapid ($\sim$ 1 µs) decay of the reflectance signal is very well described by the Debye-Waller factor, *cf.* Chapter 16, the destructive impact of the structuring pulse occur over a somewhat longer timescale. This would be consistent with a pull exerted on the atoms from the dipole force induced by the red-detuned structuring pulse.

If it is an attractive pull from the dipole force that distorts the long term mirror reproducibility, it is relevant to ask why the atoms in $|3\rangle$ are not influenced (red signal in Fig. 17.3). From a quick estimation of

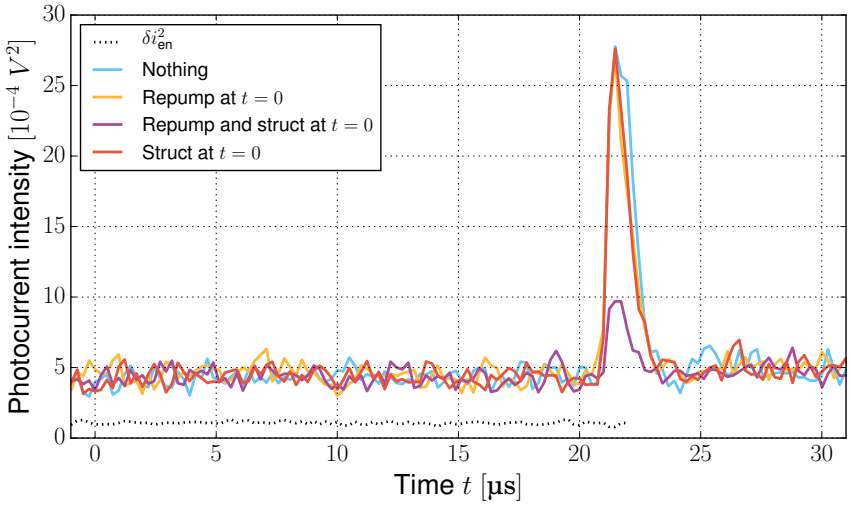

(a) Reflection signal.

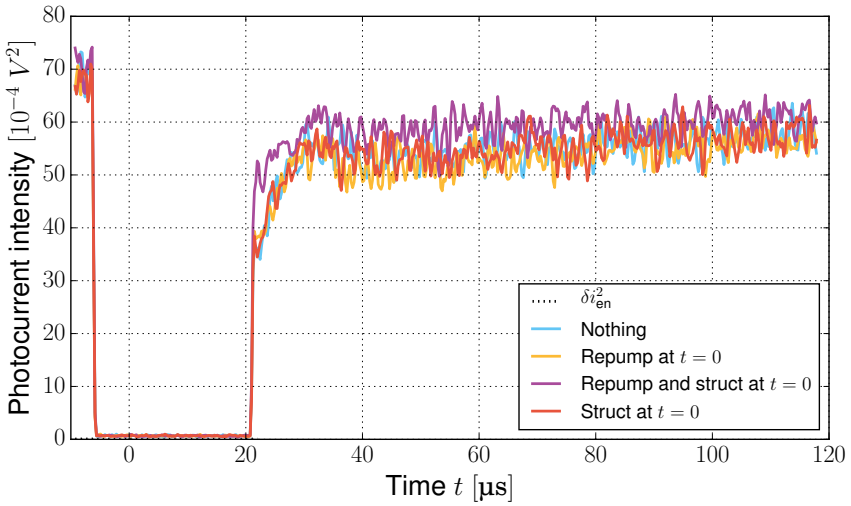

(b) Transmission signal. Note the longer time axis compared to (a).

Figure 17.3.: *Reflection (a) and transmission (b) signals off the atomic Bragg mirror under the investigation of destructive influence from either the repumper or structuring pulse. Uncertainty band has been omitted for visual clarity. Each curve is an average over* 50 *consecutive experimental runs obtained with* $P_{probe} = 150\,\text{pW}$, $\delta_{probe} = 2\pi \times 8\,\text{MHz}$, $P_{struct} = 2 \times 200\,\text{nW}$, $\delta_{struct} = 2\pi \times -175\,\text{nW}$, *and using a* $\tau = 496\,\text{ns}$ *running average.*

the relative difference between the induced AC Stark shift of the two ground state levels we find $\Delta E_3/\Delta E_4 \approx 175\,\text{MHz}/9.2\,\text{GHz} = 0.02$, when using Eq. (5.29). The influence from the structuring pulse on the 9.2 GHz lower lying ground state $|3\rangle$ is thus two orders of magnitude weaker as compared to the $|4\rangle$ level. In Chapter 20 a more in-depth

analysis of the dipole force exerted by the structuring pulse on the atoms is provided.

18

REMAINING FRACTION OF ATOMS

We would like to compare our experimental results with a theoretical model. Here the transfer matrix approach offers a very flexible platform for adding up all the field contributions from the individual atoms as we shall see in Chapter 19. In the model, we need to assign a pump probability of the atoms to be in either a dark or bright state when probing them after structuring. In Section 12.2.2 this was given as

$$p^j_{\text{dark}} = \mathrm{e}^{-\zeta \cos^2(2\pi z_j/\lambda^{\text{TOF}}_{\text{struct}})}\,, \tag{18.1}$$

where we also showed that the parameter for the pumping strength ζ, as provided by the structuring pulse, can be translated into the survival fraction of atoms in $|4\rangle$, n_4 via Eq. (12.15). In order to compare our experimental findings with this model, we therefore need to extract the fractional number of atoms left in $|4\rangle$ after the structuring pulse. If the atomic sample is optically thin, this can be achieved by measuring the relative OD between structured and unstructured atoms. In the following we show how this is done in practice.

18.1 EXTRACTING THE OPTICAL DEPTH

In Section 13.4 we showed how the OD is extracted from the transmission signal by the use of Lambert-Beer's law. This now gives a time-varying measure for the OD, whereas we are only interested in extracting a single number. As seen below, there is a lot of dynamics going on in the transmission signal after a structuring pulse. The question arises, from which time interval during the measurement we should extract the relative OD. Should it be the long-term behavior, when the transmission signals are seen to settle towards a steady value, or should it be the short-term value at the onset of the probing? To be on the safe side, we did both.

We start with the linear fit of the long-term behavior of the OD. In Fig. 18.1(a) four time traces is shown of the OD extracted from corresponding transmittance signal shown in Fig. 18.1(b). Each trace is fitted by a straight line starting when the transmission signal has settled at $t = 13.25\,\mu\text{s}$ (vertical dashed line), to the end of the signal. The OD at the probe onset time is then simply extrapolated from the fit parameters, marked as circular points on the linear fits in Fig. 18.1.

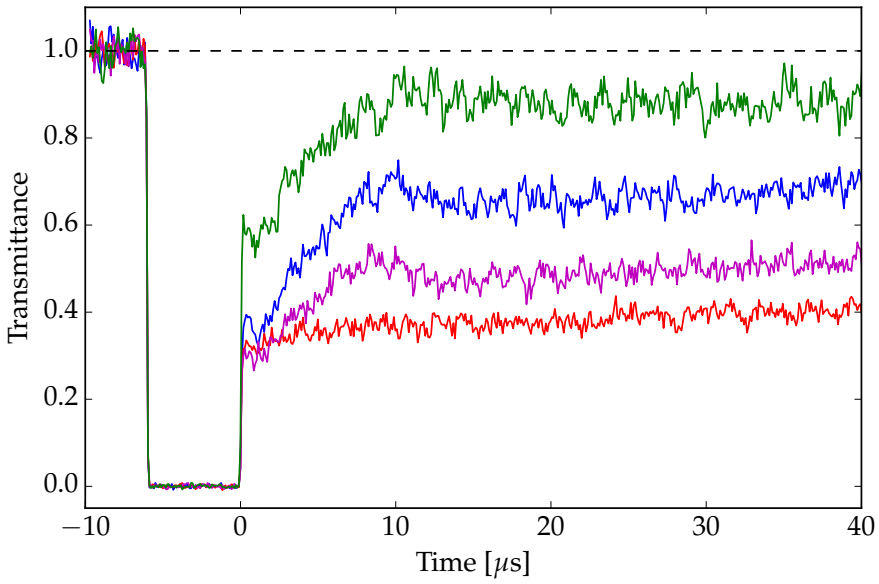

(a)

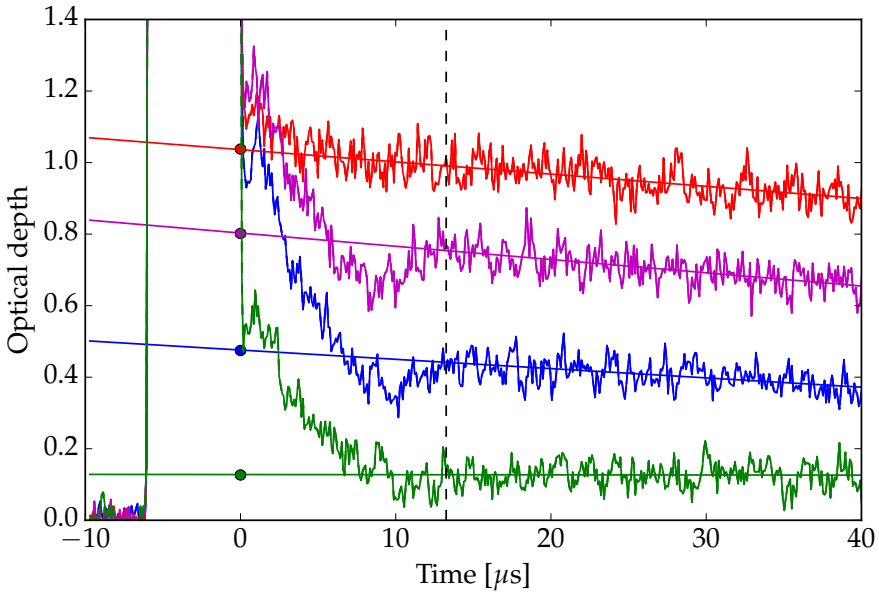

(b)

Figure 18.1.: *Sample transmittance (a) and optical depth (b) as a function of time after probe onset. The traces are obtained for* $P_{probe} = 140\,\mathrm{pW}$, $\delta_{probe} = 8\,\mathrm{MHz}$, $N_{atom} \approx 1300$, *and four different powers of the structuring pulse* P_{struct}*: Green:* $P_{struct} = 2 \times 995\,\mathrm{nW}$*; Blue:* $P_{struct} = 2 \times 204\,\mathrm{nW}$*; Purple:* $P_{struct} = 2 \times 87\,\mathrm{nW}$*; Red: no structuring.*

There is obviously a significant difference between the measured OD at $t = 0$, compared to that inferred from the linear fit procedure.

To extract the short-term value for the OD at the onset time of the probe ($t = 0$), we simply make a short 0.4 µs time average over the data.

18.2 ABSORPTION LINEWIDTH

Since the OD, in the low saturation regime, yields the absorption profile described by a Lorentzian, *cf.* Section 6.5, it is instructive to plot the OD inferred from the two different methods as a function of the probe detuning δ_{probe}. This is shown in Fig. 18.2. For further compar-

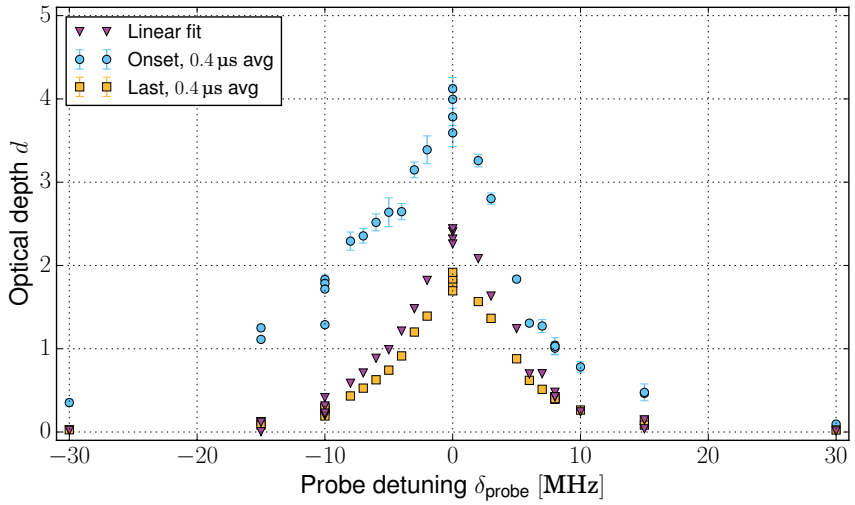

Figure 18.2.: *Extracted OD d as a function of the probe detuning δ_{probe}, for the June 8 data set in Table 18.1. The data points have been obtained by implementing three different methods as described in the text.*

ison we have also added the inferred OD from a 0.4 µs time average over the last points of the OD time traces.

DATA SET PARAMETERS	MAY 23 2015	JUN 8 2015	JUN 9 2015
P_{probe} [pW]	380	150	140
P_{struct} [nW]	150	200	200
δ_{struct} [MHz]	+140	−175	−175

Table 18.1.: *Experimental parameters belonging to the data shown in Fig. 18.3.*

It is noteworthy, that the long-term methods (purple and yellow points) are symmetric around atomic resonance, whereas the short-term method (blue points) are clearly observed to be asymmetric around $\delta_{\text{probe}} = 0$ with significantly higher ODs obtained on the red-detuned side.

The behavior of the OD obtained by both the short-term and long term methods is consistent over different experimental realization as evident from Fig. 18.3.

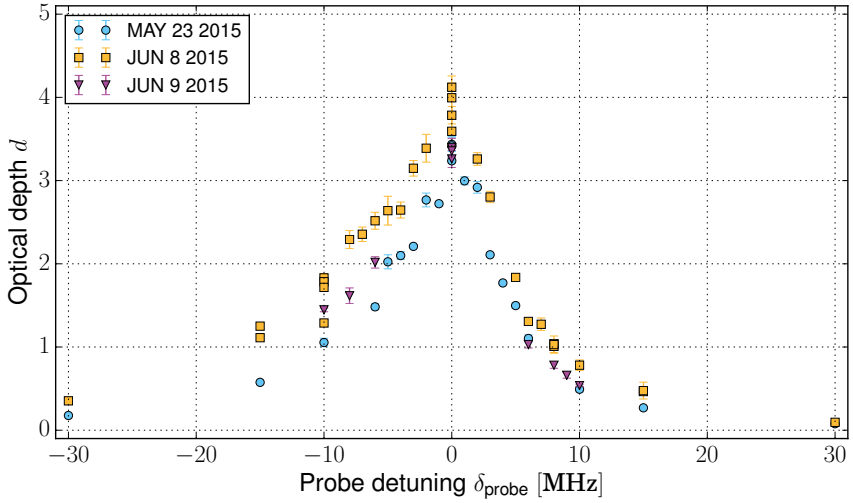

(a) Short-term OD for a 0.4 µs time average. Coherent time average is $\tau = 96$ ns.

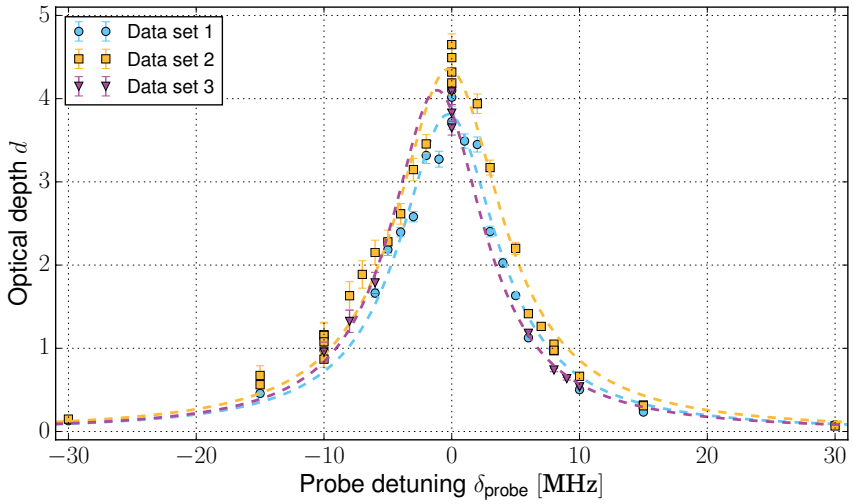

(b) Long-term OD from the linear fit procedure. Coherent time average is $\tau = 192$ ns.

Figure 18.3.: *Extracted OD as a function of the probe detuning δ_{probe}. The experimental parameters used in each data set are given in Table 18.1. Data set 1: May 23 2015, Data set 2: June 8 2015, Data set 3: June 9 2015.*

For the data set to be compared with the model, we performing occasional reference measurements (about every 6th measurement) of the OD of the unstructured atoms, denoted d_{max}, and uses the ratio between the OD of structured ensembles and unstructured ensembles, d/d_{max} as a proxy for the relative atom number $n_4 = N_4/N_{\text{atom}}$.

One of course has to be careful with this approach, since the linear relation between the OD and the total number of atoms N_{atom} is only valid for an optically thin sample. For an off-resonant probe at $\delta_{\text{probe}} = 2\pi \times 8\,\text{MHz}$, the maximum (unstructured) OD is typically found to be $d_{\text{max}} \approx 1$, as evident in Fig. 18.2, and in this limit the approach is thus justified.

19

THEORETICAL MODEL FOR THE ATOMIC BRAGG MIRROR

In collaboration with our colleagues Ivan Iakoupov and Anders S. Sørensen we have developed a theoretical model for the reflectance off a 1D atomic ensemble, build upon the transfer matrix formalism [Deutsch *et al.*, 1995; Chang *et al.*, 2012]. In the following we go through the principles behind this model and discuss how it is numerically implemented for an atomic ensemble structured by hyperfine pumping. Finally, we compare the model with our experimental findings.

19.1 HAMILTONIAN

To derive the reflection and transmission coefficients of the 1D TOF-trapped atomic ensemble we model each atom as a two-level system, see Fig. 19.1. To describe the light-atom interactions we use the fully

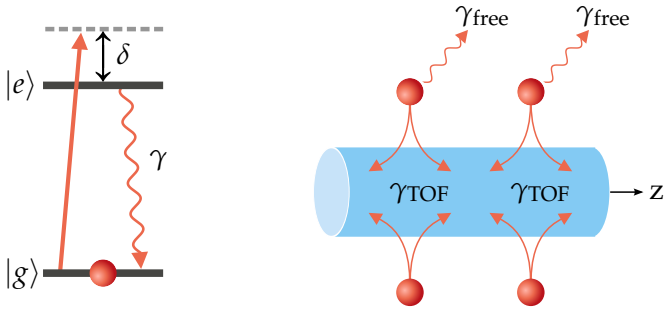

Figure 19.1.: *Light scattered off an effective two-level atom (left) into a TOF (right).*

quantized version of the Hamiltonian given in Section 5.4. Only interactions with TOF-guided modes are considered and the Hamiltonian can therefore be simplified to 1D. For a single atom positioned at z_j along the TOF-axis we then have in the RWA:

$$\hat{H} = \hbar\left(\omega_{eg} - i\frac{\gamma_{\text{free}}}{2}\right)\hat{\sigma}_{ee} + \int_{-\infty}^{\infty} \hbar c|k|\hat{a}_k^\dagger \hat{a}_k \,\mathrm{d}k \qquad (19.1)$$
$$- \hbar \int_{-\infty}^{\infty} \left(g_{eg}\hat{\sigma}_{eg}\hat{a}_k \mathrm{e}^{ikz_j} - g_{ge}^*\hat{\sigma}_{ge}\hat{a}_k^\dagger \mathrm{e}^{-ikz_j}\right)\mathrm{d}k\,.$$

The first term concerns the energy of the unperturbed atom, *cf.* Eq. (5.6), where we have included a non-Hermitian quantum jump operator to account for losses from the radiative decay of the atom into all other

channels than the TOF-guided mode. Since, we will keep track of the decay into the TOF by measuring the reflection and transmission, this is not a loss channel and should therefore not be included in the dissipative term. We will use

$$\gamma = \gamma_{\text{TOF}} + \gamma_{\text{free}}\,. \tag{19.2}$$

to designate the total decay rate out of the exited state $|e\rangle$ with γ_{TOF} and γ_{free} accounting specifically for decay into the TOF and all other modes respectively. The second term in the Hamiltonian yields the energy of the isolated light modes, here written as a continuum. For the frequency range of interest, we have assumed that a linear dispersion relation is valid such that $\omega(k) = c|k|$. Finally, the third term contains the light-atom interaction with

$$g_{eg} \equiv i\sqrt{\frac{\omega_k}{2\epsilon_0\hbar V}}\mu_{eg}\,, \tag{19.3}$$

used for the light-atom coupling of the dipole transition between the two atomic levels.

When dealing with reflections off the atomic ensemble both left- and right-propagating field modes will be present in the TOF. We therefore divide the annihilation and creation operators into two non-interacting groups consisting of the left-going modes $\hat{a}_{\text{left},k}$ and right-going modes $\hat{a}_{\text{right},k}$. Using these, we define two new field operators for the annihilation of either a left- or right-propagating photon at position z [Chang *et al.*, 2007]:

$$\hat{E}_{\text{left}}(z) = \frac{1}{\sqrt{2\pi}}\int_{-\infty}^{\infty}\hat{a}_{\text{left},k}\mathrm{e}^{ikz}\,\mathrm{d}k\,, \tag{19.4a}$$

$$\hat{E}_{\text{right}}(z) = \frac{1}{\sqrt{2\pi}}\int_{-\infty}^{\infty}\hat{a}_{\text{right},k}\mathrm{e}^{ikz}\,\mathrm{d}k\,, \tag{19.4b}$$

which obey the commutation relations:

$$\left[\hat{E}_{\text{left}}(z), \hat{E}^{\dagger}_{\text{left}}(z')\right] = \left[\hat{E}_{\text{right}}(z), \hat{E}^{\dagger}_{\text{right}}(z')\right] = \delta(z-z')\,, \tag{19.5a}$$

$$\left[\hat{E}_{\text{left}}(z), \hat{E}^{\dagger}_{\text{right}}(z')\right] = \left[\hat{E}_{\text{right}}(z), \hat{E}^{\dagger}_{\text{left}}(z')\right] = 0\,. \tag{19.5b}$$

With these definitions, and assuming $g = g_{eg}$ to be real and independent of frequency, we arrive at the final Hamiltonian (the derivation can be found in Appendix H):

$$\begin{aligned}\hat{H} = {} & \hbar\left(\omega_{eg} - i\frac{\gamma_{\text{free}}}{2}\right)\hat{\sigma}_{ee} \\ & + i\hbar c\int_{\infty}^{\infty}\left(\hat{E}^{\dagger}_{\text{left}}\frac{\partial\hat{E}_{\text{left}}}{\partial z} - \hat{E}^{\dagger}_{\text{right}}\frac{\partial\hat{E}_{\text{right}}}{\partial z}\right)\mathrm{d}z \\ & - \hbar g\sqrt{2\pi}\int_{\infty}^{\infty}\delta(z-z_j)(\hat{\sigma}_{eg}\left(\hat{E}_{\text{left}}(z) + \hat{E}_{\text{right}}(z)\right) + \text{h.c.})\,\mathrm{d}z\,.\end{aligned} \tag{19.6}$$

Solving for the dynamics of the light and atomic operators we will be able to arrive at expressions for the reflection and transmission coefficients.

19.2 REFLECTION AND TRANSMISSION COEFFICIENTS

The time-evolution for a general operator $\hat{O}$ under influence of a Hamiltonian $\hat{H}$ can be obtained by using the Heisenberg equation of motion [Sakurai, 1994]:

$$\dot{\hat{O}} = \frac{1}{i\hbar}\left[\hat{O}, \hat{H}\right] . \tag{19.7}$$

From the Hamiltonian given in Eq. (19.6) we obtain the equations of motion for the light operators[1]:

$$\left(\frac{1}{c}\frac{\partial}{\partial t} - \frac{\partial}{\partial z}\right)\hat{E}_{\text{left}} = \frac{ig\sqrt{2\pi}}{c}\delta(z - z_j)\hat{\sigma}_{ge} , \tag{19.8a}$$

$$\left(\frac{1}{c}\frac{\partial}{\partial t} + \frac{\partial}{\partial z}\right)\hat{E}_{\text{right}} = \frac{ig\sqrt{2\pi}}{c}\delta(z - z_j)\hat{\sigma}_{ge} . \tag{19.8b}$$

Similarly, we find for the (coherence) atomic operator:

$$\begin{aligned}\dot{\hat{\sigma}}_{ge} = &-(i\omega_{eg} + \frac{\gamma_{\text{free}}}{2})\hat{\sigma}_{ge} \\ &+ ig\sqrt{2\pi}\big(\hat{E}_{\text{left}}(z_j) + \hat{E}_{\text{right}}(z_j)\big)\hat{\sigma}_{gg} \\ &- ig\sqrt{2\pi}\big(\hat{E}^{\dagger}_{\text{left}}(z_j) + \hat{E}^{\dagger}_{\text{right}}(z_j)\big)\hat{\sigma}_{ee} ,\end{aligned} \tag{19.9}$$

where we have made use of the commutation relations given in Eq. (5.14b). In the low-saturation regime; $s \approx 0$, and from the steady-state solution of the populations given in Eq. (6.16a), we have that most of the population stays in the ground state. We can therefore approximate $\hat{\sigma}_{gg} \approx 1$ and $\hat{\sigma}_{ee} \approx 0$. In doing so, we also replace the quantum operators by the complex-valued expectation values instead and so Eq. (19.9) reduces to:

$$\dot{\sigma}_{ge} = -(i\omega_{eg} + \frac{\gamma_{\text{free}}}{2})\sigma_{ge} + ig\sqrt{2\pi}\big(E_{\text{left}}(z_j) + E_{\text{right}}(z_j)\big) . \tag{19.10}$$

Similarly, we then have for the wave equations of the left- and right-guided TOF models, Eq. (19.8):

$$\left(\frac{1}{c}\frac{\partial}{\partial t} - \frac{\partial}{\partial z}\right)E_{\text{left}}(z) = \frac{ig\sqrt{2\pi}}{c}\delta(z - z_j)\sigma_{ge} , \tag{19.11a}$$

$$\left(\frac{1}{c}\frac{\partial}{\partial t} + \frac{\partial}{\partial z}\right)E_{\text{right}}(z) = \frac{ig\sqrt{2\pi}}{c}\delta(z - z_j)\sigma_{ge} . \tag{19.11b}$$

Together with Eq. (19.10) these equations constitute the Maxwell-Bloch equations and from their solutions we can derive the amplitude reflection and transmission coefficients, r and t, for a single atom. This is

1 Here we have used the handy relation; $\left[\hat{A}, \hat{B}\hat{C}\right] = \left[\hat{A}, \hat{B}\right]\hat{C} + \hat{B}\left[\hat{A}, \hat{C}\right]$.

carried out in Appendix I to which we refer the interested reader, here we simply state the results:

$$r(\delta) = -\frac{\gamma_{\mathrm{TOF}}}{\gamma - 2i\delta}\,, \tag{19.12a}$$

$$t(\delta) = \frac{\gamma_{\mathrm{free}} - 2i\delta}{\gamma - 2i\delta}\,. \tag{19.12b}$$

19.2.1 *Inhomogeneous broadening*

The reflection and transmission coefficients as given in Eq. (19.12) implicitly assume all the TOF-trapped atoms to be identical. This is, however, not the case since the waist of the TOF is not perfectly homogeneous over the range of the trapped atoms. The spatially dependent AC Stark shift induced by the dual-color TOF-trap is therefore different for each atom and in effect causes an inhomogeneous broadening of the transition. In the model, this can be taken into account by assigning an additional shift of the probe detuning δ_j for each individual atom drawn from a suitable distribution. The amplitude reflection and transmission coefficients for the j'th atoms then become:

$$r_j(\delta) = -\frac{\gamma_{\mathrm{TOF}}}{\gamma - 2i(\delta + \delta_j)}\,, \tag{19.13a}$$

$$t_j(\delta) = \frac{\gamma_{\mathrm{free}} - 2i(\delta + \delta_j)}{\gamma - 2i(\delta + \delta_j)}\,. \tag{19.13b}$$

19.3 TRANSFER MATRIX

In this section we use the powerful concept of transfer matrices to extend the modeled scattering off a single atom, via the two expressions for the reflection and transmission coefficients in (19.13), to the overall scattering off an array of atoms taking their spatial distribution into account.

For an atom located at z_j we define $z_j^{\pm} \equiv z_j \pm \varepsilon$ for the positions immediately to the left and right of the atom. The left- and right-scattered fields off the atom can then we written as

$$E_{\mathrm{left}}(z_j^-) = t_j E_{\mathrm{left}}(z_j^+) + r_j E_{\mathrm{right}}(z_j^-)\,, \tag{19.14a}$$

$$E_{\mathrm{right}}(z_j^+) = t_j E_{\mathrm{right}}(z_j^-) + r_j E_{\mathrm{left}}(z_j^+)\,. \tag{19.14b}$$

The single atom transfer matrix M^j_{atom} connecting all the field modes on one side of the atom with respect to the fields modes on the other side are then defined such that

$$\begin{pmatrix} E_{\mathrm{right}}(z_j^+) \\ E_{\mathrm{left}}(z_j^+) \end{pmatrix} = M^j_{\mathrm{atom}} \begin{pmatrix} E_{\mathrm{right}}(z_j^-) \\ E_{\mathrm{left}}(z_j^-) \end{pmatrix}. \tag{19.15}$$

Combining equations Eq. (19.13) to Eq. (19.15) we obtain

$$M^j_{\text{atom}} = \frac{1}{t_j}\begin{pmatrix} t_j^2 - r_j^2 & r_j \\ -r_j & 1 \end{pmatrix} = \begin{pmatrix} 1-\xi_j & -\xi_j \\ \xi_j & 1+\xi_j \end{pmatrix}, \tag{19.16}$$

where we have introduced the single atom scattering parameter ξ_j defined as

$$\xi_j \equiv \frac{\gamma_{\text{TOF}}}{\gamma_{\text{free}} - 2i(\delta + \delta_j)}. \tag{19.17}$$

The transfer matrix for free propagation in the TOF between successive atoms is given by

$$M^j_{\text{TOF}} = \begin{pmatrix} \mathrm{e}^{ikd_j} & 0 \\ 0 & \mathrm{e}^{-ikd_j} \end{pmatrix}, \tag{19.18}$$

where d_j is the propagation distance between the j'th and $(j+1)$'th atom, *i.e.*, $z_{j+1} = z_j + d_j$, such that we have

$$\begin{pmatrix} E_{\text{right}}(z^-_{j+1}) \\ E_{\text{left}}(z^-_{j+1}) \end{pmatrix} = M^j_{\text{TOF}} \begin{pmatrix} E_{\text{right}}(z^+_j) \\ E_{\text{left}}(z^+_j) \end{pmatrix}. \tag{19.19}$$

The transfer matrix for the whole ensemble is obtained by multiplying all the transfer matrices for the scattering off all the individual atoms and the free propagation in between in the order of appearance:

$$M_{\text{ensemble}} = M^N_{\text{TOF}} M^N_{\text{atom}} \ldots M^1_{\text{TOF}} M^1_{\text{atom}}. \tag{19.20}$$

If M_{ensemble} is written out as

$$M_{\text{ensemble}} = \begin{pmatrix} M_{11} & M_{12} \\ M_{21} & M_{22} \end{pmatrix}, \tag{19.21}$$

then the reflection and transmission coefficients for the whole ensemble are simply given by, *cf.* Eq. (19.16):

$$r = \frac{M_{12}}{M_{22}}. \tag{19.22a}$$

$$t = \frac{1}{M_{22}}. \tag{19.22b}$$

With the transfer matrix given for the 1D atomic crystal we can proceed to show how we numerically implement the model to yield the ensemble reflection and transmission coefficients for a given set of input parameters. We will start out by given the input parameters to the model and then move on to explain how we the model algorithm is build up.

19.4 INPUT PARAMETERS

INITIAL ATOM NUMBER (N_{ATOM}) For an optically thin sample the reflectance scales with the number of scatterers. The initial number of trapped atoms N_{atom} is therefore a vital variable that should be known in order to predict the performance of our atomic mirror. Specifically for the numerical implementation, it is needed to set up the number of transfer matrices that should be used in the algorithm, *cf.* Eq. (19.20).

OPTICAL DEPTH PER ATOM (α) The amount of light scattered into the TOF depends on how strongly the atoms are coupled to the guided modes. In the expressions written above for the reflection and transmission coefficients, Eq. (19.13), this is given by the decay rate into the TOF γ_{TOF}. We also know another parameter for the measure of the light-atom coupling strength, namely the optical depth (OD) per atom α as given in Eq. (6.30). Since the latter variable is easy measurable we prefer to talk in terms of this rather than the former. To understand the parameter that we feed into the model and its outcome, of course, we need to establish a link between the two quantities. Taking inhomogeneous broadening of the atomic transition into account, we have for the on-resonance OD per atom (the derivation can be found in Appendix J):

$$\alpha_0 = 2\,\mathrm{Re}\int_{-\infty}^{\infty} \mathcal{D}(\delta')\frac{\gamma_{\mathrm{TOF}}}{\gamma - 2i\delta'}\,\mathrm{d}\delta', \tag{19.23}$$

with $\mathcal{D}(\delta)$ being the probability density function describing the distribution of the broadened transition. For simplicity, we have taken it to be a Gauss distribution with variance σ_δ^2 and zero mean:

$$\mathcal{D}(\delta') \to \mathcal{G}(\delta', \sigma_\delta) = \frac{1}{\sigma_\delta\sqrt{2\pi}}\exp\left(-\frac{\delta'^2}{2\sigma_\delta^2}\right). \tag{19.24}$$

We have estimated the inhomogeneous broadening to be $\sigma_\delta = 0.41\gamma$, see Section J.2 for details.

STRUCTURING PUMP STRENGTH (ζ) The shaping of the atoms into a Bragg grating is carried out by optical pumping, *cf.* Section 12.2. The degree of localization of the atoms with respect to the Bragg condition is therefore directly linked to the strength of the structuring pulse, *i.e.*, the pump beam. In the experiment this is set by either tuning the temporal length of the structuring pulse or its optical power. In the algorithm we use the dimensionless parameter ζ as a knob for the probability of an atom to be optically pumped, see Eq. (19.25) in the following section.

NUMBER OF ENSEMBLE REALIZATIONS (N_{ENSEMBLE}) Experimentally, the loading of atoms into the TOF-trap is a stochastic process which yields a different random filling of the trap sites for each realization. A single ensemble realization (both experimentally and in the theoretical model) is therefore not adequate to describe the overall average reflectance from an ensemble with otherwise fixed parameters for N_{atom}, α, and ζ, since, for example, the initial distribution of the atoms might be near-perfectly coinciding with the structuring pulse nodes or antinodes. In this extreme case the reflectance would be clearly over- or underestimated. This probabilistic nature of the initial position of each atom is therefore taken into account in the model by averaging the reflection and transmission coefficients over N_{ensemble} simulated ensemble realizations.

19.5 NUMERICAL IMPLEMENTATION

ATOMIC SEPARATION In the numerical implementation of the model, we neglect the spatial periodicity of the TOF-trap and take the atoms to be uniformly distributed along the length of the ensemble. The procedure to obtain d_j's is as follows:

- $N = N_{\text{atom}}$ random numbers $\{x_1, x_2, \ldots, x_N\}$ are drawn from the uniform distribution on the interval $[0, 1)$.
- These numbers are sorted in ascending order, such that a new sequence $\{y_1, y_2, \ldots, y_N\}$ is obtained, where $y_j \leq y_{j+1}$.
- The positions of the atoms are given by $z_j = L y_j$, where L is the total length of the ensemble.
- The distances between the atoms are then given by $d_j = z_{j+1} - z_j$, where we define $z_{N+1} = L$.

OPTICAL PUMPING In Section 12.2 we showed how we utilize a standing wave (SW) to optically pump a structure onto the internal states of the atoms that supports the Bragg condition given in Eq. (12.12). In the following, we describe how this effect can be incorporated into the theoretical model, using the dark scheme as an example (*cf.* Section 12.2.2).

To each atom we assign a probability p^j_{dark} to remain in the bright state $|g\rangle$ after the structuring pulse (with dimensionless pump strength parameter ζ and wavelength $\lambda^{\text{TOF}}_{\text{struct}}$ within the TOF):

$$p^j_{\text{dark}} = \mathrm{e}^{-\zeta \cos^2(2\pi z_j / \lambda^{\text{TOF}}_{\text{struct}})} . \tag{19.25}$$

The probability of an atom to undergo a transition from the bright state to the dark state, $|g\rangle = |4\rangle \rightarrow |3\rangle$, is thus given by $1 - p_j$. In the

numerical algorithm, this is simulated by creating an array consisting of N random numbers drawn from a uniform distribution on $[0, 1)$ and compared with p^j_{dark} for each atom, *i.e.*, each element in the array. The probability of such a random number to be smaller than p^j_{dark} is equal to p^j_{dark} and the probability to be larger than p^j_{dark} is equal to $1 - p^j_{\text{dark}}$. For the depumped atoms, M^j_{atom} is replaced by the identity matrix.

Each realization of an atomic ensemble is thus comprised of

- An array of detunings δ_j.
- An array of positions z_j (with the d_j's derived from it).
- An array of random numbers to characterize the pumping process.

From these arrays the transfer matrix M_{ensemble}, Eq. (19.20) is calculated, from which the reflection and transmission coefficients for a single ensemble realization, r_i and t_i, are obtained by the use of Eq. (19.22). In repeating this procedure N_{ensemble} times we obtain the average reflection and transmission coefficients over N_{ensemble} stochastic ensemble realizations where the std can be made arbitrarily small by simply increasing N_{ensemble}.

19.6 COMPARISON BETWEEN THEORY AND EXPERIMENT

We now compare our experimental results with the transfer matrix model for the reflection off atoms that have been structured by the SW hyperfine pump beam.

We start by considering the reflectance as a function of the remaining fraction of atoms left in $|4\rangle$ n_4 after the structuring pulse, as shown in Fig. 19.2 where we have used the normalized OD as a proxy for n_4. Evidently, the model fails to predict the data. This is obviously true qualitatively, but also quantitatively there is a discrepancy between the input parameters used in the model and the experimental parameters. Only by using an increased value for the on-resonance OD per atom of $\alpha_0 = 0.81\,\%$ (as compared to the nominal value $\alpha_0 = 0.5\,\%$), are we able to obtain a modeled reflectance above 10 %, while keeping the other input parameters fixed at experimentally measured values[2].

In Fig. 19.3 we investigate how the model compares to the data when the probe detuning is varied. Here the model performance is, at first sight, observed to be better on the qualitative side, and predicts the

2 In connection with this particular data set we measured the atom number before and after the reflection measurement series and found $N_{\text{atom}} = 1440$ and $N_{\text{atom}} = 1140$, respectively. For the modeling we therefore used the average value $\langle N_{\text{atom}} \rangle = 1292$.

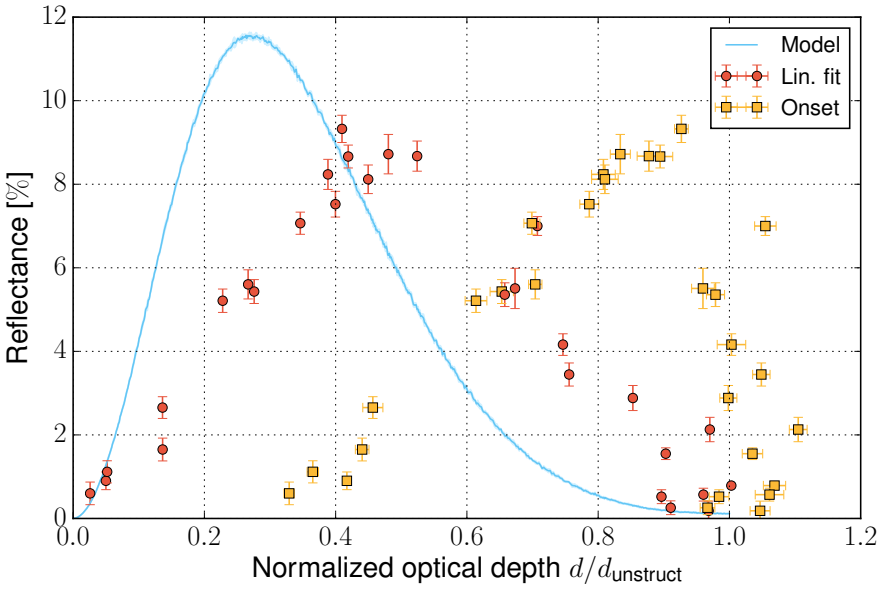

Figure 19.2.: *Model and data comparison for the atomic Bragg mirror as a function of the OD normalized to the OD obtained for unstructured atoms. Data points: The reflectance is inferred from the Debye-Waller fit,* cf. *Section 16.3, $d/d_{unstruct}$ is inferred using both the long-term linear fit procedure (red) and the short-term* 0.4 µs *time average at the probe onset (yellow),* cf. *Chapter 18. The experimental parameters belongs to the June 9 entry in Table 15.4. Model input parameters: $N_{atom} = 1292$, $\delta_{probe} = 2\pi \times 8\,\text{MHz}$, $\sigma_\delta = 0.41\gamma$, $\alpha_0 = 0.81\,\%$. The modeled curve is scaled down according to the decrease of the Debye-Waller factor f_{DW} during the time delay between the end of the structuring pulse and the probing* $(0.3\,\mu\text{s} + 0.2\,\mu\text{s})$ *with* $\langle\, \tau_{DW} \,\rangle = 0.89\,\mu\text{s}$ *for the characteristic time constant in f_{DW},* cf. *Fig. 16.2. The x-axis for the modeled curve corresponds to varying the structuring pump strength ζ, from which a corresponding n_4 is found by using Eq. (12.15).*

same double-peak structured as experimentally observed. However, this is only true when cranking up the input parameter for the total atom number N_{atom} to 1950 atoms, while keeping the remaining input parameters fixed at the same values as used in Fig. 19.2, and setting $n_4 = 42\,\%$ according to the normalized OD at which the maximum data point in Fig. 19.2 is found (when using the long-term OD). If we would use $N_{\text{atom}} = 1292$ instead, the model again performs very poorly as evident from Fig. 19.4. If we would also decrease α_0 to our nominal value the double-peak would vanish all together and the maximum modeled reflectance would be even lower.

It is thus evident, that the experimental data cannot be described by the transfer matrix formalism, when neglecting saturation effects in the model, and when hyperfine pumping is the only physical mechanism included in the model.

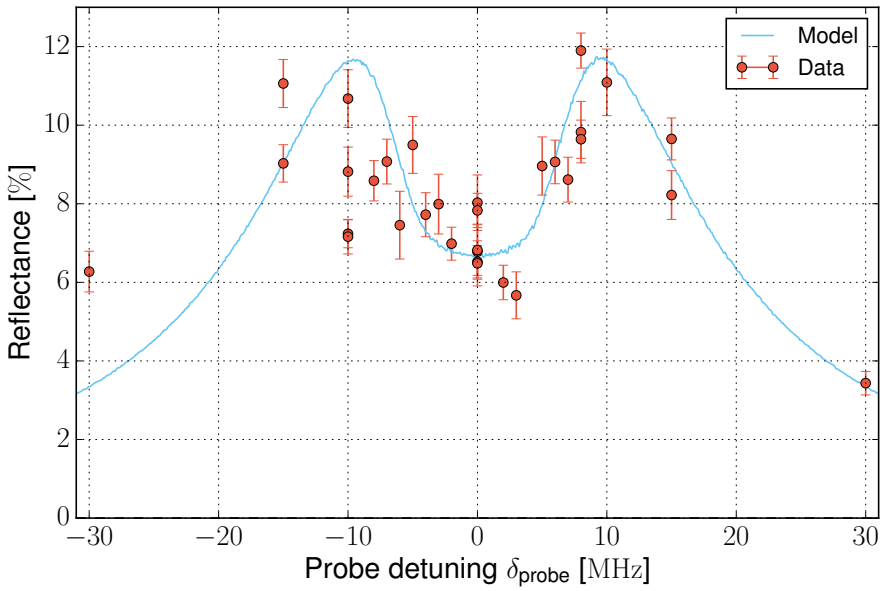

Figure 19.3.: *Model and data comparison for the atomic Bragg mirror as a function of the probe detuning. Reflectance is inferred from the Debye-Waller fit. Model input parameters:* $N_{atom} = 1950$, $n_4 = 42\,\%$, $\sigma_\delta = 0.41\gamma$, $\alpha_0 = 0.81\,\%$.

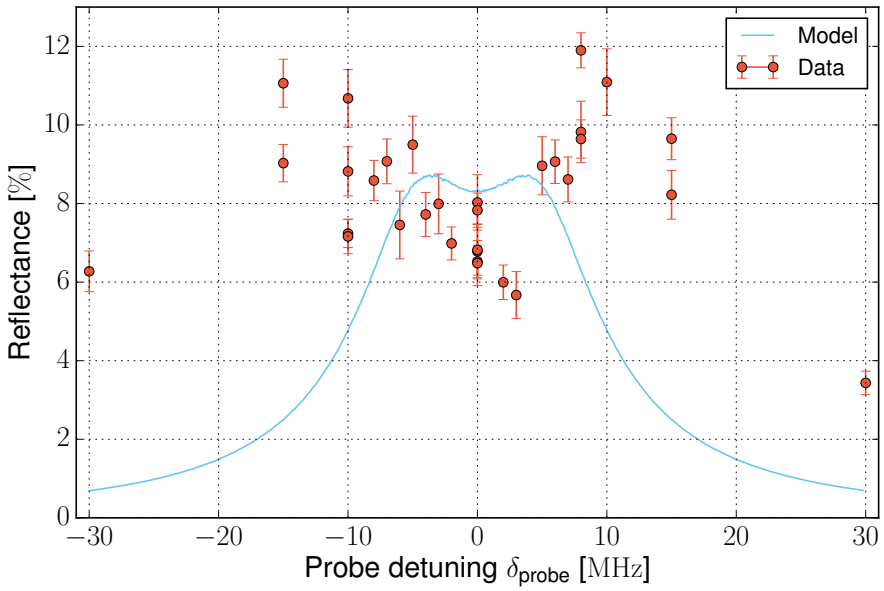

Figure 19.4.: *Model and data comparison for the atomic Bragg mirror as a function of the probe detuning. Reflectance is inferred from the Debye-Waller fit. Model input parameters:* $N_{atom} = 1292$, $n_4 = 42\,\%$, $\sigma_\delta = 0.41\gamma$, $\alpha_0 = 0.81\,\%$.

20

DIPOLE FORCE FROM THE STRUCTURING PULSE

By now, we have given several hints that the structuring pulse does not only pump the atoms out of $|4\rangle$ as described in Section 12.2, but also pulls the atoms towards the TOF and towards the antinodes of the structuring SW. In fact, a quick estimate reveals that at maximum $N_{\mathrm{sc}} = \gamma_{\mathrm{sc}} t_{\mathrm{struct}} = \gamma t_{\mathrm{struct}}/2 \approx 4$ photons can be scattered off the atoms during the short $t_{\mathrm{struct}} = 250\,\mathrm{ns}$ structuring pulse (by setting the exited state population equal to one half at saturation). So, it appears that for finite power of the structuring pulse atoms are not very efficiently pumped to the dark hyperfine ground state!

In this last chapter, we present our current interpretation of the experimental results presented for the atomic Bragg mirror by considering additionally the dipole force exerted on the atoms by the structuring pulse. Preliminary simulations, using the transfer matrix model described in Chapter 19, but with the structuring pulse dipole force now included, show closer agreement with the experimentally observed features.

20.1 TEMPORAL DYNAMICS IN THE TRANSMISSION

Let us first consider the typical dynamics we observe in the transmission signal. In Fig. 20.1 we show this in terms of the extracted OD, *cf.* Section 13.4, for a signal belonging to a realization of the atomic Bragg mirror with about $\mathcal{R} = 10\,\%$. The short 250 ns structuring pulse is turned off at $t = -0.3\,\mu\mathrm{s}$. When the probe is turned on at $t = 0$, the OD is observed to quickly increase from about 0.9 to 1.1, whereafter it makes a sudden turnaround and dramatically decrease to about 0.3. Within the first 10 µs of the measurement, the transmission thus increases by about 40 percentage points which is remarkably rapid, when compared to the trap lifetime being on the order of milliseconds.

Two things can cause the observed initial increase in OD. Either more atoms enter into the mode area of the probe, or the coupling between the probe and the atoms increases. The former is quite improbable, as the measurement is conducted 11 ms after trap loading and would require some conspiracy to explain why the observed increase in OD always occur at the same time. The latter, on the other hand, can be

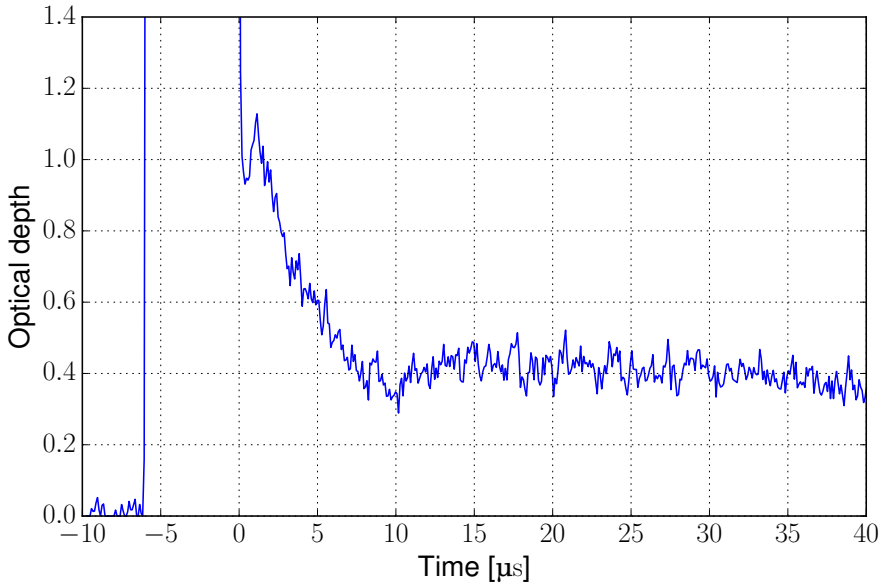

Figure 20.1.: OD *extracted from a transmission signal acquired with experimental parameters resulting in a reflectance of about* 10 %*:* $P_{struct} = 2 \times 204\,\mathrm{nW}$, $\delta_{struct} = 2\pi \times -175\,\mathrm{MHz}$, $P_{probe} = 140\,\mathrm{pW}$, $\delta_{probe} = 2\pi \times 8\,\mathrm{MHz}$.

explained by the attractive dipole force exerted on the atoms by the structuring pulse.

Approximating the inward radial trap potential as a harmonic oscillator and assuming an atom starting initially at rest, the atom after receiving a momentum kick towards the fiber reaches its maximum excursion after a quarter of a radial trap oscillation cycle. With the measured radial trap frequency of 83 kHz this happens after 3 µs. Atoms with high enough acquired radial kinetic energy will crash into the fiber surface during this time. Atoms with gained radial kinetic energy slightly below the repulsive barrier height will turn around and move towards the soft part of the radial potential far away from the fiber where they spend a long time without being efficiently coupled to fiber-guided probe light. Any additional axial acquired kinetic energy together with the true anharmonic and nonseparable nature of the trap potential makes a large fraction of these atoms never return to the vicinity of the fiber surface.

20.2 BACK OF THE ENVELOPE CALCULATION

In order to verify the above statements about the structuring pulse induced atomic motion, we present here an estimate of the strength

of the momentum kick delivered to the atoms by the dipole force of the structuring pulse, *cf.* Section 6.7.2 we have

$$\Delta p = \mathbf{F}_{\text{dipole}} \Delta t = \boldsymbol{\nabla} U_{\text{dipole}} t_{\text{struct}} \,. \tag{20.1}$$

Being in the low saturation regime[1], $s_0 \ll 1$, for the far-detuned structuring pulse, allows us to use the AC Stark shift as a proxy for the dipole potential induced by the structuring pulse. Rewriting it a bit, we have for the AC Stark shift of the $|4\rangle$ ground state:

$$\Delta E_4 = \frac{\hbar \Omega^2}{4\delta} = \hbar \gamma \frac{\Omega^2/\gamma^2}{4(\delta/\gamma)^2} \frac{\delta}{\gamma} \,. \tag{20.2}$$

We now use that the excited state population, Eq. (6.16a), for low saturation and $|\,\delta\,| \gg \gamma$ can be approximated as

$$\bar{\rho}_{ee} \approx \frac{s_0/2}{4(\delta/\gamma)^2} = \frac{\Omega^2/\gamma^2}{4(\delta/\gamma)^2} \,. \tag{20.3}$$

Collecting the three above equations, we can set up an expression for the velocity gain acquired by the atoms during the structuring pulse, if we use the propagation constant β, setting the characteristic length scale, as a proxy for the gradient. We then obtain

$$\Delta v = \frac{\Delta p}{m} = \gamma \bar{\rho}_{ee} t_{\text{struct}} \frac{\delta}{\gamma} \frac{\hbar \beta}{m} \tag{20.4a}$$

$$= N_{\text{sc}} v_{\text{recoil}} \frac{\delta}{\gamma} \,, \tag{20.4b}$$

where the second equality follows when using $N_{\text{sc}} = \gamma_{\text{sc}} t_{\text{struct}} = \gamma \bar{\rho}_{ee} t_{\text{struct}}$ for the number of scattered photons per atom and $v_{\text{recoil}} = \hbar\beta/m$ for the (axial) recoil velocity transferred to the atom, with $\beta = 2\pi/\lambda_{\text{struct}}^{\text{TOF}}$ being the effective wave number. From Table 2.1 we have $\lambda_{\text{struct}}^{\text{TOF}} = 743\,\text{nm}$ which yields $v_{\text{recoil}} = 4\,\text{mm}\,\text{s}^{-1} = 4\,\text{nm}\,\mu\text{s}^{-1}$. Setting the number of scattered photons to be on the order of one, $N_{\text{sc}} \sim 1$, and using $\delta_{\text{struct}}/\gamma = 33$ we estimate an overall velocity kick of $\Delta v \sim 130\,\text{nm}\,\mu\text{s}^{-1}$. From this quick estimate it becomes apparent that the atoms can actually move a substantial distance (recall that the trap minimum is located only about 200 nm from the TOF) in the time scales considered here.

20.3 RATE EQUATION MODEL

Since this preliminary calculation on the velocity kick given by the structuring pulse to the atoms is so significant, we would like to do it

1 If we use an on-resonant OD per atom of $\alpha_0 = 0.5$ percent for the $|4\rangle \to |5\rangle$ transition and take the CG coefficients into account, we find that the saturation power P_{sat} for the three transitions $|4\rangle \to \{|3'\rangle, |4'\rangle, |5'\rangle\}$ is given by $P_{\text{sat}} = \{7.0, 21, 44\}\,\mu\text{W}$, respectively, when $\delta_{\text{struct}} = 2\pi \times -175\,\text{MHz}$. For a typical value of $P_{\text{struct}} = 200\,\text{nW}$ we thus have $s_0 = P_{\text{struct}}/P_{\text{sat}} \approx 0.03 \ll 1$.

a bit more careful by actually calculating the excited state population taking all the three excited states, $|3'\rangle$, $|4'\rangle$, $|5'\rangle$, into account, *i.e.*,

$$\Delta v = \gamma \frac{\hbar\beta}{m} t_{\text{struct}} \sum_e \frac{\rho_{ee}\delta_e}{\gamma} \,. \tag{20.5}$$

We therefore set up a simple rate equation model for the atomic state populations:

$$\begin{pmatrix} \dot\rho_{3'} \\ \dot\rho_{4'} \\ \dot\rho_{5'} \\ \dot\rho_4 \end{pmatrix} = \begin{pmatrix} -(R_{3'}+\gamma) & 0 & 0 & R_{3'} \\ 0 & -(R_{4'}+\gamma) & 0 & R_{4'} \\ 0 & 0 & -(R_{3'}+\gamma) & R_{5'} \\ R_{3'}+\gamma & R_{4'}+\gamma & R_{5'}+\gamma & -(R_{3'}+R_{4'}+R_{5'}) \end{pmatrix} \begin{pmatrix} \rho_{3'} \\ \rho_{4'} \\ \rho_{5'} \\ \rho_4 \end{pmatrix} \tag{20.6}$$

where we have used the shorthand notation $\rho_a = \rho_{aa}$ for the population in $|a\rangle$ with $a = 4, 3', 4', 5'$, and introduced the transition rates[2] R_e between the ground state $|4\rangle$ and the excited state $|e\rangle$.

Taking saturation, the different transition strengths, and the electric field components to get the proper gradient in all directions into account, we obtain an exited state population of only $\rho_e = 4\,\%$ for a structuring power of $P_{\text{struct}} = 200\,\text{pW}$ where the highest reflectance is observed. Cranking up the structuring power to a microwatt still only yields a small population in the excited state with a total of $\rho_e = 16\,\%$. From this we can conclude that minimal hyperfine pumping takes place in the short time the structuring pulse is on. This also means that no Bragg grating is burned onto the internal states of the atoms. Instead, the observed enhancement in reflection must be explained by the atoms structured into a density grating.

20.4 PICTORIAL INTERPRETATION

Using the values for Δv obtained with the rate equation model, we provide here a schematic illustration on how the atoms are spatially focused into a density Bragg grating. In Fig. 20.2 the axial dipole potential resulting from the SW structuring pulse is shown. The dipole force is strongest when the gradient is high and atoms located halfway between a node and an antinode therefore receives the largest momentum kick during the structuring. This is illustrated with the two left-most atoms, which start to slide down the potential hills towards a common minimum. Now, from our dual-color trap geometry, the atoms are in practice separated by at least $d_{\text{trap}} = \lambda_{\text{red}}^{\text{TOF}}/2 = 493\,\text{nm}$, but for creating an efficient Bragg reflector only long range order (*i.e.*,

2 The transition rates are essentially given by $R_e = \sigma_a(\delta)\Phi$, where $\sigma_e(\delta)$ is the absorption cross section associated with the excited state $|e\rangle$, *cf.* Eq. (6.27) and Φ is the photon flux [Milonni *et al.*, 1988].

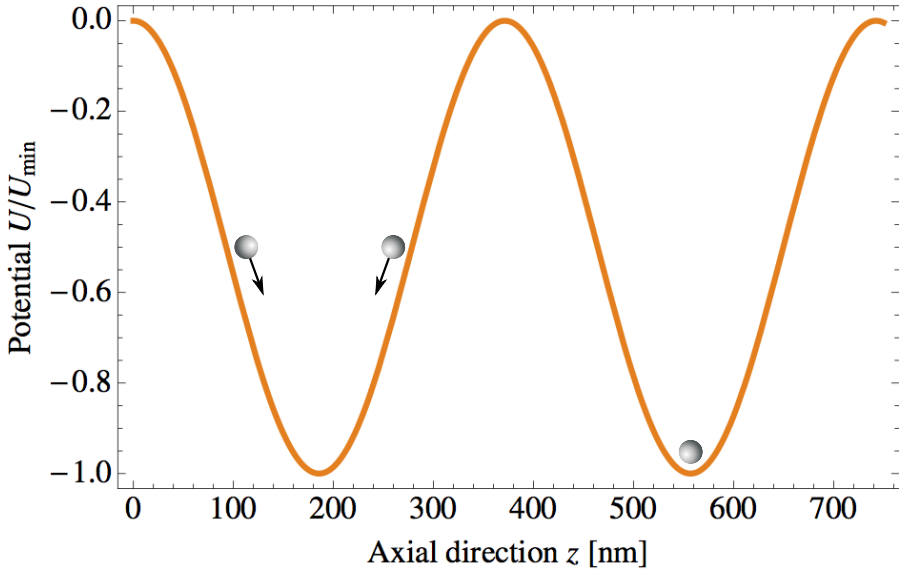

Figure 20.2.: *Axial dipole potential provided by the structuring pulse. Normalized to its minimal value. Gray balls illustrate atoms. The all-time present dual-color trap potential has not been taken into account in this figure.*

modulo half a probe wavelength) is required. The pulsed structuring SW acts on the atoms like an array of microlenses, focusing atomic trajectories towards the antinodes of the field. In fact, all atoms starting not too far from antinodes, where a parabolic approximation to the potential is valid, will reach an antinode at the same time after the structuring pulse.

Let us now consider Fig. 20.3 to see what happens in the radial direction. Here atoms sitting in the antinodes of the structuring field, *i.e.*, in the according minima in Fig. 20.2, receive the largest drag towards the TOF, and thus starts climbing the potential hill provided by the blue trap barrier. From the rate equation model we find that such atoms will move about 50 nm closer to the TOF during the time until the probe is turned on, for a structuring power of 200 nW. In the simulation program we take harmonic motion in the radial direction with the measured trap frequency, in practice the moved distance be somewhat smaller when taking the steeper blue barrier into account.

The kinetic energy of the atoms will increase as a consequence of the induced motion. From the rate equations model, this is inferred to leave the atoms at a higher bound state in the trap with a temperature increase corresponding to $U \approx -0.13\,\mathrm{mK}$ as indicated by the black dashed line in Fig. 20.3. Ultimately, this means that the atoms are heated faster out of the trap.

Overall, the axial and radial motion can be visualized as a spatial focusing of the atoms as illustrated in Fig. 20.4. As indicated by the

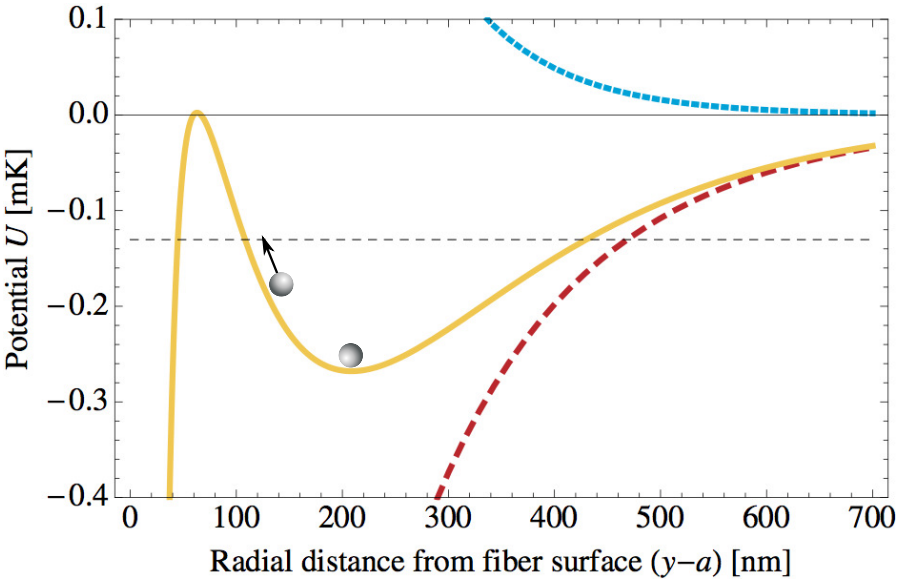

Figure 20.3.: *Structuring induced radial motion of an atom in the trap potential. The radial potential provided by the structuring pulse resemble that of the red dashed curve, but with a steeper slope due to the shorter wavelength.*

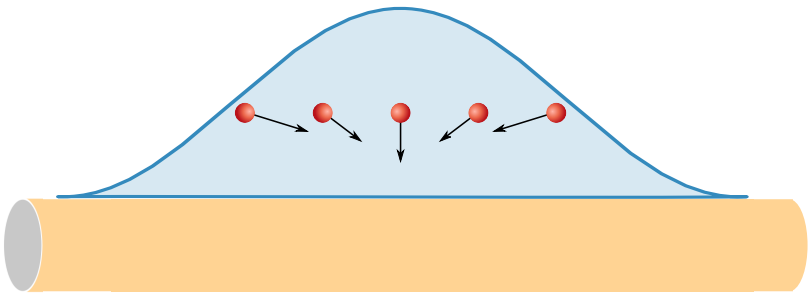

Figure 20.4.: *Atoms (red balls) are focused towards the intensity maximum of the* SW *structuring pulse (blue shaded area) and towards the* TOF.

arrows, atoms near the steep slopes of the SW structuring intensity distribution receives a large axial kick towards the axial location of the intensity maxima, but a somewhat smaller kick in the radial direction since the radial intensity gradient is smaller here. In contrast, the atom already located at the intensity maxima only experience a radial drag towards TOF. Overall, the effect alters the initial density distribution of the trapped atoms with a pitch given by the red trap laser, towards a pitch to that of the structuring SW pulse, and hence to the atomic separation required to fulfill the Bragg condition. In addition, the atoms are transiently moved closer to the fiber enhancing their coupling to the fiber-guided mode substantially.

20.5 PRELIMINARY SIMULATIONS

In Fig. 20.5, Fig. 20.6, and Fig. 20.7 preliminary results for the reflectance are shown, when including the dipole force from the structuring pulse into the model using the transfer matrix formalism, described in Chapter 19. Contrary to the simulations shown in Section 19.6 all the curves shown here are obtained for realistic experimental parameters. We thus use $T = 44\,\mu\text{K}$ for the temperature of the atoms as inferred from the Debye-Waller fit of the decay of the reflection signal, *cf.* Section 16.2.

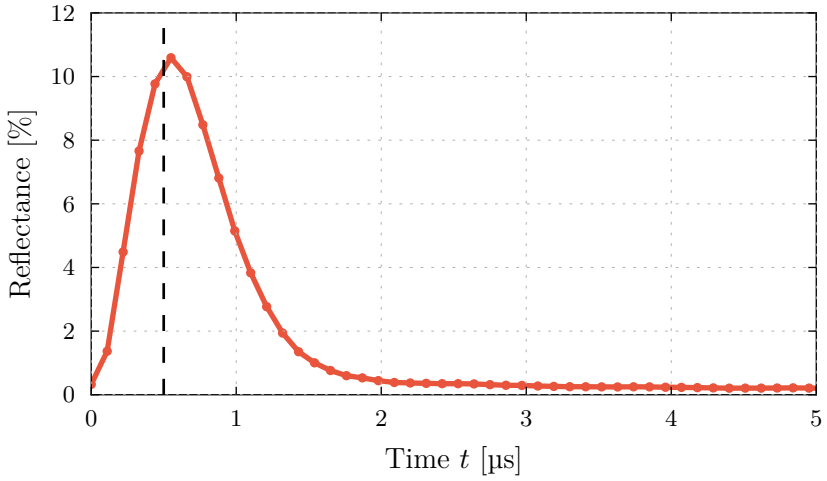

Figure 20.5.: *Simulated reflectance as a function of time. Model input parameters:* $\delta_{probe} = 2\pi \times 8\,\text{MHz}$, $P_{struct} = 200\,\text{nW}$, $\sigma_\delta = 0.41\gamma$. *The vertical dashed line marks the start of the probe interval. For comparison with experimental data see Fig. 14.1.*

In this simplified model the radial trap potential is approximated as a harmonic oscillator with the measured trap frequency, whereas the axial confinement is ignored. While the latter might seem too crude an approximation, it is actually the same approximation that has been made in connection with the Debye-Waller factor. Since the thermal dephasing of reflectance happens fast compared to an axial oscillation cycle in the real trap potential, it can be justified a posteriori. In the model atoms can not only disappear by optical pumping but also by leaving the trap, due to the received momentum kick – either towards infinity or by literally crashing into the TOF. Other input parameters to the model are the atom number and the on-resonance OD per atom, which are both set to their nominal values $N_{\text{atom}} = 1292$ and $\alpha_0 = 0.51\,\%$.

The simulation results presented in the figures match the experimental observations both qualitatively and quantitatively. With the time-

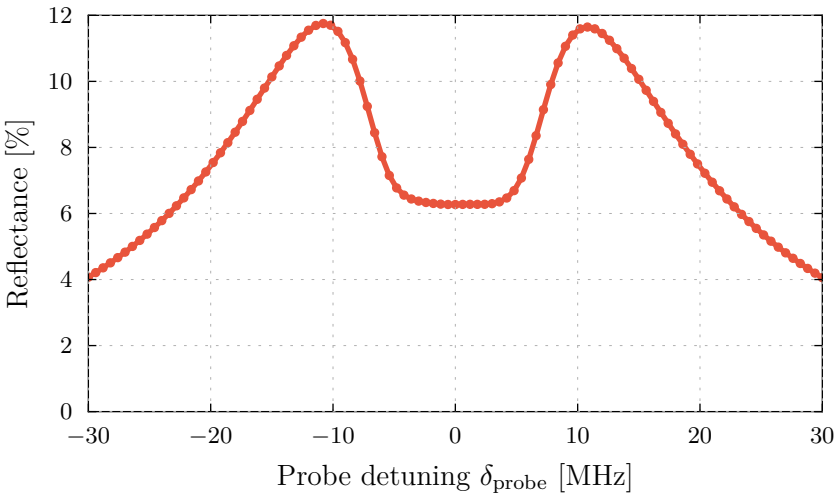

Figure 20.6.: *Simulated reflectance as a function of the probe detuning. Model input parameters:* $P_{struct} = 200\,\text{nW}$, $\sigma_\delta = 0.41\gamma$. *For comparison with experimental data see Fig. 15.2*

trace in Fig. 20.5, for example, seen to decay in about 1 µs exactly as all the reflection signals we have shown over the last chapters.

The two plots showing the predicted reflectance as a function of the probe detuning δ_{probe}, Fig. 20.6, and structuring power P_{struct}, Fig. 20.7, are both extracted at $t = 0.2\,\mu\text{s}$ corresponding to the time where we experimentally observe the reflection signal to peak. The

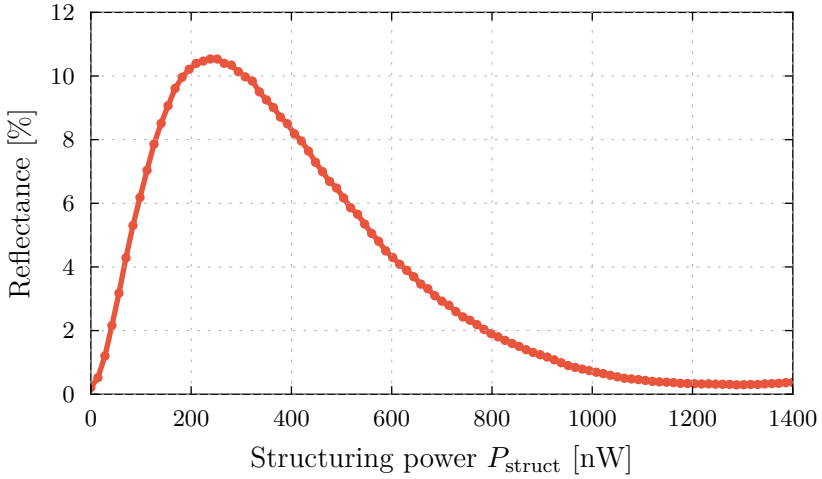

Figure 20.7.: *Simulated reflectance as a function of the structuring power. Model input parameters:* $\delta_{probe} = 2\pi \times 8\,\text{MHz}$, $\sigma_\delta = 0.41\gamma$. *For comparison with experimental data see Fig. 16.3.*

satisfactory agreement between model and data strongly suggests

that only a model including both hyperfine pumping and the mechanical forces exerted by structuring light is catching the salient features observed experimentally.

Part V

IN THE PIPELINE
OUTLOOK AND CONCLUSION

21

CONCLUSION

In this thesis we have studied the usage of a TOF as a platform for collective light-atom interaction.

We have presented a fiber pulling rig with which a standard optical fiber can be tapered reproducible down to sub-micron waist size. For a fiber with an initial diameter of $d_0 = 125\,\mu m$ we have shown that the highest attainable light transmission for a TOF symmetrically pulled with our setup is 91 %. This limitation can be assigned to non-adiabatic coupling to higher order cladding modes in the taper sections. Calculations show, that applying the same pulling procedure for a fiber with an initial diameter of $d_0 = 80\,\mu m$ should result in adiabatic tapers with better transmission.

As an aid to optimize the shape of the tapered sections, we have developed a numerical model for the prediction of the fiber shape given an arbitrary pulling procedure. This relies on an initial easy experimental calibration of the axial viscosity profile of the fiber within the heater, obtained by elongating a fiber by less than the effective width of the heater. Using this snap-shot of the fiber viscosity profile together with a set of differential equations describing the fiber flow, we have found very good agreement between modeled and measured fiber shapes.

We have demonstrated that atoms can be confined in the near proximity of a TOF by means of a dual-color dipole trap. Via an interferometric setup, utilizing a heterodyne optical detection scheme with which a few photons can be resolved within a 96 ns measurement window, we have investigated the coherent back-scattered field from about 1000 trapped atoms. By applying a near-resonant structuring pulse we detected a two order enhancement in the reflectance from Bragg structured atoms when compared to unstructured atoms.

When modeling our experimental observations, we found that sole hyperfine pumping of the atoms into a spin Bragg grating does not explain our results. For the experimental parameters in which we have acquired the highest reflectances, preliminary calculations instead show that the dipole force exerted on the atoms by the SW structuring pulse pulls the atoms into a density Bragg grating.

From about 1000 atoms we have found that more than 10 % of the guided light can be redirected in the backward propagation direction. This is a remarkable result when compared to the only 4 %

reflection found for light hitting a slab of glass containing billions of atoms. 1D free space optical lattices typically contain between hundreds and thousands of atoms in each trapping site. These are shaped as disks, with atoms much stronger localized in the axial direction of the SW than in the two radial ones [Schilke *et al.*, 2011; Slama *et al.*, 2006]. Such systems have shown Bragg reflections of 5 % when probing hundreds of atomic planes [Slama *et al.*, 2006] and 80 % when interacting with 10^7 atoms located in thousands of disks [Schilke *et al.*, 2011]. Compared to these more traditional systems, the high observed power reflectance in our setup clearly demonstrates the promising prospective of the waveguide platform for collective light-atom interaction.

22

OUTLOOK AND FUTURE PERSPECTIVES

22.1 TAPERED OPTICAL FIBER PRODUCTION

ADIABATIC TAPERS In order to use a TOF as an efficient waveguide platform for light-atom interaction, it is necessary to have adiabatic tapers. With calculations showing that this can easily be obtained by simply reducing the cladding to core radius and apply the symmetric pulling procedure, *cf.* Fig. 4.6, this is one of the next thing we should do in the fiber pulling.

Work on inverting the fiber shape model such that the pulling boundary conditions to reach a target shape can be numerically calculated was started in [Knudsen *et al.*, 2014]. The promising preliminary results motivate a continuation of this work which could lead to the production of adiabatic TOFs with the $d_0 = 125\,\mu\text{m}$ fiber we have been using so far.

INTEGRATED RESONATOR The efficient light-atom coupling in the TOF evanescent field can be further enhanced by integrating an optical cavity around the waist. This can be realized in a couple of ways. In the group of A. Rauschenbeutel a finesse $\mathcal{F} \simeq 85$ has been achieved by writing two Bragg mirrors into the fiber before tapering thus forming a Fabry-Pérot resonator around the waist. Despite this rather low finesse when compared to typical cavity QED setups, calculations indicate that this value is sufficient to reach the strong coupling regime [Wuttke *et al.*, 2012].

Another method is to create a ring-resonator by looping the TOF. Here, M. Sumetsky [Sumetsky *et al.*, 2006] has obtained a finesse of $\mathcal{F} \approx 40$ by bending the TOF such that the two tapered sections lie on top of each other. This constitutes a relatively stable loop held together by van der Waals and electrostatic forces. Light can thus either propagate into the loop or couple directly into the other taper through the evanescent field. Few tests on making looped TOFs have already been performed in our fiber pulling rig without much effort, and hence this seems like a promising path to explore.

ALL-INTEGRATED ATOMIC CHIP Currently, experimental setups with TOF-trapped atoms are based on fairly bulky free-space setups where a standard 6-beam MOT is used to provide a reservoir of

cold atoms [Vetsch *et al.*, 2010; Goban *et al.*, 2012; Grover *et al.*, 2015; Gouraud *et al.*, 2015]. It would be interesting to place several TOFs on an atomic chip utilizing a mirror MOT [Reichel *et al.*, 1999; Szmuk *et al.*, 2015], as this indeed would offer a scalable all-integrated system ideal for realizing small quantum networks [Cirac *et al.*, 1997; Choi *et al.*, 2010], with the prospective of teleporting quantum states between each of the TOF-trapped atomic ensembles [Krauter *et al.*, 2013].

22.2 MOVING TO THE NEXT LEVEL

STATE PREPARATION All experiments in the quantum domain will benefit from the preparation of a pure state in the Zeeman manifold of atomic ground states. As of writing, this next step in the experimental procedure has already been implemented. Via optical pumping on the $|4\rangle \rightarrow |4'\rangle$ atoms can be made to rain down into the dark state $|4,0\rangle$. With a subsequent microwave π-pulse on the clock transition the atoms in $|4,0\rangle$ are shelved to the $|3,0\rangle$ level, whereafter any atoms remaining in the hyperfine manifold $|4\rangle$ are heated out of the trap by applying blue detuned (external) MOT light on the $|4\rangle \rightarrow |5'\rangle$ transition. With this procedure more than 40 % of the initial trap load ends up in the target Zeeman state.

RAMAN TRANSFER BETWEEN GROUND STATES The microwave source we currently have available is limited in strength and 6 µs π-pulses are the fastest we can make between ground states. For experiments sensitive to dephasing of coherences by atomic motion, it is advantageous to be able to do state transfer on a time scale fast compared to the inverse trap frequencies. We are currently investigating the implementation of a faster Raman scheme, where two-photon resonances can be used to make coherent transfer of ground state populations.

SPIN SQUEEZING A reduction in the quantum spin projection noise offer improvements to quantum protocols in both quantum information technology applications and for quantum metrology and sensing. Such a reduction in the measurement uncertainty can be achieved by creating a spin squeezed state in the atomic ensemble [Saffman *et al.*, 2009; Appel, Windpassinger, *et al.*, 2009] which we strive to implement in the TOF-trapped atomic ensemble in the near future.

QUANTUM STATE ENGINEERING Aside from their interesting fundamental properties non-classical states are useful ingredients for the successful implementation of quantum assisted metrology and quantum information science. In [Christensen *et al.*,

2013; Christensen *et al.*, 2014] we took the first steps in creating the first excited Dicke state in a mesoscopic free-space atomic ensemble. Apart from the enhanced light-atom coupling the TOF platform offer yet a promising feature for the improvement of creating such a delocalized single spin excitation in the atomic ensemble. Due to the anisotropic scattering rate for an atom coupled to a probe polarized along the SCA, some of the bad spontaneous decay channels that are present in the scheme used in [Christensen *et al.*, 2013; Christensen *et al.*, 2014] are effectively suppressed in the TOF setup.

HYBRID SYSTEMS With the waveguide platform, where "fiber-coupled atoms" are readily offered, light mediated quantum interactions with other distant physical systems, *e.g.*, quantum dots, mechanical resonators, electrical resonators, or NV centers in diamonds, become experimentally realistic. Such a hybrid system opens for the possibility of making clever designs that take advantage of the fact that some quantum systems are more suited for the use as long-lived quantum memories while others offer fast encoding and processing [Xiang *et al.*, 2013; Kurizki *et al.*, 2015].

Part VI

APPENDIX / APPENDICES

A

FUNDAMENTAL FIBER MODE HE_{11} WITH QUASI-LINEAR POLARIZATION

Here the solution to Maxwell's equations (2.3), derived under the two-layer boundary condition (2.2), is given for the electric field mode distribution of the fundamental fiber mode HE_{11} in the case of quasi-linear polarization as given in [Béguin, 2015]. The total field is given by

$$\mathbf{E}_{11}(\mathbf{r},t) = \boldsymbol{\mathcal{E}}_{11}(\rho,\phi,\phi_0)\mathrm{e}^{i(\omega t-\beta_{11}z)}\,.$$

The components of the electric field amplitude are listed below, as expressed in the Cartesian basis. ϕ_0 is introduced in order to define the quasi-linear polarization in the fiber with respect to a fixed reference axis, chosen here to be the x-axis such that $\phi_0 = 0$ yields quasi-linear x polarization in the fiber.

INSIDE THE FIBER, $\rho < a$:

$$\mathcal{E}_x(\rho,\phi,\phi_0) = C\frac{i\beta_{11}}{h\sqrt{2}}\frac{K_1(qa)}{J_1(ha)}\Big(J_2(h\rho)(1+s)\cos(2\phi-\phi_0) - J_0(h\rho)(1-s)\cos(\phi_0)\Big)\,,$$
$$\mathcal{E}_y(\rho,\phi,\phi_0) = C\frac{i\beta_{11}}{h\sqrt{2}}\frac{K_1(qa)}{J_1(ha)}\Big(J_2(h\rho)(1+s)\sin(2\phi-\phi_0) - J_0(h\rho)(1-s)\sin(\phi_0)\Big)\,,$$
$$\mathcal{E}_z(\rho,\phi,\phi_0) = C\sqrt{2}\frac{K_1(qa)}{J_1(ha)}J_1(h\rho)\cos(\phi-\phi_0)\,.$$

OUTSIDE THE FIBER, $\rho > a$:

$$\mathcal{E}_x(\rho,\phi,\phi_0) = -C\frac{i\beta_{11}}{q\sqrt{2}}\Big(K_2(q\rho)(1+s)\cos(2\phi-\phi_0) + K_0(q\rho)(1-s)\cos(\phi_0)\Big)\,,$$
$$\mathcal{E}_y(\rho,\phi,\phi_0) = -C\frac{i\beta_{11}}{q\sqrt{2}}\Big(K_2(q\rho)(1+s)\sin(2\phi-\phi_0) + K_0(q\rho)(1-s)\sin(\phi_0)\Big)\,,$$
$$\mathcal{E}_z(\rho,\phi,\phi_0) = C\sqrt{2}K_1(q\rho)\cos(\phi-\phi_0)\,.$$

With

$$
\begin{aligned}
h^2 &= (k_0 n_{\mathrm{co}})^2 - \beta_{11}^2\,, \\
q^2 &= \beta_{11}^2 - (k_0 n_{\mathrm{cl}})^2\,, \\
s &= \left(\frac{1}{h^2a^2} + \frac{1}{q^2a^2}\right)\left(\frac{J_1^*(ha)}{haJ_1(ha)} + \frac{K_1^*(qa)}{qaJ_1(qa)}\right)^{-1}\,, \\
J_1^*(ha) &= \frac{1}{2}\Big(J_0(ha) - J_2(ha)\Big)\,, \\
K_1^*(qa) &= -\frac{1}{2}\Big(K_0(ha) + K_2(ha)\Big)\,,
\end{aligned}
$$

and

$$
\begin{aligned}
C &= \sqrt{\frac{4\omega\mu_0 P}{\pi a^2 \beta_{11}}}\left(\frac{K_1^2(qa)}{J_1^2(ha)}T_1^{\mathrm{in}} + T_1^{\mathrm{out}}\right)^{-1/2}\,, \\
T_1^{\mathrm{in}} &= (1+s)\Big(1 + \frac{\beta_{11}^2}{h^2}(1+s)\Big)\Big(J_2^2(ha) - J_1(ha)J_3(ha)\Big) \\
&\quad + (1-s)\Big(1 + \frac{\beta_{11}^2}{h^2}(1-s)\Big)\Big(J_0^2(ha) + J_1^2(ha)\Big) \\
T_1^{\mathrm{out}} &= (1+s)\Big(1 - \frac{\beta_{11}^2}{q^2}(1+s)\Big)\Big(K_2^2(qa) - K_1(qa)K_3(qa)\Big) \\
&\quad + (1-s)\Big(1 - \frac{\beta_{11}^2}{q^2}(1-s)\Big)\Big(K_0^2(qa) - K_1^2(qa)\Big)\,.
\end{aligned}
$$

SYMBOL	DESCRIPTION
$\phi_0 = 0$	Quasi-linear x polarization
$\phi_0 = \pi/2$	Quasi-linear y polarization
$U = ha$	Core parameter
$W = qa$	Cladding parameter
$\Lambda = q^{-1}$	Evanescent wave penetration length
J_l	Bessel function of the first kind of order l
K_l	Modified Bessel function of the second kind of order l
C	Normalization constant
P	Total optical power in the fiber

A.1 PROPAGATION CONSTANT

Bounded modes exists when β is a solution to the transcendental equation which must be solved numerically (for β_{11} used above, set $l = 1$):

$$(l\beta)^2\left(\frac{1}{q^2a^2}+\frac{1}{h^2a^2}\right)^2 = \frac{\omega^2}{c^2}\left(\frac{J_l'(ha)}{haJ_l(ha)}+\frac{K_l'(qa)}{qaK_l(qa)}\right) \times\left(n_{\text{co}}^2\frac{J_l'(ha)}{haJ_l(ha)}+n_{\text{cl}}^2\frac{K_l'(qa)}{qaK_l(qa)}\right),$$

which is the origin of the radial index m characterizing the bounded modes in the fiber. Here, we have used the short-hand notation

$$J_l'(ha) = \frac{\mathrm{d}J_l(ha)}{\mathrm{d}(ha)} \quad \text{and} \quad K_l'(qa) = \frac{\mathrm{d}K_l(qa)}{\mathrm{d}(qa)}.$$

In order to see how the transcendental equation should be handled in order to yield the two groups HE and EH, and how the cutoff values for fiber guidance can be extracted for each mode, the reader is encouraged to consult either [Snyder *et al.*, 1983] or [Béguin, 2015] where comprehensive treatments are provided.

A.2 ADDITIONAL FIGURES

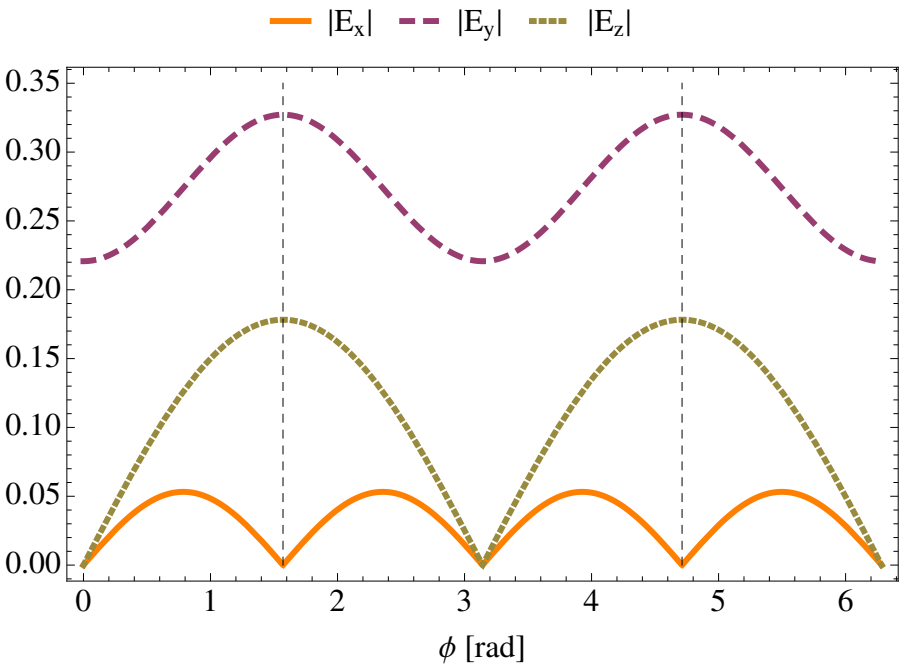

Figure A.1.: *Electric field components as a function of the aximuthal angle ϕ for a quasi-linearly y-polarized HE$_{11}$ mode. For $\phi = 0, \pi$ the field is completely polarized along y. This figure is similar to Fig. 2.12 but calculated for $\lambda = 852\,\text{nm}$.*

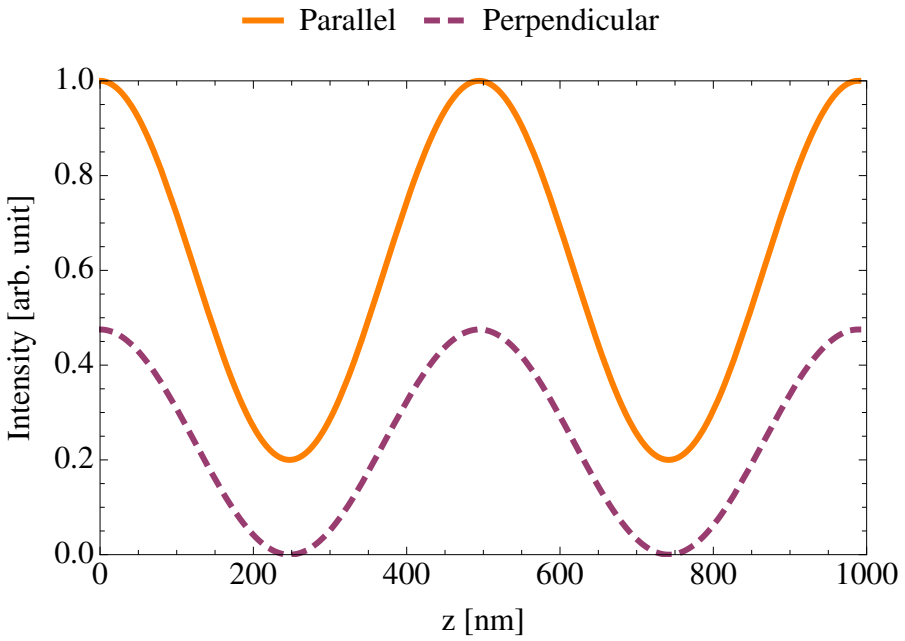

Figure A.2.: *Intensity distribution along the fiber axis for a quasi-linearly y-polarized HE$_{11}$ SW mode field. Evaluated for the two planes parallel and perpendicular to the polarization orientation. Calculated for the parameters $n_{co} = 1.4469$, $n_{cl} = 1$, $a = 250\,\text{nm}$, $\lambda = 1057\,\text{nm}$, $\rho = 442\,\text{nm}$. Total intensity of the electric field components plotted in Fig. 2.16*

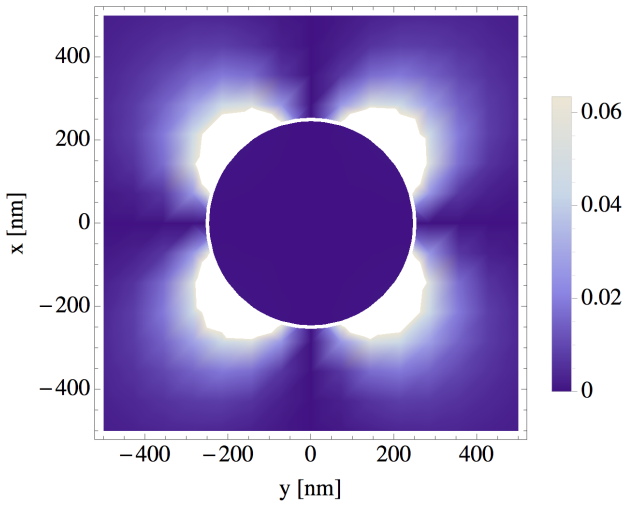

(a) $|\mathcal{E}_x|^2$.

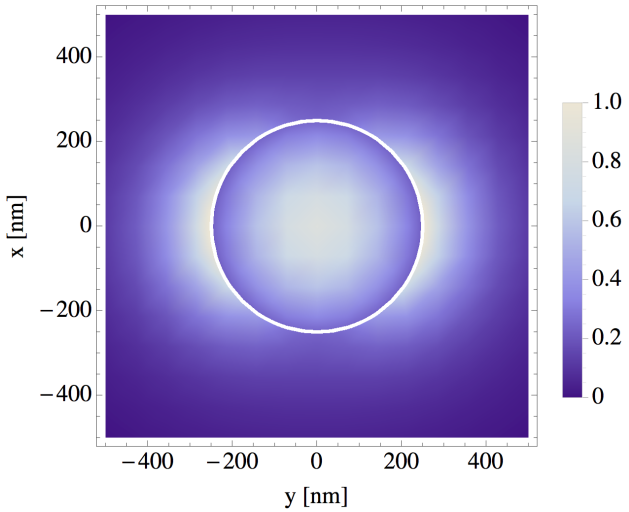

(b) $|\mathcal{E}_y|^2$.

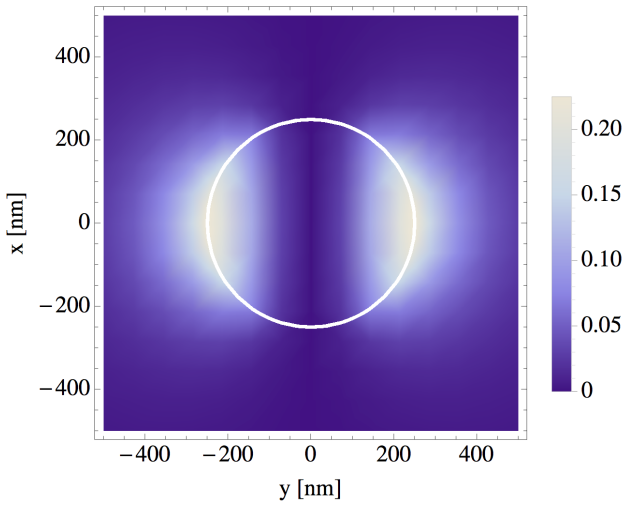

(c) $|\mathcal{E}_z|^2$.

Figure A.3.: *Field strength of the three electric field components for quasi-linearly y-polarized light. Calculated for the parameters* $n_{co} = 1.4469$, $n_{cl} = 1$, $a = 250\,\text{nm}$, $\lambda = 1057\,\text{nm}$ *at* $z = 0$. *Colorbar is normalized to the maximum value of* $|\mathcal{E}_y|^2$.

B

SPHERICAL BASIS

When dealing with atoms the most natural basis for the electric field polarization is the spherical basis $\{\mathbf{u}_q\}$ with $q = -1, 0, +1$. The unit polarization vector used in Eq. (5.11) is then given by

$$\mathbf{u}_\mathbf{k} = \sum_q \varepsilon_{jq} \mathbf{u}_q \tag{B.1}$$

where ε_{jq} yield the distribution of the polarization fulfilling $\sum_q \varepsilon_{jq} = 1$. If the quantization axis is chosen along $\mathbf{u}_z$ we have for the spherical basis vectors in terms of the Cartesian basis $\{\mathbf{u}_i\}$ with $i = x, y, z$ [Normand *et al.*, 1982]:

$$\mathbf{u}_{-1} = \frac{+\mathbf{u}_x - i\mathbf{u}_y}{\sqrt{2}}\,, \tag{B.2a}$$

$$\mathbf{u}_0 = \mathbf{u}_z\,, \tag{B.2b}$$

$$\mathbf{u}_{+1} = \frac{-\mathbf{u}_x - i\mathbf{u}_y}{\sqrt{2}}\,. \tag{B.2c}$$

When relating the light field polarization to the atomic system it is common practice to refer to it in terms of σ_-, π, and σ_+ instead of $\mathbf{u}_{-1}$, $\mathbf{u}_0$, and $\mathbf{u}_{+1}$ respectively. Eq. (B.2) can also we written as the transformation matrix

$$M_{\text{Cart2Sph}} = \frac{1}{\sqrt{2}} \begin{pmatrix} 1 & -i & 0 \\ 0 & 0 & \sqrt{2} \\ -1 & -i & 0 \end{pmatrix}. \tag{B.3}$$

Note, that the transformation matrix from the spherical basis to the Cartesian basis is easily obtained by simply taken the transpose of M_{Cart2Sph}, since it is necessarily unitary.

B.1 FOR x AS THE QUANTIZATION AXIS

When working in the fiber frame where $\mathbf{u}_z$ is chosen to be along the fiber axis, we will sometimes want the quantization axis to be perpendicular to the fiber axis (*i.e.*, to the propagation direction). For this, we need to transform the above set of equations (B.2) accordingly to still make the usual association between the atomic polarization and the spherical basis. Thus choosing the new quantization axis to be along $\mathbf{u}_x$, the indices in Eq. (B.2) should be shuffled according to

$x \to y$, $y \to z$, and $z \to x$, from which we obtain the following set of transformation equations from the Cartesian basis to the spherical basis with quantization axis along $\mathbf{u}_x$:

$$\mathbf{u}_{-1} = \frac{+\mathbf{u}_y - i\mathbf{u}_z}{\sqrt{2}}\,, \tag{B.4a}$$

$$\mathbf{u}_0 = \mathbf{u}_x\,, \tag{B.4b}$$

$$\mathbf{u}_{+1} = \frac{-\mathbf{u}_y - i\mathbf{u}_z}{\sqrt{2}}\,. \tag{B.4c}$$

C

PSEUDO-CODE FOR CALCULATING $v(z)$

The following pseudo-code illustrates the algorithm for calculating $v(z)$ in the interval $[\tilde{z}_-, \tilde{z}_+]$ with a step size $\Delta z > 0$:

1: $\mathrm{vz}_{\mathrm{table}} \leftarrow \{(v_-, \tilde{z}_-), (v_+, \tilde{z}_+)\}$;
2: $z \leftarrow \tilde{z}_-$; $v \leftarrow v_-$; $y \leftarrow \tilde{z}_- - l_-$;
3: **while** $y > z$ **do**
4: insert $(v \cdot A_{\mathrm{n}}(z), y)$ into $\mathrm{vz}_{\mathrm{table}}$;
5: $z \leftarrow z + \Delta z$;
6: $y \leftarrow y + \Delta z \cdot A_{\mathrm{n}}(z)$;
7: $v \leftarrow \texttt{interpolate}(\mathrm{vz}_{\mathrm{table}}, z)$;
8: **end while**;
9: $z \leftarrow \tilde{z}_+$; $v \leftarrow v_+$; $y \leftarrow \tilde{z}_+ - l_+$;
10: **while** $y < z$ **do**
11: insert $(v \cdot A_{\mathrm{n}}(z), y)$ into $\mathrm{vz}_{\mathrm{table}}$;
12: $z \leftarrow z - \Delta z$;
13: $y \leftarrow y - \Delta z \cdot A_{\mathrm{n}}(z)$;
14: $v \leftarrow \texttt{interpolate}(\mathrm{vz}_{\mathrm{table}}, z)$;
15: **end while**;

In this way the complete velocity profile $v(z)$ is contained in $\mathrm{vz}_{\mathrm{table}}$, and by Eq. (4.12) the fiber fluidity can be calculated.

D

UNITARY TRANSFORMATIONS

It can often be useful to transform the Hamiltonian describing a particular quantum system into another frame such that it contains relevant dynamics only. This is for example the case when doing the rotating frame transformation. Here we shown how such a general unitary transform should be made if we start out with a Hamiltonian $\hat{H}$ and some state given by $|\psi\rangle$ fulfilling the Schrödinger equation (5.1):

$$i\hbar|\dot{\psi}(t)\rangle = \tilde{H}|\psi(t)\rangle\,. \tag{D.1}$$

For any unitary operator $\hat{U}(t)$ the system can be transformed into a new state

$$|\tilde{\psi}(t)\rangle = \hat{U}(t)|\psi(t)\rangle\,. \tag{D.2}$$

This state should of course still fulfill the Schrödinger equation (5.1)

$$i\hbar|\dot{\tilde{\psi}}(t)\rangle = \tilde{H}|\tilde{\psi}(t)\rangle\,, \tag{D.3}$$

and therefore the original Hamiltonian $\hat{H}$ has to be accordingly transformed into a new Hamiltonian $\tilde{H}$. By inserting Eq. (D.2) into Eq. (D.3) we can find how this is properly done (to ease notation the time-dependence is not explicitly written in the following):

$$\begin{aligned}
i\hbar|\dot{\tilde{\psi}}\rangle &= i\hbar\big(\dot{\hat{U}}|\psi\rangle + \hat{U}|\dot{\psi}\rangle\big) && \text{(D.4a)}\\
&= i\hbar\dot{\hat{U}}|\psi\rangle + \hat{U}\hat{H}|\psi\rangle && \text{(D.4b)}\\
&= \big(i\hbar\dot{\hat{U}} + \hat{U}\hat{H}\big)|\psi\rangle && \text{(D.4c)}\\
&= \big(i\hbar\dot{\hat{U}} + \hat{U}\hat{H}\big)\hat{U}^\dagger|\tilde{\psi}\rangle && \text{(D.4d)}\\
&= \big(i\hbar\dot{\hat{U}}\hat{U}^\dagger + \hat{U}\hat{H}\hat{U}^\dagger\big)|\tilde{\psi}\rangle\,. && \text{(D.4e)}
\end{aligned}$$

And so we find that $\hat{H}$ should be transformed according to

$$\tilde{H} = i\hbar\dot{\hat{U}}\hat{U}^\dagger + \hat{U}\hat{H}\hat{U}^\dagger\,. \tag{D.5}$$

D.1 EXAMPLE: INTERACTION PICTURE

As an example we consider the transformation to the interaction picture for the semiclassical problem where a classical light field interacts with a quantized atom. The stateket can be written as a superposition of the complete set of unperturbed atomic states:

$$|\psi(t)\rangle = \sum_j c_j(t)|j\rangle\,. \tag{D.6}$$

The Hamiltonian is given as the sum of the unperturbed atomic Hamiltonian and the light-atom interaction:

$$\hat{H}(t) = \hat{H}_{\text{atom}} + \hat{V}(t)\,. \tag{D.7}$$

For this system, where the interesting dynamics lies in the interaction term $\hat{V}(t)$, it is desirable to transform into a frame such that the new Hamiltonian only involves some form of the interaction term, $\hat{H}(t) \to \hat{V}_{\text{int}}(t)$. This is commonly known as transforming into the "interaction picture". In this representation the Schrödinger equation is given by

$$i\hbar|\dot{\psi}(t)\rangle_{\text{int}} = \hat{V}_{\text{int}}(t)|\psi\rangle_{\text{int}}\,. \tag{D.8}$$

From Eq. (D.5) we know that the unitary operator $\hat{U}(t)$ bringing us to the interaction picture acts such that the transformed Hamiltonian is given by

$$\hat{V}_{\text{int}} = i\hbar\dot{\hat{U}}\hat{U}^\dagger + \hat{U}\hat{H}\hat{U}^\dagger \tag{D.9a}$$

$$= i\hbar\dot{\hat{U}}\hat{U}^\dagger + \hat{U}\hat{H}_{\text{atom}}\hat{U}^\dagger + \hat{U}\hat{V}\hat{U}^\dagger\,. \tag{D.9b}$$

We thus seek the unitary transform which makes the first two terms cancel such that only the last term containing the light-atom interaction $\hat{V}$ is left. This is achieved if

$$\hat{U}(t) = \mathrm{e}^{i\hat{H}_{\text{atom}}t/\hbar}\,. \tag{D.10}$$

Inserting $\hat{U}(t)$ into Eq. (D.9b), and noting that $\hat{U}(t)$ and $\hat{H}_{\text{atom}}$ commutes, $\left[\hat{U}(t), \hat{H}_{\text{atom}}\right] = 0$, we find

$$\hat{V}_{\text{int}} = i\hbar\frac{i\hat{H}_{\text{atom}}}{\hbar}\hat{U}\hat{U}^\dagger + \hat{H}_{\text{atom}}\hat{U}\hat{U}^\dagger + \hat{U}\hat{V}\hat{U}^\dagger \tag{D.11a}$$

$$= \hat{U}\hat{V}\hat{U}^\dagger \tag{D.11b}$$

$$= \mathrm{e}^{i\hat{H}_{\text{atom}}t/\hbar}\hat{V}\mathrm{e}^{-i\hat{H}_{\text{atom}}t/\hbar}\,. \tag{D.11c}$$

With the atomic Hamiltonian given according to Eq. (5.6):

$$\hat{H}_{\text{atom}} = \sum_b \hbar\omega_{ba}|b\rangle\langle b|\,, \tag{D.12}$$

and $\hat{V} = \hat{\mathbf{d}}\cdot\mathbf{E}(\mathbf{r},t)$ where the dipole operator is written in the from, Eq. (5.13):

$$\hat{\mathbf{d}} = \sum_{e,g}\mu_{eg}|e\rangle\langle g| + \mu_{eg}^*|g\rangle\langle e|\,, \tag{D.13}$$

we see that the transformed Hamiltonian $\tilde{H} = \hat{V}_{\text{int}}$ reduces to the expression

$$\hat{V}_{\text{int}}(t) = \sum_{e,g}\mathrm{e}^{i\omega_{eg}t}\mu_{eg}|e\rangle\langle g| + \text{h.c.} \tag{D.14}$$

Likewise we find for the transformed stateket:

$$|\psi(t)\rangle = \sum_{j,b}\mathrm{e}^{i\hat{H}_{\text{atom}}t/\hbar}c_j(t)|j\rangle \tag{D.15a}$$

$$= \sum_j \mathrm{e}^{i\omega_{ja}t}c_j(t)|j\rangle\,. \tag{D.15b}$$

E

DERIVING THE m SELECTION RULE

We wish to find a selection rule for the m quantum number of the matrix element $\langle J'\, m'|T_q^{(K)}|J\, m\rangle$ where $T_q^{(k)}$ is a spherical tensor defined such that [Sakurai, 1994]

$$[J_z, T_q^{(k)}] = \hbar q T_q^{(k)}\,, \tag{E.1a}$$
$$[J_\pm, T_q^{(k)}] = \hbar\sqrt{(k\mp q)(k\pm q+1)}\,T_{q\pm1}^{(k)}\,,$$

where $\mathbf{J}$ is the angular momentum operator. In the following we use that

$$J_z|J\, m\rangle = \hbar m|J\, m\rangle\,, \tag{E.2}$$

and

$$[J_z, T_q^{(k)}] - \hbar q T_q^{(k)} = 0\,, \tag{E.3}$$

from Eq. (E.1a). We then find

$$\langle J'\, m'|0|J\, m\rangle = \langle J'\, m'|[J_z, T_q^{(k)}] - \hbar q T_q^{(k)}|J\, m\rangle \tag{E.4a}$$
$$= \langle J'\, m'|J_z T_q^{(k)} - T_q^{(k)} J_z - \hbar q T_q^{(k)}|J\, m\rangle \tag{E.4b}$$
$$= \hbar(m'-m-q)\langle J'\, m'|T_q^{(k)}|J\, m\rangle \tag{E.4c}$$
$$\Rightarrow \quad \langle J'\, m'|T_q^{(k)}|J\, m\rangle = 0\,, \quad \text{if } m' \neq m+q\,. \tag{E.4d}$$

Making the substitutions $J \to F$, $J' \to F'$, $m \to m_F$, $m' \to m'_F$, and $T_q^{(k)} \to r_q$, we arrive at Eq. (7.10).

F

ADDITIONAL FIGURES

F.1 COMBINED LASER INTENSITY NOISE OF THE RED AND BLUE TRAPPING FIELDS

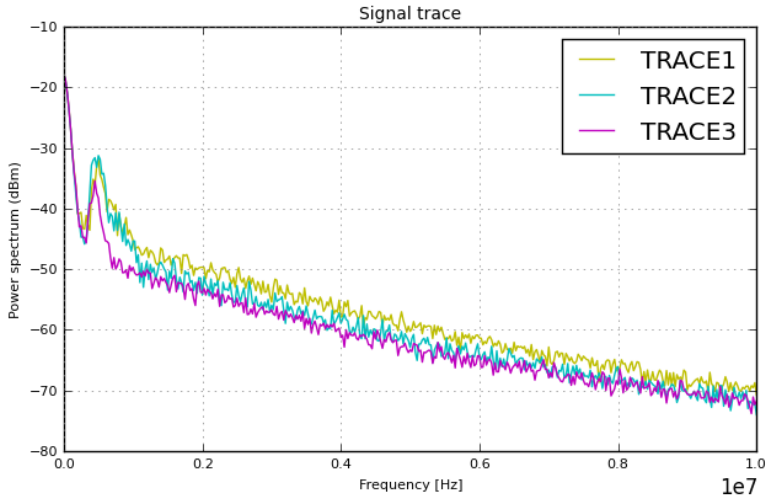

Figure F.1.: *Power spectrum of laser intensity noise. TRACE 1: Both red and blue trap lasers. TRACE 2: Blue trap laser. TRACE 3: Red trap laser, same trace as the magenta trace in Fig. 9.8(b).*

F.2 ATOM NUMBER MEASUREMENT

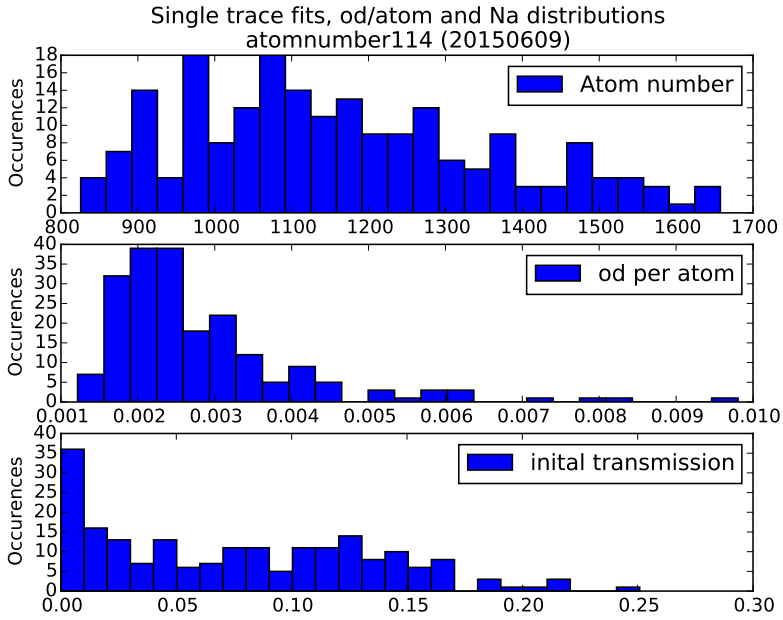

Figure F.2.: *Histogram of the free fit parameters N_{atom} and α when fitting the measurement traces individually, as compared to the mean trace fit in Fig. 11.1.*

F.3 TOTAL NOISE FULL TIME TRACE

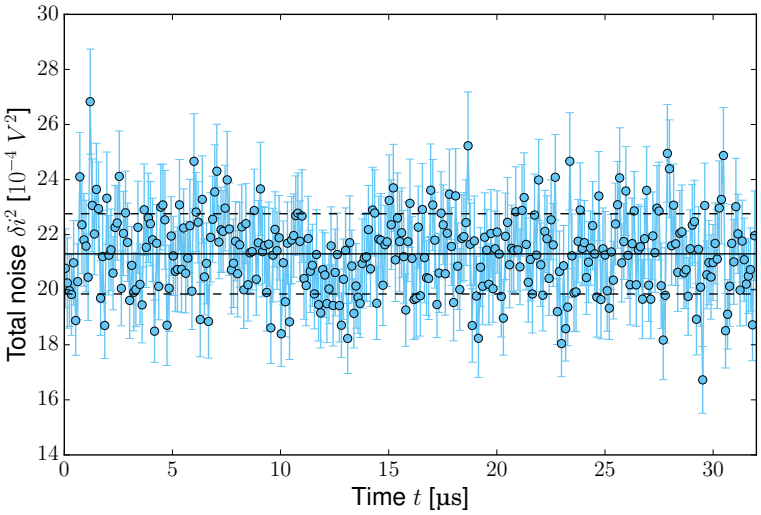

Figure F.3.: *Full time trace of the total detection noise on the reflection detector show in Fig. 13.8(a), and used for the histogram in Fig. 13.8(b).*

F.4 UNSTRUCTURED REFLECTION WITH A RESONANT PROBE

Reflected light off an unstructured ensemble of ~ 1300 atoms, yielding $\mathcal{R} = (0.10 \pm 0.01)\,\%$ (red solid line divided by the probe power).

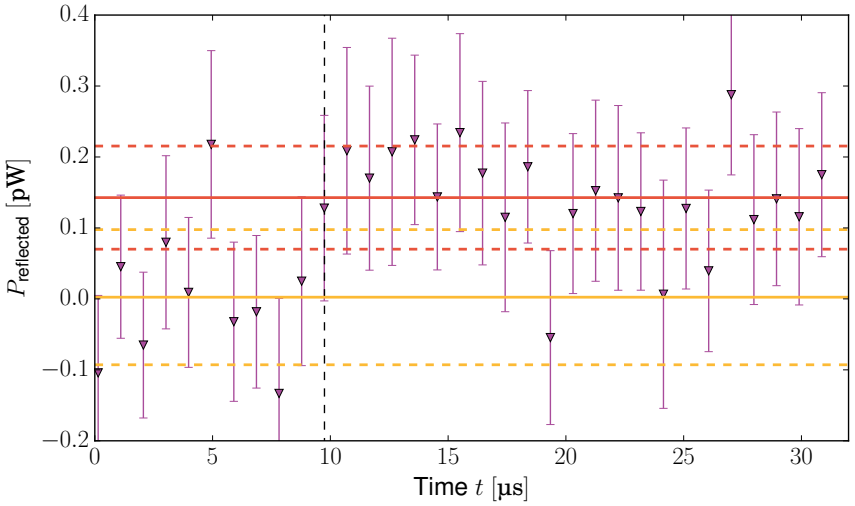

Figure F.4.: *Purple data points: Reflected power from unstructured atoms as a function of time, using a resonant* 140 pW *probe. The time sequence is the same as usual,* i.e., *the probe in on for the first* 3.7 µs *where it is turned off and then on again at* $t = 9.8\,\mu s$ *(black vertical dashed line),* cf. *Fig. 13.5. Each point is an average over* 900 MOT *loadings sampled over* $\tau = 96\,ns$*, and afterwards time averaged over* $10 \times 96\,ns$*. The errorbars are given by the statistical one-sigma uncertainty from this last* $\approx 1\,\mu s$ *time average. Yellow (Red) lines: Statistical mean (solid) and* 1 std *uncertainty band (dashed) over the data points measured before (after) the probe is turned on at* $t = 9.8\,\mu s$.

F.5 ATOMIC BRAGG MIRROR

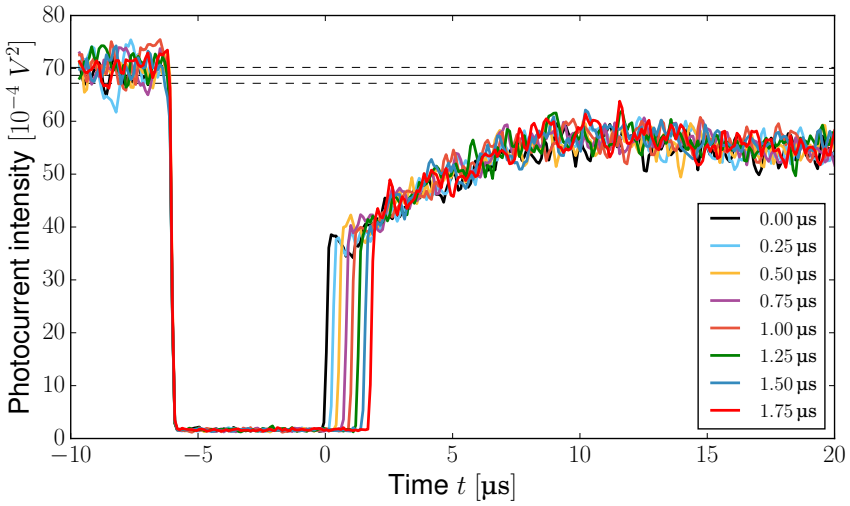

Figure F.5.: *Transmitted light through the atomic mirror for delayed probe pulses. Error bars are omitted for visual clarity. Each curve is an average over 100 consecutive experimental runs obtained for a* 150 pW *on-resonant probe.* $\tau = 192$ ns *running average. Corresponding data showing the reflected light is given in Fig. 16.5.*

G

ATOMIC BRAGG MIRROR AIDED BY AN EIT WINDOW

The idea initially laid out by Ivan Iakoupov for the atomic Bragg mirror, was actually first of all not meant as a proposal for the sole sake of making a mirror, but to implement a phase gate – indeed a very different objective. It was also first based on a quite different scheme than the optical pumping that we use to imprint the Bragg grating onto the internal states of the atoms. What he had in mind, was to utilize the effect of EIT. This bears several advantages which we believe would greatly enhance the quality of the measured reflectance presented in this thesis. Especially noteworthy is the temporal evolution of the reflectance where much longer lifetimes is expected. For technical reasons, lack of lasers *etc.*, we originally discarded the EIT idea and instead opted for the more simple solution using mere optical pumping. Here we will therefore describe the suggested protocols which will hopefully find their way into future experiments.

The EIT solutions provides a continous platform where the atoms can be probed while having the structuring beams on at the same time. This is in contrast to the optical pumping scheme, described in Section 12.2, where we first pump the atoms into the Bragg structure and then probe. In the following sections we present two suggested schemes where EIT is used as a resource to provide the spatial pattern necessary for sufficient Bragg scattering off the atoms. We will not go into any details on how this can be used to realize a phase gate, for this we refer to the work presented in [Iakoupov, 2013].

G.1 EIT IN A NUTSHELL

First, a brief presentation the main points and equations governing EIT, under the assumption that the reader is already somewhat familiar with the concept. If not, there exists plenty of textbooks covering the subject, *e.g.*, [Boyd, 2008; Milonni *et al.*, 2010; Grynberg *et al.*, 2010].

We consider the three-level Lambda (Λ) system illustrated in Fig. G.1. Two laser fields are applied, one on each to the ground to exited state transitions, $|g_i\rangle \rightarrow |e\rangle$, for $i = 1, 2$. In terms of these unperturbed

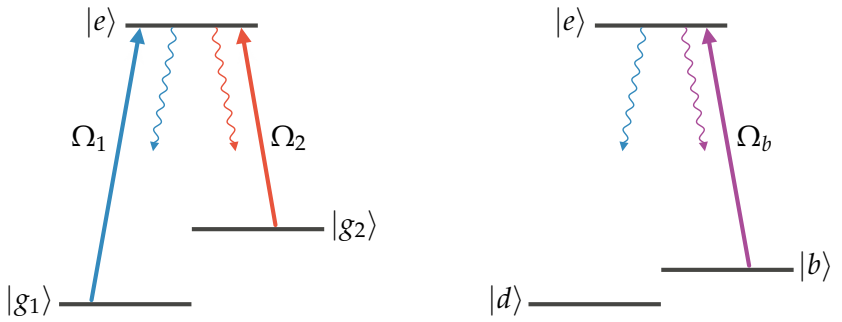

(a) Level scheme in terms of the atomic basis states.

(b) Level scheme in terms of the dark and bright basis states.

Figure G.1.: Λ *scheme for* EIT.

atomic basis states, the Hamiltonian for the light-atom interaction dynamics is given by[1]

$$\hat{H} = -\frac{-i\hbar\gamma_e}{2}|e\rangle\langle e| - \left(\hbar\left(\Omega_1^*|g_1\rangle + \Omega_2^*|g_2\rangle\right)\langle e| + \text{h.c.}\right), \tag{G.1}$$

where γ_e is the decay out of the exited state, and Ω_1, Ω_2 are the Rabi frequencies of the two coupling fields. From Eq. (G.1) it is apparent that the exited state couples to a superposition of the ground states. This motivates to introduce a new set of basis states:

$$|b\rangle \equiv \frac{\Omega_1^*|g_1\rangle + \Omega_2^*|g_2\rangle}{\Omega_b}, \tag{G.2a}$$

$$|d\rangle \equiv \frac{\Omega_2|g_1\rangle - \Omega_1|g_2\rangle}{\Omega_b}, \tag{G.2b}$$

with

$$\Omega_b \equiv \left(|\,\Omega_1\,|^2 + |\,\Omega_1\,|^2\right)^{1/2}, \tag{G.2c}$$

which simplifies the Hamiltonian to

$$\hat{H} = -\frac{-i\hbar\gamma_e}{2}|e\rangle\langle e| - \left(\hbar\Omega_b|b\rangle\langle e| + \text{h.c.}\right). \tag{G.3}$$

Evidently, there exists a dark state $|d\rangle$ which do not couple to the light fields. Since $|d\rangle$ is an eigenstate of the Hamiltonian the atoms will eventually be pumped out of the bright state $|b\rangle$ and into $|d\rangle$. Regarding Ω_1 as a control field and Ω_2 as a probe field the absorption spectrum of the latter will display a spectral window or EIT window on resonance with the width set by the strength of the control field as shown in Fig. G.2.

1 Here we used the quantum jump formalism to include the exited state decay, contained in the first term, directly into the Hamiltonian.

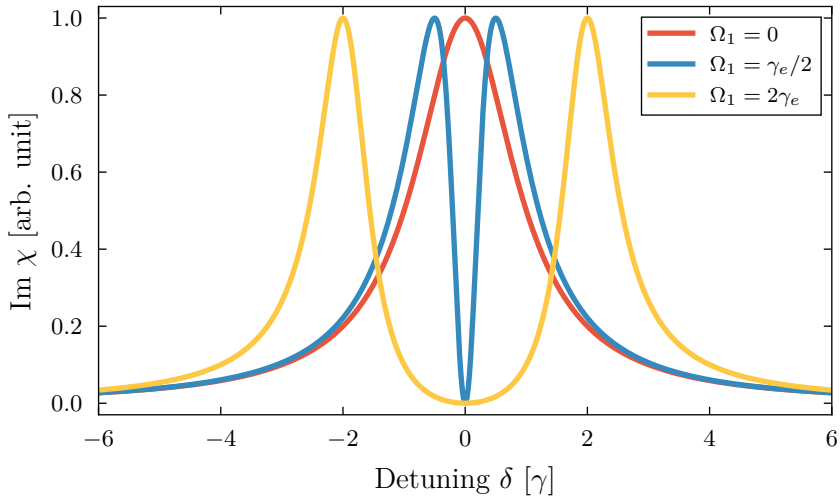

Figure G.2.: *EIT absorption spectrum of the probe field Ω_2 with the detuning defined as the frequency difference between the probe field and the atomic transition frequency: $\delta = \omega_2 - \omega_{e2}$. The control field Ω_1 is on-resonance with the atomic transition $|g_1\rangle \rightarrow |e\rangle$.*

G.2 THREE- AND FOUR-LEVEL EIT SCHEMES

The three-level EIT scheme used to imprint a Bragg grating onto the internal states of the atoms is similar to the one used in [Bajcsy *et al.*, 2003] where they observed up to $\sim 80\,\%$ power reflection off a free-space atomic ensemble consisting of $\sim 10^{12}$ ^{87}Rb atoms. All atoms are initially prepared in the ground state $|g_1\rangle$. The idea is then to apply a strong SW control field resonant with the $|g_2\rangle \rightarrow |e\rangle$ transition, as shown in Fig. G.3(a), and a weak RW probe resonant with the $|g_1\rangle \rightarrow |e\rangle$ transition. This configuration creates an EIT window at

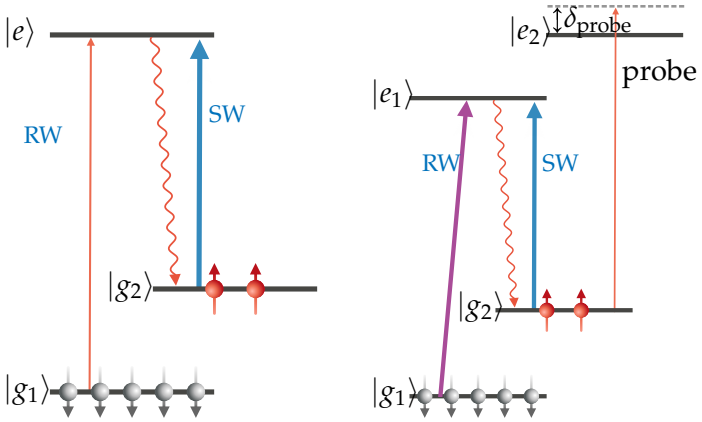

(a) Three-level Λ-system. (b) Four-level Λ-system.

Figure G.3.: *Pumping scheme for the EIT-aided atomic Bragg mirror.*

all the antinodes of the SW control field, *i.e.*, at the intensity maxima. Atoms located at these positions are thus transparent to the probe field. On the contrary, atoms located at the nodes of the SW control field, scatters off probe light as if the control field were not present at all. Effectively, an atomic Bragg grating has been established with the advantage, over the optical pumping schemes, that the atoms are continuously kept in place by the control field.

The four-level EIT scheme is nearly identical to the three-level scheme. The only difference being, that the probe field is no longer used as the second leg in the Λ-system for establishing the EIT window. Instead, an extra control field, configured as a RW, is introduced as illustrated in Fig. G.3(b). Utilizing a second exited state $|e_2\rangle$, the probe field now scatters off the atoms that has been adiabatically transferred from $|g_1\rangle$ to $|g_2\rangle$ via the two EIT control fields.

This configuration bears a couple of advantages over the three-level scheme. Choosing, *e.g.*, two Zeeman levels, one in each of the two hyperfine manifolds, $|3\rangle \equiv (6^2S_{1/2}, F = 3)$ and $|4\rangle \equiv (6^2S_{1/2}, F = 4)$, is an obvious choice for the ground states $|g_1\rangle$ and $|g_2\rangle$. This limits, however, the freedom to choose the exited state which has to be in either[2] of the two manifolds $|3'\rangle \equiv (6^2P_{3/2}, F' = 3)$ or $|4'\rangle \equiv (6^2P_{3/2}, F' = 4)$ in order to create an EIT window. Taking the probe beam out of the EIT configuration, allows us to probe the $|4\rangle \rightarrow (6^2P_{3/2}, F' = 5)$ transition instead, which couples stronger to the field mode resulting in a higher signal. This scheme further has the advantage that the probe detuning δ can be freely tuned without being concerned about modifying the EIT window.

2 Considering only the D2 line for now. It might be beneficial to also consider the possibility of using the D1 line.

H

DERIVATION OF REAL SPACE HAMILTONIAN

Here we show how to rewrite the light-atom Hamiltonian initially described in k-space, Eq. (19.1):

$$\begin{aligned}\hat{H} = \hbar\left(\omega_{e\uparrow} - i\frac{\gamma'}{2}\right)\hat{\sigma}_{ee} + \int_{-\infty}^{\infty} \hbar c|k|\hat{a}_k^\dagger \hat{a}_k \,\mathrm{d}k \\ - \hbar g \int_{-\infty}^{\infty} \left(\hat{\sigma}_{e\uparrow}\hat{a}_k \mathrm{e}^{ikz_j} - \hat{\sigma}_{\uparrow e}\hat{a}_k^\dagger \mathrm{e}^{-ikz_j}\right) \mathrm{d}k\,.\end{aligned} \tag{H.1}$$

to that given in real space, Eq. (19.6):

$$\begin{aligned}\hat{H} = \hbar\left(\omega_{e\uparrow} - i\frac{\gamma'}{2}\right)\hat{\sigma}_{ee} \\ + i\hbar c \int_{-\infty}^{\infty} \left(\hat{E}_{\text{left}}^\dagger \frac{\partial \hat{E}_{\text{left}}}{\partial z} - \hat{E}_{\text{right}}^\dagger \frac{\partial \hat{E}_{\text{right}}}{\partial z}\right) \mathrm{d}z \\ - \hbar g\sqrt{2\pi} \int_{-\infty}^{\infty} \delta(z - z_j)\left(\hat{\sigma}_{e\uparrow}\left(\hat{E}_{\text{left}}(z) + \hat{E}_{\text{right}}(z)\right) + \text{h.c.}\right) \mathrm{d}z\,,\end{aligned} \tag{H.2}$$

where the left- and right-propagating field modes are defined as, Eq. (19.4):

$$\hat{E}_{\text{left}}(z) = \frac{1}{\sqrt{2\pi}} \int_{-\infty}^{\infty} \hat{a}_{\text{left},k}\, \mathrm{e}^{ikz}\, \mathrm{d}k\,, \tag{H.3a}$$

$$\hat{E}_{\text{right}}(z) = \frac{1}{\sqrt{2\pi}} \int_{-\infty}^{\infty} \hat{a}_{\text{right},k}\, \mathrm{e}^{ikz}\, \mathrm{d}k\,. \tag{H.3b}$$

H.1 SECOND LINE

We first consider the second line in the Hamiltonian containing the isolated light description. Using the left- and right-going modes, $\hat{a}_{\text{left},k}$ and $\hat{a}_{\text{right},k}$, this can be transformed according to:

$$\hat{H}_{\text{light}} = \int_{-\infty}^{\infty} \hbar c|k|\hat{a}_k^\dagger \hat{a}_k \,\mathrm{d}k \tag{H.4a}$$

$$\to \int_{-\infty}^{\infty} \hbar ck(\hat{a}_{\text{right},k}^\dagger \hat{a}_{\text{right},k} - \hat{a}_{\text{left},k}^\dagger \hat{a}_{\text{left},k})\,\mathrm{d}k\,. \tag{H.4b}$$

Although this contains unphysical modes, that is right-going modes with negative wavevectors and vice versa for the left-going modes, it remains valid when considering near-resonant dynamics only [Chang *et al.*, 2007].

Inserting Eq. (H.3a) into Eq. (H.2) we get for the first term in the second line:

$$
\begin{aligned}
& i\hbar c \int_{-\infty}^{\infty} \hat{E}^{\dagger}_{\text{left}} \frac{\partial \hat{E}_{\text{left}}}{\partial z} \, \mathrm{d}z \\
&= \frac{i\hbar c}{2\pi} \int_{-\infty}^{\infty} \mathrm{d}z \int_{-\infty}^{\infty} \mathrm{d}k \int_{-\infty}^{\infty} \hat{a}^{\dagger}_{\text{left},k} \, \mathrm{e}^{-ikz} (ik') \hat{a}_{\text{left},k'} \, \mathrm{e}^{ik'z} \, \mathrm{d}k' \\
&= \frac{i\hbar c}{2\pi} \int_{-\infty}^{\infty} \mathrm{d}k \int_{-\infty}^{\infty} \hat{a}^{\dagger}_{\text{left},k} (ik') \hat{a}_{\text{left},k'} \, \mathrm{d}k' \int_{-\infty}^{\infty} \mathrm{e}^{i(k'-k)z} \, \mathrm{d}z \\
&= i\hbar c \int_{-\infty}^{\infty} ik \hat{a}^{\dagger}_{\text{left},k} \hat{a}_{\text{left},k} \, \mathrm{d}k \\
&= - \int_{-\infty}^{\infty} \hbar c k \hat{a}^{\dagger}_{\text{left},k} \hat{a}_{\text{left},k} \, \mathrm{d}k \,,
\end{aligned}
\tag{H.5}
$$

where we have used the Fourier transform definition of the Dirac delta function [Riley *et al.*, 2006]:

$$
\int_{-\infty}^{\infty} \mathrm{e}^{ikz} \, \mathrm{d}z = 2\pi \delta(k) \,, \tag{H.6}
$$

for the step between the third and the fourth line. It can similarly be found that

$$
i\hbar c \int_{-\infty}^{\infty} \hat{E}^{\dagger}_{\text{right}} \frac{\partial \hat{E}_{\text{right}}}{\partial z} \, \mathrm{d}z = - \int_{-\infty}^{\infty} \hbar c k \hat{a}^{\dagger}_{\text{right},k} \hat{a}_{\text{right},k} \, \mathrm{d}k \,. \tag{H.7}
$$

H.2 THIRD LINE

To obtain the third line in Eq. (H.2) we note that upon transforming the annihilation and creation operator into distinct left- and right-propagation modes we have

$$
\hat{\sigma}_{eg} \hat{a}_k \mathrm{e}^{ikz_j} \rightarrow \hat{\sigma}_{eg} (\hat{a}_{\text{left},k} + \hat{a}_{\text{right},k}) \mathrm{e}^{ikz_j} \,. \tag{H.8}
$$

Inserting this into the second line in Eq. (H.1) and using the definitions given in Eq. (H.3) we directly obtain the third line in Eq. (H.2).

I

SOLVING THE MAXWELL-BLOCH EQUATIONS

Here we show the derivation of the solutions to the Maxwell-Bloch equations:

$$\left(\frac{1}{c}\frac{\partial}{\partial t} - \frac{\partial}{\partial z}\right) E_{\text{left}}(z) = \frac{ig\sqrt{2\pi}}{c}\delta(z - z_j)\sigma_{ge}\,, \tag{I.1a}$$

$$\left(\frac{1}{c}\frac{\partial}{\partial t} + \frac{\partial}{\partial z}\right) E_{\text{right}}(z) = \frac{ig\sqrt{2\pi}}{c}\delta(z - z_j)\sigma_{ge}\,, \tag{I.1b}$$

$$\dot{\sigma}_{ge} = -(i\omega_{eg} + \frac{\gamma_{\text{free}}}{2})\sigma_{ge} + ig\sqrt{2\pi}\big(E_{\text{left}}(z_j) + E_{\text{right}}(z_j)\big)\,. \tag{I.1c}$$

We start by formally integrating the two wave equations, (I.1a) and (I.1b), for the left- and right-going fields. Introducing the positive infinitesimal ε the positions immediately to the right and left of the atom located at z_j are given by $z_j^{\pm} = z_j \pm \varepsilon$. Integrating over the atomic position from z_j^- to z_j^+ yields:

$$E_{\text{left}}(z_j^-) = E_{\text{left}}(z_j^+) + \frac{ig\sqrt{2\pi}}{c}\sigma_{ge}\,, \tag{I.2a}$$

$$E_{\text{right}}(z_j^+) = E_{\text{right}}(z_j^-) + \frac{ig\sqrt{2\pi}}{c}\sigma_{ge}\,. \tag{I.2b}$$

Since E_{left} and E_{right} are both continuous at z_j they can be written as a Taylor series. To first order we thus have;

$$E_i(z_j^{\pm}) = E_i(z_j) \pm \varepsilon E_i'(z_j) \tag{I.3a}$$

$$\Rightarrow \qquad E_i(z_j) = \frac{1}{2}\Big(E_i(z_j^-) + E_i(z_j^+)\Big) \tag{I.3b}$$

for $i = \text{left}, \text{right}$. Using this in combination with Eq. (I.2) we find:

$$E_{\text{left}}(z_j) = E_{\text{left}}(z_j^+) + \frac{ig\sqrt{2\pi}}{2c}\sigma_{ge}\,, \tag{I.4a}$$

$$E_{\text{right}}(z_j) = E_{\text{right}}(z_j^-) + \frac{ig\sqrt{2\pi}}{2c}\sigma_{ge}\,. \tag{I.4b}$$

Defining $E^{\text{in}}_{\text{left}}(z_j) \equiv E_{\text{left}}(z_j^+)$ and $E^{\text{in}}_{\text{right}}(z_j) \equiv E_{\text{right}}(z_j^-)$ for the left and right input fields to the atom we have upon insertion of Eq. (I.4) into Eq. (I.1c):

$$\dot{\sigma}_{ge} = -\left(i\omega_{eg} + \frac{\gamma_{\text{free}}}{2} + \frac{2\pi g^2}{c}\right)\sigma_{ge} + ig\sqrt{2\pi}\big(E^{\text{in}}_{\text{left}} + E^{\text{in}}_{\text{right}}\big)\,. \tag{I.5}$$

We identify the term $2\pi g^2 \sigma_{ge}/c$ as belonging to the radiative decay of the atom into one of the TOF-guided modes and hence define $\gamma_{\text{TOF}} \equiv 4\pi g^2/c$ for the decay rate into the TOF.

We will now assume that the electric field in the TOF initially only consists of a right-propagating input field; $E^{\text{in}}_{\text{left}} = 0$. After scattering off the atom the input field will be partially reflected and transmitted (and lost) and both left- and right-going field modes will be present in the TOF. This can be summarized as

$$E_{\text{left}}(z) = \begin{cases} rE^{\text{in}}_{\text{right}} & \text{if } z < z_j, \\ 0 & \text{if } z > z_j, \end{cases} \tag{I.6a}$$

$$E_{\text{right}}(z) = \begin{cases} E^{\text{in}}_{\text{right}} & \text{if } z < z_j, \\ tE^{\text{in}}_{\text{right}} & \text{if } z > z_j, \end{cases} \tag{I.6b}$$

where we have used r and t for the amplitude reflection and transmission coefficient respectively. We also make the ansatz that the atomic coherence can be written as the Fourier component:

$$\sigma_{ge}(t) = A\mathrm{e}^{-i\omega t} = A\mathrm{e}^{-i(\delta+\omega_{eg})t}\,, \tag{I.7}$$

that is, the fast oscillations of the atomic dipole transition is given by the near-resonant electric field frequency ω, and the amplitude A will be slowly-varying over the time-scales considered such that we can neglect its time-dependence altogether.

Using Eq. (I.6) in Eq. (I.2) we find:

$$E^{\text{in}}_{\text{right}} = \frac{ig\sqrt{2\pi}}{rc}\sigma_{ge}\,. \tag{I.8}$$

With $\gamma = \gamma_{\text{TOF}} + \gamma_{\text{free}}$ for the total decay rate of the atom, we finally obtain the reflection coefficient upon inserting Eq. (I.7) and Eq. (I.8) into Eq. (I.1c):

$$r(\delta) = -\frac{\gamma_{\text{TOF}}}{\gamma - 2i\delta}\,. \tag{I.9}$$

Since $t = 1 + r$ by continuity of the electric field at $z = z_j$, the transmission coefficient is found to:

$$t(\delta) = 1 - \frac{\gamma_{\text{TOF}}}{\gamma - 2i\delta} = \frac{\gamma_{\text{free}} - 2i\delta}{\gamma - 2i\delta}\,. \tag{I.10}$$

J

RELATION BETWEEN THE OD AND THE ATOMIC EMISSION RATE INTO THE TOF

We seek the relation between the optical depth (OD) of the atomic crystal and the decay rate into the tapered optical fiber (TOF). Treating the atomic crystal as an ensemble with 1D linear atom number density $\mathcal{N} = N_{\text{atom}}/L$, we have from Appendix I the equations of motion

$$\left(\frac{1}{c}\frac{\partial}{\partial t} + \frac{\partial}{\partial z}\right) E_{\text{right}}(z,t) = \frac{ig\sqrt{2\pi}}{c}\mathcal{N}P(z,t)\,, \tag{J.1a}$$

$$\frac{\partial}{\partial t}P(z,t) = -(i\omega_{eg} + \frac{\gamma_{\text{free}}}{2})P(z,t) + ig\sqrt{2\pi}E_{\text{right}}(z,t)\,. \tag{J.1b}$$

Where we have replaced the discrete atomic operator for the coherences σ_{eg} with the continuous polarization $P(z,t)$, and set the left-going field equal to zero. We make the ansatz that both the electric field and the polarization can be separated into slowly and fast varying parts:

$$E_{\text{right}}(z,t) = \mathcal{E}(z)\mathrm{e}^{-i\omega t}\,, \tag{J.2a}$$

$$P(z,t) = \mathcal{P}(z)\mathrm{e}^{-i\omega t}\,, \tag{J.2b}$$

with ω being the optical frequency of the light field and any time dependence of the amplitudes $\mathcal{E}$ and $\mathcal{P}$ are neglected all together. Inserting Eq. (J.2) into Eq. (J.1) we find:

$$\left(-ik + \frac{\partial}{\partial z}\right) E_{\text{right}}(z,t) = \frac{ig\sqrt{2\pi}}{c}\mathcal{N}P(z,t)\,, \tag{J.3a}$$

$$P(z,t) = \frac{2ig\sqrt{2\pi}}{\gamma_{\text{free}} - 2i\delta}E_{\text{right}}(z,t)\,, \tag{J.3b}$$

with the field detuning from atomic resonance defined as $\delta \equiv \omega - \omega_{eg}$. Inserting the solution for the polarization, Eq. (J.3b), into Eq. (J.3a) we obtain the linear differential equation for the electric field:

$$\frac{\partial}{\partial z}E_{\text{right}}(z,t) = -\left(\frac{\gamma_{\text{TOF}}\mathcal{N}}{\gamma_{\text{free}} - 2i\delta} - ik\right)E_{\text{right}}(z,t)\,, \tag{J.4}$$

where we have used $\gamma_{\text{TOF}} = 4\pi g^2/c$. Integration this equation from $z = 0$ to $z = L$ we get the solution:

$$E_{\text{right}}(L,t) = E_0(t)\exp\left(-\gamma_{\text{TOF}}N_{\text{atom}}\frac{\gamma_{\text{free}}}{\gamma_{\text{free}}^2 + 4\delta^2} + i\phi\right), \tag{J.5}$$

with the imaginary term in the exponent merged into a single constant ϕ. From Lambert-Beer's law given in Eq. (6.29) the OD d is defined such that

$$I(z) = I_0 \mathrm{e}^{-d} \,. \tag{J.6}$$

Taking the norm squared of $E_{\mathrm{right}}(L,t)$ we then find for the single atom OD:

$$\alpha = 2\gamma_{\mathrm{TOF}} \frac{\gamma_{\mathrm{free}}}{\gamma_{\mathrm{free}}^2 + 4\delta^4} \,. \tag{J.7}$$

Since the emission rate in the TOF is much smaller than that into free space, $\gamma_{\mathrm{TOF}} \ll \gamma_{\mathrm{free}}$, we can make the approximation $\gamma_{\mathrm{free}} \approx \gamma = \gamma_{\mathrm{TOF}} + \gamma_{\mathrm{free}}$. For the on-resonance OD per atom we then have

$$\alpha_0 = 2\frac{\gamma_{\mathrm{TOF}}}{\gamma} \,. \tag{J.8}$$

J.1 INCLUDING INHOMOGENEOUS BROADENING

We now include the effect of inhomogeneous broadening by adding a shift δ', described by the distribution $\mathcal{D}(\delta')$, to the natural atomic resonance frequency ω_{eg}. Starting again from the Maxwell-Bloch equations they are now given by

$$\left(\frac{1}{c}\frac{\partial}{\partial t} + \frac{\partial}{\partial z}\right) E_{\mathrm{right}}(z,t) = \frac{ig\sqrt{2\pi}}{c}\mathcal{N}\int \mathcal{D}(\delta')P(z,t,\delta')\,\mathrm{d}\delta' \,, \tag{J.9a}$$

$$\frac{\partial}{\partial t}P(z,t,\delta') = -\big(i(\omega_{eg} - \delta') + \frac{\gamma_{\mathrm{free}}}{2}\big)P(z,t,\delta') + ig\sqrt{2\pi}E_{\mathrm{right}}(z,t) \,. \tag{J.9b}$$

Using again the ansatz for the solutions of E_{right} and P, Eq. (J.2), we find:

$$\left(\frac{\partial}{\partial z} - ik\right) E_{\mathrm{right}}(z,t) = \frac{ig\sqrt{2\pi}}{c}\mathcal{N}\int \mathcal{D}(\delta')P(z,t,\delta')\,\mathrm{d}\delta' \,, \tag{J.10a}$$

$$P(z,t,\delta') = \frac{2ig\sqrt{2\pi}}{\gamma_{\mathrm{free}} - 2i(\delta + \delta')} E_{\mathrm{right}}(z,t) \,, \tag{J.10b}$$

Inserting Eq. (J.10b) into Eq. (J.10a) and integrating from $z = 0$ to $z = L$, we find for the norm squared of the electric field:

$$\frac{|\,E_{\mathrm{right}}(L,t)\,|^2}{|\,E_0(t)\,|^2} = \exp\left(-2N_{\mathrm{atom}}\,\mathrm{Re}\int \mathcal{D}(\delta')\frac{\gamma_{\mathrm{TOF}}}{\gamma_{\mathrm{free}} - 2i(\delta+\delta')}\,\mathrm{d}\delta'\right). \tag{J.11}$$

The on-resonance single atom OD is then given by

$$\alpha_0 = 2\,\mathrm{Re}\int_{-\infty}^{\infty} \mathcal{D}(\delta')\frac{\gamma_{\mathrm{TOF}}}{\gamma - 2i\delta'}\,\mathrm{d}\delta', \tag{J.12}$$

under the approximation $\gamma_{\mathrm{free}} \approx \gamma$.

J.2 ESTIMATING THE INHOMOGENEOUS BROADENING

To estimate the amount of inhomogeneous broadening of the atomic transition, we fit the inferred optical depth as a function of the probe detuning (Fig. J.1) with a Voigt profile:

$$V(\delta;\sigma_\delta,\alpha) = \int_{-\infty}^{\infty} G(\delta',\sigma_\delta L(\delta-\delta')\,\mathrm{d}\delta'\,. \tag{J.13}$$

Here G and L are the Gauss- and Lorentz-distributions given by:

$$G(\delta',\sigma_\delta) = \frac{1}{\sqrt{2\pi}\sigma_\delta}\exp\left(-\frac{\delta^2}{2\sigma_\delta^2}\right), \tag{J.14}$$

$$L(\delta-\delta') = \frac{\alpha}{1+(\delta-\delta')^2/(\gamma/2)^2+s_0}\,. \tag{J.15}$$

$s_0 = P/P_{\mathrm{sat}} = 150\,\mathrm{pW}/750\,\mathrm{pW} = 0.2$ is the saturation parameter. The free parameters in the fit are the homogeneous on-resonant optical depth α, and the inhomogeneous broadening σ_δ. From this we obtain $\sigma_\delta = 0.41\gamma$.

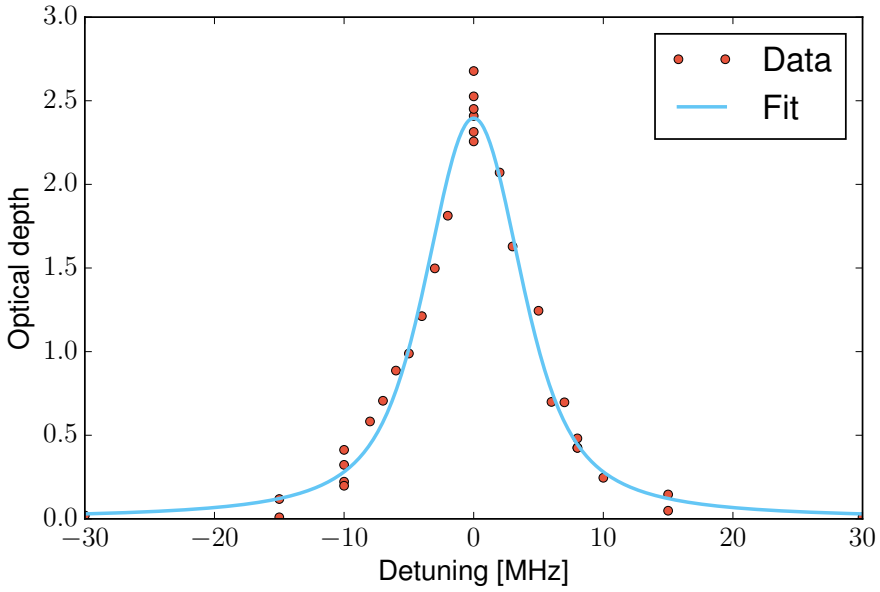

Figure J.1.: *OD as a function of the probe detuning. Data points are derived using the long-term linear fit procedure described in Chapter 18 for the June 8 data set.*

BIBLIOGRAPHY

[A. Kramida *et al.*, 2015] A. Kramida, Yu. Ralchenko, J. Reader, and and NIST ASD Team (2015). NIST Atomic Spectra Database (ver. 5.3), [Online]. Available: http://physics.nist.gov/asd [2015, December 6]. National Institute of Standards and Technology, Gaithersburg, MD. (Cit. on p. 110).

[Appel, Windpassinger, *et al.*, 2009] J. Appel, P. J. Windpassinger, D. Oblak, U. B. Hoff, N. Kjaergaard, and E. S. Polzik (2009). "Mesoscopic atomic entanglement for precision measurements beyond the standard quantum limit." *Proceedings of the National Academy of Sciences* **106.27**, pp. 10960–10965. DOI: 10.1073/pnas.0901550106 (cit. on pp. 2, 228).

[Appel, MacRae, *et al.*, 2009] J. Appel, A. MacRae, and A. I. Lvovsky (2009). "A versatile digital GHz phase lock for external cavity diode lasers." *Measurement Science and Technology* **20.5**, p. 055302. DOI: 10.1088/0957-0233/20/5/055302 (cit. on p. 106).

[Bachor *et al.*, 2004] H.-A. Bachor and T. C. Ralph (2004). *A Guide to Experiments in Quantum Optics*. Wiley-VCH (cit. on p. 125).

[Bajcsy *et al.*, 2009] M. Bajcsy, S. Hofferberth, V. Balic, T. Peyronel, M. Hafezi, A. S. Zibrov, V. Vuletic, and M. D. Lukin (2009). "Efficient All-Optical Switching Using Slow Light within a Hollow Fiber." *Physical Review Letters* **102.20**, p. 203902. DOI: 10.1103/PhysRevLett.102.203902 (cit. on p. 1).

[Bajcsy *et al.*, 2003] M. Bajcsy, A. S. Zibrov, and M. D. Lukin (2003). "Stationary pulses of light in an atomic medium." *Nature* **426**, pp. 638–641. URL: http://cds.cern.ch/record/684564 (cit. on p. 255).

[Baker *et al.*, 2011] C. Baker and M. Rochette (2011). "A generalized heat-brush approach for precise control of the waist profile in fiber tapers." *Optical Materials Express* **1.6**, pp. 1065–1076. URL: http://www.opticsinfobase.org/abstract.cfm?URI=ome-1-6-1065 (cit. on p. 54).

[Balykin *et al.*, 2004] V. I. Balykin, K. Hakuta, F. Le Kien, J. Q. Liang, and M. Morinaga (2004). "Atom trapping and guiding with a subwavelength-diameter optical fiber." *Physical Review A* **70.1**, p. 011401. DOI: 10.1103/PhysRevA.70.011401 (cit. on pp. 1, 109).

[Béguin *et al.*, 2014] J.-B. Béguin, E. M. Bookjans, S. L. Christensen, H. L. Sørensen, J. H. Müller, E. S. Polzik, and J. Appel (2014). "Gen-

eration and Detection of a Sub-Poissonian Atom Number Distribution in a One-Dimensional Optical Lattice." *Physical Review Letters* **113.26**, p. 263603. DOI: 10.1103/PhysRevLett.113.263603 (cit. on pp. 1, 109, 133, 135, 153).

[Béguin, 2015] J.-B. Béguin (2015). "A one-dimensional quantum interface between a few atoms and weak light." PhD thesis. Niels Bohr Institute (cit. on pp. 9, 22, 78, 103, 105, 113, 119, 125, 126, 133, 135, 153, 233, 235).

[Birkl *et al.*, 1995] G. Birkl, M. Gatzke, I. H. Deutsch, S. L. Rolston, and W. D. Phillips (1995). "Bragg Scattering From Atoms in Optical Lattices." *Physical Review Letters* **75.15**, pp. 2823–2826. DOI: 10.1103/PhysRevLett.75.2823 (cit. on pp. 175, 181, 185, 187).

[Birks *et al.*, 1992] T. A. Birks and Y. W. Li (1992). "The shape of fiber tapers." *Journal of Lightwave Technology* **10.4**, pp. 432–438. URL: http://links.isiglobalnet2.com/gateway/Gateway.cgi?GWVersion=2&SrcAuth=mekentosj&SrcApp=Papers&DestLinkType=FullRecord&DestApp=WOS&KeyUT=A1992HR22000007 (cit. on pp. 54, 56).

[Bojor, 2005] L. Bojor (2005). *Fiber modes*. URL: http://www.mathworks.com/matlabcentral/fileexchange/9126-fiber-modes (cit. on p. 14).

[Boyd, 2008] R. Boyd (2008). *Nonlinear Optics*. Nonlinear Optics Series. Elsevier Science. ISBN: 9780080485966 (cit. on pp. 9, 253).

[Baade, 2009] A. Baade (2009). "Light induced trapping potential for neutral atoms by mode interference of a blue detuned light field in ultra thin fibres." PhD thesis. Diploma (cit. on p. 22).

[Cassany, 2009] G. S. Cassany (2009). "Cold atom physics using ultra-thin optical fibres." PhD thesis. University of Bonn (cit. on pp. 9, 12, 22).

[Chang *et al.*, 2013] D. E. Chang, J. I. Cirac, and H. J. Kimble (2013). "Self-Organization of Atoms along a Nanophotonic Waveguide." *Physical Review Letters* **110.11**, p. 113606. DOI: 10.1103/PhysRevLett.110.113606 (cit. on p. 2).

[Chang *et al.*, 2012] D. E. Chang, L. Jiang, A. V. Gorshkov, and H. J. Kimble (2012). "Cavity QED with atomic mirrors." *New Journal of Physics* **14.6**, p. 063003. DOI: 10.1088/1367-2630/14/6/063003 (cit. on pp. 2, 203).

[Chang *et al.*, 2007] D. E. Chang, A. S. Sørensen, E. A. Demler, and M. D. Lukin (2007). "A single-photon transistor using nanoscale surface plasmons." *Nature Physics* **3.11**, pp. 807–812. DOI: 10.1038/nphys708 (cit. on pp. 204, 257).

[Choi *et al.*, 2010] K. S. Choi, A. Goban, S. B. Papp, S. J. van Enk, and H. J. Kimble (2010). "Entanglement of spin waves among four quantum memories." *Nature* **468.7322**, pp. 412–416. DOI: 10.1038/nature09568 (cit. on p. 228).

[Christensen *et al.*, 2014] S. L. Christensen, J. B. Béguin, E. Bookjans, H. L. Sørensen, J. H. Müller, J. Appel, and E. S. Polzik (2014). "Quantum interference of a single spin excitation with a macroscopic atomic ensemble." *Physical Review A* **89.3**, p. 033801. DOI: 10.1103/PhysRevA.89.033801 (cit. on p. 229).

[Christensen *et al.*, 2013] S. L. Christensen, J. B. Béguin, H. L. Sørensen, E. Bookjans, D. Oblak, J. H. Müller, J. Appel, and E. S. Polzik (2013). "Toward quantum state tomography of a single polariton state of an atomic ensemble." *New Journal of Physics* **15.1**, p. 015002. DOI: 10.1088/1367-2630/15/1/015002 (cit. on pp. 228, 229).

[Christensen, 2014] S. L. Christensen (2014). "Generation of exotic quantum states of a cold atomic ensemble." PhD thesis. Niels Bohr Institute. URL: http://quantop.nbi.ku.dk/publications/thesis/ (cit. on pp. 78, 133, 135, 153).

[Chu *et al.*, 1986] S. Chu, J. E. Bjorkholm, A. Ashkin, and A. Cable (1986). "Experimental Observation of Optically Trapped Atoms." *Physical Review Letters* **57.3**, pp. 314–317. DOI: 10.1103/PhysRevLett.57.314 (cit. on p. 108).

[Cirac *et al.*, 1997] J. Cirac, P. Zoller, H. Kimble, and H. Mabuchi (1997). "Quantum state transfer and entanglement distribution among distant nodes in a quantum network." *Physical Review Letters* **78.16**, pp. 3221–3224. URL: http://authors.library.caltech.edu/2635/1/CIRprl97.pdf (cit. on pp. 1, 228).

[Deutsch *et al.*, 1995] I. H. Deutsch, R. J. C. Spreeuw, S. L. Rolston, and W. D. Phillips (1995). "Photonic band gaps in optical lattices." *Physical Review A* **52.2**, pp. 1394–1410. DOI: 10.1103/PhysRevA.52.1394 (cit. on pp. 181, 203).

[Dewynne *et al.*, 1989] J. Dewynne, J. R. Ockendon, and P. Wilmott (1989). "On a mathematical model for fiber tapering." *Siam Journal on Applied Mathematics* **49.4**, pp. 983–990. URL: http://gateway.webofknowledge.com/gateway/Gateway.cgi?GWVersion=2&SrcAuth=mekentosj&SrcApp=Papers&DestLinkType=FullRecord&DestApp=WOS&KeyUT=A1989AH66300001 (cit. on pp. 53, 54).

[Ding *et al.*, 2010] L. Ding, C. Belacel, S. Ducci, G. Leo, and I. Favero (2010). "Ultralow loss single-mode silica tapers manufactured by a microheater." *Applied Optics* **49.13**, pp. 2441–2445. URL: http://www.opticsinfobase.org/abstract.cfm?URI=ao-49-13-2441 (cit. on pp. 50, 59).

[Douglas *et al.*, 2015] J. S. Douglas, H. Habibian, C. L. Hung, A. V. Gorshkov, H. J. Kimble, and D. E. Chang (2015). "Quantum many-body models with cold atoms coupled to photonic crystals." *Nature Photonics*, pp. 1–6. DOI: 10.1038/nphoton.2015.57 (cit. on p. 2).

[Duan *et al.*, 2001] L. Duan, M. Lukin, J. Cirac, and P. Zoller (2001). "Long-distance quantum communication with atomic ensembles and linear optics." *Nature* **414.6862**, pp. 413–418. URL: http://links.isiglobalnet2.com/gateway/Gateway.cgi?GWVersion=2&SrcAuth=mekentosj&SrcApp=Papers&DestLinkType=FullRecord&DestApp=WOS&KeyUT=000172304500034 (cit. on p. 1).

[Eggers *et al.*, 1994] J. Eggers and T. F. Dupont (1994). "Drop formation in a one-dimensional approximation of the Navier-Stokes equation." *Journal of Fluid Mechanics* **262**, pp. 205–221. DOI: 10.1017/S0022112094000480 (cit. on p. 53).

[Feynman, 1982] R. P. Feynman (1982). "Simulating Physics with Computers." *International Journal of Theoretical Physics* **21**, pp. 467–488. URL: http://links.isiglobalnet2.com/gateway/Gateway.cgi?GWVersion=2&SrcAuth=mekentosj&SrcApp=Papers&DestLinkType=FullRecord&DestApp=WOS&KeyUT=A1982NR25300003 (cit. on p. 2).

[Foot, 2005] C. J. Foot (2005). *Atomic physics*. Oxford master series in physics. Oxford University Press. ISBN: 9780198506966 (cit. on pp. 69, 75, 87).

[Frawley *et al.*, 2011] M. Frawley, A. Petcu-Colan, and S. Nic Chormaic (2011). "Higher Order Mode Generation in Optical Nanofibers for the Purpose of Cold Atom Trapping." *Frontiers in Optics*. URL: http://www.opticsinfobase.org/abstract.cfm?URI=FiO-2011-FMN2 (cit. on p. 49).

[Garcia-Fernandez *et al.*, 2011] R. Garcia-Fernandez, W. Alt, F. Bruse, C. Dan, K. Karapetyan, O. Rehband, A. Stiebeiner, U. Wiedemann, D. Meschede, and A. Rauschenbeutel (2011). "Optical nanofibers and spectroscopy." *Applied Physics B* **105.1**, pp. 3–15. DOI: 10.1007/s00340-011-4730-x (cit. on p. 49).

[Geyling, 1976] F. T. Geyling (1976). "Basic fluid-dynamic considerations in the drawing of optical fibers." *Bell System Technical Journal* **55.8**, pp. 1011–1056. URL: http://gateway.webofknowledge.com/gateway/Gateway.cgi?GWVersion=2&SrcAuth=mekentosj&SrcApp=Papers&DestLinkType=FullRecord&DestApp=WOS&KeyUT=A1976CH30400001 (cit. on p. 53).

[Ghatak *et al.*, 1998] A. Ghatak and K. Thyagarajan (1998). *An Introduction to Fiber Optics*. Cambridge University Press. ISBN: 9780521577854 (cit. on p. 9).

[Goban *et al.*, 2012] A. Goban, K. Choi, D. Alton, D. Ding, C. Lacroûte, M. Pototschnig, T. Thiele, N. Stern, and H. Kimble (2012). "Demonstration of a State-Insensitive, Compensated Nanofiber Trap." *Physical Review Letters* **109.3**, p. 033603. DOI: 10.1103/PhysRevLett.109.033603 (cit. on pp. 1, 109, 182, 228).

[Goban *et al.*, 2015] A. Goban, C. L. Hung, J. D. Hood, S. P. Yu, J. A. Muniz, O. Painter, and H. J. Kimble (2015). "Superradiance for Atoms Trapped along a Photonic Crystal Waveguide." *Physical Review Letters* **115.6**, p. 063601. DOI: 10.1103/PhysRevLett.115.063601 (cit. on p. 1).

[Gouraud *et al.*, 2015] B. Gouraud, D. Maxein, A. Nicolas, O. Morin, and J. Laurat (2015). "Demonstration of a Memory for Tightly Guided Light in an Optical Nanofiber." *Physical Review Letters* **114.18**, p. 180503. DOI: 10.1103/PhysRevLett.114.180503 (cit. on p. 228).

[Grimm *et al.*, 2000] R. Grimm, M. Weidemüller, and Y. N. Ovchinnikov (2000). "Optical dipole traps for neutral atoms." *Adv. At. Mol. Opt. Phys.* **42.physics/9902072**, p. 170. URL: http://cds.cern.ch/record/380296 (cit. on pp. 84, 108).

[Grover *et al.*, 2015] J. A. Grover, P. Solano, L. A. Orozco, and S. L. Rolston (2015). "Photon-correlation measurements of atomic-cloud temperature using an optical nanofiber." *Physical Review A* **92.1**, p. 013850. DOI: 10.1103/PhysRevA.92.013850 (cit. on p. 228).

[Grynberg *et al.*, 2010] G. Grynberg, A. Aspect, C. Fabre, and C. Cohen-Tannoudji (2010). *Introduction to Quantum Optics: From the Semi-classical Approach to Quantized Light*. Cambridge University Press. ISBN: 9781139490849 (cit. on pp. 70, 79, 81, 124, 125, 253).

[Hammerer *et al.*, 2010] K. Hammerer, A. S. Sørensen, and E. S. Polzik (2010). "Quantum interface between light and atomic ensembles." *Reviews of Modern Physics* **82.2**, pp. 1041–1093. DOI: 10.1103/RevModPhys.82.1041 (cit. on p. 1).

[Haroche *et al.*, 2006] S. Haroche and J. Raimond (2006). *Exploring the Quantum: Atoms, Cavities, and Photons*. Oxford Graduate Texts. OUP Oxford. ISBN: 9780198509141 (cit. on p. 1).

[Hecht, 2002] E. Hecht (2002). *Optics*. Addison-Wesley Longman, Incorporated. ISBN: 9780805385663 (cit. on pp. 7, 32).

[Hobbs, 2009] P. Hobbs (2009). *Building Electro-Optical Systems: Making It all Work*. Wiley Series in Pure and Applied Optics. Wiley. ISBN: 9780470466322 (cit. on pp. 123, 127).

[Hoffman *et al.*, 2014] J. E. Hoffman, S. Ravets, J. A. Grover, P. Solano, P. R. Kordell, J. D. Wong-Campos, L. A. Orozco, and S. L. Rolston

(2014). "Ultrahigh transmission optical nanofibers." *AIP Advances* **4.6**, p. 067124. DOI: 10.1063/1.4879799.1 (cit. on p. 49).

[Iakoupov, 2013] I. Iakoupov (2013). "Photon gates in atomic ensembles." MSc. Niels Bohr Institute (cit. on pp. 139, 253).

[Kenny *et al.*, 1991] R. P. Kenny, T. A. Birks, and K. P. Oakley (1991). "Control of optical fibre taper shape." *Electronics letters* **27.18**, pp. 1654–1656. URL: http://ieeexplore.ieee.org/xpls/abs_all.jsp?arnumber=132865 (cit. on pp. 56, 59).

[Ketterle *et al.*, 1993] W. Ketterle, K. B. Davis, M. A. Joffe, A. Martin, and D. E. Pritchard (1993). "High densities of cold atoms in a dark spontaneous-force optical trap." *Physical Review Letters* **70**, pp. 2253–2256. DOI: 10.1103/PhysRevLett.70.2253 (cit. on p. 133).

[Kittel, 2004] C. Kittel (2004). *Introduction to Solid State Physics*. 8th ed. Wiley. ISBN: 9780471415268 (cit. on p. 181).

[Kluge, 2015] K. Kluge (2015). "Characterization of Collective Spin States in Atomic Ensem- bles Trapped Around Tapered Nanofibers." MSc. Copenhagen University (cit. on p. 190).

[Knudsen *et al.*, 2014] S. Knudsen and F. T. Pedersen (2014). *Producing adiabatic fiber tapers*. BSc. URL: http://quantop.nbi.ku.dk/publications/thesis/ (cit. on pp. 46, 227).

[Krauter *et al.*, 2013] H. Krauter, D. Salart, C. A. Muschik, J. M. Petersen, H. Shen, T. Fernholz, and E. S. Polzik (2013). "Deterministic quantum teleportation between distant atomic objects." *Nature Physics* **9.6**, pp. 1–5. DOI: 10.1038/nphys2631 (cit. on p. 228).

[Kuppens *et al.*, 2000] S. Kuppens, K. Corwin, K. Miller, T. Chupp, and C. Wieman (2000). "Loading an optical dipole trap." *Physical Review A* **62.1**, p. 013406. URL: http://links.isiglobalnet2.com/gateway/Gateway.cgi?GWVersion=2&SrcAuth=mekentosj&SrcApp=Papers&DestLinkType=FullRecord&DestApp=WOS&KeyUT=000088139800073 (cit. on p. 113).

[Kurizki *et al.*, 2015] G. Kurizki, P. Bertet, Y. Kubo, K. Mølmer, D. Petrosyan, P. Rabl, and J. Schmiedmayer (2015). "Quantum technologies with hybrid systems." *Proceedings of the National Academy of Sciences* **112.13**, pp. 3866–3873. DOI: 10.1073/pnas.1419326112 (cit. on p. 229).

[Le Kien, Balykin, *et al.*, 2004] F. Le Kien, V. I. Balykin, and K. Hakuta (2004). "Atom trap and waveguide using a two-color evanescent light field around a subwavelength-diameter optical fiber." *Physical Review A* **70.6**. DOI: 10.1103/PhysRevA.70.063403 (cit. on pp. 1, 109, 110).

[Le Kien, Liang, *et al.*, 2004] F. Le Kien, J. Q. Liang, K. Hakuta, and V. I. Balykin (2004). "Field intensity distributions and polarization orientations in a vacuum-clad subwavelength-diameter optical fiber." *Optics Communications* **242.4-6**, pp. 445–455. DOI: 10.1016/j.optcom.2004.08.044 (cit. on pp. 22, 23).

[Le Kien *et al.*, 2005] F. Le Kien, S. Dutta Gupta, V. I. Balykin, and K. Hakuta (2005). "Spontaneous emission of a cesium atom near a nanofiber: Efficient coupling of light to guided modes." *Physical Review A* **72.3**. DOI: 10.1103/PhysRevA.72.032509 (cit. on p. 95).

[Le Kien *et al.*, 2014] F. Le Kien and A. Rauschenbeutel (2014). "Anisotropy in scattering of light from an atom into the guided modes of a nanofiber." *Physical Review A* **90.2**, p. 023805. DOI: 10.1103/PhysRevA.90.023805 (cit. on pp. 95–98, 145, 174).

[Lee *et al.*, 2015] J. Lee, J. A. Grover, J. E. Hoffman, L. A. Orozco, and S. L. Rolston (2015). "Inhomogeneous broadening of optical transitions of." *Journal of Physics B: Atomic, Molecular and Optical Physics* **48.16**, pp. 1–6. DOI: 10.1088/0953-4075/48/16/165004 (cit. on p. 109).

[Lodahl *et al.*, 2015] P. Lodahl, S. Mahmoodian, and S. Stobbe (2015). "Interfacing single photons and single quantum dots with photonic nanostructures." *Reviews of Modern Physics* **87.2**, pp. 347–400. DOI: 10.1103/RevModPhys.87.347 (cit. on p. 1).

[Love *et al.*, 1986] J. D. Love and W. M. Henry (1986). "Quantifying loss minimization in single-mode fibre tapers." *Electronics letters* **22.17**, pp. 912–914. DOI: 10.1049/el:19860622 (cit. on p. 18).

[Love *et al.*, 1991] J. D. Love, W. M. Henry, W. J. Stewart, R. J. Black, S. Lacroix, and F. Gonthier (1991). "Tapered single-mode fibres and devices. I. Adiabaticity criteria." *IEE Proceedings-J Optoelectronics* **138.5**, pp. 343–354. URL: http://gateway.webofknowledge.com/gateway/Gateway.cgi?GWVersion=2&SrcAuth=mekentosj&SrcApp=Papers&DestLinkType=FullRecord&DestApp=WOS&KeyUT=A1991GL16600011 (cit. on pp. 18, 20, 49).

[Lukin *et al.*, 2011] M. Lukin, L. Childress, A. S. Sørensen, and O. Unknown (2011). *Lecture notes for Modern Atomic and Optical Physics II*. URL: https://www.openrev.org/paper/lily-notes-285b-mikhail-lukin (cit. on p. 84).

[Metcalf *et al.*, 1999] H. Metcalf and P. van der Straten (1999). *Laser Cooling and Trapping*. Graduate Texts in Contemporary Physics. Springer New York. ISBN: 9780387987286 (cit. on pp. 77, 81, 84, 103).

[Miller *et al.*, 2005] R. Miller, T. E. Northup, K. M. Birnbaum, A. Boca, A. D. Boozer, and H. J. Kimble (2005). "Trapped atoms in

cavity QED: coupling quantized light and matter." *Journal of Physics B: Atomic, Molecular and Optical Physics* **38.9**, S551–S565. DOI: 10.1088/0953-4075/38/9/007 (cit. on p. 1).

[Milonni *et al.*, 1988] P. W. Milonni and J. H. Eberly (1988). *Lasers*. Wiley Series in Pure and Applied Optics. Wiley. ISBN: 9780471627319 (cit. on pp. 65, 74, 125, 128, 216).

[Milonni *et al.*, 2010] P. W. Milonni and J. H. Eberly (2010). *Laser Physics*. Wiley. ISBN: 9780470409701 (cit. on pp. 125, 253).

[Nagai *et al.*, 2014] R. Nagai and T. Aoki (2014). "Ultra-low-loss tapered optical fibers with minimal lengths." *Optics Express* **22.23**, p. 28427. DOI: 10.1364/OE.22.028427 (cit. on p. 49).

[Nielsen *et al.*, 2000] M. Nielsen and I. Chuang (2000). *Quantum Computation and Quantum Information*. Cambridge Series on Information and the Natural Sciences. Cambridge University Press. ISBN: 9780521635035 (cit. on p. 1).

[Normand *et al.*, 1982] J.-M. Normand and J. Raynal (1982). "Relations between Cartesian and spherical components of irreducible Cartesian tensors." *J.Phys.A* **A15**, p. 1437. DOI: 10.1088/0305-4470/15/5/008 (cit. on pp. 89, 239).

[Oblak, 2009] D. Oblak (2009). "Quantum State Engineering in Cold Caesium Atoms: An entangled tale of non-destructively induced collapse and squeezing of atomic states." PhD thesis. Niels Bohr Institute (cit. on p. 130).

[Ovchinnikov *et al.*, 1991] Y. B. Ovchinnikov, S. S V, and V. I. Balykin (1991). "An atomic trap based on evanescent light waves." *Journal of Physics B: Atomic, Molecular and Optical Physics* **24.14**, pp. 3173–3178. URL: http://gateway.webofknowledge.com/gateway/Gateway.cgi?GWVersion=2&SrcAuth=mekentosj&SrcApp=Papers&DestLinkType=FullRecord&DestApp=WOS&KeyUT=A1991FZ74300009 (cit. on pp. 1, 109).

[Pedersen, 2015] C. P. Pedersen (2015). MSc. Niels Bohr Institute (cit. on p. 46).

[Pricking *et al.*, 2010] S. Pricking and H. Giessen (2010). "Tapering fibers with complex shape." *Optics Express* **18.4**, pp. 3426–3437. DOI: 10.1364/OE.18.003426 (cit. on pp. 54, 58).

[Reichel *et al.*, 1999] J. Reichel, W. Hansell, and T. W. Hänsch (1999). "Atomic micromanipulation with magnetic surface traps." *Physical Review Letters* **83.17**, pp. 3398–3401. DOI: 10.1103/PhysRevLett.83.3398 (cit. on p. 228).

[Reitz *et al.*, 2014] D. Reitz, C. Sayrin, B. Albrecht, I. Mazets, R. Mitsch, P. Schneeweiss, and A. Rauschenbeutel (2014). "Backscattering properties of a waveguide-coupled array of atoms in the strongly nonparaxial regime." *Physical Review A* **89.3**, p. 031804. DOI: 10.1103/PhysRevA.89.031804 (cit. on pp. 142, 145, 168).

[Reitz *et al.*, 2013] D. Reitz, C. Sayrin, R. Mitsch, P. Schneeweiss, and A. Rauschenbeutel (2013). "Coherence Properties of Nanofiber-Trapped Cesium Atoms." *Physical Review Letters* **110.24**, p. 243603. DOI: 10.1103/PhysRevLett.110.243603 (cit. on pp. 184, 185, 187).

[Riehle, 2006] F. Riehle (2006). *Frequency Standards*. Basics and Applications. Wiley-VCH. ISBN: 9783527605958 (cit. on p. 105).

[Riley *et al.*, 2006] K. K. F. Riley, M. P. Hobson, and S. S. J. Bence (2006). *Mathematical Methods for Physics and Engineering*. Cambridge University Press. ISBN: 9780521861533 (cit. on pp. 10, 141, 258).

[Saffman *et al.*, 2009] M. Saffman, D. Oblak, J. Appel, and E. Polzik (2009). "Spin squeezing of atomic ensembles by multicolor quantum nondemolition measurements." *Physical Review A* **79.2**. DOI: 10.1103/PhysRevA.79.023831 (cit. on p. 228).

[Sakurai, 1994] J. Sakurai (1994). *Modern Quantum Mechanics*. Ed. by S. F. Tuan. Revised. Addison-Wesley. ISBN: 9780201539295 (cit. on pp. 63, 71, 72, 90, 91, 205, 245).

[Schilke *et al.*, 2011] A. Schilke, C. Zimmermann, P. W. Courteille, and W. Guerin (2011). "Photonic Band Gaps in One-Dimensionally Ordered Cold Atomic Vapors." *Physical Review Letters* **106.22**, p. 223903. DOI: 10.1103/PhysRevLett.106.223903 (cit. on p. 226).

[Schlosser *et al.*, 2002] N. Schlosser, G. Reymond, and P. Grangier (2002). "Collisional blockade in microscopic optical dipole traps." *Physical Review Letters* **89.2**, pp. 023005–023005. DOI: 10.1103/PhysRevLett.89.023005 (cit. on p. 113).

[Slama *et al.*, 2005] S. Slama, C. von Cube, B. Deh, A. Ludewig, C. Zimmermann, and P. W. Courteille (2005). "Phase-Sensitive Detection of Bragg Scattering at 1D Optical Lattices." *Physical Review Letters* **94.19**, p. 193901. DOI: 10.1103/PhysRevLett.94.193901 (cit. on p. 181).

[Slama *et al.*, 2006] S. Slama, C. von Cube, M. Kohler, C. Zimmermann, and P. W. Courteille (2006). "Multiple reflections and diffuse scattering in Bragg scattering at optical lattices." *Physical Review A* **73.2**, p. 023424. DOI: 10.1103/PhysRevA.73.023424 (cit. on pp. 174, 226).

[Snyder *et al.*, 1983] A. W. Snyder and J. Love (1983). *Optical Waveguide Theory*. Science Paperbacks, 190. Springer. ISBN: 9780412099502 (cit. on pp. 9, 12, 13, 15–17, 19, 235).

[Steck, 2003] D. Steck (2003). "Cesium D line data." *Los Alamos National Laboratory (unpublished)*. URL: http://george.ph.utexas.edu/~dsteck/alkalidata/cesiumnumbers.pdf (cit. on pp. 91, 92).

[Stiebeiner *et al.*, 2010] A. Stiebeiner, R. Garcia-Fernandez, and A. Rauschenbeutel (2010). "Design and optimization of broadband tapered optical fibers with a nanofiber waist." *Optics Express* **18.22**, pp. 22677–22685. DOI: 10.1364/OE.18.022677 (cit. on p. 49).

[Sumetsky *et al.*, 2006] M. Sumetsky, Y. Dulashko, J. M. Fini, A. Hale, and D. J. DiGiovanni (2006). "The microfiber loop resonator: Theory, experiment, and application." *Journal of Lightwave Technology* **24.1**, pp. 242–250. DOI: 10.1109/JLT.2005.861127 (cit. on p. 227).

[Szmuk *et al.*, 2015] R. Szmuk, V. Dugrain, W. Maineult, J. Reichel, and P. Rosenbusch (2015). "Stability of a trapped-atom clock on a chip." *Physical Review A* **92.1**, p. 012106. DOI: 10.1103/PhysRevA.92.012106 (cit. on p. 228).

[Sørensen *et al.*, 2014] H. L. Sørensen, E. S. Polzik, and J. Appel (2014). "Heater Self-Calibration Technique for Shape Prediction of Fiber Tapers." *Journal of Lightwave Technology* **32.10**, pp. 1886–1891. DOI: 10.1109/JLT.2014.2314319 (cit. on pp. 45–48, 52, 57–60).

[Sørensen, 2013] H. L. Sørensen (2013). "Controlling the shape of subwavelength-diameter tapered optical fibers." MSc. Niels Bohr Institute. URL: http://quantop.nbi.ku.dk/publications/thesis/ (cit. on pp. 7, 45, 46, 48–50, 52, 54, 55).

[Tong *et al.*, 2003] L. Tong, R. R. Gattass, J. B. Ashcom, S. He, J. Lou, M. Shen, I. Maxwell, and E. Mazur (2003). "Subwavelength-diameter silica wires for low-loss optical wave guiding." *Nature* **426.6968**, pp. 816–819. DOI: 10.1038/nature02193 (cit. on pp. 1, 109).

[Vetsch *et al.*, 2012] E. Vetsch, S. T. Dawkins, R. Mitsch, D. Reitz, P. Schneeweiss, and A. Rauschenbeutel (2012). "Nanofiber-Based Optical Trapping of Cold Neutral Atoms." *IEEE Journal of Selected Topics in Quantum Electronics* **18.6**, pp. 1763–1770. DOI: 10.1109/JSTQE.2012.2196025 (cit. on pp. 31, 32, 113, 184, 187).

[Vetsch *et al.*, 2010] E. Vetsch, D. Reitz, G. Sagué, R. Schmidt, S. T. Dawkins, and A. Rauschenbeutel (2010). "Optical interface created by laser-cooled atoms trapped in the evanescent field surrounding an optical nanofiber." *Physical Review Letters* **104.20**, p. 203603. DOI: 10.1103/PhysRevLett.104.203603 (cit. on pp. 1, 109, 182, 190, 228).

[Ward *et al.*, 2014] J. M. Ward, A. Maimaiti, V. H. Le, and S. N. Chormaic (2014). "Contributed Review: Optical micro- and nanofiber pulling rig." *Review of Scientific Instruments* **85.11**, 111501. DOI: http://dx.doi.org/10.1063/1.4901098 (cit. on p. 49).

[Ward *et al.*, 2006] J. M. Ward, D. G. O'Shea, B. J. Shortt, M. J. Morrissey, K. Deasy, and S. G. Nic Chormaic (2006). "Heat-and-pull rig for fiber taper fabrication." *Review of Scientific Instruments* **77.8**, p. 083105. DOI: 10.1063/1.2239033 (cit. on p. 59).

[Warken, 2007] F. Warken (2007). "Ultradünne Glasfasern als Werkzeug zur Kopplung von Licht und Materie." PhD thesis (cit. on p. 49).

[Warken *et al.*, 2008] F. Warken, A. Rauschenbeutel, and T. Bartholomäus (2008). "Fiber pulling profits from precise positioning." *Photonics Spectra* **42.3**, p. 73. URL: http://www.newport.com/Support/Magazine_Features/pdf/308_Newport%20Reprint.pdf (cit. on p. 45).

[Weidemüller *et al.*, 1998] M. Weidemüller, A. Görlitz, T. W. Hänsch, and A. Hemmerich (1998). "Local and global properties of light-bound atomic lattices investigated by Bragg diffraction." *Physical Review A* **58.6**, pp. 4647–4661. DOI: 10.1103/PhysRevA.58.4647 (cit. on p. 181).

[Wieman *et al.*, 1976] C. Wieman and T. W. Hänsch (1976). "Doppler-free laser polarization spectroscopy." *Physical Review Letters* **36.2**, pp. 1170–1173. DOI: 10.1103/PhysRevLett.36.1170 (cit. on p. 105).

[Wuttke *et al.*, 2012] C. Wuttke, M. Becker, S. Brückner, M. Rothhardt, and A. Rauschenbeutel (2012). "Nanofiber Fabry-Perot microresonator for nonlinear optics and cavity quantum electrodynamics." *Optics Letters* **37.11**, pp. 1949–1951. DOI: 10.1364/OL.37.001949 (cit. on p. 227).

[Xiang *et al.*, 2013] Z.-L. Xiang, S. Ashhab, J. Q. You, and F. Nori (2013). "Hybrid quantum circuits: Superconducting circuits interacting with other quantum systems." *Reviews of Modern Physics* **85.2**, pp. 623–653. DOI: 10.1103/RevModPhys.85.623 (cit. on p. 229).

[Xue *et al.*, 2007] S. Xue, M. A. van Eijkelenborg, G. W. Barton, and P. Hambley (2007). "Theoretical, numerical, and experimental analysis of optical fiber tapering." *Journal of Lightwave Technology* **25.5**, pp. 1169–1176. DOI: 10.1109/JLT.2007.893028 (cit. on p. 54).

LIST OF FIGURES

LIST OF TABLES

ACRONYMS

1D	one-dimensional
2D	two-dimensional
3D	three-dimensional
AC	alternating current
AOM	acousto optical modulator
BS	beam sampler
CCD	charge-coupled device
CG	Clebsch–Gordan
CMOS	complementary metal–oxide–semiconductor
CS	caesium-133
D1	transition line between the ground state and the lowest energy state of the fine-structure split first exited state
D2	transition line between the ground state and the highest energy state of the fine-structure split first exited state
DC	direct current
DM	dichroic mirror
ECDL	external cavity diode laser
EH	hybrid mode with $\mathcal{E}_z > \mathcal{H}_z$
EIT	electromagnetically induced transparency
GUI	graphical user interface
H	horizontal polarization component
HE	hybrid mode with $\mathcal{E}_z < \mathcal{H}_z$
HWP	half-wave plate
KU	University of Copenhagen
Λ	Lambda-system
LHS	left-hand side
LO	local oscillator
LP	linearly polarized

LTI	linear time-invariant
MM	Mickey-Mice – fiber polarization controller
MOT	magneto-optical trap
MZI	Mach-Zehnder interferometer
NA	numerical aperture
NBI	Niels Bohr Institute
ND	neutral density
OD	optical depth
PBS	polarizing beam-splitter
PLL	phase-locked loop
NPM	nonpolarization maintaining
QED	quantum electrodynamics
QND	quantum-nondemolition
QUANTOP	Danish Center for Quantum Optics
QWP	quarter-wave plate
RBW	resolution bandwidth
RB	rubidium-87
RHS	right-hand side
RF	radio frequency
RMS	root mean square
RW	running wave
RWA	rotating-wave approximation
SCA	strong coupling axis
SEM	scanning electron microscope
SIF	step-index fiber
SPCM	single-photon-counting module
SW	standing wave
STD	standard deviation
TE	transverse electric mode
TM	transverse magnetic mode
TOF	tapered optical fiber
V	vertical polarization component

VBW video bandwidth

WCA weak coupling axis

WP waveplate

COLOPHON

This document was typeset in LaTeX using the typographical look-and-feel `classicthesis` developed by André Miede. The graphics were made using `PGF/TikZ` and `Inkscape`. The bibliography was typeset using `biblatex`.

Final Version as of December 21, 2015 (`HLS thesis` version 1.0).